General relativistic accretion flow for a diverse class of black holes

SUBHANKAR PATRA

A thesis
submitted for the degree of

Doctor of Philosophy

Supervisor
Dr. Bibhas Ranjan Majhi

DEPARTMENT OF PHYSICS
INDIAN INSTITUTE OF TECHNOLOGY GUWAHATI
GUWAHATI - 781039, ASSAM, INDIA

TH-3714_206121049


भारतीय प्रौद्योगिकी संस्थान गुवाहाटी
Indian Institute of Technology Guwahati

General relativistic accretion flow for a diverse class of black holes

A thesis submitted by

Subhankar Patra

Supervisor: **Dr. Bibhas Ranjan Majhi**

Department of Physics
Indian Institute of Technology Guwahati

A thesis submitted to Indian Institute of Technology Guwahati in accordance with the requirements of the degree of Doctor of Philosophy in the Department of Physics.

August 11, 2025

TH-3714_206121049

भारतीय प्रौद्योगिकी संस्थान गुवाहाटी
Indian Institute of Technology Guwahati

To my parents - *for everything*
To my wife - *for being the pillar of my life*
To my teachers - *for helping me reach this far*
To my friends - *for believing in me*

Indian Institute of Technology Guwahati

STATEMENT

Subhankar Patra
Roll No.: 206121049
Department of Physics
Indian Institute of Technology Guwahati
Guwahati - 781039, Assam, India

I hereby declare that the works presented in the thesis entitled **"General relativistic accretion flow for a diverse class of black holes"** have been carried out by me under the supervision of Dr. Bibhas Ranjan Majhi at the Department of Physics, Indian Institute of Technology Guwahati, India. The materials in this thesis have not been submitted elsewhere for any other degree. The works presented in this thesis are entirely my own, unless otherwise referenced.

Subhankar Patra

Subhankar Patra

Date: August 11, 2025

TH-3714_206121049

भारतीय प्रौद्योगिकी संस्थान गुवाहाटी • Indian Institute of Technology Guwahati •

DISCLAIMER

The bibliography included in this thesis is by no means complete, but it contains the sources that I have thoroughly consulted. I apologize for inadvertently missing some research papers, review articles, and other scientific documents relevant to the focus of this thesis that should also have been cited. For illustrative purposes, some figures in this thesis are taken from other sources and properly cited.

Subhankar Patra

– Subhankar Patra

Indian Institute of Technology Guwahati

TH-3714_206121049

भारतीय प्रौद्योगिकी संस्थान गुवाहाटी • Indian Institute of Technology Guwahati •

CERTIFICATE

Dr. Bibhas Ranjan Majhi
Associate Professor
Department of Physics
Indian Institute of Technology Guwahati
Guwahati - 781039, Assam, India
Email: bibhas.majhi@iitg.ac.in

It is certified that the work contained in the thesis entitled **“General relativistic accretion flow for a diverse class of black holes”** by Mr. Subhankar Patra (Roll No.: 206121049), a Ph.D. student in the Department of Physics, Indian Institute of Technology Guwahati, has been carried out under my supervision and has not been submitted elsewhere for the award of any other degree.

Dr. Bibhas Ranjan Majhi

Date: August 11, 2025

LIST OF PUBLICATIONS

1⋆. **Properties of accretion flow in deformed Kerr spacetime**
Subhankar Patra, Bibhas Ranjan Majhi and Santabrata Das
Physics of the Dark Universe 37 (2022) 101120 [arXiv: 2202.10863 [astro-ph.HE]].

2⋆. **Accretion flow in deformed Kerr spacetime: Spectral energy distributions from free-free emission**
Subhankar Patra, Bibhas Ranjan Majhi and Santabrata Das
JCAP 01 (2024) 060 [arXiv: 2308.12839 [astro-ph.HE]].

3⋆. **General relativistic viscous accretion flow around Konoplya-Zhidenko black hole**
Subhankar Patra, Bibhas Ranjan Majhi and Santabrata Das
JHEAP 44 (2024) 371-380 [arXiv: 2407.07968 [astro-ph.HE]].

4. **Transonic accretion flow in the mini discs of a binary black hole system**
Subhankar Patra, Bibhas Ranjan Majhi and Santabrata Das
Under communication with the journal [arXiv: 2412.17108 [astro-ph.HE]].

5⋆. **Effect of dark matter halo on transonic accretion flow around a galactic black hole**
Subhankar Patra and Bibhas Ranjan Majhi
JCAP (In Press) [arXiv: 2501.07456 [astro-ph.HE]].

Note: ⋆ marked publications are included in the thesis.

WORKS PRESENTED IN THE CONFERENCES

1. Delivered a talk titled **"Properties of accretion flow in deformed Kerr spacetime"** at the *8th North East Meet of Astronomers (NEMA-VIII)* at Manipur University, India, through online mode during November 21-23, 2022.
2. Delivered a talk titled **"Properties of accretion flow in deformed Kerr spacetime"** at the *32nd meeting of Indian Association of General Relativity and Gravitation (IAGRG32)* at Indian Institute of Science Education and Research (IISER) Kolkata, India, during December 19-21, 2022.
3. Delivered a talk titled **"Spectral energy distributions for transonic accretion flow in non-Kerr spacetime"** at the *10th International Conference on Gravitation and Cosmology (ICGC 2023)* at Indian Institute of Technology Guwahati (IITG), India, during December 6-9, 2023.
4. Presented a poster titled **"Thermal bremsstrahlung emission from accretion disc in non-Kerr spacetime"** at the *32nd Texas Symposium on Relativistic Astrophysics*, at Tsung-Dao Lee Institute (TDLI), Shanghai, China, during December 10-15, 2023.
5. Delivered a talk titled **"Transonic accretion flow around a gravitational wave tested black hole"** at the *10th North East Meet of Astronomers (NEMA-X)* at Tezpur University, India, during October 23-25, 2024.

भारतीय प्रौद्योगिकी संस्थान गुवाहाटी • Indian Institute of Technology Guwahati •

ACKNOWLEDGEMENTS

This research would not have reached its current form without the consistent support, guidance, advice, and encouragement from many individuals in various capacities, whether official or otherwise. I truly believe that, collectively, they were a source of inspiration for me.

First and foremost, I would like to express my heartfelt gratitude to my supervisor, Dr. Bibhas Ranjan Majhi, for his continuous guidance and support throughout my Ph.D. journey. He provided me with the freedom to explore my research interests, tackle challenging problems, and collaborate with new individuals. I will always remember the extent of his generosity, as he created every opportunity for me to advance in my research.

I would like to extend special thanks to Prof. Santabrata Das for being a supportive and friendly collaborator. His vast expertise and invaluable advice have helped me navigate the complexities of accretion physics.

I would like to thank my doctoral committee members – Prof. Santabrata Das (Chairperson), Prof. Debaprasad Maity, and Dr. Sayan Chakrabarti – for their insightful remarks and suggestions during the yearly assessments of my research. Also, I am grateful to the instructors who taught us during the Ph.D. coursework. I appreciate the excellent teaching provided by Prof. Padma K. Padmanabhan (Computational Methods), Prof. Arunansu Sil (Quantum Field Theory), and Dr. Sayan Chakrabarti (General Theory of Relativity). I thank all the past heads of the Physics Department – Prof. Subhradip Ghosh, Prof. Perumal Alagarsamy, and the current head, Prof. Bosanta Ranjan Boruah – for their various academic supports. I thank all the technical assistants, as well as the academic and non-academic staff of the Physics Department and Academic Affairs, who assisted me in various ways throughout my research. My special acknowledgment goes to the University Grants Commission (UGC) for providing financial support through the National Eligibility Test (NET) fellowship.

I am grateful to Dr. Nishant K. Singh, Dr. Dipanjan Mukherjee, and Prof. Ranjeev Misra for hosting my visit to the Inter-University Centre for Astronomy and Astrophysics

TH-3714_206121049

(IUCAA). It was a pleasure to meet them and share ideas.

I am immensely grateful to my former and present group members, who are also my friends – Subhajit Da, Gopal Da, Soumya Da, Sudip Da, Surojit, Sumit, Mousumi, Dipankar, Bhera, Pradeep, and Mainak – for their unconditional support and encouragement, which have strengthened me during difficult times and brought joy during the good ones. Special thanks to Surojit for his help and support throughout this entire journey. I truly appreciate his dedication to assisting me at every step. His willingness to lend a helping hand made this experience much more rewarding, and I am deeply grateful for his presence throughout the process. I would like to extend special thanks to Sumit for his help in clarifying the mathematical framework of this research. He has always encouraged me to think deeper.

I would like to thank my fellow batch mates, seniors, juniors, and dear friends – Suraj (Mama), Pritiranjan, Riya, Dipendu, Indrajit, Sanjib, Sourav, Utsab, Anterdipan, Ayan, Subhasis, Akhil, Rajesh, Dipankar (Dipu), Soumen, Niloy, Abhik, Arpita, Bhoomika, Camelia, Samik, Monu, Gargi, Seshadri, Sreetama, Rajat, Rohan, Indu Da, Chiranjeeb Da, Suman, Anup, Anirban, Nisith, Balaram, Girish, Pratap, Soumen Da, Partha, and Suraj Kumar – for being a part of my Ph.D. journey. Meeting these amazing people has been a true pleasure, and I am grateful for every bit of your help throughout this voyage. Special thanks to Gargi for her support in understanding the mathematical framework of accretion physics during the initial phase of my Ph.D. I am grateful to Mama, who always had faith in me. I am fortunate to have a friend like Dipendu, whose constant support has been invaluable at every moment. I am indebted to Suraj Kumar for making my hostel feel like home.

I am deeply grateful to my wife, Aninda, whose love, unwavering support, and belief in me inspired me to pursue this Ph.D. She is one of the people who introduced me to the field of research, and this achievement is as much hers as it is mine. I am grateful to my parents for their sacrifices, boundless affection, and encouragement throughout my life. In this list, I would like to express my gratitude to my parents-in-law for their constant support and blessing. Finally, I am thankful to my sister-in-law, Anusrita, for her unconditional love, which have brought immense happiness into my life.

– Subhankar Patra

ABSTRACT

Astrophysical sources like active galactic nuclei (AGNs) and black hole X-ray binaries (BH-XRBs) emit electromagnetic radiation across all frequency domains due to the accretion of matter onto the black holes. By analyzing their spectra, we can determine the properties of the accretion disc (e.g., scale height, photon index, quasi-periodic oscillation (QPO) frequencies, etc.) as well as the spacetime parameters of the central black hole. To model these systems, the Kerr metric is often used, which is characterized by the mass and spin parameters of the black hole. In Einstein's general relativity (GR), the Kerr metric describes the geometry of an isolated, uncharged, rotating astrophysical black hole. However, in recent years, several non-Kerr metrics have been constructed in the literature for testing GR in strong-field regimes. Some of these metrics have been proposed to account for the presence of other matter fields in galaxies, such as dark matter halos. Non-Kerr metrics are described by one or more deformation parameters in addition to mass and spin. A number of studies have used these metrics to analyze electromagnetic signals from the accretion disc, providing constraints on the deformation parameters. This aspect has also been explored using shadow data from the EHT collaboration and gravitational wave data from the LIGO-Virgo collaboration. In essence, all these studies indicate that, at the current accuracy levels of the observations, various non-Kerr metric can also be compatible with the observed data (which are usually described by the Kerr metric in GR). Therefore, whether an alternative to GR is necessary remains an ongoing debate. To find the answer to this long-standing question, we need to understand the effects of these alternative metrics on different astrophysical phenomena. Furthermore, the characterization of the deformation parameters in these metrics is not yet fully understood.

Motivated by this, the first part of this thesis aims to address these concerns by studying the general relativistic accretion flows around some bottom-up non-Kerr black holes, where the exact gravity theories are unknown (e.g., the Johannsen-Psaltis (JP) and Konoplya-Zhidenko (KZ) metrics). To begin with, in Chapter 2, we investigate steady, inviscid, axisymmetric accretion flow in the JP spacetime, characterized by a single deformation parameter, ϵ. We obtain different accretion solution topologies (e.g., O, A, W, and I) by numerically solving the hydrodynamical equations. We observe that the accreting matter can experience discontinuous jumps in the flow variables, manifesting as shock waves. By studying these shock solutions, we notice that the shock radius, density compression, and temperature compression across the shock fronts are influenced by ϵ. We observe that the effective region of the shock parameter space, spanned by the specific angular momentum (λ) and energy (E), is altered by ε. In addition, a BH object can alter into a naked singularity (NkS) when ε exceeds a critical value ($\varepsilon^{\max}$), which depends on the spin a_k. For NkS object, we further investigate the accretion flow, and obtain all types of solution topologies similar to those found for BHs. Based on the nature of accretion solutions, we divide the entire $a_k - \varepsilon$ parameter space into the BH and NkS domains. We continue the study of accretion physics for the JP spacetime in Chapter 3, where we examine the spectral properties of the accretion disc. To do this, we employ the relativistic thermal bremsstrahlung emission process. For BH and NkS models, we calculate the bolometric disc luminosity (L) and spectral energy distribution (SED) associated with the accretion solutions, where I-type solutions appear to produce larger L and SED compared to the other solution topologies. Moreover, we examine the changes in the SED as a function of ε and observe that the SED modulates with ε. For a given set of flow parameters (λ,E), we compare the SEDs for the BH and NkS models and find that the SED is larger for NkS than for BH. In Chapter 4, we investigate the viscous accretion flow around a KZ black hole, which is also modeled by deforming the Kerr metric with a single deformation parameter, η_0. Due to the effects of viscosity, we obtain a new accretion solution topology, A$'$, in addition to the O, A, W, and I-type solutions. We observe that the flow exhibits shock transitions, and accordingly, we examine the impact of η_0 on the shock properties. We also analyze the SED for bremsstrahlung radiation as a function of η_0, in the presence and absence of shocks. Further, we explore the influence of η_0 on QPO frequencies, assuming the shocks are oscillating. We demonstrate that the KZ spacetime is consistent with the high-frequency QPOs commonly detected in the hard X-ray spectra of BH-XRBs. By comparing these accretion features, we characterize the JP and KZ deformations in non-Kerr metric theories.

In the second part of the thesis, Chapter 5 investigates the effect of dark matter halos on the accretion properties around supermassive black holes (SMBHs). We aim to determine if there is a way to detect the presence of dark halos in galaxies. For this purpose, we choose to study the inviscid accretion flow around the Cardoso BHs, defined by the halo mass ($M_{\rm H}$) and its length scale (a_0). The Cardoso metric represent the spacetime of a non-spinning SMBH immersed in a dark matter fluid with a Hernquist density profile. We specifically examine the role of the compactness parameter C (= $M_{\rm H}/a_0$) on the accretion features and compare them with the results for Schwarzschild BHs. We find that when the dark matter distribution concentrates near the event horizon, the thermodynamical and spectral properties of different solution topologies (O, A, I-types) significantly differ from those of the Schwarzschild BHs. In this high-compactness region, the shock properties also show significant modulation compared to those around Schwarzschild BHs. This analysis provides a valuable tool for characterizing the presence of dark matter halos at the galactic center. Finally, Chapter 6 concludes the thesis with a brief discussion of our findings and potential future applications.

TABLE OF CONTENTS

TH-3714_206121049

भारतीय प्रौद्योगिकी संस्थान गुवाहाटी • Indian Institute of Technology Guwahati •

LIST OF FIGURES

FIGURE **Page**

Indian Institute of Technology Guwahati

LIST OF TABLES

TABLE **Page**

TH-3714_206121049

भारतीय प्रौद्योगिकी संस्थान गुवाहाटी • Indian Institute of Technology Guwahati •

CHAPTER 1

INTRODUCTION

The idea that stars were the sole source of visible light was an early understanding of the cosmos. As astronomical knowledge advanced, it became clear that the universe contains many more other light emitting objects beyond just stars. Stars shine because of the nuclear fusion happening in their cores, where hydrogen atoms combine to form helium, releasing enormous amounts of energy. However, it has been proposed that not all luminous objects are powered by nuclear fusion, like stars. Compact objects such as black holes (BHs), neutron stars (NSs), and white dwarfs (WDs) can also emit vast amounts of energy, but their energy comes from a different process known as '*accretion*'. This involves matter being drawn toward the compact object by its strong gravity, and as the matter spirals in and heats up, it emits radiation in the form of X-rays, ultraviolet light, or other electromagnetic radiation, or internal/thermal energy for NSs and WDs. The astrophysical sources that include accretion are pre-main-sequence stars, semi-detached interacting binaries[1] (hereafter called interacting binaries only), active galactic nuclei (AGNs), and various types of supernovae and gamma-ray bursts. Although these objects are not as common as normal stars, they are very much essential for studying high energy events in the universe. In this thesis, we will concentrate on interacting binaries and AGNs, as they are the most well studied accretion powered systems.

In an interacting binary star system, two stars revolve around each other due to their

---

[1] Interacting binaries are classified into three categories: (a) detached binary, where neither star fills its Roche lobe; (b) semi-detached binary, where one star fills its Roche lobe; and (c) contact binary, where both stars fill their Roche lobes.

TH-3714_206121049

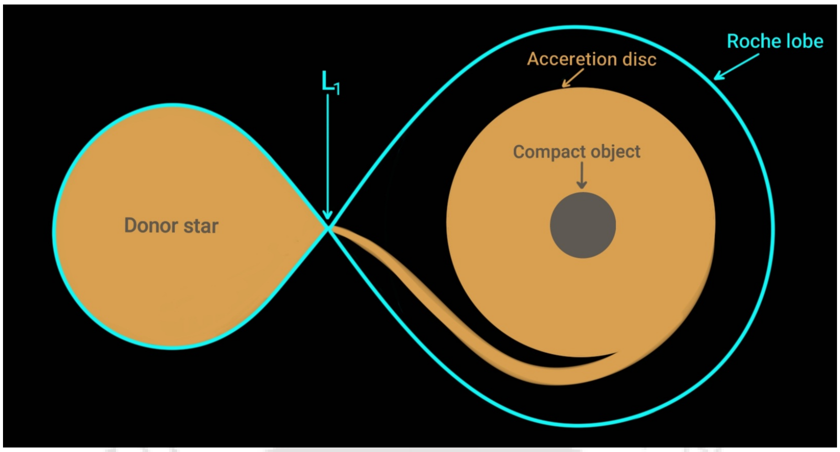

Figure 1.1: An artist's depiction of the Roche lobe overflow from a donor star onto an accreting compact object. The donor star (on the left) fills its Roche lobe, and the material flows through the First Lagrange point (L_1) before falling onto the accretor. Once the material enters the Roche lobe of the accretor (on the right), it acquires angular momentum, leading to the formation of an accretion disc around the compact object (Credit: Bhoomika Das, IIT Guwahati).

mutual gravitational pull. Many stars are known to exist in binary systems. Current data indicates that the likelihood of stars being in binary systems depends on their mass, with most massive stars being part of binaries, while the majority of low-mass stars remain single [1, 2]. The stars in a binary system are typically arranged in an orbital plane where the axis of orbit aligns with the spin axis of both stars. Also, due to the intense tidal forces exerted by each star on the other, rotation periods of the stars synchronize with their orbital period, so one side of each star always faces the other. This phenomenon is known as tidal locking in a binary system. Before the stars reach this phase, they are undergoing frictional forces because their shapes are being deformed as they move through their orbit. The friction between these deformed parts of the stars causes them to lose energy over time. Once tidal locking is achieved, the stars no longer deform in response to each other's gravity, and they stop losing energy. From a reference frame that co-rotates with the binary, the system appears stable, and it has reached a state where energy loss is minimized. In that co-rotating reference frame, the isopotential surfaces near each star appear roughly symmetrical because the gravitational influence is dominated by the respective star. But farther away from the stars, the combined gravitational pull of both stars stretches these surfaces into elliptical or oval shapes (see Fig. 4.12 in Ref. [3]). At a certain distance from the two stars, the isopotential surface is distorted into a shape that looks like two pointed lobes, called

‘*Roche lobes*’ [4, 5]. The radial point between the two stars where the Roche lobes meet is known as the First Lagrange Point, L_1. At this point the gravitational forces from the two stars and the centrifugal force due to their orbital motions balance out. The Roche lobe is roughly the region within which material is gravitationally attracted to a particular star, with negligible influence from the other star. When one of the stars in the binary system expands (e.g., it evolves into a red giant) beyond its Roche lobe, it can begin to lose material through L_1. This material will flow toward the companion star as its gravitational pull becomes stronger than the self-gravity of the star, a process known as ‘*Roche lobe overflow*’ (see Fig. 1.1). This can lead to mass transfer, where material from the donor star is transferred to the accreting star, often forming an ‘*accretion disc*’ around the companion. The nature of the receiving star plays a critical role in determining the resulting observational phenomena in binary star systems. In an Algol-type binary, the recipient is typically a main-sequence star. A cataclysmic variable (which often shows novae and type-Ia supernovae phenomena) consists of a white dwarf as the recipient. In an X-ray binary (XRB) system, the receiving star is a neutron star or a black hole.

In addition to the black hole X-ray binaries (BH-XRBs), AGNs are also very powerful astrophysical sources. AGN refers to the exceptionally bright and energetic center of a galaxy, where a supermassive black hole (SMBH) is actively accreting matter from the surrounding interstellar medium. The accretion disc around the black hole emits enormous amounts of radiation, which is what makes the nucleus of the galaxy active. AGNs can manifest in various forms, including Seyfert galaxies, radio galaxies, and quasars. While they all involve the same fundamental process of SMBH, i.e., accretion, their appearance can vary significantly depending on different factors, such as orientation of the accretion disc and relativistic jets, luminosity, distance from Earth, etc.

1.1 Accretion disc

The material accumulating around compact objects typically possesses angular momentum because of its initial motion. When gas, dust, or other substances fall toward a compact object, they generally originate from regions where the material is already in motion. In most cases, these materials carry some degree of angular momentum, which results from the rotation of stars, galaxies, or the original gas cloud as it orbits the black hole. Even if the material initially moves along a straight path, slight gravitational forces can impart angular momentum to it. As a result, the material surrounding the compact object does not fall directly inward. Instead, it tends to form a rotating structure known as '*accretion disc*'. In an accretion disc, the transport of angular momentum is a vital process that enables material within the disc to gradually spiral inward toward the central object. It has been observed that molecular viscosity alone is insufficient to transport angular momentum. One of the primary mechanisms for angular momentum transfer is viscous stress, which may arise from turbulence. However, the exact physical process that triggers turbulence remains unclear. In several studies [6, 7], authors have shown that when a magnetic field is present in the accretion disc, the interaction between the gas and the magnetic fields can give rise to the Magneto-Rotational Instability (MRI). Such MRI in the system rapidly amplifies small disturbances, triggering turbulence in the disc, known as magnetohydrodynamic (MHD) turbulence. This MHD turbulence aids in the outward transport of angular momentum, allowing material from the outer edge to move toward the inner edge of the disc. Angular momentum transport is key to the dynamics of interacting binaries and AGNs, as it governs the accretion disc's structure, stability, and luminosity. It is important to note that the angular momentum of the flow generally aligns with the orbital angular momentum of the system, which is directed along the spin axis of the central objects.

As the accreting material moves toward smaller radii, it loses gravitational potential energy. A fraction of this lost gravitational potential energy is emitted as electromagnetic radiation. Here, we present estimates for the luminosity and the flow temperature of the disc. We assume that the particles in the accretion disc move in nearly Keplerian circular orbits. Also, we apply the virial theorem, considering a classical non-relativistic system of particles. According to this theorem, half of the lost potential energy is converted into kinetic energy that rotates the material with high Keplerian velocity at a smaller radius, and the other half is transformed into heat. Moreover, we assume that the optical thickness of the disc is very high, so the thermal energy emitted at each radius of the disc can be treated as perfect black body radiation. Under these assumptions, the flow temperature at a given radial distance (r) is found to be [3, 8],

$$T(r) = \left(\frac{GM\dot{M}}{8\pi\sigma}\right)^{1/4} r^{-3/4}, \tag{1.1}$$

where G is the gravitational constant, M is the mass of the accreting compact object, $\dot{M}$ is the mass accretion rate, and σ is the Stefan-Boltzmann constant. In a steady state, $\dot{M}$ is independent of r, as any variation would lead to material accumulating at certain radii or depleting at smaller radii. From Eq. (1.1), we observe that the inner region of the accretion disc is much hotter than the outer region. Therefore, the luminosity of the disc is primarily contributed by the inner region. If we define the inner edge of the disc as the radius of the compact object (r_0) and the outer radius of the disc as $r_{\rm edge}$, then the disc luminosity is obtained as [3],

$$L = \frac{GM\dot{M}}{2}\left(\frac{1}{r_0} - \frac{1}{r_{\rm edge}}\right). \tag{1.2}$$

As $r_0 << r_{\rm edge}$, one can write Eq. (1.2) as,

$$L \simeq \frac{GM\dot{M}}{2r_0} = \eta_a \dot{M} c^2, \tag{1.3}$$

where η_a ($= r_g/(2r_0)$) refers the radiative efficiency of accretion disc, and r_g ($= GM/c^2$, c is the light speed) denotes the gravitational radius. The radiative efficiency, also known as the conversion efficiency, measures the fraction of the rest mass energy that is converted into radiation energy. Its value depends on the parameters (M, r_0) of the accreting objects. For a neutron star with a mass $M = 1.4M_\odot$ ($M_\odot$ is the Solar mass) and a radius $r_0 = 10$ km, we get $\eta_a \simeq 0.1$. Similarly, for a white dwarf with $M = M_\odot$ and $r_0 = 10^4$ km, we find $\eta_a \simeq 0.75 \times 10^{-4}$. When the accretors are black holes, η_a depends on its spin, as the spin parameter determines the location of disc inner edge r_0 [9, 10]. In general relativity (GR), particles can reach the innermost stable circular orbit (ISCO), which is located at $r_0 = r_{\rm ISCO} = 6r_g$ for non-rotating (Schwarzschild) black holes. Therefore, in this case, we obtain $\eta_a \simeq 0.06$. On the other hand, for maximally rotating black holes (i.e., spin parameter $a_k \sim 0.99$), $r_0 = r_{\rm ISCO} \simeq r_g$, and thus $\eta_a \simeq 0.5$.

Now we calculate the typical luminosity and temperature of the accretion disc in various scenarios. When the accretor is a white dwarf with the same mass and radius as mentioned above, and assuming the mass accretion rate is $\dot{M} = 10^{-9} M_\odot$ yr^{-1}, the disc luminosity can be calculated from Eq. (1.3) as $L \simeq L_\odot$, where $L_\odot$ denotes the Solar luminosity. Also, from Eq. (1.1), the temperature at the disc inner edge is obtained as $T(r_0) \simeq 5 \times 10^4$ K. Therefore, for cataclysmic variables, the thermal spectrum emitted by the disc peaks in the far ultraviolet part of the spectrum. This spectral peak is typically distinct from the spectrum of the main-sequence or red giant donor star. If the accretors are black holes or neutron stars, r_0 is much smaller compared to that of a white dwarf. For instance, if we consider a neutron star accretor, the inner edge radius of the disc is $r_0 \sim 10$ km. In this case, for a $1.4M_\odot$ neutron star with the same mass accretion rate as the cataclysmic variables mentioned earlier, we find $L \simeq 10^4 L_\odot$ and the temperature at the disc inner edge is $T_0 \simeq 9.5 \times 10^7$ K. Therefore, in these cases, the disc luminosity peaks in the X-ray regime of the electromagnetic spectrum. As a result, the name '*X-ray binaries*' is well suited for these objects.

It is important to note that the mass accretion rate of compact objects cannot become arbitrarily large; instead, it has a limiting value known as the '*Eddington accretion rate*'. To calculate it, we consider the accretion of a fully ionized hydrogen plasma onto an accretor of mass M. For an electron-proton pair in hot plasma, the gravitational force primarily acts on the proton due to its much higher mass compared to the electron. This force can be calculated at a distance r from the accretor as,

$$F_{\rm grav} \simeq \frac{GMm_p}{r^2}, \tag{1.4}$$

where m_p is the proton mass. As the photons are Thomson scattered by the electrons in the ionized medium, the electrons gain momentum from the photons. The total radiative force acting on an electron during this process is given by,

$$F_{\rm rad} = \frac{L\sigma_T}{4\pi r^2 c}, \tag{1.5}$$

where σ_T is the Thomson scattering cross section. In an accretion disc, the flow typically satisfies the condition $F_{\rm grav} > F_{\rm rad}$. If this condition is not met, the accretion flow would be halted by the radiative pressure. From equating Eqs. (1.4) and (1.5), the Eddington luminosity is derived as,

$$L_{\rm Edd} = \frac{4\pi GcMm_p}{\sigma_T} = 1.3 \times 10^{38} \frac{M}{M_\odot} \text{ erg s}^{-1}. \tag{1.6}$$

If we take a nominal disc radiative efficiency $\eta_a = 0.1$, the Eddington mass accretion rate is calculated from Eq. (1.3) as,

$$\dot{M}_{\rm Edd} = \frac{10L_{\rm Edd}}{c^2} \simeq 1.39 \times 10^{18} \frac{M}{M_\odot} \text{ gm s}^{-1}. \tag{1.7}$$

We would like to highlight that the Eddington limit serves as an useful benchmark for non-spherical accreting systems. Various accretion models have demonstrated that when the disc luminosity approaches $L_{\rm Edd}$, the system may become unstable. It is important to note that this luminosity limit is only applicable when the system is undergoing steady-state accretion. However, in non-steady cases, such as novae and supernovae, the luminosity can exceed the Eddington limit [11].

1.2 Spectral states of accretion disc

As discussed in the previous section, accretion onto black holes is regarded as the primary physical process for energy generation in AGNs and BH-XRBs. For AGNs, the disc luminosity typically ranges from $L \sim 10^{42} - 10^{48}$ erg s^{-1} [12–17], while for BH-XRBs, the disc luminosity is typically $L \sim 10^{36} - 10^{39}$ erg s^{-1} [18–24]. AGNs are believed to contain supermassive black holes, with masses ranging from $M_{\rm BH} \sim 10^6 - 10^9 M_\odot$. On the other hand, the black holes in BH-XRBs are much smaller and typically fall within the stellar-mass range, i.e., $M_{\rm BH} \sim 5 - 20 M_\odot$[2]. The energy emitted by these objects generally consists of a relatively low-energy multi-colored black body component and one or more power-law components at higher energies. Usually, BH-XRBs undergo spectral state transitions from the low-hard state (LHS) to the high-soft state (HSS) through several intermediate states, within the timescales ranging from a few days to months. In the LHS, the disc luminosity is low, but the radiative power is maximized in the high-energy power-law part. In contrast, in the HSS, the disc is luminous, but the radiative power maximizes in the low-energy thermal part of the spectra. It has been observed that the transition between spectral states follows a repetitive cycle, resembling hysteresis. In the hardness-intensity plane, this cycle forms a shape similar to the letter '*Q*', known as the '*Q-diagram*' (see Fig. 1.2) [5, 25–28].

In case of BH-XRBs, fluctuations in X-ray emission from the accretion disc are often observed, commonly referred to as quasi-periodic oscillations (QPOs) (see Ref. [18] for review). Depending on the oscillation frequencies, QPOs are generally classified into two categories: (a) low-frequency QPOs (LFQPOs), which have frequencies in the range of $0.1 \le \nu_{\rm QPO} \le 30$ Hz (e.g., a stable and persistent QPO in the range of $2-4.5$ Hz is observed in GRS 1915+105 [29]), and (b) high-frequency QPOs (HFQPOs), which have oscillation frequencies ranging from 40 Hz to a few hundred Hz (e.g., QPOs with frequencies of 300 Hz and 450 Hz have been observed in GRO J1655-40 [30, 31]). LFQPOs are classified into three categories – type-A, type-B, and type-C – based on their intrinsic properties. Type-A QPOs are characterized by weak oscillations (i.e., amplitude is very low) and a broad peak ($\nu_0/\Delta\nu_0 \le 3$, where ν_0 is the central frequency of the QPO). Moreover, type-A QPOs do not exhibit harmonics in the power density spectrum, which is commonly used to analyze QPOs. Such QPOs are usually observed in the HSS. Type-B QPOs are characterized by relatively strong and narrow peaks ($\nu_0/\Delta\nu_0 \le 6$) compared to type-A QPOs. Also, a weak second harmonic may appear alongside the fundamental frequency. These QPOs are commonly observed in the soft-intermediate spectral state. Finally, type-C QPOs are known for very strong and narrow peaks ($\nu_0/\Delta\nu_0 \le 10$). Additionally, harmonics are often observed in type-C QPOs. These QPOs are typically seen at the

---

[2] For most BH-XRBs, the black hole mass is less than $20M_\odot$. However, few cases have been detected with black hole masses exceeding $20M_\odot$.

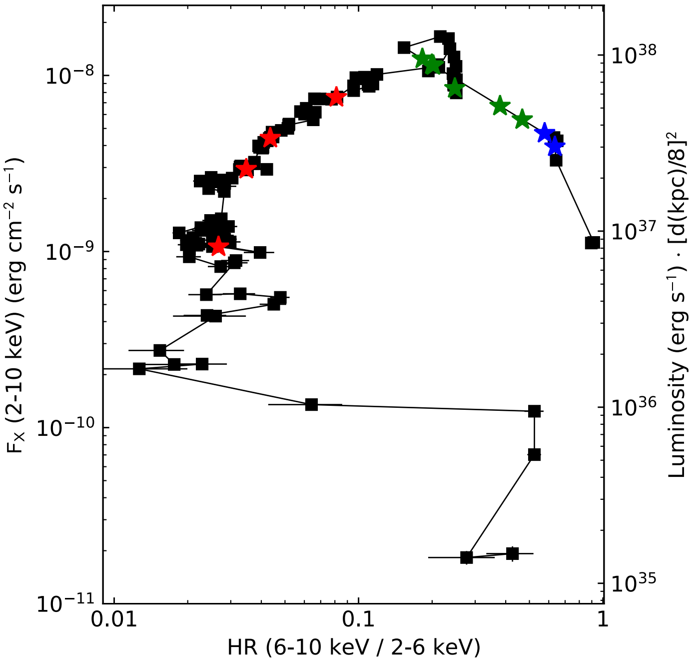

Figure 1.2: Hardness-intensity diagram for the black hole candidate MAXI J1803-298 during its outburst period, as observed by the Neutron Star Interior Composition Explorer (NICER) instrument. In this figure, the star markers represent different spectroscopic epochs. The blue, green, and red markers correspond to the hard, intermediate, and soft states, respectively [27].

bright end of the LHS and in the hard-intermediate state.

Along with accretion flows, jets or collimated outflows are commonly observed for AGNs and microquasars (which specifically refer to BH-XRBs that exhibit relativistic jets) [32–39, and references therein]. During the accretion process, a portion of the accreting matter is expelled from the disc along the axis of rotation of the black hole in the form of outflows. Outflows are thought to be the initial stage of the process, where the material is still dispersed, and that they eventually lead to the formation of jets, which are more structured and directed flows. It has been observed that the disc-jet connection is similar for both AGNs and microquasars, with only difference being the timescales, which are attributed to the difference in their black hole masses [40]. In recent years, scientists have been attempting to link the jets or outflows to the different spectral states of the accretion disc in microquasars [25, 41–43]. They found that weak, steady jets begin to form in the LHS. As the accretion disc transits into the hard-intermediate state, the strength of the jets increases. Strong jets are then ejected when the accretion disc transitions from the hard-intermediate to the soft-intermediate state. Finally, when the disc enters the HSS, the jets disappear. These observations have largely established that jets are generated from the inner region of the accretion disc.

To understand the different spectral states (e.g., LHS, HSS, and intermediate states) and their associated features, such as QPOs, jets, etc., several accretion disc models have been proposed in the literature (see the review papers [11, 44]). Although a vast number of accretion flow models have been developed to date, this field remains an active area of research, as each model has its own set of strengths and weaknesses, and none of them is complete. Indeed, all these analyses provide essential properties of the accretion disc, such as mass accretion and outflow rates, size of the post-shock corona (PSC), disc inclination angle, QPO frequency, photon index, etc. [28, 45–54]. Also, these studies offer information about the central black holes, i.e., their mass and spin [45, 47, 50, 51, 55, 56]. In the next section, we will briefly discuss few accretion models and their applicability in explaining the aforementioned spectral features.

1.3 Accretion models

In this section, we review various accretion models, starting with spherical accretion and then examining several disc accretion models.

1.3.1 Bondi (Spherical) accretion flows

The theory of accretion flow around stars from the interstellar medium was studied long ago by Hoyle and Lyttleton [57]. However, this model does not provide satisfactory results, as it considers pressure-less fluid motion around the star surface. Later, Bondi and Hoyle [58] and Bondi [59] developed a model for spherical accretion flows by incorporating gas pressure, popularly known as ‘*Bondi flows*’. This model assumes a simplified and idealized scenario in which the angular momentum of the matter is neglected. As a result, the inflowing matter moves smoothly and spherically toward a central object under its gravitational influence. In this model, the gas surrounding the compact object is initially at rest and gradually falls toward the object. As the gas approaches the object, its velocity increases, and the flow becomes directed radially inward. There is a specific radial distance from the central object, known as the Bondi radius, at which the gas begins to fall inward. The Bondi radius is given by,

$$R_B = \frac{GM}{C_s^2}, \tag{1.8}$$

where C_s is the local sound speed of the surrounding gas around the central object with mass M. In this model, the accretion flow is subsonic at large distances from the central object. However, as the flow approaches the central object, it undergoes a sonic state transition, becoming moderately supersonic near the object and remaining so until it reaches the surface of the central object. As a result, relativistic effects are often neglected in this model. However, later on, several studies [60, 61, and the references therein] introduced the general relativistic version of Bondi flows around black holes. Although Bondi accretion provides a useful baseline model for understanding accretion onto compact objects, it does not account for the observed luminosity of quasars and XRBs [62]. To address this issue, astrophysicists developed models of disc accretion, where the material accreting onto compact objects possesses significant angular momentum, preventing direct infall and thus breaking spherical symmetry. In the following section, we briefly summarize various accretion disc models.

1.3.2 Shakura-Sunyaev disc (Standard disc)

The first viable accretion disc model around black holes was proposed by Shakura and Sunyaev [63], and is known as the Shakura-Sunyaev (SS) disc or Standard disc. Later, a relativistic version of the standard disc was developed by Novikov and Thorne [64]. This disc model is based on the assumption that the angular velocity (Ω) of the flow in orbit is nearly Keplerian, i.e., $\Omega = \Omega_k$, where Ω_k is the Keplerian angular velocity. As a result, the radial velocity of the flow is negligible (completely subsonic), and most of the inflowing matter settles in the disc mid-plane. Eventually, a geometrically thin disc forms. They also consider that the accreting matter can reach up to the ISCO, with the angular momentum at the inner edge given by the Keplerian angular momentum at ISCO, i.e., $\lambda_{\rm in} = \lambda_k(\rm ISCO)$. This assumption corresponds to the condition of zero torque at ISCO. Moreover, the viscous stress responsible for the transport of angular momentum in the disc is assumed to arise from MRI. They modeled such turbulent viscosity using the α-viscosity prescription, where the $r-\phi$ component of the tangential viscous stress is written as,

$$\Pi_{r\phi} = \alpha P_{\rm tot}, \tag{1.9}$$

where α is the dimensionless viscosity parameter, and $P_{\rm tot}$ is the vertically integrated pressure, which can include both gas and radiation pressures, or either of them depending on the physical conditions. Furthermore, in this model, it is assumed that the energy from viscous dissipation ($Q_{\rm vis}$) is locally and efficiently radiated away from the disc, with a negligible fraction being advected with the flow. Therefore, most of the radiative energy of the accretion disc comes from viscous dissipation, i.e.,

$$Q_{\rm rad} = Q_{\rm vis} >> Q_{\rm adv}, \tag{1.10}$$

where $Q_{\rm rad}$ is the radiated energy, and $Q_{\rm adv}$ is the advected energy in the disc. As a consequence, the temperature of the accreting gas is much cooler than the local virial temperature. Therefore, the height of the disc remains much smaller than its radius. The underlying assumption of this model can provide the disc temperature as,

$$T(r) = 6 \times 10^7 \text{ K } M_{\rm BH}^{1/4} \dot{M}^{1/4} r^{-3/4}. \tag{1.11}$$

With this setup, the disc temperature can vary in the range of $10^4 - 10^7$ K. The standard disc is also characterized by an optically thick medium. Therefore, the disc emits as a perfect black body. Since each annulus of the disc has a different temperature (see Eq. (1.11)), the overall spectrum of the disc is the sum of all black body components from each of the annuli. As a result, the disc produces a multicolored black body spectrum as a whole. The standard disc model therefore successfully accounts for the HSS of the accretion disc, where a strong thermal component is present. However, observations show that the characteristic disc temperature can exceed 10^9 K for both AGNs and BH-XRBs (see Ref. [11] for review). Therefore, while the thermal components of the accretion disc are well handled by the SS disc model, it fails to generate the hard power-law components of the disc spectra. These hard components are believed to originate from the inner regions of the disc, where the flow is sub-Keplerian and the disc is geometrically thick. To address this, several other models have been proposed, such as the SLE, slim disc, and advection-dominated accretion flow (ADAF) models, which are capable of generating the hard power-law components.

1.3.3 SLE disc

The standard disc model was the foundation of accretion studies for many years. However, it is known to suffer from viscous and thermal instabilities under certain conditions. These instabilities can lead to the formation of a two-temperature disc, where the electron and ion temperatures are decoupled. Shapiro, Lightman, and Eardley [65] (hereafter SLE) were the pioneers in proposing a sub-Eddington accretion model, in which they found solutions for two-temperature accretion. In the accreting plasma, ions are significantly hotter than the electrons. Similar to the standard disc model, the SLE model follows the same energy balance equation (1.10). Since the disc is optically thin, the electrons are cooled through bremsstrahlung and the Comptonization of bremsstrahlung photons. In these emission processes, the electron temperature can reach up to $T_e \sim 10^9$ K. However, the ion temperature can reach the local virial temperature, $T_i \sim 10^{12}$ K. As a result, in the SLE model, the gas is much hotter than in the SS thin disc model. Due to the high thermal pressure supported by the ions, the disc remains geometrically thick. This hot disc model has successfully explained the hard X-ray and γ-ray emissions from AGNs and BH-XRBs. However, the main drawback of this model is that the accretion solutions are thermally unstable, even though they remain viscously stable [66–68]. The thermal instability arises because, if an equilibrium SLE flow is perturbed to a slightly higher temperature, its density decreases, which in turn reduces the cooling efficiency. As a result, the gas heats up further, leading to a thermal runaway instability.

1.3.4 Slim disc

The SS and SLE disc models assume that accretion is radiatively efficient. This means that all the heat produced by viscosity at a given radius is promptly radiated away. In other words, the viscous heating is locally balanced by radiative cooling, with no need for additional cooling mechanisms. However, what occurs when radiative cooling becomes inefficient, and the majority of the heat generated by viscous dissipation is carried along with the flow? Abramowicz et al. [69] first developed such an accretion formalism for high mass accretion rates. They demonstrated that when the mass accretion rate is comparable to or exceeds the Eddington accretion rate, the disc becomes optically thick so that the photon diffusion time scale ($t_{\rm diff} \sim H\tau/c$ [70], where H is the half-thickness of the disc and τ is the optical depth) exceeds the accretion time scale ($t_{\rm acc} \sim r/v$, where v is the radial velocity), i.e., $t_{\rm diff} > t_{\rm acc}$. As a result, some of the viscously generated heat is carried away with the inflowing material, which reduces the radiative cooling efficiency. Therefore, the energy balance equation can be expressed as,

$$Q_{\rm vis} = Q_{\rm rad} + Q_{\rm adv}. \tag{1.12}$$

In this model, the flow velocity is high, and the angular momentum is sub-Keplerian near the inner edge of the disc. Therefore, the flow is typically transonic in nature [71]. This means that the flow must pass through a critical point near the horizon where it transitions from a subsonic to a supersonic state. After crossing this critical point, the flow enters the black hole event horizon. Additionally, the disc is thicker compared to the SS disc model. At mass accretion rates close to the Eddington rate, the relative thickness (i.e., H/r, where H is the half-thickness of the disc at radius r) can reach a value of ~ 1 [44]. Moreover, the accreting plasma is primarily radiation pressure-dominated. Interestingly, since the dissipated heat is advected with the flow, the disc becomes thermally stable. The full relativistic version of the slim disc model was initially investigated in Beloborodov's work [72]. Subsequently, Sądowski [73] build the slim disc model for a wide range of parameters and explored its relevance to X-ray binaries. Slim discs are considered more physically realistic than thin discs for several reasons. One key reason is that they provide a more general set of solutions. In the case of low accretion rates, they converge to the standard thin disc solutions. Additionally, slim discs extend all the way to the black hole horizon, unlike thin discs, which formally terminate at the ISCO. Furthermore, the flow in slim discs can have an angular momentum profile that differs significantly from the Keplerian one (see Fig. 9 in [44]).

1.3.5 Advection dominated accretion flow (ADAF)

The ADAF, or advection-dominated accretion flow solution, also incorporates advective cooling similar to the slim disc model. However, in contrast to latter one, in this model, nearly all of the viscously dissipated energy is advected into the black hole rather than being radiated (i.e., rapid advection). Therefore, the energy balance equation of the ADAF model is given by,

$$Q_{\rm vis} = Q_{\rm adv} >> Q_{\rm rad}. \tag{1.13}$$

Also, unlike the slim disc model, ADAF is applicable to accreting systems (e.g., AGNs, BH-XRBs in the Low-Hard State) with low mass accretion rates ($\dot{M} << \dot{M}_{\rm Edd}$). Due to the extremely low radiative efficiency of the ADAF model, the disc luminosity is much lower compared to the SS and slim disc models. Here, in contrast to the cooling-dominated thin discs, the accretion solutions tend to approach the local virial temperature, making the flow significantly hotter, often referred to as a hot accretion flow (HAF) [11]. Moreover, the disc is optically thin and quasi-spherical, with $H/r < 1$ (see Fig. 12 in [44]). Their spectra are non-thermal, typically exhibiting a power-law component, often accompanied by a strong Compton component. This makes them a potential candidate for the LHS observed in X-ray binaries. Even though the disc is optically thin, the viscosity generated heat does not have sufficient time to cool locally due to the high radial velocity (sub-Keplerian angular momentum profile) and the low matter density. Since these optically thin solutions are not valid above a critical mass accretion rate, these models are unable to explain disc luminosities greater than about 10% of the Eddington luminosity

[11]. Ichimaru [74] was the first to investigate the ADAF solutions. Subsequently, these solutions were further explored by Rees et al. [75] to study the origin of jets. Later, several notable works [68, 76–83] derived ADAF solutions under the Newtonian approximation. Most of these studies found self-similar solutions (i.e., flow variables are simple functions of the radial distance r) using the Paczýnsky and Wiita pseudo potential [84]. However, the full general relativistic version of this model was later investigated in the following papers [85–87] around Kerr black holes. Since then, several works [88–90] have revisited the ADAF model, incorporating more accurate viscosity and disc height prescriptions.

As mentioned earlier, the flow angular momentum must be sub-Keplerian near the black hole in order to satisfy the inner boundary conditions imposed by the event horizon. Therefore, in addition to the SS disc (or Keplerian disc), the study of the sub-Keplerian regime is also important. Up to this point, we have discussed several accretion flow models in either the Keplerian or sub-Keplerian regimes. Now, we will discuss an accretion model that simultaneously accounts for both components, commonly known as the two-component advective flow (TCAF).

1.3.6 Two-component advective flow (TCAF)

The two-component advective flow (TCAF) is one of the successful accretion models in the literature, effectively explaining both the thermal and hard power-law components of the accretion disc spectra. This model was proposed by the authors in Ref. [91], where a Keplerian disc in the equatorial plane of the black hole is sandwiched between sub-Keplerian halo components. There are several semi-analytical studies, along with some numerical simulations of the TCAF, have analyzed the spectral and timing properties of black holes and neutron stars [92, 93]. Such sub-Keplerian flow becomes supersonic when it passes through the critical points. Usually, the flow has one critical point very close to the horizon. However, depending on the angular momentum and energy, the flow can exhibit multiple critical points. These multiple critical point solutions can give rise to shock transitions at specific radial distances between the critical points [94, 95]. During the accretion process, the inflowing rotating matter can experience centrifugal repulsion against gravity under certain physical conditions, which may trigger shock waves. A shock solution, therefore, can pass through both critical points. The shock fronts are formed at a few tens of r_g, defining the size of the post-shock corona (PSC). These shock solutions are thermodynamically favorable because they have a higher entropy content compared to shock-free solutions. The shock transition causes an increase in the density and temperature of the flow. As a result, some of the soft photons from the Keplerian disc are upscattered by the hot electrons in the PSC, producing hard X-ray radiation. Therefore, this model incorporates both thermal and hard power-law components, making it suitable for the analysis of a broad class of AGNs and BH-XRBs [96–98]. In addition, the TCAF model can also explain the properties of jets or outflows from black holes. Due to the significant thermal gradient across the shock fronts, a portion of the matter can be ejected from the disc in the form of jets or outflows [37, 38, 99–103]. Furthermore, when these shocks oscillate around their mean positions, QPOs can be observed in the disc spectrum as modulations in the X-ray spectrum of black holes [28, 104–107], as discussed in detail in Section 1.2. Therefore, the TCAF model can also provide one possible explanation for the origin of QPOs. In the subsequent chapters, we examined the shock solutions in detail. From these discussions, it is evident that all the aforementioned accretion models can provide various properties of the accretion disc and compact objects. However, we have not yet addressed the theoretical background of these models. In the next section, we will discuss this elaborately.

1.4 Overview of theoretical background of accretion

In this section, we highlight the gravitational potentials around black holes using both the Newtonian approximation and full general relativistic formalism. Black holes serve as ideal laboratories for testing the general relativity (GR) in the strong-field regime. In GR, the spacetime around black holes is highly exotic and curved. Therefore, the hydrodynamic theories of fluids around black holes are quite complex, requiring rigorous calculations to handle them accurately. To simplify the complexity, people often adopt a pseudo potential, which effectively mimics the black hole geometry outside the event horizon. Several studies have investigated the accretion dynamics around black holes under this Newtonian approximation and have produced satisfactory results. One such widely used potential for non-rotating black holes is the Paczýnsky and Wiita potential [84] (hereafter PW80), which is given by,

$$\Phi_{\rm PW}(r) = -\frac{1}{r-2}. \tag{1.14}$$

It is worth noting that the PW80 potential can reproduce the exact Keplerian angular momentum profile and ISCO position as derived in GR for Schwarzschild black holes [10]. This potential represents a simplistic situation, as it does not account for spin. However, the majority of astrophysical black holes do possess spin. To address this, several attempts have been made to find pseudo potentials for Kerr black holes. Initially, Chakrabarti and Khanna [108] (hereafter CK92) derived a pseudo potential that could potentially replicate the Kerr geometry. Later, Artemova et al. [109] (hereafter ABN96) proposed a pseudo-Kerr potential by considering the free-fall acceleration, which is written outside the event horizon as ($r > r_{\rm H}$, $r_{\rm H}$ is the horizon radius) as,

$$\Phi_{\rm ABN}(r) = \begin{cases} \frac{1}{(\beta-1)r_{\rm H}}\left[1-\left(\frac{1}{1-r_{\rm H}/r}\right)^{\beta-1}\right] & \text{for } \beta \neq 1, \\ \frac{1}{r_{\rm H}}\ln\left(1-\frac{r_{\rm H}}{r}\right) & \text{for } \beta = 1. \end{cases} \tag{1.15}$$

This potential can reproduce the accretion disc structure obtained from GR with an accuracy of about $10-20\%$, even for maximally rotating black holes (i.e., spin parameter $a_k \sim 0.99$). Then, Mukhopadhyay [110] (hereafter MU02) derived a pseudo-Kerr potential that improves the accretion disc solutions compared to the previously mentioned simplistic models. In that study, the proposed potential is found to be,

$$\Phi_{\rm MU}(r) = \int_{\infty}^{r} F(r)\,dr, \tag{1.16}$$

where the gravitational force $F(r)$ in terms of spin parameter a_k is given by,

$$F(r) = \frac{\left(r^2 - 2a_k\sqrt{r} + a_k^2\right)^2}{r^3\left((r-2)\sqrt{r}+a_k\right)^2}. \tag{1.17}$$

Note that the MU02 potential reduces to the PW80 potential (Eq. (1.14)) when $a_k = 0$. Later on, Chakrabarti and Mondal [111] (hereafter CM06) proposed an ad-hoc prescription for the pseudo-Kerr potential (modified version of CK92 potential), and it is given by,

$$\Phi_{\rm CM}(r) = -\frac{B+\sqrt{B^2-4AC}}{2A}, \tag{1.18}$$

with

$$A = \frac{\epsilon^2\lambda^2}{2x^2},\ B = -1 + \frac{\omega\epsilon^2\lambda r^2}{x^2} + \frac{2a_k\lambda}{r^2 x},\ C = 1 - \frac{1}{r-x_0} + \frac{2a_k\omega}{x} + \frac{\omega^2\epsilon^2 r^4}{2x^2}, \tag{1.19}$$

where x and r are the cylindrical and spherical radial coordinates, ϵ is the redshift factor, and λ is the specific angular momentum of the flow. Here,

$$x_0 = 0.04 + 0.97a_k + 0.085a_k^2,\ \omega = \frac{2a_k}{x^3 + a_k^2 x + 2a_k^2},\ \alpha = \frac{x^2 - 2x + a_k^2}{x^2 + a_k^2 + 2a_k^2/x}. \tag{1.20}$$

The CM06 potential does not exactly reduce to the PW80 potential for $a_k = 0$. Moreover, this potential is limited in providing satisfactory accretion properties in Kerr geometry for spins $a_k \lesssim 0.8$. It is evident that while all the aforementioned pseudo-potentials produce good results for low to moderate spin values, they fail to deliver satisfactory results for high spin values. Therefore, these potentials cannot be used to study the accretion flow of XRBs that harbor rapidly rotating black holes (e.g., Cyg X-1, LMC X-1, GRO J1655-40, etc. [112, 113]).

From the above discussion, it is clear that studying the accretion flow using the Newtonian approximation cannot accurately reproduce the true dynamics. This highlights the need for the relativistic hydrodynamics in curved spacetime. In the literature, there are numerous accretion models around Schwarzschild and Kerr black holes within a relativistic hydrodynamic set up. In the early seventies, Novikov and Thorne [64] examined relativistic accretion flow around Kerr black holes. Later, the properties of transonic accretion flow were revisited by Fukue [94] within the full general relativistic framework. Riffert and Herold [114] investigated the structure of the accretion disc around Kerr black holes. The global solutions for ADAF in the Kerr background were explored by Abramowicz et al. [85]. Subsequently, Chakrabarti [86, 87] revisited the global ADAF accretion solutions for viscous flow around Kerr black holes in the weak viscosity limit. Peitz and Appl [88] also studied the viscous accretion disc around Kerr black holes and derived an accurate expression for the disc height by considering the vertical equilibrium of the disc. Note that, in this thesis, we use this disc height prescription. Soon after that, two important works by Gammie and Popham [89], and Popham and Gammie [90], found the steady-state general relativistic ADAF solutions by incorporating a proper viscosity prescription that had not been considered in Chakrabarti's work [86, 87]. Then, Chattopadhyay and Chakrabarti [115] studied the effect of plasma composition on the accretion properties around Schwarzschild black holes. Chattopadhyay and Kumar [37] depicted the outflow rates from the relativistic viscous accretion disc in the Schwarzschild background, and later on, Kumar and Chattopadhyay [38] extended this work to Kerr black holes. Thereafter, Dihingia et al. [116] highlighted the limitations of the pseudo-Newtonian approach for examining the accretion flow around Kerr black holes. In that study, the authors developed an accretion model in a generic stationary and axisymmetric background and applied it to the Kerr metric. Specifically, they reduced the momentum equations into Newtonian-like equations with an effective potential, often known as DDMC potential, which is found to be,

$$\Phi^{\rm eff}_{\rm DDMC}(r) = 1 + \frac{1}{2}\ln\left[\frac{g^2_{t\phi} - g_{tt}g_{\phi\phi}}{g_{\phi\phi} + 2\lambda g_{t\phi} + \lambda^2 g_{tt}}\right], \tag{1.21}$$

where g_{ik} is the metric tensor (i and k take values from 0 to 3) in Boyer-Lindquist coordinates (t, r, θ, ϕ) [117]. A detailed derivation of the DDMC potential is provided in Section 2.2 of the next chapter. Subsequently, Dihingia et al. [118] found the shock-induced accretion solutions for viscous flow around the Kerr black holes. In recent times, the DDMC potential has been widely used as a pseudo-Kerr potential while studying the Newtonian hydrodynamics around black holes [39, 47, 119, 120]. However, in this thesis, we study low angular momentum, advective accretion flows within the full general relativistic framework of Dihingia et al. [116, 118], instead of employing the pseudo-Newtonian approach. Soon after the discoveries by Dihingia et al. [116, 118], the relativistic accretion properties around the Kerr-Taub-NUT (KTN) charged black holes were studied by Dihingia et al. [121] and Sen et al. [122]. Thereafter, in the context of two-temperature accretion flows (see Section 1.3.3), Sarkar et al. [123] analyzed the effect of the interplay between viscous heating and cooling on accretion solutions around Schwarzschild black holes. Very recently, few studies on general relativistic accretion flows around Kerr black holes have been explored by Mitra et al. [124, 125], considering both the radial and toroidal components of magnetic fields.

Needless to mention, all the black holes (e.g., Kerr [117], KTN [126]) mentioned above are solutions of Einstein's equations in GR. However, several other black holes beyond GR have been proposed in the literature (e.g., Kerr-Sen black holes [127], Einstein-dilaton-Gauss-Bonnet black holes [128], Chern-Simons black holes [129]). The purpose of proposing these alternative prescriptions is discussed in the next section.

1.5 The need for alternative gravity theories beyond general relativity

GR continues to be the most successful theory to date, offering predictive power across a wide range of astrophysical and cosmological phenomena [130, and references therein]. Within the GR framework, certain observations, such as galaxy rotation curves, dynamics of galaxy clusters, gravitational lensing, and cosmic microwave background, can only be explained by an invisible form of matter known as dark matter [131–137]. Additionally, the accelerated expansion of the universe is attributed to a mysterious force called dark energy within the same framework [138, 139]. While these explanations are effective, the major issues lie in the fact that the nature of dark matter and dark energy remains unknown, and there is no direct evidence for either. To address these mysteries, theorists have developed alternative models to GR, such as Tensor-Vector-Scalar (TeVeS) [140], f(R) gravity (where R is the Ricci scalar) [141], Chern-Simons (CS) gravity [129], and Scalar-Gauss-Bonnet (SGB) gravity [142]. These theories modify gravity itself, eliminating the need to invoke dark matter or dark energy altogether. In addition to addressing large-scale phenomena, GR also requires modifications at small scales, particularly near singularities or the origin of the universe (i.e., Big Bang), as it does not incorporate quantum mechanics. In this context, CS and SGB gravity theories serve as rich and promising extensions of GR, offering potential quantum gravity effects. These alternative gravity theories can also yield new black hole solutions that differ from those predicted by standard GR [143]. Their structures are modified, and as a result, additional complexity arises. For instance, in SGB gravity, these solutions may exhibit new features, such as scalar hair (non-trivial scalar field configurations outside the black hole), which is a notable departure from standard GR, where black holes are thought to be bald (i.e., no scalar field outside them).

There have been numerous observational tests of GR in regimes where gravitational fields are weak, spacetime curvature is small, and characteristic velocities are not close to the speed of light. These weak-field experiments have been conducted in the Solar system [144], as well as through observations of binary pulsars [144] and cosmological phenomena [145, 146]. However, the strong-field tests of GR are more challenging due to observational difficulties, technological limitations, and the complex nature of the environments involved [147, 148]. In recent years, gravitational-wave (GW) observations by the LIGO-Virgo collaborations [130, 149–152] and electromagnetic (EM) observations by the Event Horizon Telescope (EHT) collaboration [153–158] have provided compelling evidence for the existence of black holes, as predicted by GR. These observations essentially probe GR in extreme environments of strong gravitational fields, large spacetime curvatures, and velocities close to the speed of light. However, due to the uncertainties accompanying these observations, there is still considerable room for black hole models beyond GR that could be compatible with the data. Therefore, predicting the features of such observations requires a detailed understanding of black hole spacetimes, both within and outside GR.

The no-hair theorem states that stationary and isolated black holes in GR are uniquely defined by their mass and spin, and are represented by the Kerr metric, a solution to the Einstein field equations in a vacuum [159, 160]. However, astrophysical black holes are unlikely to be perfectly stationary or exist in a perfect vacuum due to the influence of nearby objects or fields, such as stars, accretion discs, or dark matter, which could modify the Kerr nature of the black hole. As a result, it is important to test the no-hair theorem in the strong-field regime. For this purpose, several parametric deviations from the Kerr metric have been suggested in the literature, using one or few parameters known as deformation parameters [161–168]. If these non-Kerr spacetimes are solutions to the Einstein field equations, they cannot remain regular outside the event horizon. Instead, they are usually characterized by naked singularities or closed timelike curves in regions of the spacetime that are accessible to an external observer. In recent years, numerous studies have focused on placing constraints on the deformation parameters of non-Kerr metrics by analyzing the observational signatures in both EM and GW spectra of black holes [165, 167, 169–174]. Indeed, these studies suggest that the non-Kerr black hole solutions could be consistent with modern observational data. As a result, whether alternative prescriptions in metric theories of gravity are necessary will remain unresolved until more precise observational data becomes available. Therefore, it will be helpful from the observational standpoint, if the theoretical predictions corresponding to the individual astrophysical phenomenon can be listed. Moreover, the characterization of different types of parametric deviations is still incomplete, particularly regarding their impact on various astrophysical phenomena. The primary goal of this thesis is to address these issues by focusing on accretion flows onto black holes, which represent one of the most intricate black hole environments, alongside other features such as photon rings and GWs. We believe this approach can serve as a valuable tool in exploring the non-Kerr metrics.

Several potential scenarios and observations indicate the presence of dark matter surrounding the supermassive black hole at the center of galaxies, including our own Milky Way [175]. Some of these, such as anomalous galaxy rotation curves and gravitational lensing observations, have already been discussed earlier in this section. In many galaxies, the stars at the outer edges of the galaxy move at much higher velocities than would be expected if only visible matter were present. This discrepancy suggests that there is an unseen mass exerting gravitational influence. If this extra mass is concentrated around the galactic center near the supermassive black hole, it could be a sign of dark matter in that region. Additionally, the gravitational lensing effect is commonly observed in galaxies, where light from background objects is bent by the gravitational influence of a massive object, such as a black hole or a dark matter halo. If dark matter is present near the supermassive black hole, it could create additional lensing effects, distorting light in ways that are not entirely explained by the black hole alone. These scenarios point to the possibility that dark matter is not only present in the halos surrounding galaxies but might also be influencing the behavior of matter in the galactic centers, potentially around supermassive black holes. Although dark matter is invisible because it does not emit or interact with electromagnetic radiation, its presence can be inferred from its gravitational interaction with normal matter. It can influence the spacetime geometry surrounding the galactic black holes. In recent years, several studies have proposed exact analytical solutions of such black hole configuration within fully GR framework by considering various dark matter density profiles [176, 177, and references therein]. Numerous attempts have been made to investigate how the presence of a dark matter halo influences different gravitational signatures of black hole environments [178–181, and references therein]. However, the impact of dark matter halos on accretion flows around galactic black holes has not yet been extensively explored. Therefore, another goal of this thesis is to investigate how the presence of a dark matter halo can be detected by studying its influence on the accretion dynamics.

In a nutshell, the goal of this thesis is twofold. First, we aim to investigate the accretion properties in various backgrounds of deformed Kerr spacetimes. Through this analysis, we seek to provide insights into the existence and characterization of such metrics. Second, we examine the impact of a dark matter halo on the physical properties of accretion flows around galactic black holes. By comparing these properties with those of an isolated Schwarzschild black hole, we aim to offer a valuable tool for detecting the presence of dark matter. The entire thesis is structured in two parts, excluding the introduction and conclusion. Chapter 1 provides an overview of some well-known black hole accretion models. While many of the models discussed in this chapter are not directly related to the accretion model used in this thesis, their purpose is to offer a comprehensive introduction to black hole accretion, particularly for readers who may not be experts in accretion physics. In our case, we adopt a sub-Keplerian, advective accretion flow model within a full general relativistic treatment. This model accounts for the transonic nature of accretion dynamics, where the flow radial velocity crosses the sound speed at a certain radial distance. Such accretion models are crucial because they can explain a variety of observational signatures, including high-energy X-ray radiation and QPOs, which are commonly detected in the spectra of AGN and BH-XRBs. In the latter half of the introductory chapter, we raise some open questions regarding the non-Kerr black holes in different gravity theories and as well as cases where the gravitational dynamics remain unknown (known as bottom-up metrics [167]), and wrap off the chapter with some motivations behind the thesis. Now, we move on to Part I, which consists of Chapters 2, 3, and 4, where we present results regarding the transonic accretion properties in the Johannsen-Psaltis (JP) [161] and Konoplya-Zhidenko (KZ) [166] black hole spacetimes, two emerging bottom-up non-Kerr metrics. Interestingly, the JP spacetime can accommodate a naked singularity (NkS), which is a horizon-less compact object. In Chapters 2 and 3, we also investigate the dynamical and spectral properties of the accretion flow around these NkS objects. By analyzing these properties, we aim to distinguish them from BHs. Part II consists of Chapter 5, which is dedicated to studying the transonic accretion behavior of galactic black holes immersed in a dark matter halo with Hernquist density profiles (i.e., Cadoso BH model [176]). Finally, Chapter 6 presents a brief conclusion and outlines potential future directions based on our findings. Overall, this thesis is structured into four main chapters, each offering a comprehensive and in-depth analysis of the various aspects investigated.

1.6 Chapter-wise outline of the thesis

The results discussed in this thesis is based on the works in [182–185]. Here, we have summarized the research guidelines of the thesis as follows,

Chapter 2 :

Chapter 2 presents a novel approach to analyze the global structure of advective accretion flows around a generic stationary and axisymmetric spacetime in a fully general relativistic regime. In this venture, we started our work by inventigating the accretion flow in the JP deformed spacetime [161], which is described by a deformation parameter (ϵ), in addition to the mass ($M_{\rm BH}$) and spin (a_k) of the black hole. We solve the governing equations that describe the flow motion in terms of input parameters, namely energy (E), specific angular momentum (λ), and spacetime parameters ($a_{\rm k}, \epsilon$). We find that global transonic accretion solutions (e.g., O, A, W, and I-types) continue to exist in non-Kerr spacetime. Depending on the input parameters, accretion flow is seen to experience shock transition and we find that shock-induced accretion solutions are available for a wide range of the parameter space in $\lambda - E$ plane. We examine the modification of the shock parameter space with ϵ, and find that as ϵ is increased, the effective region of the parameter space is reduced, and gradually shifted towards the higher λ and lower E domain. We also noticed that as the JP deformation increases, critical points are formed at the smaller radii. Consequently, the shock front recedes away from the horizon, resulting in a decrease in the change of flow variables such as density, temperature, etc., across the shock fronts. Interestingly, we found that beyond a critical value of ϵ, the nature of central object alters from BH to NkS. We analyzed the accretion dynamics for NkS model as well, where we isolated the BH and NkS objects in the light of the behavior accretion solutions.

Chapter 3:

We have seen in the previous chapter that the deformation of JP spacetime can significantly affect accretion properties, particularly some dynamic and thermodynamic features. However, the spectral characteristics of the disc have yet to be explored. The study of spectral features from the accretion flow around compact objects is a powerful tool to probe the spacetime geometry in the strong gravity regime. Keeping this in mind, in Chapter 3, we study the spectral features of accretion flow in the JP spacetime. In doing so, we numerically solve the governing equations that describe the flow motion around the compact objects in a full general relativistic framework, where the spin a_k and deformation parameter ε demonstrate the nature of the central source, namely black hole or naked singularity. With this, we obtain O, A, W and I-types global accretion solutions by varying the energy E and angular momentum λ of the relativistic accretion flow, and examine the role of thermal bremsstrahlung emission in studying the spectral energy distributions (SEDs) of the accretion disc. We divide the parameter space in $\lambda - E$ plane in terms of the different classes of accretion solutions for the BH and NkS models. We further calculate the bolometric disc luminosity (L) corresponding to these accretion solutions, and observe that I-type solutions yield higher L and SEDs than the remaining types of solutions for both BH and NkS models. For BH model, SEDs for W and I-type solutions differ significantly from the results for O and A-type solutions for low E values. On the contrary, for NkS model, SEDs for different accretion solutions are almost identical in the whole parameter space of λ and E. We also examine the effect of ε on the SEDs and observe that a non-Kerr BH yields higher SEDs than the usual Kerr BH. In the end, for accretion solutions of identical λ and E, we compare the SEDs obtained from BH and NkS models, and find that NkS objects produce more luminous power spectra than the BHs.

Chapter 4:

Chapter 4 investigates the the properties of accretion flows around the KZ black hole [166], another non-Kerr BH recently proposed by deforming the Kerr metric with a single deformation parameter (η_0) to test the no-hair theorem using GW observations. The dynamical equations describing the general relativistic viscous accreting flow are solved self-consistently to find the transonic accretion solutions in terms of global constants, such as energy (E), angular momentum ($\mathscr{L}$), viscosity parameter (α), spin (a_k), and deformation parameter (η_0). We obtain five distinct types of accretion solutions (O, A, A$'$, W, and I-types), and observe that those solutions are not unique but rather continue to exist for wide range of parameter spaces in the $\mathscr{L}-E$ plane. Furthermore, we find that the viscous accretion flows can harbor shock waves when the relativistic shock conditions are satisfied. Consequently, the shock-induced global accretion solutions are obtained, and the effect of η_0 on shock properties, such as shock radius ($r_{\rm sh}$) and change in electron temperature ($T_{\rm e}$) across the shock front are investigated. Moreover, we calculate the spectral energy distributions (SEDs) of accretion flow using the relativistic thermal bremsstrahlung emission coefficient and study the modification of SEDs due to the increase of η_0 for both shock-induced and shock-free solutions. In addition, it has been noticed that the observable quantities, like QPO frequency ($\nu_{\rm QPO}$) and bolometric disc luminosity (L), are strongly dependent on η_0. Further, we phenomenologically show that the KZ black hole is consistent with the HFQPOs, commonly observed in black hole binaries and black hole candidates. Finally, we characterize the KZ and JP deformations in the light of transonic accretion physics.

Chapter 5:

In reality, supermassive black holes at the galactic centers are immersed in the dark matter halos. Since dark matter interacts gravitationally, it can alter the spacetime geometry. As a result, we expect it may influence the accretion features of the central object. Following this, in Chapter 5, we explore the effect of dark halo on accretion flow around a galactic black hole. We investigate the transonic accretion flow in the spacetime of a supermassive black hole coupled to an anisotropic dark matter fluid, as proposed by Cardoso et al. [176]. We essentially compare the accretion properties of the Cardoso BH with those of an isolated Schwarzschild BH. The Cardoso BH is described by the halo mass ($M_{\rm H}$) and its characteristic length scale (a_0). Various classes of accretion solution topologies (e.g., O, A, and I-types), including the shock solutions, are obtained by solving the dynamical equations of the flow in a fully general relativistic framework. We find that the accretion solutions are substantially influenced by the halo parameters ($M_{\rm H}, a_0$) when the dark matter distribution is concentrated near the BH horizon. In this context, we also observe that various shock properties (e.g., flow density compression and temperature compression across the shock fronts) are potentially affected by the dark halo. Furthermore, in the high compactness regime, different observational signatures of the accretion disc, like the spectral energy distribution (SED), slope of the SED, and bolometric luminosity, are found to exhibit strong deviations from the known results in the Schwarzschild BH model, particularly for shock-free solutions. However, for shock solutions, these spectral features are nearly identical to the results for Schwarzschild BHs, even for high halo compactness. Interestingly, the existing shock parameter space, defined by the flow angular momentum and energy, is largely reduced for higher halo compactness compared to that of the Schwarzschild BH. These unique features offer a possible valuable tool for characterizing the presence or absence of a dark matter halo around a galactic black hole.

Following these chapters, in Chapter 6, we present the overall conclusion of the thesis. Also, this final chapter is dedicated to exploring potential extensions of the results discussed, along with a list of new problems that could be pursued in the future.

CHAPTER 2

PROPERTIES OF ACCRETION FLOW IN JOHANNSEN-PSALTIS SPACETIME

2.1 Introduction and Motivation

The no-hair theorem highlights a key feature of Einstein's general relativity (GR): astrophysical black holes (BHs) are fully characterized by only their mass and spin. According to this theorem, the spacetime of a black hole in GR is described solely by the Kerr metric, which offers a stationary, axisymmetric, and asymptotically flat black hole solution with no closed timelike curves (CTCs) outside the event horizon [159, 186–190]. To test the no-hair theorem observationally, we need some metrics that deviate from the usual Kerr metric by one or more parameters [162, 191–194]. However, these parametric deviations often violate one of the prerequisites of this theorem, as they can introduce singularities or CTCs near the event horizon. Due to these pathologies, their applicability to the observational tests of the no-hair theorem is limited to the phenomena occurring far from the central black hole, such as the extreme mass-ratio inspirals [192–204] and the motion of stars [205, 206] and pulsars [204, 207] around the black holes. They essentially become prohibitive for tests of the no-hair theorem using observations of quasiperiodic oscillations (QPOs) in the X-ray disc spectrum, continuum spectrum of the accretion discs, fluorescent iron lines and some related phenomena [147, 160, 208–212]. This is simply because all these observations are associated with the physical processes near the event horizon, where the pathologies arise naturally. It

TH-3714_206121049

is noted that for black holes with low to moderate spins, pathologies appear well inside the photon orbit and the innermost stable circular orbit (ISCO). In these cases, it is possible to avoid them by introducing an artificial cut off boundary between the location of pathologies and the location of ISCO. However, for rapidly spinning black holes, where the ISCO radius becomes comparable to the horizon radius, such an artificial boundary cannot be placed. This restricts the applicability of all deformed Kerr metrics for testing the no-hair theorem using electromagnetic observations of black holes that do not spin rapidly. In theoretical astrophysics, finding a Kerr-like metric that includes parametric deviations while remaining free of the aforementioned pathologies for arbitrary spin values is a challenging task. In the literature, only a limited number of metrics exist that satisfy Einstein's equivalent principles [213], such as few non-rotating black holes [214] and slowly rotating black holes in modified gravity theories, e.g., Chern-Simons (CS) black holes [129, 215], and Einstein-dilaton-Gauss-Bonnet (EDGB) black holes [216]. Meanwhile, Johannsen and Psaltis [161] modeled a non-Kerr metric characterized by a single deformation parameter, in addition to the black hole's mass and spin (hereafter called the JP metric). This metric is regular everywhere outside the event horizon for the entire range of allowed spin values, as usual for the Kerr black holes. As a result, it can be applied to the observational tests of the no-hair theorem in rich black hole environments, such as accretion flows and photon rings around the black holes. For such fascinating characteristics of the JP spacetime, researchers are paying a lot of attention not only to understanding the spacetime properties of this non-Kerr metric but also the kind of phenomena close to the horizon.

To construct the JP metric, the authors followed a standard framework. They first include a deformation function, which contains infinite terms, over the Schwarzschild metric (following Ref. [214]) and then apply the Newman-Jenis algorithm [217] to convert into a rotational metric. After that, deformation terms are restricted through the observational constraints [218] on the weak-field deviations from the Kerr metric in the parameterized post-Newtonian (PPN) approach [219–221] and asymptotic flatness as well. The finally obtained metric is characterized by the mass, spin and only one deviation parameter (ε). When ε is set to zero, it is reduced to the original Kerr metric [117]. Their analysis also inflicts one valuable outcome in the calculation of the ISCO and circular photon orbits, and their dependency on the spin and deviation parameters under this proposed background. They showed that, depending on the spin parameter, the central singularity of the spacetime becomes naked for outside observers when the deviation parameter crosses some limiting value. Usually, these irregularities in spacetime are described by the negative precession of the CTCs, which are the observational signature of the naked singularity (NkS) exotic objects. In Ref. [222], the authors constrain the parameter ε to a maximum value of 19 (i.e., $\varepsilon \leq 19$) by observing Faraday rotation of the polarization angles of electromagnetic (EM) radiations emitted from the accretion disc.

In the last decade, various investigations have been performed on the JP metric. For example, Ref. [223] found the restriction to the spin parameter for non-Kerr black holes through the observational inconsistency in the radiative efficiency for luminous AGNs. In [224], the spacial topology of the event horizon for non-Kerr spacetime has been investigated. The properties of the ergosphere and the energy extraction by the Penrose process in a rotating deformed black hole are carried out in [225]. Ref. [226] analysed the strong gravitational lensing effect in a background of non-Kerr compact objects. Ref. [227] distinguished between the original Kerr black holes hypothesis and non-Kerr black holes, and tested the no-hair theorem through the spectro-polarimetric observational data of the black hole X-ray binaries (BH-XRBs). A detailed investigation of shadows and restriction to the spacetime parameters have been presented through the observation of polarization angels in [222]. The inclusion of new parametric deviation approach and its challenge to the JP metric are encountered in [164]. A review on the signatures of alternative gravity by employing the gravitational waves (GWs) from the black holes merging is presented in [228]. A general ray-tracing formalism for black hole shadow calculations and its application to several deformed black holes have been reported in [229]. The simultaneous existence of CTCs with negative precession and shadows is reported for the non-Kerr naked singular spacetime in [230]. Very recently, the properties of the accretion disc around a non-Kerr black hole without reflection symmetry have been revealed in [231]. All these works evidently indicate that the JP metic attracts huge focus on it and also gets tremendous success for different applications in gravity. However, to the best of our knowledge, no one has conveyed the hydrodynamics of the accreting matter in the background of JP compact objects. Such deficiency in the literature pushes us to serve the present work, where we explore the accretion dynamics of fluids in a spacetime of the JP metric. We expect this analysis will lead to a better understanding of the non-Kerr spacetime in the light of accretion dynamics.

In this chapter, we solve the general relativistic Euler's equation in the JP spacetime by utilizing the standard definitions of three velocities in a co-rotating frame [232]. Even in the strong-field regime, flow equations mimics the Newtonian-like equations and provide the effective potential corresponding to a gravitating object [116]. We derive the radial velocity gradient and temperature gradient equations using the relativistic equation of state (REoS) that endure variable adiabatic index. After developing the mathematical framework, our primary motivation is to express the influence of the deformed term on the flow properties. We start our analysis accommodating the effect of ε on the nature of critical points and the global transonic solutions around the black hole. Next, we separate the parameter space in specific angular momentum (λ) - energy (E) plane by means of the nature of the solution topologies and show their modifications with the input parameters. The global shock-induced accretion solutions, including their inherent properties, have been studied in detail. An important result is presented where we depict that even zero angular momentum flow (ZAMF) can possesses multiple critical points and consequently suffer the shock transitions. This eventually provides new signatures of accretion dynamics in the non-Kerr black hole spacetime. We show that for a given spin parameter (a_k), the usual black hole accretion solutions continue to present up to a maximum value of the deformation parameter ($\varepsilon^{\max}$). When $\varepsilon > \varepsilon^{\max}$, the nature of the solution changes due to the presence of an extra critical point very close to the compact object. This possibly happens as the central source seems to appear as naked singularity [121] which is examined using numerical as well as analytical means. We further calculate a parameter space spanned by a_k and ε according to the nature of accretion solution topologies around either BH or NkS state of the central objects. A comparison between obtained $\varepsilon^{\max}$ from the accretion model and calculated $\varepsilon^{\max}$ from an analytical approach to determine the event horizon shows good agreement between the two. This evidently indicates that the accretion dynamics provides an alternative window to isolate the subtle nature of the compact objects. We wish to emphasize that for the strong field modifications to GR theory, these findings can be considered observational evidence to distinguish the deformed Kerr metric from the original Kerr metric.

In the following sections, we shall start by introducing the basic general relativistic hydrodynamics that govern the accretion theory in a generic stationary, axisymmetric spacetime. Then, we shall build the mathematical framework for the JP metric and set up the critical point conditions. Further, we shall present effect of the JP deformation parameter ε on critical points, accretion solutions, and their associated parameter spaces. Thereafter, we shall analyze the shock-induced global accretion solutions, their parameter spaces, and various shock properties as a function of ε. We shall depict the accretion solutions associated with zero angular momentum flows. Next, we shall depict how ε incorporates the naked singularity exotic objects. We shall investigate the critical point analysis and transonic accretion solutions for NkS objects. Finally, we shall discuss the properties of the spacetime parameters of the JP metric.

2.2 Relativistic hydrodynamics in generic stationary and axisymmetric spacetime

2.2.1 Stationary and axisymmetric spacetime

A stationary and axisymmetric spacetime is characterized by two Killing vectors $(\partial_t, \partial_\phi)$ those commute and are mutually orthogonal: one along the time (t) direction and the other along the azimuthal angle (ϕ) direction. The remaining two basis vectors $(\partial_r, \partial_\theta)$ correspond to the radial coordinate (r) and the polar angle (θ) directions are orthogonal to the Killing vectors $(\partial_t, \partial_\phi)$. Under such a choice of mutually orthogonal coordinates (t, r, θ, ϕ), the general form of this spacetime takes the form,

$$ds^2 = g_{ik} dx^i dx^k = g_{tt} dt^2 + 2 g_{t\phi} dt d\phi + g_{\phi\phi} d\phi^2 + g_{rr} dr^2 + g_{\theta\theta} d\theta^2, \tag{2.1}$$

where g_{ik} is the metric tensor. The spacetime indices (i, k) run from 0 to 3. In this case, the metric coefficients do not explicitly depend on (t, ϕ); they are functions of (r, θ) only. Therefore, the spacetime is invariant under time translation and rotation around the axis of symmetry. Such spacetime properties are crucial in describing astrophysical objects like black holes. Not only that, it also helps to simplify the equations in GR to understand the complex black hole environments. All the non-zero components of the inverse metric tensor (g^{ik}) are calculated as [44],

$$\begin{aligned}
g^{tt} &= -\frac{g_{\phi\phi}}{g_{t\phi}^2 - g_{tt} g_{\phi\phi}}, \\
g^{t\phi} &= \frac{g_{t\phi}}{g_{t\phi}^2 - g_{tt} g_{\phi\phi}}, \\
g^{\phi\phi} &= -\frac{g_{tt}}{g_{t\phi}^2 - g_{tt} g_{\phi\phi}}, \\
g^{\theta\theta} &= \frac{1}{g_{\theta\theta}}, \\
g^{rr} &= \frac{1}{g_{rr}}.
\end{aligned} \tag{2.2}$$

We consider the curvature singular point of the black hole coincide with the origin of the coordinate system. The event horizon radius $(r_{\rm H})$ is defined by the equation $g_{rr}^{-1}(r = r_{\rm H}) = 0$. For a stationary, axisymmetric black hole, the event horizon is often described by a two-dimensional (2D) surface of revolution.

2.2.2 Basic relativistic hydrodynamics

In this section, we model the dynamics of the accretion flow in the generic spacetime described by equation (2.1). This model is based on the underlying symmetries of the spacetime and the conservation laws of general relativistic hydrodynamics. The energy-momentum tensor of a viscous fluid is given by [233],

$$T^{ik} = (e+p)u^i u^k + p g^{ik} + \pi^{ik}, \tag{2.3}$$

where e ($= \rho + \Pi$, ρ is the mass density and Π is the internal energy density) is the total energy density, p is the isotropic pressure, u^i is the four velocity, $\pi^{ik} = -2\eta\sigma^{ik}$ is the viscous stress tensor, and η is the dynamic viscosity. The shear tensor σ^{ik} can be written as [88],

$$\sigma^{ik} = \frac{1}{2}\left[(\nabla^i u^k + \nabla^k u^i + a^i u^k + a^k u^i) - \frac{2}{3}\Theta_{\rm exp}\mathfrak{h}^{ik}\right], \tag{2.4}$$

where $a^i = u^l \nabla_l u^i$ is the four acceleration, $\Theta_{\rm exp}$ ($= \nabla_l u^l$) is the expansion of fluid world line, and l takes the values from 0 to 3.

The flow hydrodynamics is primarily based on the conservation of energy-momentum tensor (T^{ik}) and the conservation of mass flux (ρu^k). These two are the basic building blocks of the dynamical equations of accretion flow, and respectively written as,

$$\nabla_k T^{ik} = 0 \tag{2.5}$$

and

$$\nabla_k(\rho u^k) = 0. \tag{2.6}$$

As the spacetime (2.1) possesses timelike (along t direction) and spacelike (along ϕ direction) Killing vectors, it is always associated with the conserved quantities. We assume that the fluid follows the spacetime symmetry along a generic Killing vector ξ^l, i.e., it obeys the equation $\xi^l \nabla_l Q = 0$, where Q refers to any fluid parameter, such as mass density, pressure, temperature, etc. The Killing equation corresponding to ξ^l is given by [234],

$$\nabla_k \xi_l + \nabla_l \xi_k = 0. \tag{2.7}$$

Using Eqs. (2.5) and (2.7), we get a new conservation equation as [116, 121, 235–237],

$$\nabla_i \left(T^i_k \xi^k\right) = 0. \tag{2.8}$$

Taking the projection of Eq. (2.5) along the four velocity vector field u^i, we get the energy equation of the flow. Subsequently, by incorporating Eq. (2.6) into the energy equation, we can express it in the form [38, 116, 121, 238, 239],

$$u_i \nabla_k T^{ik} = u^k \left(h_0 \nabla_k \rho - \nabla_k e \right) - Q^+ = 0, \tag{2.9}$$

where h_0 $(= (e+p)/\rho)$ is the specific enthalpy and Q^+ $(= -u_i \nabla_k \pi^{ik} = \pi^{ik} \sigma_{ik})$ is the viscous heating term. This equation is also known as entropy generation equation.

We define the projection operator as $\mathfrak{h}^l_i = u^l u_i + \delta^l_i$, which is perpendicular to u^i i.e., satisfy the equation $\mathfrak{h}^l_i u^i = 0$. Here, δ^l_i is the Kronecker delta and l takes the values from 0 to 3. The projection of Eq. (2.5) onto the tensor $\mathfrak{h}^l_i$ yields the momentum equation of the flow as [38, 116, 121, 238, 239],

$$\mathfrak{h}^l_i \nabla_k T^{ik} = (e+p) u^k \nabla_k u^l + \left(g^{lk} + u^l u^k \right) \nabla_k p + \mathfrak{h}^l_i \nabla_k \pi^{ik} = 0. \tag{2.10}$$

The flow assume to be steady (i.e., $\partial_t Q = 0$) and asymmetric (i.e., $\partial_\theta Q = 0$). Note that the inclusion of the viscous acceleration term ($\mathfrak{h}^l_i \nabla_k \pi^{ik}$) introduces higher-order derivatives of flow variables into the momentum equation, complicating the numerical computation. To simplify the process, we neglect the viscous acceleration term, which reduces the momentum equation to a first-order derivative of the flow variables. The authors in [89, 90] have demonstrated that gravitational acceleration is significantly higher than viscous acceleration. Hence, it is justifiable to neglect the viscous acceleration term from this perspective. Under these assumptions, the radial component of the momentum equation is obtained by putting $l = r$ in Eq. (2.10) as,

$$\begin{aligned} & 2 g_{rr} u^r \partial_r u^r + u^r u^r \partial_r g_{rr} + 2 u^r u^\theta \partial_\theta g_{rr} + 2 g_{rr} u^\theta \partial_\theta u^r - u^\theta u^\theta \partial_r g_{\theta\theta} \\ & + 2 g_{rr} \frac{(g^{rr} + u^r u^r) \partial_r p}{e+p} + 2 g_{rr} \frac{u^r u^\theta \partial_\theta p}{e+p} - u^t u^t \partial_r g_{tt} - 2 u^t u^\phi \partial_r g_{t\phi} - u^\phi u^\phi \partial_r g_{\phi\phi} = 0. \end{aligned} \tag{2.11}$$

Similarly, the polar component of the momentum equation is calculated by replacing $l = \theta$ in Eq. (2.10) as,

$$\begin{aligned} & 2 g_{\theta\theta} u^r \partial_r u^\theta - u^r u^r \partial_\theta g_{rr} + 2 u^r u^\theta \partial_r g_{\theta\theta} + 2 g_{\theta\theta} u^\theta \partial_\theta u^\theta + u^\theta u^\theta \partial_\theta g_{\theta\theta} \\ & + 2 g_{\theta\theta} \frac{\left(g^{\theta\theta} + u^\theta u^\theta \right) \partial_\theta p}{e+p} - u^t u^t \partial_\theta g_{tt} - 2 u^t u^\phi \partial_\theta g_{t\phi} - u^\phi u^\phi \partial_\theta g_{\phi\phi} = 0. \end{aligned} \tag{2.12}$$

For an accretion flow with rotating matter, the static observer frame is not a suitable choice, because it is not convenient to compare the physical three-velocity of the flow with the local sound speed. For this purpose, the ideal choice is to define an observer frame that rotates with the fluid's angular velocity Ω ($= u^\phi/u^t$), which is called the corotating frame (CRF). Also, the choice of CRF allows Eqs. (2.11) and (2.12) to be written in a form similar to the Newtonian equations [116]. Following Refs. [86–90, 232], we define the polar component of the physical three velocity as $v_{\hat\theta} = \gamma_\phi v_\theta$, where $v_\theta = \left(u^\theta u_\theta/(-u^t u_t)\right)^{1/2}$ and $\gamma_\phi = 1/(1-v_\phi^2)^{1/2}$ is the azimuthal Lorentz factor corresponding to $v_\phi = \left(u^\phi u_\phi/(-u^t u_t)\right)^{1/2}$. Similarly, the radial component of the three velocity is found to be $v_{\hat r} = v = \gamma_{\hat\theta}\gamma_\phi v_r$, where $v_r = \left(u^r u_r/(-u^t u_t)\right)^{1/2}$ and the polar Lorentz factor $\gamma_{\hat\theta} = 1/(1-v_{\hat\theta}^2)^{1/2}$. Here, the hat sign refers to measurements from CRF. With this setup, and using the normalization condition of four velocity (i.e., $u^k u_k = -1$), one can obtain [121, 239],

$$u^r u_r = v^2\gamma_v^2,\ u^\theta u_\theta = \gamma_v^2\gamma_{\hat\theta}^2 v_{\hat\theta}^2,\ u^t u_t = -\gamma_v^2\gamma_{\hat\theta}^2\gamma_\phi^2, \tag{2.13}$$

where $\gamma_v = 1/(1-v^2)^{1/2}$ is the Lorentz factor associated with radial velocity v in CRF.

Substituting Eq. (2.13) into Eqs. (2.11) and (2.12), we get the compactified forms of the radial and polar components of the momentum equation as [116],

$$\begin{aligned}&\gamma_v^2 v\partial_r v + \gamma_v^2\gamma_{\hat\theta} v_{\hat\theta}\sqrt{\frac{g_{rr}}{g_{\theta\theta}}}\partial_\theta v + \frac{\gamma_{\hat\theta} v v_{\hat\theta}}{2\sqrt{g_{rr}g_{\theta\theta}}}\partial_\theta g_{rr} - \frac{\gamma_{\hat\theta}^2 v_{\hat\theta}^2}{2g_{\theta\theta}}\partial_r g_{\theta\theta}\\&+\frac{1}{e+p}\partial_r p + \frac{\gamma_{\hat\theta} v v_{\hat\theta}}{e+p}\sqrt{\frac{g_{rr}}{g_{\theta\theta}}}\partial_\theta p + \gamma_{\hat\theta}^2\partial_r\Phi^{\rm eff} = 0\end{aligned} \tag{2.14}$$

and

$$\begin{aligned}&\gamma_{\hat\theta}^3 v\partial_r v_{\hat\theta} + \gamma_{\hat\theta}^4 v_{\hat\theta}\sqrt{\frac{g_{rr}}{g_{\theta\theta}}}\partial_\theta v_{\hat\theta} + \gamma_v^2\gamma_{\hat\theta} v^2 v_{\hat\theta}\partial_r v + \gamma_v^2\gamma_{\hat\theta}^2 v v_{\hat\theta}^2\sqrt{\frac{g_{rr}}{g_{\theta\theta}}}\partial_\theta v\\&-\frac{v}{2}\sqrt{\frac{g_{rr}}{g_{\theta\theta}}}\left(\frac{v}{g_{rr}}\partial_\theta g_{rr} - \frac{\gamma_{\hat\theta} v_{\hat\theta}}{\sqrt{g_{rr}g_{\theta\theta}}}\partial_r g_{\theta\theta}\right) + \frac{\gamma_{\hat\theta}^2 - v^2}{e+p}\sqrt{\frac{g_{rr}}{g_{\theta\theta}}}\partial_\theta p + \frac{\gamma_{\hat\theta} v v_{\hat\theta}}{e+p}\partial_r p\\&+\gamma_{\hat\theta}^2\sqrt{\frac{g_{rr}}{g_{\theta\theta}}}\partial_\theta\Phi^{\rm eff} = 0,\end{aligned} \tag{2.15}$$

where λ ($= -u_\phi/u_t$) denotes the specific angular momentum of the flow and $\Phi^{\rm eff}$ refers the effective potential of the system. The expression of $\Phi^{\rm eff}$ is presented in terms of the metric coefficients as,

$$\Phi^{\rm eff} = 1 + \frac{1}{2}\ln(\Phi),\ \Phi = \frac{g_{t\phi}^2 - g_{tt}g_{\phi\phi}}{g_{\phi\phi} + 2\lambda g_{t\phi} + \lambda^2 g_{tt}}. \tag{2.16}$$

Integrating the mass flux conservation equation (2.6) over the four volume $\sqrt{-g}\,d^4x$, the mass accretion rate of the flow is given by [38, 89, 90, 116],

$$\dot M = -\int \sqrt{-g}\,\rho u^r\, d\theta d\phi = -\frac{4\pi H\sqrt{-g}\,\rho u^r}{r}, \tag{2.17}$$

where H is the half thickness of the disc and g $(=-g_{rr}g_{\theta\theta}[g_{t\phi}^2-g_{tt}g_{\phi\phi}])$ is the determinant of metric tensor g_{ik}.

The above equations are generic for studying the accretion flow in the background of any stationary and axisymmetric spacetime. In this chapter, we shall derive those equations for the JP metric, which is of the same kind, and discuss the accretion flow properties in detail.

2.3 Flow equations governing the accretion disc in Johannsen-Psaltis spacetime

2.3.1 Governing equations

In this section, we derive accretion flow equations in the background of the Johannsen-Psaltis (JP) metric, which describes a stationary, axisymmetric non-Kerr spacetime. The JP metric is expressed in the standard Boyer-Lindquist coordinates (t,r,θ,ϕ) as [161],

$$\begin{aligned} ds^2 = & -(1-\frac{2M_{\rm BH}r}{\Sigma})[1+h(r,\theta)]dt^2 - \frac{4M_{\rm BH}ra_k\sin^2\theta}{\Sigma}[1+h(r,\theta)]dtd\phi \\ & + \frac{\Sigma[1+h(r,\theta)]}{\Delta+a_k^2h(r,\theta)\sin^2\theta}dr^2 + \Sigma d\theta^2 + \left[\Sigma + a_k^2[1+h(r,\theta)](1+\frac{2M_{\rm BH}r}{\Sigma})\sin^2\theta\right]\sin^2\theta d\phi^2, \end{aligned} \tag{2.18}$$

where $\Sigma = r^2 + a_k^2\cos^2\theta$ and $\Delta = r^2 - 2M_{\rm BH}r + a_k^2$. Here, $h(r,\theta)$ $(=\epsilon M_{\rm BH}^3 r/\Sigma^2)$ denotes the deformation that accounts the deviation of the metric under consideration from the original Kerr metric. And, $M_{\rm BH}$ and a_k $(=J/M_{\rm BH}$, J is the angular momentum of the black hole) are the mass and the spin (or rotation) parameter of the central black hole, respectively, while ϵ refers the deformation parameter. In $\epsilon \rightarrow 0$ limit, Eq. (2.18) leads to the original Kerr metric [117]. In this work, we choose a geometric unit system: $G = M_{\rm BH} = c = 1$, where G is the gravitational constant and c is the speed of light. This choice of unit system makes all the physical quantities dimensionless. Therefore, the measurements of mass, velocity, length, and time can be written in units of $M_{\rm BH}$, c, $GM_{\rm BH}/c^2$, and $GM_{\rm BH}/c^3$, respectively.

In the introduction section, we elaborately mention that the origin of the proposed form of the JP metric and its importance in explaining various observational evidences. In particular, the suggested metric (2.18) is put forward by considering the deviation of the usual Kerr solution, and the deformation parameter, measure of the spacetime deviation, is then constrained by the observational data (see e.g. [161]). Because of this, the metric is not a solution of the vacuum Einstein's equations of motion, otherwise it would render the no-hair theorem false. Under such circumstances, one is usually interested in searching for the gravity dynamics that predict such a solution. However, to date, no such concrete theory of gravity has been found that mimics the JP metric. Since the adopted spacetime introduces the deviations from the usual Kerr solution, and it has the potential to explain recent observational phenomena [173], there are growing interests to examine its influence in understanding the various astrophysical phenomena including its own physical properties. The accretion process is one of such phenomenon that is yet to be investigated for the black holes considering the above mentioned spacetime. Since the deformed Kerr metric offers novel features, the accretion dynamics are expected to be influenced. Hence, in this chapter, we intend to investigate the properties of the accretion flow in the deformed Kerr spacetime.

We present the basic equations governing the accretion flow in the JP metric (2.18) within the framework of general relativistic hydrodynamics, as discussed in Section 2.2. To avoid the mathematical complexity, the accretion flow is assumed to remain confined around the equatorial plane (i.e., $\theta = \pi/2$) of the central object. Hence, there is no transverse motion of the fluid, i.e., $u^\theta = 0$ and $\partial_\theta Q = 0$ as well. We further consider the flow to be steady, axisymmetric, and inviscid. Also, the thermal conduction and the radiative cooling are neglected in our analysis.

The JP spacetime, due to its temporal and azimuthal symmetries, is associated with two Killing vectors: $\xi^k_{(t)} = \delta^k_t$ and $\xi^k_{(\phi)} = \delta^k_\phi$. Since the fluid obey the same symmetries of the spacetime, corresponding conserved quantities are calculated from Eqs. (2.6) and (2.8) as,

$$-h_0 u_t = E \quad \text{and} \quad h_0 u_\phi = \mathscr{L}, \tag{2.19}$$

where E is the Bernoulli constant and $\mathscr{L}$ is the bulk angular momentum per unit mass of the fluid. Therefore, the specific angular momentum λ $(= -u_\phi/u_t = \mathscr{L}/E)$ remains conserved along the streamlines of the flow. Here, the time component of the covariant four velocity (u_t) is obtained from Eq. (2.13) as,

$$u_t = -\gamma_v \sqrt{\frac{(\Delta + a_k^2 h)(1+h)r}{r^3 + a_k^2(r+2)(1+h) - 4a_k\lambda(1+h) - \lambda^2(r-2)(1+h)}}. \tag{2.20}$$

The above relation is explicitly written for the metric (2.18) with $h(r, \theta = \pi/2) = \varepsilon/r^3$.

As $u^\theta = 0$, we have $v_{\hat{\theta}} = 0$ and $\gamma_{\hat{\theta}} = 1$. Therefore, the radial momentum equation (2.14) simplifies to,

$$\gamma_v^2 v \frac{dv}{dr} + \frac{1}{e+p}\frac{dp}{dr} + \left(\frac{d\Phi^{\rm eff}}{dr}\right)_\lambda = 0. \tag{2.21}$$

For the JP background (2.18), the effective potential ($\Phi^{\rm eff}$) of the system is calculated using Eq. (2.16) as,

$$\Phi^{\rm eff} = 1 + \frac{1}{2}\ln(\Phi),\ \Phi = \frac{(\Delta + a_k^2 h)(1+h)r}{r^3 + a_k^2(r+2)(1+h) - 4a_k\lambda(1+h) - \lambda^2(r-2)(1+h)}. \tag{2.22}$$

On the other hand, the polar component of the momentum equation (2.15) is trivially satisfied and therefore does not lead to any new equation. Note that for both $l = t$ and ϕ, Eq. (2.10) governs the conservation of specific angular momentum λ, which we already encountered through the spacetime Killing symmetries (see Eq. (2.19)).

The energy equation (2.9) is simplified to,

$$h_0 \frac{d\rho}{dr} - \frac{de}{dr} = 0. \tag{2.23}$$

Following the work of Ref. [240], we adopt a relativistic equation of state (REoS) that relates the total energy density (e) and pressure (p) of the flow as,

$$e = \frac{\rho f}{\tau} \quad \text{and} \quad p = \frac{2\rho\Theta}{\tau}, \tag{2.24}$$

where $\tau = 2 - \xi(1-1/\chi)$, the composition ratio $\xi = n_p/n_e$, and the mass ratio $\chi = m_e/m_p$. The number density and mass of the ith species (electron, proton) are denoted by $n_i \in \{n_e, n_p\}$ and $m_i \in \{m_e, m_p\}$, respectively. Moreover, we consider $\xi = 1$, throughout our analysis. Here, the quantity f is obtained in terms of dimensionless temperature ($\Theta = k_B T/m_e c^2$, k_B is the Boltzmann constant and T is the flow temperature in Kelvin) as,

$$f = (2-\xi)\left[1 + \Theta\left(\frac{9\Theta+3}{3\Theta+2}\right)\right] + \xi\left[\frac{1}{\chi} + \Theta\left(\frac{9\Theta+3/\chi}{3\Theta+2/\chi}\right)\right]. \tag{2.25}$$

For REoS (2.24), the polytropic index (N), the adiabatic index (Γ), and the sound speed (C_s) are defined as,

$$N = \frac{1}{2}\frac{df}{d\Theta},\ \Gamma = 1 + \frac{1}{N},\ \text{and}\ C_s^2 = \left(\frac{dp}{de}\right)_s = \frac{\Gamma p}{e+p} = \frac{2\Gamma\Theta}{f+2\Theta}, \tag{2.26}$$

where s denotes the specific entropy of the flow. Integrating Eq. (2.23) and using Eq. (2.24), the mass density is obtained as [121, 241, 242],

$$\rho = \mathcal{K} \exp(k_3)\Theta^{3/2}(3\Theta+2)^{k_1}(3\Theta+2/\chi)^{k_2}, \tag{2.27}$$

where $k_1 = 3(2-\xi)/4$, $k_2 = 3\xi/4$, $k_3 = (f-\tau)/(2\Theta)$, and $\mathcal{K}$ refers the entropy constant.

Using Eq. (2.17), the globally conserved mass accretion rate ($\dot{M}$) is given by,

$$\dot{M} = -4\pi H \rho v \gamma_v \sqrt{(\Delta + a_k^2 h)(1+h)}. \tag{2.28}$$

In the above expression, the local half thickness of the disc is calculated by considering the hydrodynamic equilibrium in the vertical direction [88, 114, 243], resulted in,

$$H = \sqrt{\frac{pr^3}{\rho F}} = \sqrt{\frac{2r^3\Theta}{\tau F}}, \tag{2.29}$$

where

$$F = \gamma_\phi^2 \frac{(r^2+a_k^2)^2 + 2\Delta a_k^2}{(r^2+a_k^2)^2 - 2\Delta a_k^2}, \; \gamma_\phi^2 = \frac{1}{1-\Omega\lambda}. \tag{2.30}$$

The angular velocity of the fluid is obtained as [86],

$$\Omega = \frac{u^\phi}{u^t} = \frac{[\lambda(r-2)+2a_k](1+h)}{r^3 + a_k^2(1+h)(r+2) - 2a_k\lambda(1+h)}. \tag{2.31}$$

Using Eqs. (2.27) and (2.28), we derive the entropy accretion rate as [37, 38],

$$\mathcal{M} = \frac{\dot{M}}{4\pi\mathcal{K}} = -\upsilon\gamma_\upsilon H\sqrt{(\Delta+a_k^2h)(1+h)}\exp(k_3)\Theta^{3/2}(3\Theta+2)^{k_1}(3\Theta+2/\chi)^{k_2}. \tag{2.32}$$

Considering the logarithmic derivative of Eq. (2.28) and setting the condition of constant mass accretion rate at steady state, i.e., $d\dot{M}/dr = 0$, the temperature gradient of the flow is expressed as,

$$\frac{d\Theta}{dr} = -\frac{2\Theta}{2N+1}\left[\frac{\gamma_\upsilon^2}{\upsilon}\frac{d\upsilon}{dr} + N_{11} + N_{12} - \frac{3\varepsilon}{2r^4}\left(\frac{a_k^2}{\Delta+a_k^2h} + \frac{1}{1+h}\right)\right], \tag{2.33}$$

where

$$N_{11} = \frac{5}{2r} + \frac{r - a_k^2(1+h)}{r(\Delta+a_k^2h)} \quad \text{and} \quad N_{12} = -\frac{1}{2F}\frac{dF}{dr}. \tag{2.34}$$

The explicit form of the quantity $\frac{1}{F}\frac{dF}{dr}$ is computed by taking the logarithmic derivative of Eq. (2.30) and is given by,

$$\frac{1}{F}\frac{dF}{dr} = \gamma_\phi^2\lambda\Omega' + 4a_k^2(r^2+a_k^2)\left[\frac{(r^2+a_k^2)\Delta' - 4\Delta r}{(r^2+a_k^2)^4 - 4\Delta^2 a_k^4}\right], \tag{2.35}$$

where

$$\begin{aligned}
\Delta' &= \frac{d\Delta}{dr} = 2(r-1), \\
\Omega' &= \frac{d\Omega}{dr} = -2(1+h)\left[\frac{a_k^3(1+h) - 2a_k^2\lambda(1+h) + a_k[\lambda^2(1+h)+3r^2] + r^2\lambda(r-3)}{\left[r^3 + a_k^2(r+2)(1+h) - 2a_k\lambda(1+h)\right]^2}\right] \\
&\quad - \frac{3\varepsilon[\lambda(r-2)+2a_k]}{r\left[r^3 + a_k^2(r+2)(1+h) - 2a_k\lambda(1+h)\right]^2}.
\end{aligned} \tag{2.36}$$

Finally, we capitalize Eq. (2.26) and obtain the radial velocity gradient of the flow from Eq. (2.21) as,

$$\frac{dv}{dr} = \frac{\mathscr{N}}{\mathscr{D}}, \tag{2.37}$$

where the explicit form of the numerator $\mathscr{N}$ and that of the denominator $\mathscr{D}$ are represented by,

$$\mathscr{N} = \frac{2C_s^2}{\Gamma+1}\left[N_{11} + N_{12} - \frac{3\varepsilon}{2r^4}\left(\frac{a_k^2}{\Delta + a_k^2 h} + \frac{1}{1+h}\right)\right] - \frac{d\Phi^{\rm eff}}{dr} \tag{2.38}$$

and

$$\mathscr{D} = \gamma_v^2\left[v - \frac{2C_s^2}{(\Gamma+1)v}\right]. \tag{2.39}$$

2.3.2 Critical point conditions

In an accretion process around a gravitating object, infalling matter starts accreting with negligible radial velocity from the disc outer edge (usually far away from the horizon) and remain sub-sonic. On the other hand, accretion flow enters into the black hole supersonically in order to satisfy the inner boundary conditions imposed by the event horizon. These conditions imply that the angular momentum of the flow should be sub-Keplerian near the horizon and cross the horizon at the speed of light. Since the motion of the flow generally remains smooth everywhere, accreting matter experiences sonic state transition at some point to become transonic [244, 245] and such a point is referred as critical point (r_c). At r_c, the radial velocity gradient takes $(dv/dr)_{r_c} = 0/0$ (Eq. 2.37) form as it must be real and finite, and hence, we obtain the critical point conditions by setting $\mathscr{N} = 0$ and $\mathscr{D} = 0$ simultaneously, which are given by,

$$C_{sc}^2 = \frac{\Gamma_c+1}{2}\left(\frac{d\Phi^{\rm eff}}{dr}\right)_c\left[(N_{11})_c + (N_{12})_c - \frac{3\varepsilon}{2r_c^4}\left(\frac{a_k^2}{\Delta_c + a_k^2 h_c} + \frac{1}{1+h_c}\right)\right]^{-1} \tag{2.40}$$

and

$$v_c^2 = \frac{2C_{sc}^2}{(\Gamma_c+1)}, \tag{2.41}$$

where the subscript “c” refers the physical quantities measured at the critical point. We evaluate $(dv/dr)_{r_c}$ by applying l′Hôpital’s rule which is obtained as,

$$\left.\frac{dv}{dr}\right|_c = \frac{-B \pm \sqrt{B^2 - 4AC}}{2A}, \tag{2.42}$$

where the resulted form of quantities A, B and C are presented in Appendix 2.A. In general, critical points are classified in three different categories. For *saddle* type critical points, both values of $(dv/dr)_{r_c}$ are real with opposite sign. For *nodal* type critical points, both values of $(dv/dr)_{r_c}$ are real and same sign, whereas for *spiral* or O-type critical point, $(dv/dr)_{r_c}$ becomes imaginary. It is noteworthy to mention that any physically acceptable accretion solution only passes through the saddle type critical points [246, 247, and references therein], and hence, in this work, we focus only those accretion solutions that possess saddle type critical point (hereafter critical point). We further mention that accretion flow may contain multiple critical points depending of the flow parameters and flow of this kind are potentially favourable to contain shock waves (see Section 2.5).

2.4 Hydrodynamics with deformation

In this section, we explore the role of the deformation parameter (ε) in deciding the nature of the critical points as well as the accretion solutions in deformed Kerr spacetime. While doing this, we identify the range of parameters that allows accretion solutions around black holes. We also put efforts in examining the nature of the accretion solutions beyond the black hole compact objects, such as naked singularities.

2.4.1 Critical points analysis

As the accretion solutions embrace the critical points, we start our analysis by understanding the nature of critical points. For that we calculate the specific energy (E) at a critical point (r_c) by solving equations (2.19), (2.40), and (2.41) using the global parameters, namely λ, ε and a_k, respectively. In Fig. 2.1, the variation of E as a function of r_c is presented for different λ with $\varepsilon = 3$ (see panel (a)) and for different ε with $\lambda = 2.8$ (see panel (b)). Presently, we choose the Kerr parameter $a_k = 0$. However, we mention that there are no qualitative differences between the characteristics of critical points for the non-spinning and spinning black holes. Hence, in this work, most of the analyses have been carried out considering $a_k = 0$, although there are instances where results for $a_k \neq 0$ are presented according to the necessity. In the figure, different λ and ε values are marked in the respective panels. We use black, blue, red and green curves for λ = 2.5, 2.7, 2.9 and 3.1 respectively. The same color sequence is used to represent results for ε = 0, 3, 6, and 9, respectively. In each panel, a given curve is generally comprised with saddle, nodal and O-type critical points and they are demonstrated by the solid, dotted and dashed curves respectively. Moreover, these critical points appear in sequence as saddle-nodal-spiral-nodal-saddle as r_c is increased. In addition, we observe that all

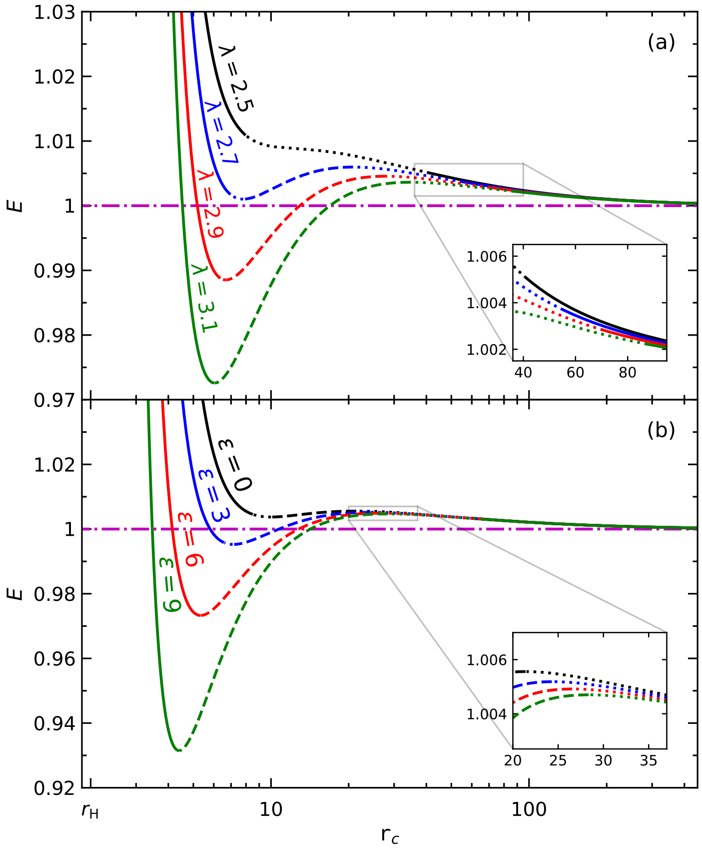

Figure 2.1: Plot of specific energy (E) as the function of critical point locations (r_c) for (a) different angular momentums λ = 2.5 (black), 2.7 (blue), 2.9 (red) and 3.1 (green) with deformation parameter $\varepsilon = 3$, and (b) different deformation parameters ε = 0 (black), 3 (blue), 6 (red) and 9 (green) with the specific angular momentum $\lambda = 2.8$. Solid, dotted and dashed curves denote saddle, nodal and O-type critical points, respectively. The dot-dashed horizontal line indicates the specific energy $E = 1$. In each panel, we zoom a part of the plots for the purpose of clarity. See text for details.

curves have an asymptotic behavior towards $E \simeq 1$ (dot-dashed horizontal line) for larger values of r_c irrespective of λ and ε values. Depending on E, λ and ε, flow may contain either single or multiple critical points. Usually, critical points formed near and far away from the the horizon are called as inner ($r_{\rm in}$) and outer critical points ($r_{\rm out}$), respectively. It is evident from the figure that there exists a range of E that yields multiple critical points and such energy range is strictly depends on λ and ε values. Following this, in Section 2.4.3, we put effort to identify the effective region of the parameter space based on the nature of the accretion solutions. Overall, it is now evident that ε, λ and E play pivotal role in determining the nature of the critical points and its associated properties.

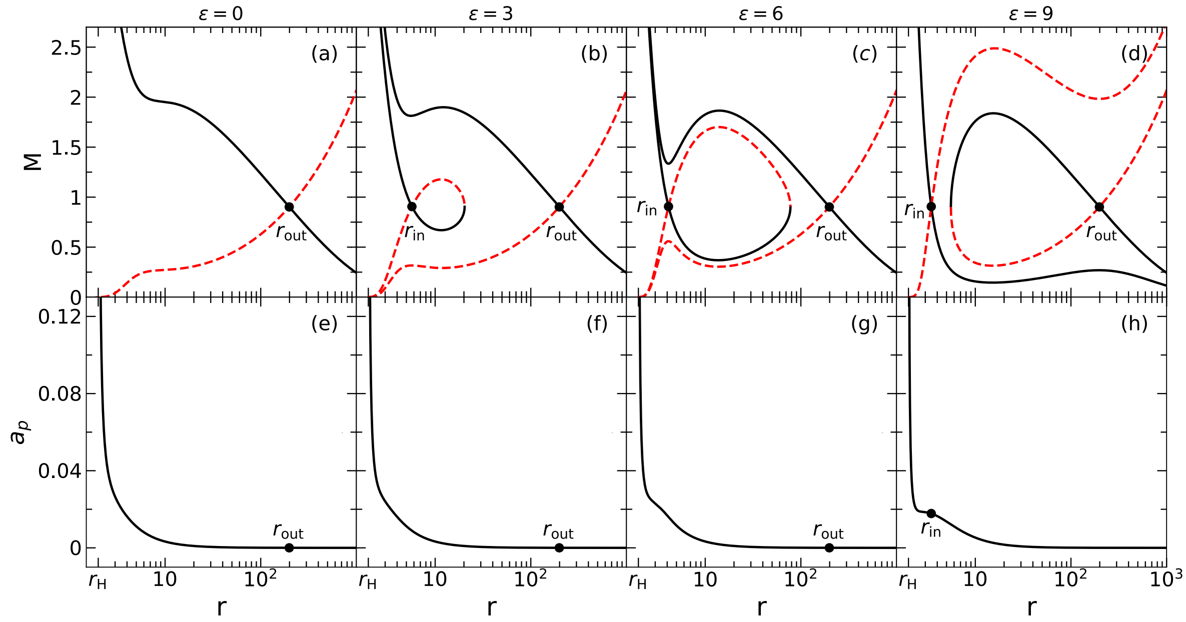

Figure 2.2: *Top panels:* Plot of Mach number M $(= v/C_s)$ as a function of radial distance r. Solid and dashed curves denote the accretion solution and wind solution, respectively. Filled circles denote the critical points. In this figure, we choose $a_k = 0$, $\lambda = 2.8$ and $E = 1.001$. Results in panels (a), (b), (c) and (d) are obtained for $\varepsilon = 0, 3, 6$ and 9, respectively. *Bottom panels:* Plot of the magnitude of four-acceleration (a_p) with r corresponding to the global accretion solution (solid) presented in the top panel. See text for details.

2.4.2 Effect of ε on the global accretion solutions

Here, we examine the impact of ε on the accretion solutions. While doing so, we calculate the location of the critical point (r_c), and the corresponding radial velocity (v_c) and dimensionless temperature (Θ_c) at r_c by simultaneously solving Eqs. (2.19), (2.26), (2.40), and (2.41) for a given set of input parameters (λ, E, a_k and ε). We employ Θ_c and v_c as the initial values at r_c to simultaneously solve Eqs. (2.33) and (2.37) once inward up to the horizon ($r_{\rm H}$) and then outward up to the outer edge of the disc ($r_{\rm edge}$). Finally, we join this two parts of the solution to obtain the complete radial profiles of velocity (v) and temperature (Θ). In Fig. 2.2, we depict the accretion solutions (M versus r plots) for different ε, where $E = 1.001$, $\lambda = 2.8$ and $a_k = 0$ are chosen. In panels (a-d), the variation of Mach number (M) as function of radial distances (r) is presented for $\varepsilon = 0, 3, 6$ and 9, respectively. Here, the solid curve represents the accretion solution whereas dashed curve denotes the corresponding wind solution. In the figure, filled circles refer the critical points, where inner ($r_{\rm in}$) and outer ($r_{\rm out}$) critical points are marked. We observe that for $\varepsilon = 0$, the flow passes through the outer critical point at $r_{\rm out} = 198.6333$ and connects the outer edge of the accretion disc ($r_{\rm edge} = 1000$) to the black hole horizon ($r_{\rm H}$) (see panel (a)). Solutions of this kinds are often called by some authors as *heteroclinic* solutions [248, 249]. As the deformation parameter is increased (say $\epsilon = 3$) keeping other input parameters unchanged, inner critical point is appeared at $r_{\rm in} = 5.7136$ along with the outer critical point at $r_{\rm out} = 198.5498$. Interestingly, the solution passing through the outer critical point continues to connect $r_{\rm H}$ and $r_{\rm edge}$, however the inner critical point solutions fail to do so as it terminates at a radius $r_{\rm t} = 20.3336$ in between inner and outer critical points as $r_{\rm in} < r_{\rm t} < r_{\rm out}$ as shown in panel (b). The closed transonic solutions that unable to connect $r_{\rm edge}$ and $r_{\rm H}$ are also called as *homoclinic* solutions [235, 248]. For $\epsilon = 6$, the nature of the flow solution remains qualitatively similar to panel (b) although $r_{\rm t} = 77.7947$ is increased (see panel (c)). We wish to emphasize that solutions presented in panel (b-c) may experience shock transition and we plan to discuss it elaborately in Section 2.5. With the further increase of deformation parameter $\epsilon = 9$, the solution characteristics are changed completely as shown in panel (d). We find that the solution passing through $r_{\rm in} = 3.4628$ smoothly connects $r_{\rm edge}$ to $r_{\rm H}$, but the solution with $r_{\rm out} = 198.3757$ fails to do so. Hence, it is evident that ϵ plays a decisive role in determining the nature of the accretion solutions around the central object under consideration. In Fig. 2.2e-h, we present the variation of the magnitude of the proper four acceleration a_p ($= \sqrt{\mathrm{a}^i \mathrm{a}_i}$, where four acceleration $\mathrm{a}^i = u^k \nabla_k u^i$ [236]) with r corresponding to the global transonic solutions depicted in panels (a), (b), (c), and (d), respectively. In each panel, we notice that a_p increases as flow accretes towards the horizon and diverges at $r_{\rm H}$ as $v \rightarrow 1$. The divergent nature of a_p at the horizon is quite consistent with the theoretical prediction, e.g., see discussion in Section 6.3 of Ref. [234]. This evidently indicates that, with respect to any static observer at spatial infinity, instead of timelike fluid only photons can stay at $r = r_{\rm H}$. In a way, this defines a boundary region of the spacetime (usually called the static limit) of the black holes, where $g_{tt}(r_{\rm H}) = 0$.

2.4.3 Parameter space based on nature of accretion solutions

In this section, we separate the effective region of the parameter space in $\lambda - E$ plane according to the nature of the accretion solutions. The obtained results are plotted in Fig. 2.3, where parameter space is divided into four regions marked as O, A, W, and I. Examples of different solution topologies obtained using flow parameters (λ,E) from these regions are depicted at the insets where the Mach number ($M = v/C_s$) is plotted with the radial distances (r). Here, we choose $a_k = 0$ and $\epsilon = 5$. In each panel, the accretion

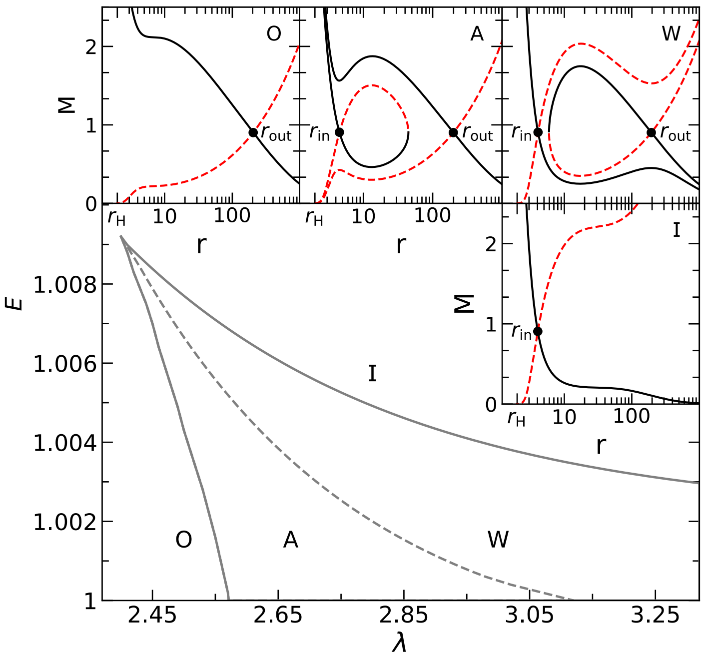

Figure 2.3: Division of parameter space in $\lambda - E$ plane according to the nature of the flow solutions. Here, we fix $\varepsilon = 5$. Four regions are identified which are marked as O, A, W and I. Examples of representative flow solutions from individual regions are shown in each panel. See text for details.

and wind solutions are presented using solid (black) and dashed (red) curves and the filled circle denotes the critical point. Inside the bounded region of the parameter space, flow solutions are found to possess multiple critical points which is further sub-divided based on the entropy accretion rate ($\dot{\mathcal{M}}$) measured at the critical points. Accordingly, the regions A and B are obtained for $\dot{\mathcal{M}}(r_{\rm in}) > \dot{\mathcal{M}}(r_{\rm out})$ and $\dot{\mathcal{M}}(r_{\rm in}) < \dot{\mathcal{M}}(r_{\rm out})$, respectively. For flow solutions presented in panel O, we choose $(\lambda, E) = (2.5, 1.001)$ and get only outer critical points at $r_{\rm out} = 203.562$. We set $(\lambda, E) = (2.80, 1.001)$ to obtain the flow solutions in panel A, where $r_{\rm in} = 4.5132$ and $r_{\rm out} = 198.4749$. Similarly, for panel W, we fix (λ, E) = $(3.0, 1.007)$ and find $r_{\rm in} = 4.0795$ and $r_{\rm out} = 194.5943$. Finally, in panel I, we choose $(\lambda, E) = (3.0, 1.0045)$ that yields only inner critical point at $r_{\rm in} = 4.0445$. Note that all the above findings are in general qualitatively similar to the results obtained for the original Kerr black hole [116], but differs quantitatively due to the deformation present in the adopted spacetime. The nature of the accretion flows obtained from the different regions in Fig. 2.3 is summarized in Table 2.1.

Next, we examine the modification of the parameter space for multiple critical points in $\lambda - E$ plane for different ε. We present the obtained results in Fig. 2.4, where $a_k = 0$

Table 2.1: The nature of the accretion solutions presented in Fig. 2.3.

Type	Nature of accretion solutions
O	Open solution containing $r_{\rm out}$
A	Closed solution containing $r_{\rm in}$ and open solution containing $r_{\rm out}$
W	Open solution containing $r_{\rm in}$ and closed solution containing $r_{\rm out}$
I	Open solution containing $r_{\rm in}$

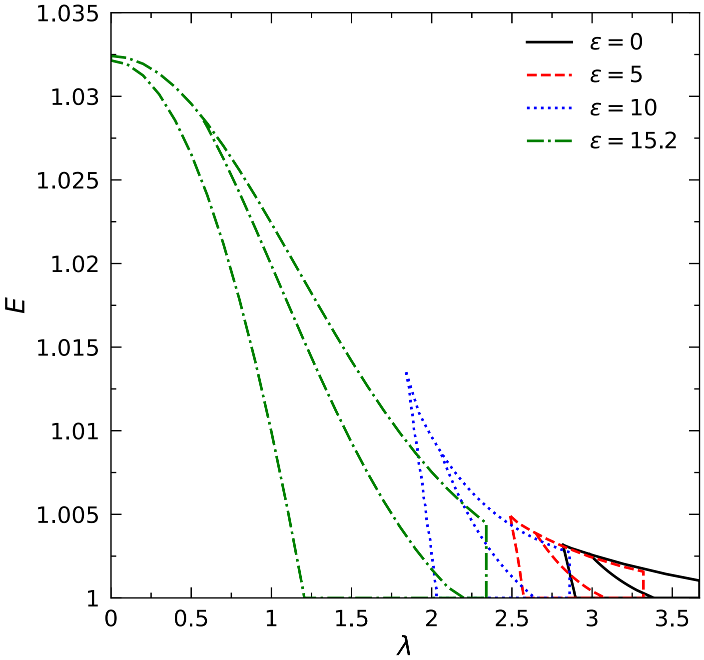

Figure 2.4: Modification of the parameter space (in $\lambda - E$ plane) for multiple critical points due to the increase of the deformation parameter (ε). Regions bounded with solid (black), dashed (red), dotted (blue) and dot-dashed (green) curves are for $\varepsilon = 0, 5, 10$ and 15.2, respectively. In each parameter space, middle curve refers $\dot{\mathcal{M}}(r_{\rm in}) = \dot{\mathcal{M}}(r_{\rm out})$. See text for details.

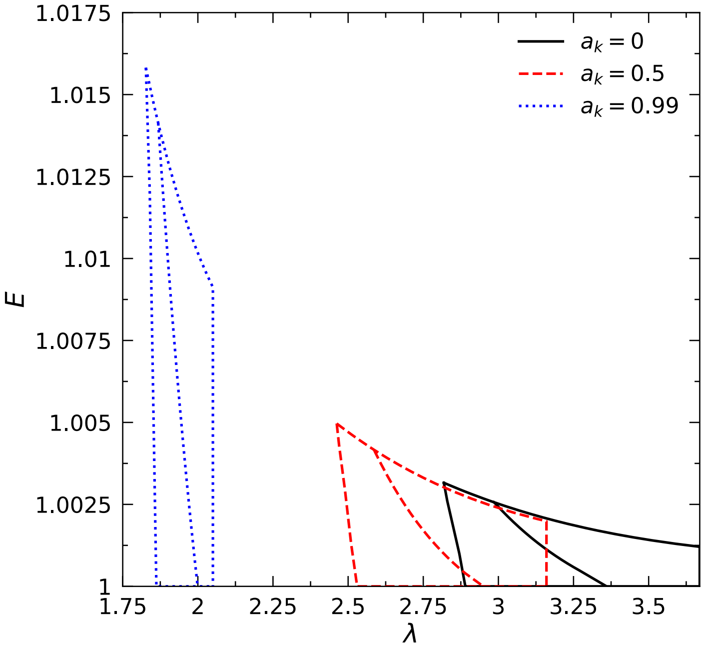

Figure 2.5: Modification of the parameter space for multiple critical points for different Kerr parameter (a_k). The area within solid (black), dashed (red) and dotted (blue) boundaries are for $a_k = 0, 0.5$ and 0.99, where $\varepsilon = 0.02$ is chosen. In each parameter space, middle curve refers $\dot{\mathcal{M}}(r_{\rm in}) = \dot{\mathcal{M}}(r_{\rm out})$. See text for details.

is used, and the regions bounded by solid (black), dashed (red), dotted (blue), and dot-dashed (green) are for $\varepsilon = 0, 5, 10$, and 15.2, respectively. Each parameter space is further sub-divided based on entropy accretion rate at the critical points, where the middle curve is associated with $\dot{\mathcal{M}}(r_{\rm in}) = \dot{\mathcal{M}}(r_{\rm out})$. We observe that the effective domain of the parameter space is increased and also shifted towards lower angular momentum and higher energy sides as ε is increased. Further, for the first time to the best of our knowledge, we report that for $\varepsilon = 15.2$, multiple critical points continue to exist even for zero angular momentum flow. Indeed, the choice of $\varepsilon = 15.2$ is not arbitrary, in fact, it is the lower limit of the ε that provides multiple critical points for $\lambda = 0$. Needless to mention that such a lower limit is not universal, instead it depends on a_k.

Fig. 2.5 shows the alteration of the parameter space for multiple critical points for different a_k. Here, we choose $\varepsilon = 0.02$. The region bounded using solid (black), dashed (red), and dotted (blue) curves correspond to the result for $a_k = 0, 0.5$, and 0.99 respectively. In each parameter space, middle curve refers $\dot{\mathcal{M}}(r_{\rm in}) = \dot{\mathcal{M}}(r_{\rm out})$. It is evident from the figure that parameter space is moved to lower angular momentum and higher energy domains with the increase of a_k. With this, we indicate that the effect of a_k and ε in regulating

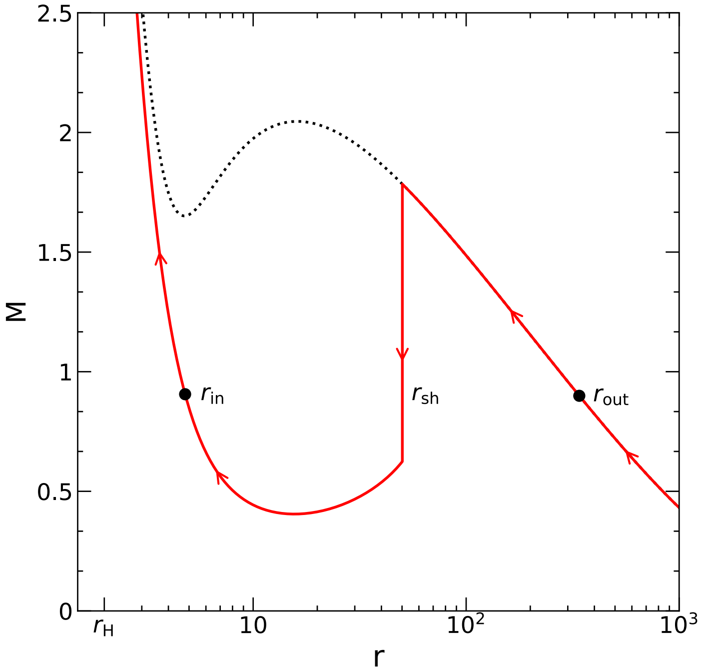

Figure 2.6: Example of a shock induced global accretion solution around black hole where the variation of Mach number (M) with the radial coordinate (r) is shown. The solution is obtained for $a_k = 0$, $\varepsilon = 3$, $\lambda = 3.0$ and $E = 1.0005$. Vertical arrow indicates the location of the shock transition at $r_{\rm sh} = 50.1706$. Arrows denote the overall flow motion towards the black hole. See the text in Section 2.5 for details.

the parameter space for multiple critical points appears to be analogous in nature.

2.5 Accretion solutions with shock transitions

In this section, we focus on those accretion solutions that may contain shocks. In an accretion process, flow starts accreting towards black hole subsonically from the outer edge of the disc. Depending on the input parameters, flow becomes supersonic after crossing the outer critical point ($r_{\rm out}$) and continues to accreate towards the horizon. Meanwhile, flow experiences virtual barrier due to the centrifugal repulsion that eventually triggers the discontinuous transition of the flow variables, when relativistic shock conditions are satisfied [37, 38, 94, 95, 116, 118, 122, 239, 247, 250–252]. Generally, the shocked-accretion solution is preferred over the shock-free solutions as the entropy associated to the former solution remain always higher at the inner part of the disc [253]. In order to calculate the location of the shock transition, we use the relativistic shock conditions which are given by [254],

$$\left[\rho u^r\right]=0,\ \left[(e+p)u^r u^t\right]=0,\ \left[(e+p)u^r u^r+pg^{rr}\right]=0. \tag{2.43}$$

In Eq. (2.43), the quantities within the square bracket refer the difference of their values across the shock front.

In Fig. 2.6, we present an example of a global accretion solutions comprising shock, where the Mach number (M) is plotted with the radial distances (r). Here, we choose flow parameters as $(\lambda, E)=(3, 1.0005)$, and black hole parameters as $(a_k, \epsilon)=(0,3)$. In this figure, the accretion solution is plotted using solid curve. In reality, accretion flow can smoothly enters into the black hole after crossing $r_{\rm out}=339.7504$ as indicated by the dotted (black) curve. However, the flow finds a possibility of the shock transition at $r_{\rm sh}=50.1706$ and it jumps from supersonic to subsonic branch which is shown using vertical arrow. After the shock, flow again become supersonic after crossing $r_{\rm in}=4.7916$ before falling into the black hole. Overall arrows indicate the direction of flow motion towards the horizon from the outer edge of the disc.

2.5.1 Shock properties

Fig. 2.7 shows the dynamical structure of the shocked accretion flow resulted due to the variation of spacetime deformation (ϵ). We consider accretion flow with energy $E=1.0013$ and angular momentum $\lambda=3$ that are injected from the outer edge of the disc at $r_{\rm edge}=300$ towards the black hole of spin $a_k=0$. Here, we choose mass accretion rate $\dot{M}=0.1\dot{M}_{\rm Edd}$ with $M_{\rm BH}=10M_{\odot}$, where $\dot{M}_{\rm Edd}(=1.39\times10^{18}\frac{M_{\rm BH}}{M_{\odot}}$ gm s^{-1}) refers the Eddington accretion rate and $M_{\odot}$ denotes the solar mass. The point is to note that we take energy conversion efficiency $\eta=0.1$ in $\dot{M}_{\rm Edd}$. For $\epsilon=0$, flow encounters shock transition at $r_{\rm sh}=22.5278$ and the solution is depicted using solid (black) curve. We now increase the spacetime deformation keeping other input parameters fixed, and observe that shock radius gradually recedes away from the black hole horizon. For $\epsilon=1$, 2 and 2.5, we obtain $r_{\rm sh}=36.1334, 61.0066$ and 86.8639, respectively and these solutions are shown using dashed (red), dotted (blue) and dot-dashed (green) curves. Needless to mention that indefinite increase of ϵ is not possible because of the fact that beyond a critical limit, shock ceases to exist as the shock conditions (2.43) fail to satisfy.

In Fig. 2.8, we present the profile of various flow variables corresponding to the shock-induced global accretion solutions illustrated in Fig. 2.7. In Fig. 2.8a, the radial velocity (v) profile is plotted as a function of radial coordinate (r) where discontinuous jump of v is clearly seen. Solid (black), dashed (red), dotted (blue) and dot-dashed (green)

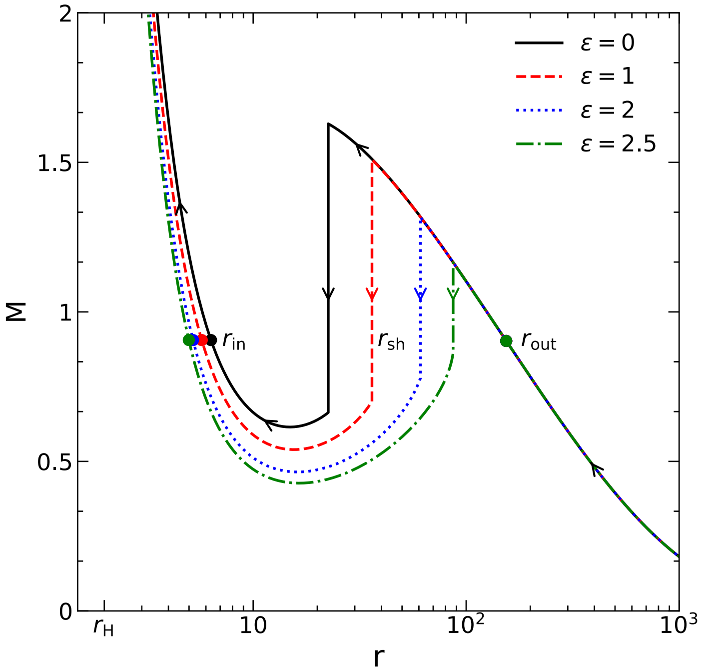

Figure 2.7: Variation of Mach number (M) with the radial coordinates (r) for different deformation parameters (ε). Here, we choose $a_k = 0$, $\lambda = 3$ and $E = 1.0013$. Vertical arrows indicate the radius of the shock transition at $r_{\rm sh} = 22.5278, 36.1334, 61.0066$ and 86.8639 corresponding to $\varepsilon = 0, 1, 2$ and 2.5, respectively. Critical points ($r_{\rm in}$ and $r_{\rm out}$) are annotated by the filled circles. See text for details.

curves denote the results obtained for $\varepsilon = 0, 1, 2$, and 2.5, respectively. It is noteworthy that the difference of flow velocity across the shock front decreases with ε and beyond a critical limit of ε, smooth transonic accretion solutions containing $r_{\rm out}$ only remains as shock disappears. We discuss the critical limit of ε in the subsequent sections while studying the shock properties. In Fig. 2.8b, we show the variation of the mass density (ρ) with r. Across the shock front, since the flow velocity drops down, the density of the post-shock corona (hereafter PSC) jumps to higher value. This happens simply due to the conservation of mass flux across the shock front (see Eq. (2.43)). Indeed, the density compression decreases as ε is increased. We show the temperature (T) profile of the accretion flows in Fig. 2.8c, where we find that the temperature jumps suddenly at PSC. In reality, most of the kinetic energy of the pre-shock flow is converted into the thermal energy after the shock transition and hence, the rise of post-shock temperature is observed as a consequence of the PSC heating. We tabulate the temperature of the shock induced accretion solutions at different radii ($r_{\rm in}$, $r_{\rm out}$ and $r_{\rm sh}$) in Table 2.2. In Fig. 2.8d, we present the radial dependence of the relative thickness (H/r) of the accretion

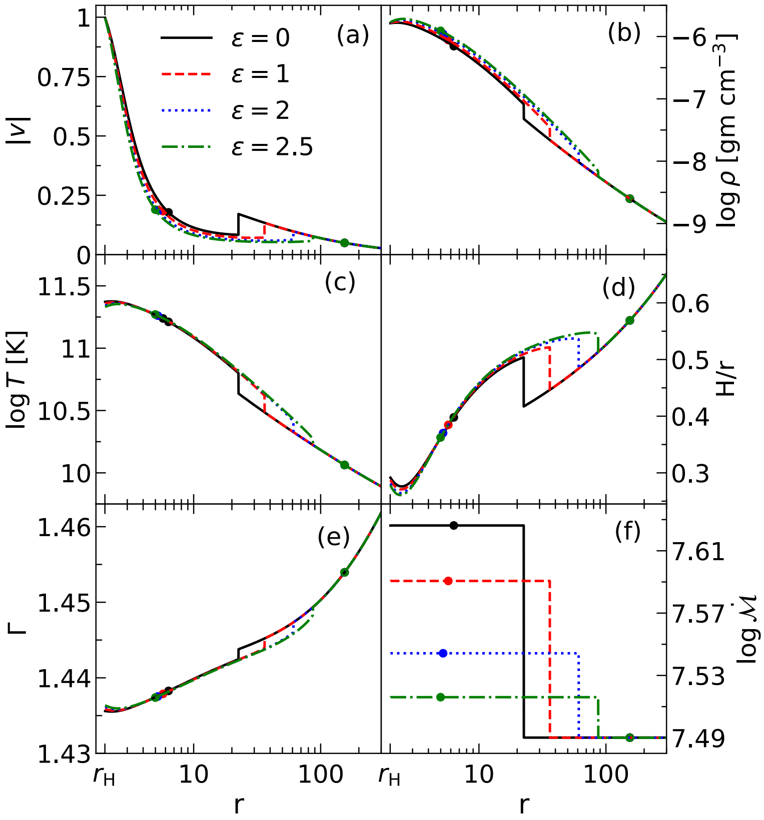

Figure 2.8: Variation of (a) radial velocity (v), (b) density (ρ), (c) temperature (T), (d) vertical scale-height (H/r), (e) adiabatic index (Γ) and (f) entropy accretion rate ($\dot{\mathcal{M}}$) as a function of radial coordinates (r) in a spacetime with different deformation parameters (ϵ). Each solid (black), dashed (red), dotted (blue) and dot-dashed (green) curves are used for $\epsilon = 0, 1, 2$ and 2.5, respectively. Here, we choose $(\lambda, E) = (3, 1.0013)$, and $a_k = 0$. In each panel, shock locations are indicated by the vertical lines at $r_{\rm sh} = 22.5278, 36.1334, 61.0066$ and 86.8639, respectively. Critical points ($r_{\rm in}$ and $r_{\rm out}$) are marked by the filled circles. See text for details.

disc. We find that accretion flow maintains $H/r < 1$ all throughout from the outer edge to the horizon even in the presence of shock transition. In Fig. 2.8e, we show the profile of the adiabatic index (Γ) as function of r. As expected, Γ anti-correlates with the flow temperature at all radii. Finally, in Fig. 2.8f, we depict the profile of the entropy accretion rate ($\dot{\mathcal{M}}$) and observe that flow at PSC possesses high entropy content. With this, we wish to emphasize that the location of the shock eventually provides the size of the PSC that contains swarm of hot electrons. When soft photons from the pre-shock disc interact with these hot electrons via inverse Comptonization process, high energy radiations are produced which are commonly observed in active galactic nuclei (AGNs) and black hole

Table 2.2: Deformation parameter (ϵ), critical point locations ($r_{\rm in}$,$r_{\rm out}$), critical point temperatures ($T(r_{\rm in})$, $T(r_{\rm out})$), shock location ($r_{\rm sh}$), pre-shock temperatures ($T_-(r_{\rm sh})$) and post-shock temperatures ($T_+(r_{\rm sh})$) for shock-induced global accretion solutions presented in Fig. 2.8.

ϵ	$r_{\rm in}$	$r_{\rm out}$	$T(r_{\rm in})$ ($\times\ 10^{10}$K)	$T(r_{\rm out})$ ($\times\ 10^{10}$K)	$r_{\rm sh}$	$T_-(r_{\rm sh})$ ($\times\ 10^{10}$K)	$T_+(r_{\rm sh})$ ($\times\ 10^{10}$K)
0	6.3388	154.2915	16.2554	1.1567	22.5278	4.3280	6.3134
1	5.7364	154.2562	17.3149	1.1568	36.1334	3.0595	4.1752
2	5.2186	154.2115	18.2422	1.1571	61.0066	2.1224	2.5985
2.5	4.9869	154.1944	18.6363	1.1572	86.8639	1.6735	1.8726

X-ray binaries (BH-XRBs) [91, 105, 255, and references therein].

In the next, we study the properties of shocks in terms of the input parameters. For that we consider accretion flow with $E = 1.0012$ and calculate shock radius ($r_{\rm sh}$) as function of ϵ for a set of angular momentum (λ). Here, we choose $a_k = 0$. The obtain results are presented in Fig. 2.9a, where solid (black), dashed (red), dotted (blue), dot-dashed (green), and big-dashed (cyan) curves are for $\lambda = 3.0, 3.025, 3.05, 3.075$, and 3.1, respectively. We find that for a fixed λ, $r_{\rm sh}$ increases with ϵ, however, shock is seen to disappear when ϵ exceeds its critical value $\epsilon^{\rm cri}$. It is evident from the figure that for a fixed E, $\epsilon^{\rm cri}$ decreases as λ is increased. Therefore, for relatively lower λ, the possibility of obtaining the shocked-induced global accretion solutions is very much likely even the strength of deformation is higher and vice versa. We also notice that for given ϵ, $r_{\rm sh}$ settles down at larger radius for flows with higher λ. This clearly suggests that shocks under consideration are centrifugally drive. Since both density and temperature of the accreting flow are increased substantially at PSC, it is therefore worthy to study the compression ratio (R) and shock strength (S). In reality, compression ratio ($R = \Sigma_+/\Sigma_-$, '–' and '+' refer quantities just before and after the shock transition) measures the density compression across the shock front. In Fig. 2.9b, we show the variation of R as a function of ϵ for the same set of input parameters as in Fig. 2.9a. As expected, R decreases with the increase of ϵ. This happens because the density compression at PSC generally weakens as shock recedes outward (see Fig. 2.8b). In Fig. 2.9c, we depict the variation of S, defined as $S = M_-/M_+$ and is a measure of temperature jump at PSC, with ϵ corresponding to the results presented in Fig. 2.9a. We observe that S decreases with ϵ for a given λ which agrees with our previous findings (see Fig. 2.8c).

Similarly, in Fig. 2.10, we examine the shock properties for flows having $\lambda = 3$ but different energies E. Here, we set $a_k = 0$. In panels (a-c), we present the variation of

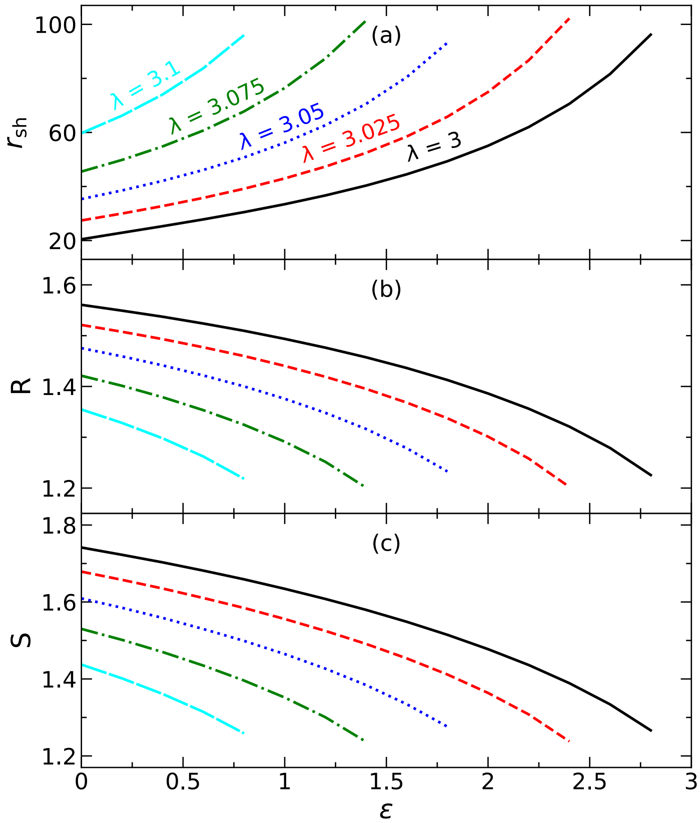

Figure 2.9: Variation of (a) shock location ($r_{\rm sh}$), (b) compression ration (R) and (c) shock strength (S) with the deformation parameters (ε). Solid (black), dashed (red), dotted (blue), dot-dashed (green) and big-dashed (cyan) curves denote results for $\lambda = 3, 3.025, 3.05, 3.075$ and 3.1, respectively. Here, we choose $a_k = 0$ and $E = 1.0012$. See text for details.

$r_{\rm sh}$, R and S with ε, where solid (black), dashed (red), dotted (blue), dot-dashed (green), and big-dashed (cyan) curves are for $E = 1.0011, 1.0013, 1.0015, 1.0017$, and 1.0019, respectively. We find that for a fixed E, $r_{\rm sh}$ increases with ε and beyond $\varepsilon < \varepsilon^{\rm cri}$ shock disappears. We notice that for a given λ, $\varepsilon^{\rm cri}$ decreases for flows with higher energies. It is worth mentioning that $\varepsilon^{\rm cri}$ does not bear universal values as it explicitly depends on the other input parameters. We also find that for a fixed ε, flow experiences shock transition ($r_{\rm sh}$) at larger radii when energy (E) is increased. Further, we observe that for a given set of (λ,E), both R and S decreases with the increase of ε. This happens because the enhanced ε pushes the shock front outwards that reduces the overall density compression as well as temperature jump at PSC.

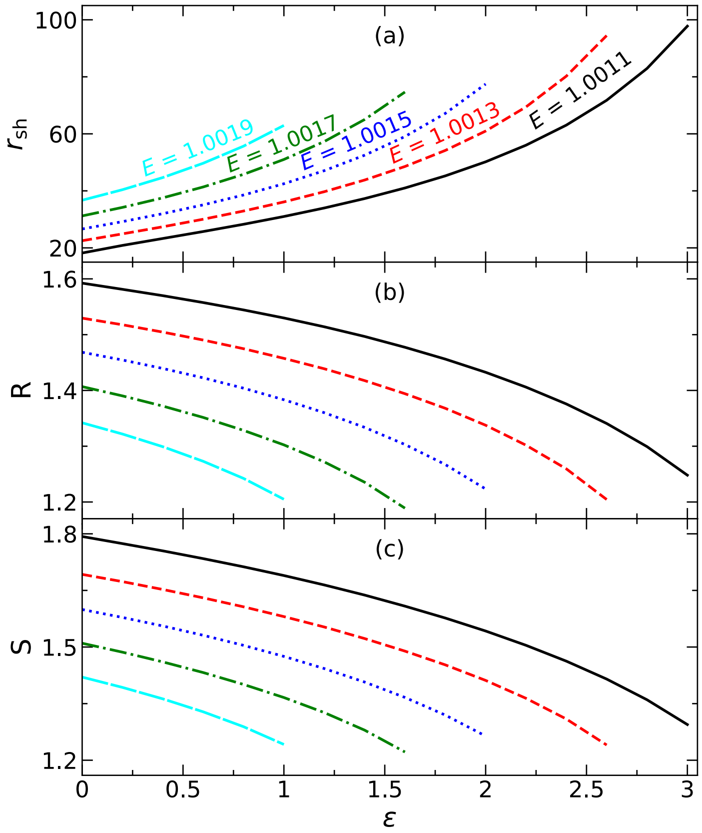

Figure 2.10: Variation of (a) shock location $r_{\rm sh}$, (b) compression ration (R) and (c) shock strength (S) as a function of the deformation parameters (ε). Solid (black), dashed (red), dotted (blue), dot-dashed (green) and big-dashed (cyan) curves are for $E = 1.0011, 1.0013, 1.0015, 1.0017$ and 1.0019, respectively. Here, we fix $a_k = 0$ and $\lambda = 3$. See text for details.

2.5.2 Parameter space for shocks

We already indicate that shock-induced global accretion solutions are not isolated solutions, in fact they exist for wide range of input parameters. In order to quantify the allowed range of input parameters, we separate the effective region of the parameter space in $\lambda - E$ plane that admits shock solutions. In Fig. 2.11, we show the modification of the shock parameter space due to the increase of ε, where regions bounded by the solid (black), dashed (red), dotted (blue) and dot-dashed (green) are obtained for $\varepsilon = 0, 5, 10$ and 15, respectively. Here, we choose $a_k = 0$. The solid curve depicted the region that agrees with Fig. 5 in Ref. [239]. We note that the domain of the parameter space for shock gradually increases with the increase of ε and shifts towards the higher energy and lower angular momentum sides. This findings clearly indicate that the possibility

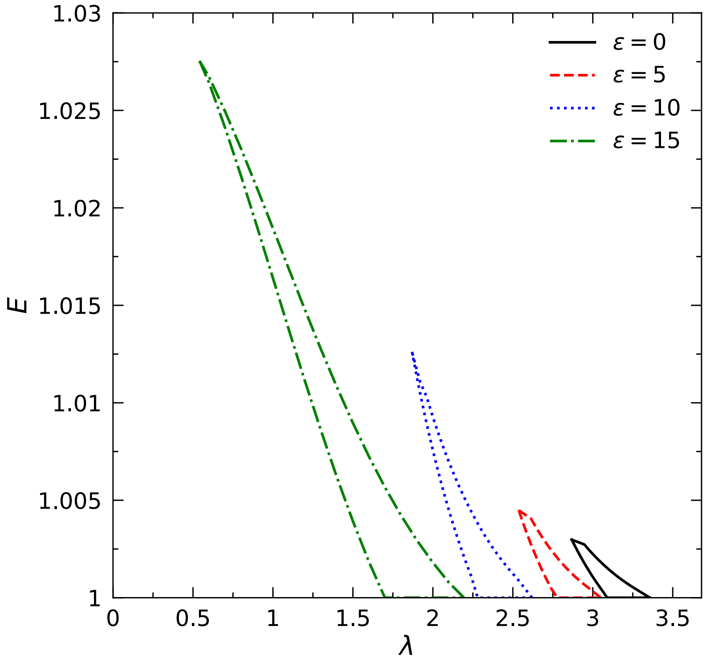

Figure 2.11: Modification of the shock parameter space in $\lambda - E$ plane as a function of deformation parameter (ε). Here, we fix $a_k = 0$. Regions bounded with solid (black), dashed (red), dotted (blue) and dot-dashed (green) curves are obtained for $\varepsilon = 0, 5, 10$ and 15, respectively. See text for details.

of shock formation is eventually increased as the spacetime deformation is increased. In addition, low angular momentum flow around black hole seems to possess standing shock provided the level of spacetime deformation is relatively high and vice versa.

Next, we intend to examine the role of black hole spin (a_k) in modifying the effective region of parameter space in $\lambda - E$ plane for standing shock. In Fig. 2.12, we show the results where the shock parameter space is calculated for $\varepsilon = 0.02$ considering different a_k. The effective regions bounded with solid (black), dashed (red), and dotted (blue) curves correspond to $a_k = 0, 0.5$, and 0.99, respectively. We find that the allowed region for the standing shock solution shifts toward lower angular momentum as a_k increases. This shift occurs because the marginally stable angular momenta of the accreting material goes down when a_k is increased [256].

2.5.3 Zero angular momentum flow

In this section, we study the zero angular momentum flow (ZAMF, characterized by $\lambda = 0$) in the deformed Kerr spacetime. While doing this, we separate the region in the

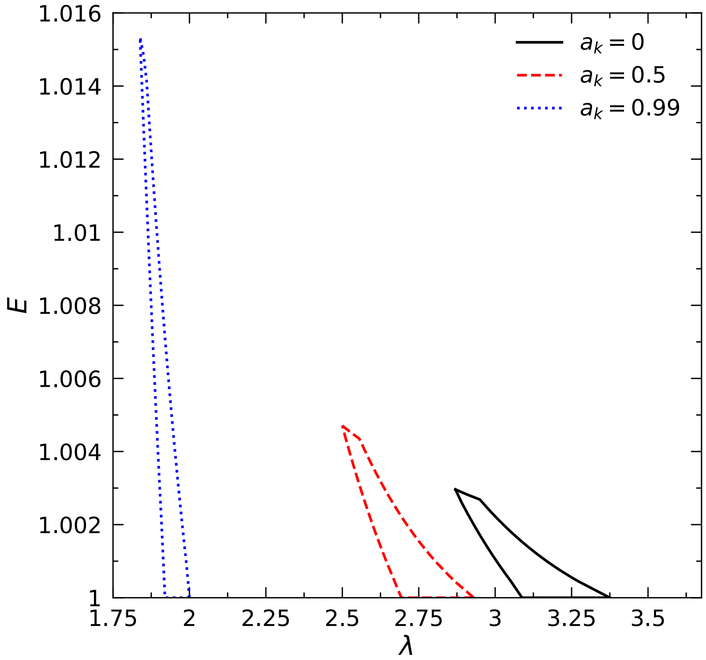

Figure 2.12: Modification of shock parameter space in $\lambda - E$ for different Kerr parameters (a_k). Here, we choose $\varepsilon = 0.02$. Effective regions bounded using solid (black), dashed (red) and dotted (blue) curves are obtained for $a_k = 0, 0.5$ and 0.99, respectively. See text for details.

$\varepsilon - E$ plane according to the nature of the accretion solutions (see Fig. 2.3). In Fig. 2.13, we depict the obtained results for $\lambda = 0$ and $a_k = 0$, where the region bounded using red curves are obtained for multiple critical points. This region is further sub-divided into two domains using dashed (blue) curves ($\dot{\mathcal{M}}_{\rm in} = \dot{\mathcal{M}}_{\rm out}$), namely A and W, respectively. The shaded region (cyan) marked as S admits shock-induced global accretion solutions for ZAMF. The remaining regions marked as A and I allow accretion solutions that possess single critical points ($r_{\rm in}$ for I-type solutions and $r_{\rm out}$ for O-type solutions).

Next, we examine how the accretion solutions are modified due to the change of ε for ZAMF. In Fig. 2.14, we depict the obtained results where Mach number (M) is plotted as function of radial coordinate (r). Here, we choose $\lambda = 0$, $E = 1.0255$ and $a_k = 0$. In each panel, solid (black) curve denotes accretion solution whereas dashed (blue) curve refers the corresponding wind branch. In panel (a), (b), (c) and (d), we consider $\varepsilon = 0, 5, 10$ and 15 that yield only outer critical points at $r_{\rm out} = 16.7040, 15.8656, 14.8279$ and 13.3763, respectively. As the spacetime deformation is increased further to $\varepsilon = 16$, we observe that the inner critical point appears at $r_{\rm in} = 4.3305$ along with $r_{\rm out} = 12.9792$, which is shown in panel (e). We further find $\dot{\mathcal{M}}_{\rm in} > \dot{\mathcal{M}}_{\rm out}$ and observe that standing shock conditions are

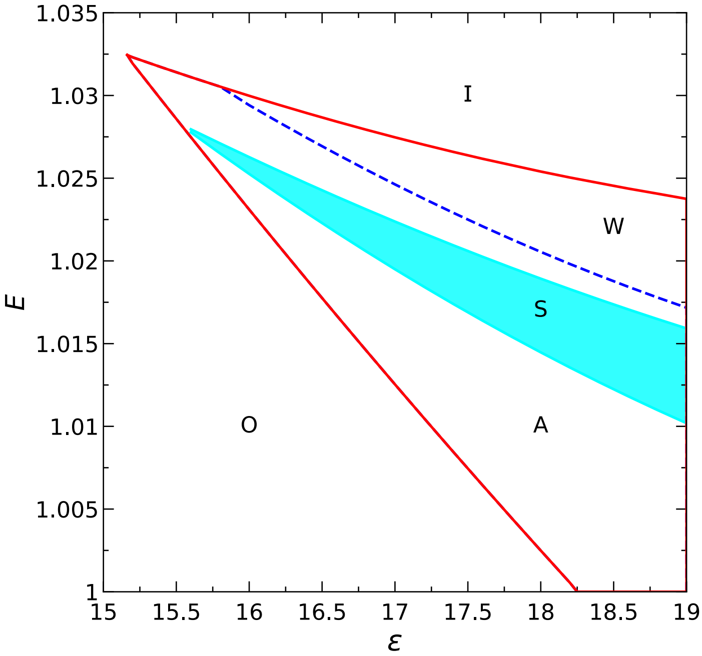

Figure 2.13: Separation of parameter space in the $\varepsilon - E$ plane according to the nature of flow solutions (O, A, W, S, I). Here, we choose $\lambda = 0$ and $a_k = 0$. See text for details.

satisfied at $r_{\rm sh} = 6.0645$ as shown using vertical arrow. The compression ratio and shock strength for this shock jump are calculated as $R = 1.2408$ and $S = 1.2677$, respectively. Needless to mention that the formation of shock in ZAMF is evidently resulted due to the spacetime deformation under consideration. The arrows indicate the overall direction of the flow motion. Here, we wish to emphasize that for the first time to our knowledge, we obtain the zero angular momentum shocked accretion solution around black holes embedded in deformed Kerr spacetime. In panel (f), flow solutions are plotted for $\varepsilon = 16.5$, where the critical points are calculated as $(r_{\rm in}, r_{\rm out}) = (4.0617, 12.7550)$. Although flow contains multiple critical points and $\dot{\mathcal{M}}_{\rm in} > \dot{\mathcal{M}}_{\rm out}$, shock transition does not happen as shock conditions (2.43) are not satisfied. For $\varepsilon = 17$, accretion flow still possesses multiple critical points, however, changes its character as shown in Fig. 2.14g. We notice that the solution passing through $r_{\rm out} = 12.5073$ no longer connects the horizon ($r_{\rm H}$) with the outer edge of the disc ($r_{\rm edge}$), instead the solution passing through $r_{\rm in} = 3.9067$ smoothly connects $r_{\rm H}$ and $r_{\rm edge}$. Moreover, we get $\dot{\mathcal{M}}_{\rm in} < \dot{\mathcal{M}}_{\rm out}$ that disfavors the shock transition. For further increase of $\varepsilon = 18$, we obtain qualitatively similar solution as shown in panel (h), but the critical points are shifted as $(r_{\rm in}, r_{\rm out}) = (3.7102, 11.9028)$. For the limiting value of $\varepsilon = 19$, outer critical point disappears leaving only the inner critical point at

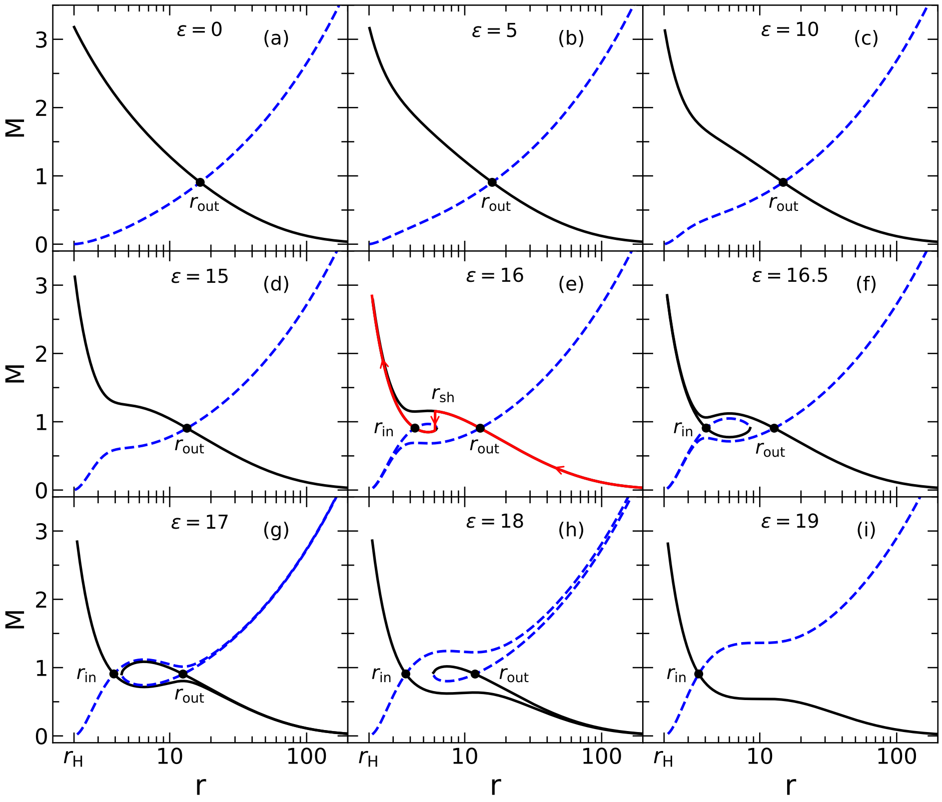

Figure 2.14: Variation of Mach number (M) with the radial distances (r) for zero angular momentum ($\lambda = 0$) flows. Here, we set $E = 1.0255$ and $a_k = 0$. Results depicted in panels (a) to (i) correspond to smooth variation of ε marked in respective panels. Solid (black) and dashed (blue) curves denote the accretion and wind solutions, respectively. Critical points ($r_{\rm in}, r_{\rm out}$) are marked using filled circles. Arrows (red) indicate the direction of flow motion for shock-induced global accretion solution (solid, red line) is shown where we obtain $r_{\rm sh} = 6.0645$. See text for details.

$r_{\rm in} = 3.5821$ as depicted in Fig. 2.14i. Solutions of this kind resemble the advection-dominated accretion flows (ADAF) as reported in earlier works [71, 83, 95]. With this, we indicate that spacetime deformation plays viable role in determining the overall nature of the accretion solutions around black hole including shocks. We summarize the critical point locations and the nature of the accretion solutions for Fig. 2.14 in Table 2.3.

2.6 Naked singularity in deformed Kerr spacetime

It is well known that the end state of the gravitational collapse of a massive matter distribution does not necessarily result in a black hole. Several studies have shown that under

Table 2.3: Deformation parameters (ε), inner critical points ($r_{\rm in}$) and orbit, outer critical points ($r_{\rm out}$) and orbit, shock location ($r_{\rm sh}$), flow types for accretion solutions presented in Fig. 2.14.

ε	$r_{\rm in}$ (saddle)	Orbits	$r_{\rm out}$ (saddle)	Orbits	$r_{\rm sh}$	Types
0	—	—	16.7040	Heteroclinic	—	O
5	—	—	15.8656	Heteroclinic	—	O
10	—	—	14.8279	Heteroclinic	—	O
15	—	—	13.3763	Heteroclinic	—	O
16	4.3305	Homoclinic	12.9792	Heteroclinic	6.0645	A, S
16.5	4.0617	Homoclinic	12.7550	Heteroclinic	—	A
17	3.9067	Heteroclinic	12.5073	Homoclinic	—	W
18	3.7102	Heteroclinic	11.9028	Homoclinic	—	W
19	3.5821	Heteroclinic	—	—	—	I

certain initial conditions, the continuous gravitational collapse of an inhomogeneous dust cloud can lead to the formation of a naked singularity [257–279]. However, according to the cosmic censorship conjecture, such horizonless compact objects are not physically viable [280–283]. As a result, the existence of naked singularities remains a topic of ongoing theoretical debate. Naked singularities appear as solutions to the field equations in GR [126, 284–287] as well as in various alternative gravity theories [288–292]. The ambiguous nature of NkS objects highlights the need for studies on how to detect such objects. A particularly relevant question is whether their physical properties could enable a robust distinction between BH and NkS objects. In this regard, many studies have explored the orbital precession of timelike geodesics, gravitational lensing, shadow formation, and accretion properties in NkS spacetime [293–304]. All these analyses depicted that the astrophysical phenomena of naked singularities strongly deviate from those of black holes. Recent analyses of GR hydrodynamics simulation of accretion flows around these exotic objects have revealed distinct signatures that separate the black holes from naked singularities [305–307]. Note that all the aforementioned works have been carried out within the context of several NkS spacetimes in both GR and beyond GR. But here, we want to study the accretion phenomena in a non-Kerr NkS spacetime, where a definite gravity theory is still unknown (called bottom-up metrics [167]).

It has been found that the JP spacetime (a bottom-up case) can yield a NkS object under a certain combination of a_k (even if $a_k < 1$) and ε. Towards this, we employ the horizon condition as $g_{rr}^{-1}(r_{\rm H}) = 0$ and upon simplification, we get,

$$r_{\rm H}^5 - 2r_{\rm H}^4 + a_k^2 r_{\rm H}^3 + a_k^2 \varepsilon = 0. \tag{2.44}$$

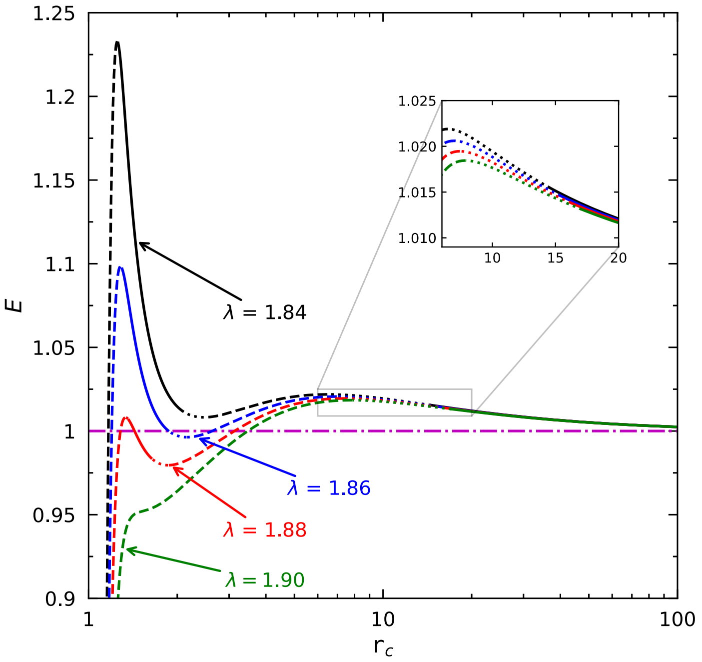

Figure 2.15: Variation of flow energy (E) with the critical points (r_c) for different angular momentum (λ). Here, we choose $a_k = 0.99$ and $\epsilon = 0.03$. Saddle, nodal and O-type critical points are indicated with the solid, dotted and dashed curves. Horizontal line (dot-dashed) is plotted at specific energy $E = 1$. A part of the plot is zoomed for the purpose of clarity. See text for details.

For a suitable choice of (a_k, ϵ), when Eq. (2.44) does not provide any real roots, the central object evidently represents the naked singularity, instead of black hole. Considering such scenario, in this section, we study the properties of the accretion flow around the JP NkS objects and examine how a_k and ϵ regulate the nature of the accretion solutions. While doing so, we follow the same methodologies as discussed in Section 2.4.

2.6.1 Critical point properties

In Fig. 2.15, we present the variation of the flow energy (E) with r_c for $(a_k, \epsilon) = (0.99, 0.03)$ that renders naked singularity. The obtained results plotted using black, blue, red and green curves are for $\lambda = 1.84, 1.86, 1.88$ and 1.90, respectively. For each λ, solid, dotted and dashed curves represent saddle, nodal and spiral (O-type) critical points. We observe that unlike black hole case, there exists four critical points in an energy range ($E \geq 1$) that eventually depends on the flow angular momentum λ. On the contrary, when $E < 1$, flow may have single or at most three critical points depending on λ. Interestingly, we note that the critical points located closest to the central singularity are of spiral type

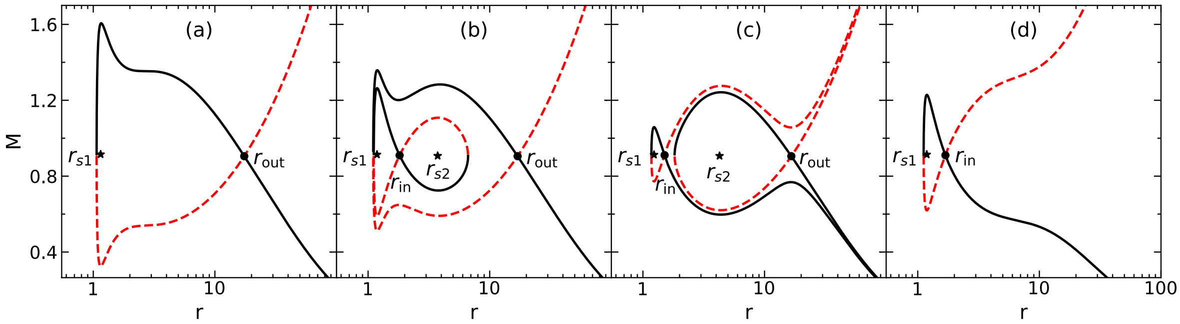

Figure 2.16: Variation of Mach number ($M = v/C_s$) with the radial distances (r) for $a_k = 0.99$ and $\varepsilon = 0.03$. In each panel, solid (black) and dashed (red) curves represent the accretion and wind solutions, respectively. Filled circles and asterisks denote saddle and O-type critical points, respectively. Here, we choose $(\lambda, E) = (1.82, 1.0137)$, $(1.85, 1.0137)$, $(1.87, 1.0137)$, and $(1.85, 1.025)$ in respective panels (a-d). See text for details.

and hence they are not physical as accretion flow can not pass through them. For a given λ, the critical points are in general arise in sequence starting from the inner most one as spiral-saddle-nodal-spiral-nodal-saddle, provided flow possesses multiple critical points.

2.6.2 Flow solutions of different kinds

In Fig. 2.16, we present all possible type of flow solutions around naked singularity, where the variation of Mach number (M) as function of radial distance (r) is depicted in each panel. Here, we choose $a_k = 0.99$ and $\varepsilon = 0.03$ that yields naked singularity. In panel (a), we fix $\lambda = 1.82$ and $E = 1.0137$, and obtain two critical points; the closest one from the singularity is of spiral type formed at $r_{s1} = 1.1493$ (filled asterisk) and the furthest one is of saddle type located at $r_{\rm out} = 17.4339$ (filled circle). We calculate the flow solutions passing through $r_{\rm out}$ and plot the accretion and wind branches using solid and dashed curves, respectively. We note that during the course of accretion, rotating transonic flow usually piles up and hence tends to co-rotate along a surface close to the naked singularity usually known as *naked surface* [121]. This feature is clearly seen in panel (a) as M for accretion drops down around the singular point. In Fig. 2.16b, we show the flow solutions for $\lambda = 1.85$ and $E = 1.0137$, where four critical points are obtained. Among them, two are saddle type ($r_{\rm in} = 1.8155$ and $r_{\rm out} = 16.9517$ marked as filled circles) and remaining two are spiral type ($r_{s1} = 1.1832$ and $r_{s2} = 3.7319$ marked as filled asterisks). As before, solid and dashed curves denote the accretion and wind branches. We notice that solution passing through $r_{\rm out}$ connects the *naked surface* and the outer edge of the disc ($r_{\rm edge}$), however, flow possesses $r_{\rm in}$ does not extend up to $r_{\rm edge}$,

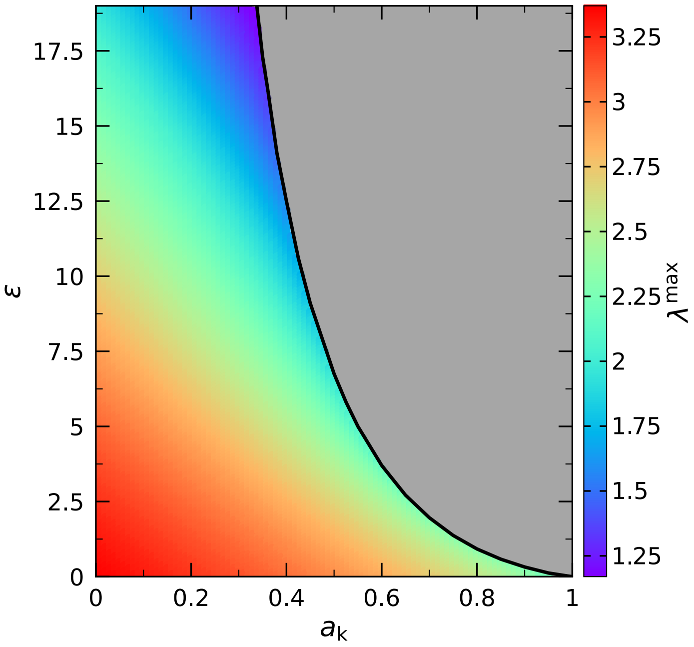

Figure 2.17: Parameter space in $a_k - \varepsilon$ plane that admits flow solutions. Thick solid curve separates the effective domains for BH and NkS, respectively. In BH region, color map denotes the 2D projection of 3D plot of a_k, ε and maximum angular momentum $\lambda^{\max}$. The vertical color bar indicates the range of $\lambda^{\max}$. See text for details.

instead it becomes closed in between $r_{\rm in}$ and $r_{\rm out}$. Moreover, we find $\dot{\mathcal{M}}_{\rm in} > \dot{\mathcal{M}}_{\rm out}$. In panel (c), we choose $\lambda = 1.87$ and $E = 1.0137$ and again obtain two saddle and two spiral critical points at $r_{\rm in} = 1.5073$, $r_{\rm out} = 16.6046$, $r_{s1} = 1.2339$, and $r_{s2} = 4.2651$, respectively. Here we observe that the overall nature of the flow solutions is changed compared to the solutions presented in (b) and $\dot{\mathcal{M}}_{\rm in} < \dot{\mathcal{M}}_{\rm out}$. In fact, solution passing through $r_{\rm out}$ becomes closed, but the same containing $r_{\rm in}$ smoothly connects *naked surface* and $r_{\rm edge}$. In panel (d), we set $\lambda = 1.85$ and $E = 1.025$, and find $r_{s1} = 1.1856$ (filled asterisk) and $r_{\rm in} = 1.6893$ (filled circle). As before, solid and dashed curves passing through $r_{\rm in}$ denote the accretion and wind branches. Finally, we wish to mention that all these flow solutions are in agreement with the results reported in [121].

2.6.3 Deformation parameter (ε) separating BH and NkS

In this section, we intend to determine the range of deformation parameter (ε) that yields the black hole spacetime. While doing this, for a given a_k, we freely vary ε, λ, and E (> 1) that provides a maximum limit of ε ($= \varepsilon^{\max}$) such that the flow from the outer edge of the disc smoothly accretes onto the black hole (see inset panels of Fig. 2.3). When

$\varepsilon > \varepsilon^{\max}$, the accreting matter starts to pile up around the O-type critical points very close to the central singularity (see Fig. 2.16) resulting the inaccessible region (called naked surface) to the flows. With this, in Fig. 2.17, we present the obtained results where solid (black) curve denotes the upper limit of deformation parameter ($\varepsilon^{\max}$) as function of a_k that separates the domain of black holes (shaded in rainbow color) from the naked singularities (shaded in gray). This findings are in agreement with $\varepsilon^{\max}(a_k)$ which is obtained by solving Eq. (2.44). In the figure, color code denotes the maximum angular momentum ($\lambda^{\max}$) corresponding to a given set of (a_k, ε) that admits closed solution passing through $r_{\rm in}$ (see A-type accretion solutions in Fig. 2.3). The colorbar indicates the range of $\lambda^{\max}$. We find that for $\varepsilon \to 0$, $\lambda^{\max}$ gradually decrease with the increase of a_k which is consistent with Fig. 5 of Ref. [239]. On the contrary, we note that for a given a_k, $\lambda^{\max}$ decreases with the increase of ε. Here, we restrict our analysis to the observational limit of the deformation parameter $\varepsilon \le 19$ [222] and observe that the present analysis carried out based on accretion theory appears is consistent with the works [161, 230]. With this, we emphasize that accretion phenomenon offers an alternative approach in distinguishing the nature of the central source embedded in deformed Kerr spacetime. Moreover, since the accretion solutions successfully delineate the observational findings of extremely gravitating objects, we also infer that the present formalism would be immensely useful in explaining the astrophysical sources.

2.7 Chapter Summary and Conclusions

In this chapter, we study the structure of a relativistic, inviscid, accretion flow in the JP spacetime [161] that describes the compact gravitating object embedded in deformed spacetime. We solve the conservation equations that governs the dynamics of the accretion flow around the central object and examine the role of spacetime deformation (ε) in controlling the global accretion solutions in presence and absence of shock waves. We note that the spacetime geometry under consideration represents either BH or NkS depending on the spacetime parameters (a_k, ε). We summarize our findings below.

We find that depending on the input parameters, namely energy (E), angular momentum (λ), spin parameter (a_k), and deformation parameter (ε), flow may contain either single or multiple critical points around BH and NkS (see Fig. 2.1 and Fig. 2.15). We obtain the flow solutions containing single critical point and find that for increasing ε, the nature of the solutions changes as it possesses multiple critical points (see Fig. 2.2 and Fig. 2.16). We identify the effective domain of the parameter space in $\lambda - E$ plane for multiple critical points which is further sub-divided based on the entropy criteria *i.e.*, $\dot{\mathcal{M}}_{r_{\rm in}} \lessgtr \dot{\mathcal{M}}_{r_{\rm out}}$, $r_{\rm in}$ and $r_{\rm out}$ being the inner and outer critical points, respectively (see Fig. 2.3). Further, we classify the multiple critical point parameter space in terms of both a_k and ε, and find that parameter space strongly depends on them (see Fig. 2.4 and Fig. 2.5). Accretion flows containing multiple critical points are of special interest as they may contain shock waves and shock-induced global accretion solution is perhaps essential to understand the observational signatures of black holes [47, 104–107, 308].

One of the aims of the present work is to calculate the global shock-induced accretion solutions in deformed spacetime and examine the shock dynamics as a function of ε. We find that for flows with fixed input parameters, shock settles down at larger radius as the ε is increased (see Fig. 2.7). Since the shock location provides the size of PSC and PSC inverse Comptonizes the soft photons from the pre-shock flow to produce high energy radiations, it is therefore worthy to examine the shock properties as they are likely to decide the nature of emitted photons from PSC. Accordingly, we examine the variation of shock location ($r_{\rm sh}$), compression ratio (R) and shock strength (S) as function of input parameters (see Fig. 2.9 and Fig. 2.10).

We separate the region of the parameter space in $\lambda - E$ plane that admits standing shock. We find that for $a_k = 0$, as ε is increased, the effective region of the parameter space is increased and shifted to lower angular momentum and higher energy sides. This suggests that the possibility of shock formation is enhanced for higher ε provided the relativistic shock conditions are satisfied (see Fig. 2.11). Similarly, for fixed ε, we obtain the shock parameter space at relative higher angular momentum when a_k is small and vice versa (see Fig. 2.12).

Further, for the first time to our knowledge, we report that the zero angular momentum flow (ZAMF) can harbor standing shock around BHs embedded in deformed Kerr spacetime. We find that shock solutions are possible when the spacetime deformation is sufficiently high (see Fig. 2.13). Accordingly, we infer that the spacetime deformation plays pivotal role for the formation of standing shock in ZAMF (see Fig. 2.14).

We also observe that the nature of the central source in deformed Kerr spacetime may yields naked singularity (NkS). This happens when the horizon condition (2.44) does not provide real roots for a given set of (a_k, ε). We calculate the accretion solutions involving either single or multiple critical points (see Fig. 2.16). Moreover, analyzing the accretion dynamics, we separate the domain of BH from NkS in $a_k - \varepsilon$ plane and find that obtained results are in agreement with [161, 230]. With this, we infer that the present formalism offers an alternative approach to examine the nature of the central object (either BH or NkS) embedded in deformed Kerr spacetime (see Fig. 2.17).

So far, we have investigated various types of accretion solutions and their associated dynamical and thermodynamical properties in terms of JP deformation. Also, we have offered a valuable tool to distinguish between BH and NkS objects based on the behavior of their accretion solutions. In this context, few interesting question arise: What role does the JP deformation play in the spectral properties of the accretion flow? Are there any distinguishing characteristics in the disc luminosity spectra of BH and NkS objects that could help to isolate them? In the next chapter, we address all these questions by studying the spectral properties of accretion disc in JP spacetime by considering the thermal bremsstrahlung (or free-free) emission mechanism.

Appendices

2.A Derivation of $\frac{dv}{dr}$ at the critical point r_c

Applying l'Hôpital's rule, we get the radial velocity gradient at the critical point (r_c) as,

$$\left.\frac{dv}{dr}\right|_c = \frac{-B \pm \sqrt{B^2-4AC}}{2A},$$

where the explicit form of the quantities A, B and C are calculated as follows:

$$A = \gamma_v^2\left[1+\frac{2C_s^2}{(\Gamma+1)v^2}\right]+\frac{4\gamma_v^4\Theta}{v^2(2N+1)}\frac{\partial}{\partial\Theta}\left(\frac{C_s^2}{\Gamma+1}\right),$$

$$B = \frac{8\gamma_v^2\Theta}{v(2N+1)}\left[N_{11}+N_{12}-\frac{3\varepsilon}{2r^4}N_{13}\right]\frac{\partial}{\partial\Theta}\left(\frac{C_s^2}{\Gamma+1}\right),$$

$$C = \frac{d^2\Phi^{\rm eff}}{dr^2}+\frac{4\Theta}{2N+1}\left[N_{11}+N_{12}-\frac{3\varepsilon}{2r^4}N_{13}\right]^2\frac{\partial}{\partial\Theta}\left(\frac{C_s^2}{\Gamma+1}\right)$$
$$-\frac{2C_s^2}{\Gamma+1}\left[N'_{11}+N'_{12}+N_{14}+\frac{3a_k^2\varepsilon}{2r^4(\Delta+a_k^2h)^2}\left(\Delta'-\frac{3a_k^2\varepsilon}{r^4}\right)\right],$$

$$N_{11}=\frac{5}{2r}+\frac{r-a_k^2(1+h)}{r(\Delta+a_k^2h)},\ N_{12}=-\frac{1}{2F}\frac{dF}{dr},\ N_{13}=\frac{1}{1+h}+\frac{a_k^2}{\Delta+a_k^2h},$$

$$N_{14}=\frac{6\varepsilon}{r^5(1+h)}-\frac{9\varepsilon^2}{2r^8(1+h)^2}+\frac{6a_k^2\varepsilon}{r^5(\Delta+a_k^2h)},$$

$$\frac{\partial}{\partial\Theta}\left(\frac{C_s^2}{\Gamma+1}\right)=\frac{2\Gamma}{(f+2\Theta)(\Gamma+1)}-\frac{2\Theta\Gamma(2+f')}{\big(f+2\Theta)^2(\Gamma+1)\big)}-\frac{2\Theta\Gamma\Gamma'}{(f+2\Theta)(\Gamma+1)^2}+\frac{2\Theta\Gamma'}{(f+2\Theta)(\Gamma+1)},$$

$$f'=\frac{\partial f}{\partial\Theta}=N_1+N_2,\ \Gamma'=\frac{\partial\Gamma}{\partial\Theta}=-2\frac{N'_1+N'_2}{(N_1+N_2)^2},$$

$$N_1=(2-\xi)\left[\frac{9\Theta}{3\Theta+2}-\frac{3\Theta(9\Theta+3)}{(3\Theta+2)^2}+\frac{9\Theta+3}{3\Theta+2}\right],\ N_2=\xi\left[\frac{9\Theta}{3\Theta+\frac{2}{\chi}}-\frac{3\Theta\left(9\Theta+\frac{3}{\chi}\right)}{\left(3\Theta+\frac{2}{\chi}\right)^2}+\frac{9\Theta+\frac{3}{\chi}}{3\Theta+\frac{2}{\chi}}\right],$$

$$N'_1=\frac{\partial N_1}{\partial\Theta}=(2-\xi)\left[\frac{18\Theta(9\Theta+3)}{(3\Theta+2)^3}-\frac{54\Theta}{(3\Theta+2)^2}+\frac{18}{3\Theta+2}-\frac{6(9\Theta+3)}{(3\Theta+2)^2}\right],$$

$$N'_2=\frac{\partial N_2}{\partial\Theta}=\xi\left[\frac{18\Theta\left(9\Theta+\frac{3}{\chi}\right)}{\left(3\Theta+\frac{2}{\chi}\right)^3}-\frac{54\Theta}{\left(3\Theta+\frac{2}{\chi}\right)^2}+\frac{18}{3\Theta+\frac{2}{\chi}}-\frac{6\left(9\Theta+\frac{3}{\chi}\right)}{\left(3\Theta+\frac{2}{\chi}\right)^2}\right],$$

$$\frac{d^2\Phi_{\rm eff}}{dr^2}=\frac{1}{2}\left(N_{21}+N_{22}+N_{23}-\frac{1}{2r^2}\right),\ N_{21}=\left(\frac{N'_{111}}{N_{111}}\right)^2-\frac{N''_{111}}{N_{111}},$$

Indian Institute of Technology Guwahati

$$N_{22} = \frac{h''}{1+h} - \left(\frac{h'}{1+h}\right)^2, \; N_{23} = \frac{2+a_k^2 h''}{\Delta + a_k^2 h} - \left(\frac{\Delta' + a_k^2 h}{\Delta + a_k^2 h}\right)^2, \; \Delta' = \frac{d\Delta}{dr} = 2(r-1), \; h' = \frac{dh}{dr} = -\frac{3\varepsilon}{r^4},$$

$$h'' = \frac{dh'}{dr} = \frac{12\varepsilon}{r^5}, \; N_{111} = r^3 + a_k^2(r+2)(1+h) - 4a_k\lambda(1+h) - \lambda_k^2(r-2)(1+h),$$

$$N'_{111} = \frac{dN_{111}}{dr} = 3r^2 + a_k^2(r+2)h' + a_k^2(1+h) - 4a_k\lambda h' - \lambda^2(1+h) - \lambda^2(r-2)h',$$

$$N''_{111} = \frac{dN'_{111}}{dr} = 6r + \left[a_k^2(r+2) - 4a_k\lambda - \lambda^2(r-2)\right] h'' + \left(2a_k^2 - \lambda^2\right) h'.$$

Here, all the quantities have their usual meaning.

Indian Institute of Technology Guwahati

CHAPTER 3

ACCRETION FLOW IN JOHANNSEN-PSALTIS SPACETIME: LUMINOSITY SPECTRA FROM FREE-FREE EMISSION

3.1 Introduction and Motivation

In the previous chapter, we examined the accretion properties of transonic flows in the Johannsen-Psaltis (JP) spacetime that can represent both black hole (BH) and naked singularity (NkS), depending on the spacetime parameters. The JP metric is characterized by a deformation parameter (ϵ), in addition to the mass ($M_{\rm BH}$) and spin (a_k) of the central object. In that chapter, we discussed the motivations behind the proposal of the JP metric and highlighted why it has drawn considerable attention from researchers over the past decade. Our analysis has found different transonic accretion solution topologies (e.g., O, A, W, and I-types), including shock solutions in the JP spacetime, as usually observed in the Kerr spacetime. We have demonstrated the modifications of the identified accretion solutions and the variation of their associated flow properties with ϵ for both the BH and NkS models. We also distinguished the BH and NkS objects by analyzing the behaviors of the accretion solutions around them. However, in that study, we did not explore the spectral properties of the existing transonic accretion solutions. It is important to examine how the luminosity distributions of accretion discs change with the deformation parameter. The distinctive signatures in the luminosity spectrum, bolometric luminosity, and some other observational features of the accretion disc around BH and NkS objects may offer a more promising way to detect them. Inspired by this, we present the current chapter, where we study the thermal properties of the accretion disc in the JP spacetime.

In this work, we consider the thermal bremsstrahlung emission from the hot accreting plasma around the supermassive compact objects. Even though the theory of thermal bremsstrahlung is well established, an accurate expression of the emission coefficient and its applicability in different temperature regimes is still an unresolved problem. In these circumstances, several formulas have been developed in the literature (e.g., see [309] and references therein). As the electron temperature is in the relativistic regime for hot accretion flow [11], we use an approximate analytical expression of thermal bremsstrahlung emissivity derived by Novikov and Thorne [64]. We find that the relativistic bremsstrahlung emissivity overestimates the disc luminosity compared to the non-relativistic model (NR-model). Therefore, the relativistic model (R-model) for thermal bremsstrahlung is used in our analysis.

We calculate the disc luminosity and spectral energy distributions (SEDs) corresponding to O, A, W and I-types accretion solution topologies in the black hole spacetime. We infer that I-type solutions produce high luminous power spectra compared to O, A and W-type solutions. Moreover, SEDs for W and I-type solutions significantly differ from O and A-type solutions, particularly for low flow energy (E). Also, the effect of deformation parameter ε on the luminosity spectrum has been investigated. We notice that SEDs increase with ε, indicating that an accretion disc around a non-Kerr black hole generates more luminous power spectrum than the usual Kerr black hole. We further extend our analysis for a naked singularity object embedded in the JP non-Kerr metric. Like the black hole model, we notice that SEDs for I-type solutions are greater than the other flow topologies. But, in contrast to the black hole model, luminosity distributions for W and I-type solutions moderately differ from O and A-type solutions. Most importantly, from a comparative study between the SEDs, we wish to emphasize that a naked singularity object can produce a high luminous power spectrum at both low and high-frequency regions compared to the black hole. These results open up a window to isolate black holes and naked singularity objects through the spectral analysis of accretion disc.

The present chapter is arranged as follows. We begin by developing the mathematical framework for thermal bremsstrahlung emission process and highlighting the importance of the relativistic model over the non-relativistic one. Next, we investigate the luminosity distribution for different flow topologies in both black hole and naked singularity spacetimes. We then examine the effect of the JP deformation on the disc luminosity spectrum. Finally, we conduct a comparative study of the spectral energy distributions for the black hole and naked singularity models.

3.2 Flow hydrodynamics and bremsstrahlung

In this work, we carry out the emission properties of the accretion flow in the Johannsen-Psaltis (JP) spacetime (see the metric in Eq. (2.18)). We consider a steady, inviscid, and axisymmetric accretion flow along the equatorial plane of the central object. We also choose a unit system as $G = c = M_{\rm BH} = 1$, where G is the gravitational constant and c is the speed of light. Therefore, we adopt the same set of flow equations as those modeled in Section 2.3, using the general relativistic hydrodynamics framework and the relativistic equation of state (REoS). These governing equations enable us to obtain accretion solutions of different kinds, which are crucial for calculating the emission spectrum in the JP spacetime. Note that when we set the deformation function $h = 0$ (i.e., $\varepsilon = 0$), we recover the usual GR flow hydrodynamics in the Kerr spacetime [116].

In our analysis, we consider the bremsstrahlung (or free-free) emission from the accelerating electrons in the field of heavy ions. For simplicity, we consider negligible deviation of the electron's path during a close encounter with an ion. Further, we consider Maxwell-Boltzmann speed distribution of the thermal electrons. Under these assumptions, we obtain an expression of the non-relativistic bremsstrahlung emissivity (or power density) at a particular emission frequency ν_e as [310],

$$\mathcal{E}_{\nu_e}^{\rm ff,\,ei} = \frac{32\pi e^6}{3m_e c^3}\sqrt{\frac{2\pi}{3m_e k_B}}\, n_e n_i Z^2 T_e^{-1/2} e^{-h\nu/k_B T_e}\, \bar{g}_{\rm ff}^{\rm ei}, \tag{3.1}$$

where e is the electron charge, m_e is the electron mass, k_B is the Boltzmann constant, n_e is electron number density, n_i is ion number density, Z is ion atomic number, T_e is electron temperature, and h is the Planck constant. The thermally averaged electron-ion Gaunt factor $\bar{g}_{\rm ff}^{\rm ei}$ includes quantum mechanical correction to the classical electrodynamics. Depending on the energy of emitting electrons, $\bar{g}_{\rm ff}^{\rm ei}$ varies from 1 to 5 [311, 312]. However, we take $\bar{g}_{\rm ff}^{\rm ei} = 1.2$ [309] in our analysis. Moreover, we set $Z = 1$ for hydrogen plasma.

When the plasma temperature is in the non-relativistic regime (i.e., $k_B T_e < m_e c^2$), radiations due to the encounter between like particles e.g., electron-electron and ion-ion are negligible in comparison with the electron-ion emission. This is simply due to the conservation of dipole moment, and the contributions from quadrupole and higher order moments have very less intensity in comparison to the dipole part [310]. But, when $k_B T_e \geq m_e c^2$, electron-electron bremsstrahlung dominates the power over the electron-ion emission [309, 313, 314]. In case of hot accretion flow (HAF), plasma temperature can vary from 10^9 K to 10^{12} K [11, 47, 123, 315]. So, in this temperature range, relativistic effect and electron-electron emission can modify the emissivity in Eq. (3.1). An approximate expression of the total bremsstrahlung emissivity is given by [64],

$$\mathscr{E}^{\mathrm{ff}}_{\nu_e} = \frac{32\pi e^6}{3m_e c^3}\sqrt{\frac{2\pi}{3m_e k_B}}\, n_e n_i Z^2 T_e^{-1/2}(1+4.4\times 10^{-10}T_e)e^{-h\nu/k_B T_e}\bar{g}_{\mathrm{B}}, \tag{3.2}$$

where $\bar{g}_{\mathrm{B}}$ is the thermally-averaged Gaunt factor, which is taken as 1.2 [309]. The additional terms in Eq. (3.2) incorporate the relativistic effect and electron-electron bremsstrahlung as well.

In general, the radiations from the hot plasma flowing through the disc come out isotropically. For an observer at static infinity, such radiation gets red-shifted while it travels into the immense potential well of the central compact object. In addition, emitting gas proceeds toward the observer or away from the observer due to disc rotation, producing Doppler shift. Therefore, resulting redshift factor $(1+z)$ depends on the combined effect of both the gravitational and Doppler parts. For simplicity, we neglect the light-bending effect to the emitting photons. As a result, the redshift factor, defined as the ratio of emitted frequency (ν_e) to observed frequency (ν_o), is calculated as [316],

$$\frac{\nu_e}{\nu_o} = 1+z = u^t\left(1+\frac{r\Omega}{c}\sin\theta_0\sin\phi\right), \tag{3.3}$$

where θ_0 is the inclination angle of the accretion disc with respect to the distant observer direction, which is taken as 45° [121, 122]. Following Eq. (2.13), we obtain the time component of the contravariant four velocity (u^k) as,

$$u^t = \gamma_v\gamma_\phi\sqrt{\frac{r}{(2a_k\Omega+(r-2))(1+\mathfrak{h})}}, \tag{3.4}$$

where γ_ϕ ($= 1/\sqrt{1-v_\phi^2} = 1/\sqrt{1-\Omega\lambda}$, λ is the specific angular momentum of the flow) and γ_v ($= 1/\sqrt{1-v^2}$) are the Lorentz factors corresponding to azimuthal and radial components (v_ϕ and v) of physical three velocity, respectively. The flow angular velocity (Ω) is given by Eq. (2.31). Here, we consider positive u^t just to ensure that flow energy E ($= -(e+p)u_t/\rho$) remains positive.

In the hot plasma, we consider the electron and ion number densities are identical. They relate with the mass density (ρ) as $n_e = n_i \approx \rho/m_p$, where m_p is the proton mass. Therefore, the monochromatic disc luminosity for an observer at infinity is obtained from

Eqs. (3.2) and (3.3) as,

$$
\begin{aligned}
L_{\nu_o} &= 2\int_{r_0}^{r_{\rm edge}}\int_0^{2\pi} \mathscr{E}^{\rm ff}_{\nu_o} Hr\, dr d\phi \\
&= 4.875\times 10^{10}\bar{g}_{\rm B}\ {\rm erg\ s^{-1}\ Hz^{-1}} \\
&\times \int_{r_0}^{r_{\rm edge}}\int_0^{2\pi}\left[\rho^2 T_e^{-1/2}(1+4.4\times 10^{-10}T_e)e^{-(1+z)h\nu_o/k_B T_e} Hr\right] dr d\phi,
\end{aligned}
\tag{3.5}
$$

where r_0 and $r_{\rm edge}$ are the inner and outer edges of the accretion disc, respectively.

Finally, we get the frequency-integrated (or bolometric) disc luminosity by using Eq. (3.5) as,

$$
\begin{aligned}
L &= \int_0^{\infty} L_{\nu_o} d\nu_o \\
&= 1.015\times 10^{21}\bar{g}_{\rm B}\ {\rm erg\ s^{-1}}\int_{r_0}^{r_{\rm edge}}\int_0^{2\pi}\frac{\rho^2 T_e^{1/2}(1+4.4\times 10^{-10}T_e)Hr}{u^t\left(1+\frac{r\Omega\sin\phi}{\sqrt{2}c}\right)}\, dr d\phi.
\end{aligned}
\tag{3.6}
$$

As the mass of electrons is less than the mass of protons, electron temperature (T_e) must be less than the proton temperature ($T_p = T$) at least in the vicinity of the central source. This findings are already addressed while studying the two temperature accretion flows [65, 91, 123, 251, 252, 315, 317–320]. However, in this work, we take $T_p/T_e = T/T_e = 10$ [309] throughout the accretion disc for the purpose of simplicity. We consider a supermassive black hole of mass $M_{\rm BH} = 10^6 M_\odot$, where $M_\odot$ being the Solar mass. As the mass accretion rate ($\dot{M}$) of the flow is very low for supermassive black hole [11, 309], we set $\dot{M} = 10^{-5}\dot{M}_{\rm Edd}$, where $\dot{M}_{\rm Edd} = 1.39\times 10^{18} M_{\rm BH}/M_\odot$ gm s^{-1} is the Eddington mass accretion rate. At this low $\dot{M}$, we neglect the effect of radiative cooling on the flow dynamics [309, 321]. Moreover, for the black hole model, inner and outer edges of the accretion disc are taken as $r_0 = r_{\rm H}$ (event horizon) and $r_{\rm edge} = 1000$, respectively.

In order to determine $r_{\rm H}$, one needs to find the maximum root of the equation $g_{rr}^{-1}(r_{\rm H}) = 0$. As the accretion flow is confined around the disc equatorial plane (i.e., $\theta = \pi/2$), we obtain $r_{\rm H}$ by numerically solving the following equation,

$$
r_{\rm H}^5 - 2r_{\rm H}^4 + a_k^2 r_{\rm H}^3 + a_k^2\varepsilon = 0. \tag{3.7}
$$

It is noteworthy that for NkS model, r_0 can not be determined apriori as NkS does not contain a inner boundary similar to the horizon as in the case of BH model. Hence, in this work, we estimate r_0 according to the model input parameters and choose $r_{\rm edge} = 1000$. A detailed discussion in obtaining r_0 for NkS model is presented in Section 3.4.3.

As the bremsstrahlung emission can only be detected when the emitting medium is optically thin, we need to calculate the optical depth of the accretion disc. We consider a

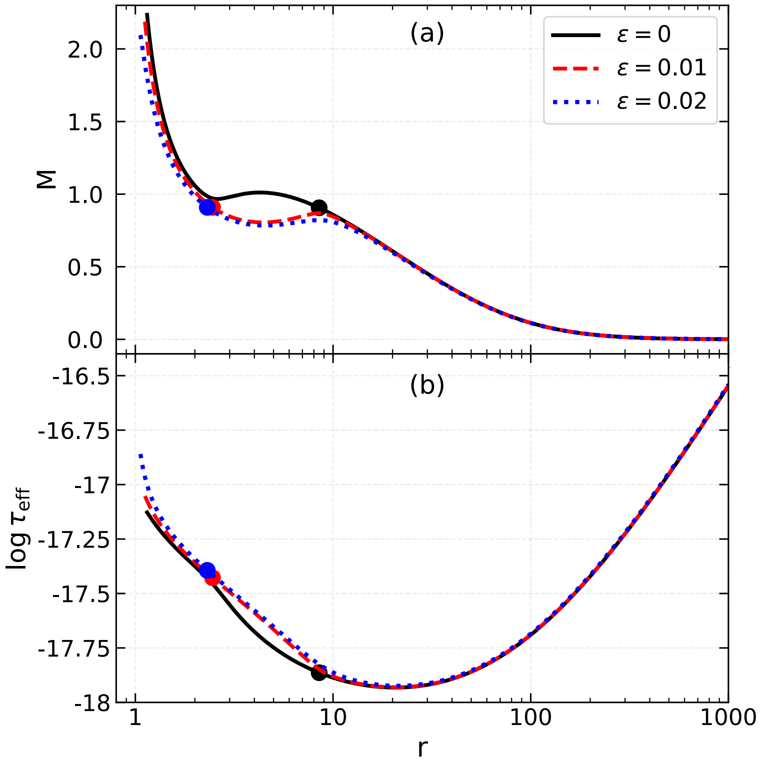

Figure 3.1: (a) Global accretion solutions (M versus r plots) for different deformation parameter (ε) and (b) plot of effective optical depth ($\tau_{\rm eff}$) as a function of radial distance (r) corresponding to the accretion solutions presented in the panel (a). In this figure, we choose $a_k = 0.99$ and $(\lambda, E) = (1.825, 1.0215)$. Here, critical points are marked by the filled circles. See the text for details.

photon generated deep inside the medium due to thermal emission. It suffers several coherent and isotropic scattering during its propagation into the medium and ends with a true absorption. One of the vital sources of opacity is the Thomson scattering of photons by the free electrons. The scattering optical depth is given by $\tau_s = \kappa_s \rho H$, where $\kappa_s \approx 0.4$ cm^2 gm^{-1} is the opacity coefficient. Here, the typical length scale of the medium is taken as the local half thickness (H) of the disc. Other significant opacity sources are bound-bound, bound-free (or photoionization) and free-free absorption (or inverse bremsstrahlung), which depend on the photon frequency, flow density, temperature and plasma composition. However, for a fully ionized medium, only free-free absorption is present [3]. The Rosseland mean opacity coefficient for free-free absorption is calculated from Eq. (3.2) as [322],

$$\kappa_{\rm R}^{\rm ff} = 6.45 \times 10^{22} \rho T_e^{-3.5} (1 + 4.4 \times 10^{-10} T_e) \bar{g}_{\rm R} \ {\rm cm}^2 \ {\rm gm}^{-1}, \tag{3.8}$$

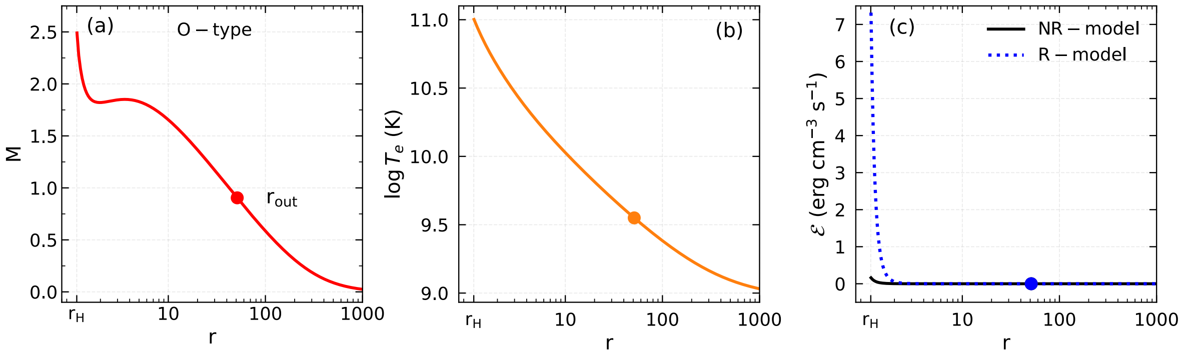

Figure 3.2: Plot of (a) Mach number ($M = v/C_s$), (b) Electron temperatures, and (c) frequency-integrated emissivity as a function of radial distance (r). Here, we choose the input parameters as $a_k = 0.99$ and $\lambda = 1.85$ and $E = 1.005$. Critical point is marked using filled circle. See the text for details.

where $\bar{g}_{\rm R}$ is the frequency-averaged Gaunt factor of $\bar{g}_{\rm B}$, which is of the order unity. The corresponding absorption optical depth is given by $\tau_a = \kappa^{\rm ff}_{\rm R}\rho H$. Therefore, the effective optical depth of the medium is obtained as [310],

$$\tau_{\rm eff} \approx \sqrt{\tau_a(\tau_a + \tau_s)}. \tag{3.9}$$

Now, we intend to calculate the optical depth of the accretion disc for different deformation parameters ϵ. In this case, input parameters are taken as $a_k = 0.99$ and $(\lambda, E) = (1.825, 1.0215)$. Flow topologies corresponding to $\epsilon = 0, 0.01$, and 0.02 are A, W, and I-types, respectively. In the subsequent sections, a clear prescription for isolating these flow topologies has been given. Using Eq. (3.9), we calculate $\tau_{\rm eff}$ associated with the global solutions (see Fig. 3.1a) for the above flow topologies. Obtained results are plotted as a function of radial coordinate (r) in Fig. 3.1b. We see that the accretion disc remains effectively thin throughout the disc. Therefore, most photons leave the medium before being absorbed and fails to maintain thermal equilibrium with the matter.

Next, we explore the relativistic effect and electron-electron emission on the emitted radiation in the Kerr spacetime. Here, we choose a rapidly-rotating Kerr black hole of spin $a_k = 0.99$. Further, angular momentum and energy of the flow are taken to be $\lambda = 1.85$ and $E = 1.005$, respectively. With these input parameters, we first obtain a flow solution (*i.e.*, variation of Mach number ($M = v/C_s$) as function of radial distance (r)) by numerically solving Eqs. (2.33) and (2.37). We see that flow possesses outer critical point only at $r_{\rm out} = 51.2471$. The solution passes through $r_{\rm out}$ globally connects $r_{\rm H} = 1.1413$ and $r_{\rm edge} = 1000$, and often called it as O-type flow topology (see Fig. 3.2a). Temperature profile of the electrons (i.e., T_e as a function of r) in the accretion disc is

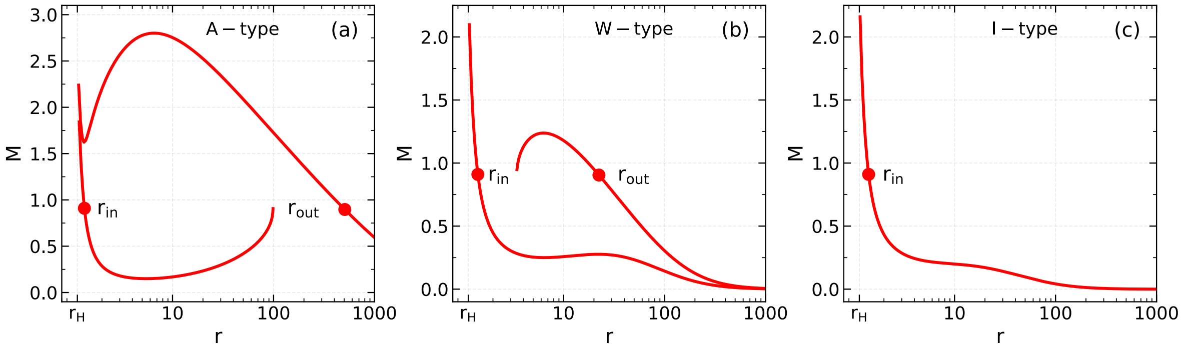

Figure 3.3: Variation of Mach number (M) as a function of radial distance (r) for a BH model with $a_k = 0.99$. Here, critical points are marked by the filled circles. In this figure, we choose flow parameters as $(\lambda, E) = (2.05, 1.0005)$, $(2, 1.01)$ and $(2, 1.02)$ for the respective panels (a-c). See the text for details.

presented in Fig. 3.2b. We see that T_e increases monotonically toward the inner edge of the disc. After that the frequency-integrated emissivity ($\mathscr{E}$) is calculated using Eq. (3.1) for non-relativistic (NR) model and using Eq. (3.2) for relativistic (R) model. Obtained results are plotted in Fig. 3.2c, where we present the variation of $\mathscr{E}$ as a function of r. In the figure, solid (black) and dotted (blue) curves represent $\mathscr{E}$ for NR and R-models, respectively. We find that for both cases, $\mathscr{E}$ does not differ too much from $r > 2$ to $r_{\rm edge}$. However, for $r_{\rm H} < r < 2$, the difference in $\mathscr{E}$ substantially increases as we proceed toward $r_{\rm H}$. Needless to mention that the above range in r is not universal, which depends on the input parameters. But, we always get a significant difference in $\mathscr{E}$ very close to $r_{\rm H}$ for any set of flow parameters providing in the transonic accretion solutions. As T_e exceeds the non-relativistic temperature limit 5.8×10^9 K $(= m_e c^2/k_{\rm B})$ [64] very close to the horizon, the second term in Eq. (3.2) starts dominating over the first term. As a result, power density of the electron-electron emission surpasses that of the electron-ion emission. Therefore, one should not neglect the contribution from electron-electron emission to the total emitted power, especially for hot accretion flow in active galactic nuclei (AGNs) [309] and black hole X-ray binaries (BH-XRBs) [251, 315, 318].

We then calculate the frequency-integrated disc luminosity for non-relativistic ($L_{\rm NR}$) and relativistic ($L_{\rm R}$) models in Kerr spacetime. Here, we fix the flow energy as $E = 1.0005$, and vary the angular momentum as $\lambda = 2.05$, 2.45 and 2.9. We find that the flow possesses multiple critical points (*i.e.*, flows have both inner ($r_{\rm in}$) and outer ($r_{\rm out}$) critical points) for these input parameters. The solutions passing through $r_{\rm out}$ successfully connect $r_{\rm H}$ to

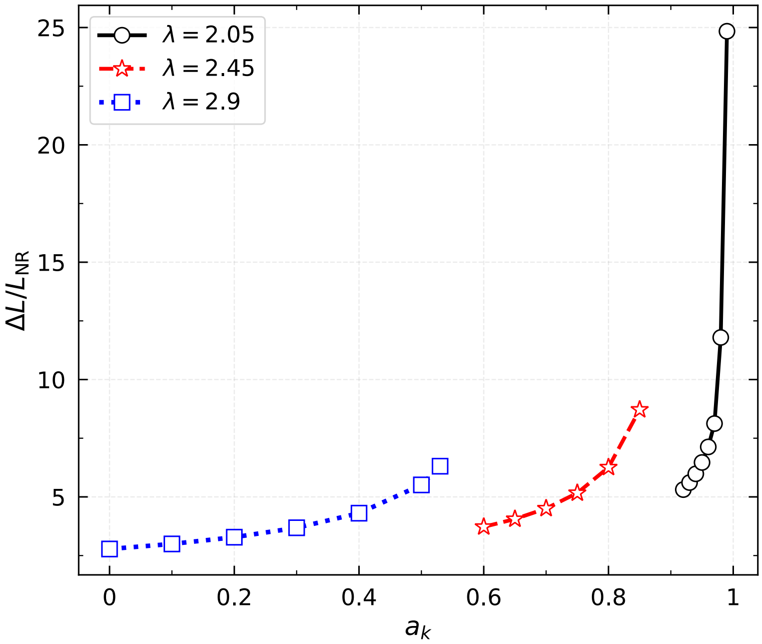

Figure 3.4: Variation of relative change in the bolometric luminosity ($\Delta L/L_{\rm NR}$) as a function of spin parameter (a_k) for different angular momentum (λ). Here, we set $E = 1.0005$. See the text for details.

$r_{\rm edge}$ (open solutions[1]). However, the solutions passing through $r_{\rm in}$ unable to connect $r_{\rm H}$ to $r_{\rm edge}$ as they terminate at some r values (closed solutions[2]). Such flow solution is defined as A-type topology and an example of such accretion solution is presented in Fig. 3.3a. The variation of relative change in bolometric luminosity ($\Delta L/L_{\rm NR} = (L_{\rm R} - L_{\rm NR})/L_{\rm NR}$) as a function of spin parameter (a_k) for different λ is presented in Fig. 3.4. In this figure, open circles joined by the solid curve (black), open asterisks joined by the dashed curve (red) and open squares joined by the dotted curve (blue) denote the quantity $\Delta L/L_{\rm NR}$ associated with the angular momentum $\lambda = 2.05$, 2.45 and 2.9, respectively. It is observed that $\Delta L/L_{\rm NR}$ increases with a_k, irrespective of λ values. It is noteworthy to mention that the change in $\Delta L/L_{\rm NR}$ for R-model is marginal for weakly spinning black holes ($a_k \rightarrow 0$), however it becomes significant for rapidly rotating black holes ($a_k \rightarrow 1$).

Indeed, the above analysis involving the Kerr spacetime indicates that the relativistic effect becomes important when electron temperature (T_e) is high and the central source spins rapidly. Hence, it seems reasonable to consider the R-model in carrying out the emission analyses for wide ranges of T_e and a_k. Accordingly, we study the emission

---

[1] Open solutions are also called global solutions as they extend from $r_{\rm edge}$ to r_0. In this chapter, all calculations have been carried out for global solutions only.

[2] As closed solutions are not physically acceptable, we do not consider such solutions.

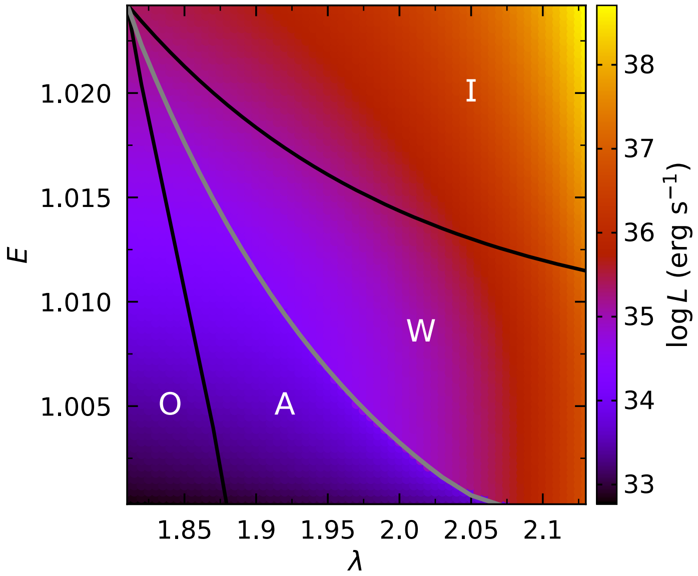

Figure 3.5: Division of parameter space in $\lambda - E$ plane according to the nature of flow solutions in the BH model. Four regions are marked as O, A, W and I. Here, we choose $a_k = 0.99$. Color map denotes the 2D projection of 3D plot of λ, E and L. Vertical color bar indicates L in erg s^{-1}. See the text for details.

properties of the accretion flow considering R-model in the subsequent sections.

3.3 Luminosity distribution for Kerr black hole

In this section, we study the disc luminosity corresponding to different flow solutions in Kerr spacetime, where $a_k = 0.99$ is chosen for the purpose of representation. We calculate the parameter space according to the flow topologies (e.g., O, A, W and I-types) in the angular momentum (λ) and energy (E) plane and depict it in Fig. 3.5. These flow topologies have different physical properties. For example, O-type solutions only contain outer critical points ($r_{\rm out}$), whereas I-type solutions only have inner critical points ($r_{\rm in}$). In both cases, flow solutions passing through the critical points smoothly connect $r_{\rm edge}$ and $r_{\rm H}$ (*i.e.*, open solutions (see Figs. 3.2a and 3.3c for O and I-type solutions, respectively)). Therefore, the flow topologies in which the existing accretion solutions pass through single critical points $r_{\rm out}$ or $r_{\rm in}$ can be distinguished as O or I-type flow topologies. However, for both the A and W-type flow topologies the accretion solutions must contain multiple critical points (*i.e.*, $r_{\rm in}$ and $r_{\rm out}$). In the A-type topology, solution passes through $r_{\rm in}$ ($r_{\rm out}$) remain closed (open) (see Fig. 3.3a) and satisfy the

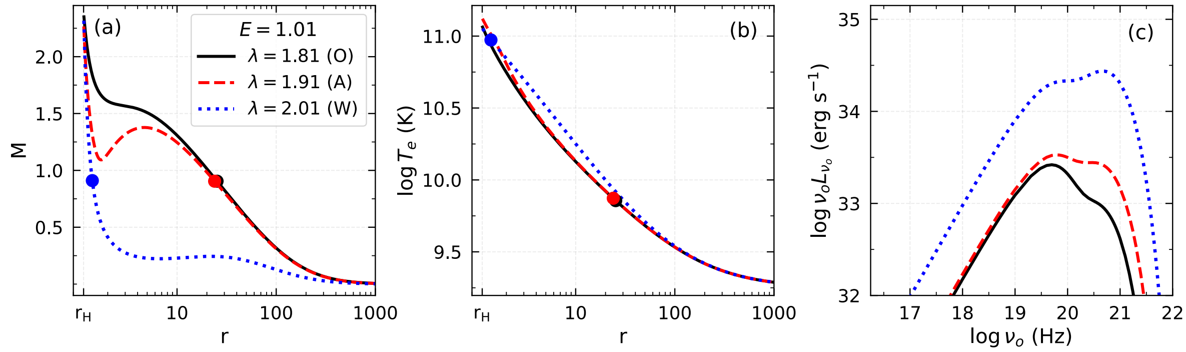

Figure 3.6: Global accretion solutions (M versus r plots in panel (a)), electron temperature profiles (T_e versus r plots in panel (b)) and spectral energy distributions ($\nu_o L_{\nu_o}$ versus ν_o in panel (c)) for O, A and W-type flow topologies. Angular momentum (λ) for different flow solutions have been marked in panel (a). Here, critical points are marked by the filled circles. In this figure, we choose a BH model with $a_k = 0.99$. And, flow energy is taken as $E = 1.01$. See the text for details.

condition $\dot{\mathscr{M}}_{\rm in} > \dot{\mathscr{M}}_{\rm out}$, where $\dot{\mathscr{M}}_{\rm in}$ and $\dot{\mathscr{M}}_{\rm out}$ are the entropy accretion rate at $r_{\rm in}$ and $r_{\rm out}$, respectively (see Eq. (2.32)). On the contrary, for the W-type flow topology, solution passes through $r_{\rm in}$ ($r_{\rm out}$) remain open (closed) (see Fig. 3.3b) and satisfies the condition $\dot{\mathscr{M}}_{\rm in} < \dot{\mathscr{M}}_{\rm out}$. Therefore, it is useful to separate the effective domain of the parameter space for different flow solutions (O, A, W and I-types) in terms of the entropy accretion rate along with the number of critical points [116, 118, 121, 122, 182]. In the figure, the region within black curves provides flow solutions containing multiple critical points (i.e., both $r_{\rm in}$ and $r_{\rm out}$). The gray curve separates the regions A and W and it corresponds to $\dot{\mathscr{M}}_{\rm in} = \dot{\mathscr{M}}_{\rm out}$. We make use of the global accretion solutions corresponding to a given set of (λ,E) and calculate the frequency-integrated luminosity (L) using Eq. (3.6). The obtained results are presented using color map in Fig. 3.5, where the color bar at the right refers the range of L in erg s^{-1}. Note that for a given λ, L increases with E. Similarly, for a given E, L increases with λ. This happens because of the fact that as λ (or E) is increased keeping E (or λ) fixed, the flow temperature increases due to the shifting of critical point towards the horizon (see Table 2 in [182]). In general, the critical points for I-type solutions are formed very close to the central object that results higher the luminosity values compared to the other flow orbits. We further investigate the spectral features of different global accretion solutions and delineate them in the subsequent sections.

Next, we explore the spectral energy distributions (SEDs) corresponding to the four types of accretion solution topologies in the Kerr spacetime. Here, we choose the flow energy as $E = 1.01$, and vary the angular momentum of the flow as $\lambda = 1.81, 1.91$ and 2.01

Table 3.1: Flow energy (E), angular momentum (λ), inner critical points ($r_{\rm in}$), outer critical points ($r_{\rm out}$) and type of accretion solutions are presented in columns 1-5. These solutions are associated with the SEDs in Figs. 3.6 and 3.7.

E	λ	$r_{\rm in}$	$r_{\rm out}$	Type
1.010	1.81	—	25.3308	O
	1.91	1.7184	23.9365	A
	2.01	1.3981	22.2109	W
1.015	1.81	—	15.7051	O
	1.87	1.9952	14.6330	A
	1.93	1.6078	13.1974	W
	1.99	1.4136	—	I
1.020	1.81	—	10.3324	O
	1.83	2.5479	9.7945	A
	1.85	2.1608	9.0972	W
	1.87	1.9008	—	I

to obtain the O, A and W-type solutions (see Fig. 3.5). We identify the global accretion solutions that pass through either outer or inner critical points as $r_{\rm out} = 25.3308$ (O-type solution), $r_{\rm out} = 23.9365$ (A-type solution), and $r_{\rm in} = 1.3981$ (W-type solution), respectively (see Table 3.1 for details). These solutions are shown in Fig. 3.6a, where solid (black), dashed (red) and dotted (blue) curves are for O, A and W-type solutions. In Fig. 3.6b, we show the profile of electron temperature (T_e) corresponding to the solutions presented in Fig. 3.6a. Using Eq. (3.5), we compute the SED for these solutions and present the obtained results in Fig. 3.6c, where the variation of $\nu_o L_{\nu_o}$ is plotted as a function of frequency ν_o. We observe that the bremsstrahlung emission dominates at $\nu_o \approx 10^{20}$ Hz [309] and has a sharp cut-off at $\nu_o \approx 10^{22}$ Hz ($= k_B T_{e0}/h$) [64], where $T_{e0} \approx 10^{11}$ K is the electron temperature at disc inner edge (r_0). Note that SEDs for O and A-type solutions are almost identical at the low frequencies, however a reasonable difference is seen at the high frequencies. For A-type solution, the critical point is formed at relatively smaller distance compared to the O-type solution that results the higher temperature at the inner part of the disc (see Fig. 3.6b). Consequently, the A-type solutions generate high luminous power spectra than the O-type solutions. In comparison, SED for W-type solution is extremely high compared to the O and A-type solutions at the both frequency ends. Since the critical point for W-type solution is formed near the central object, the overall temperature profile is enhanced and therefore, hot plasma in the accretion disc produces high luminous spectra compared to O and A-type solutions.

We continue the study of SEDs for higher flow energies and in Figs. 3.7a-b, we

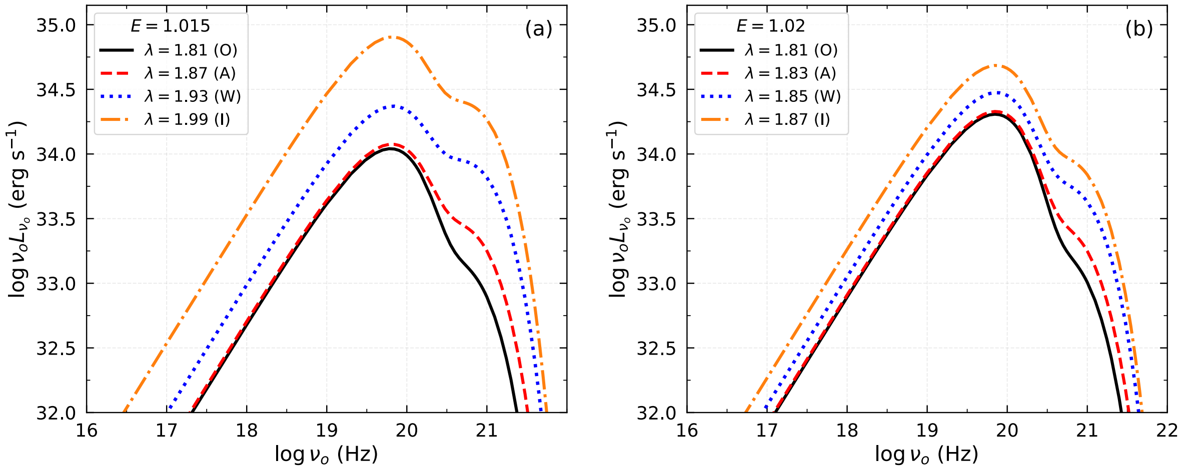

Figure 3.7: Spectral energy distributions (SEDs) for O, A, W and I-type solutions corresponding to the flow energies at $E = 1.015$ (panel a) and 1.02 (panel b). Angular momentum (λ) for different flow solutions are marked in each panels. Here, we consider a BH model with $a_k = 0.99$. See the text for details.

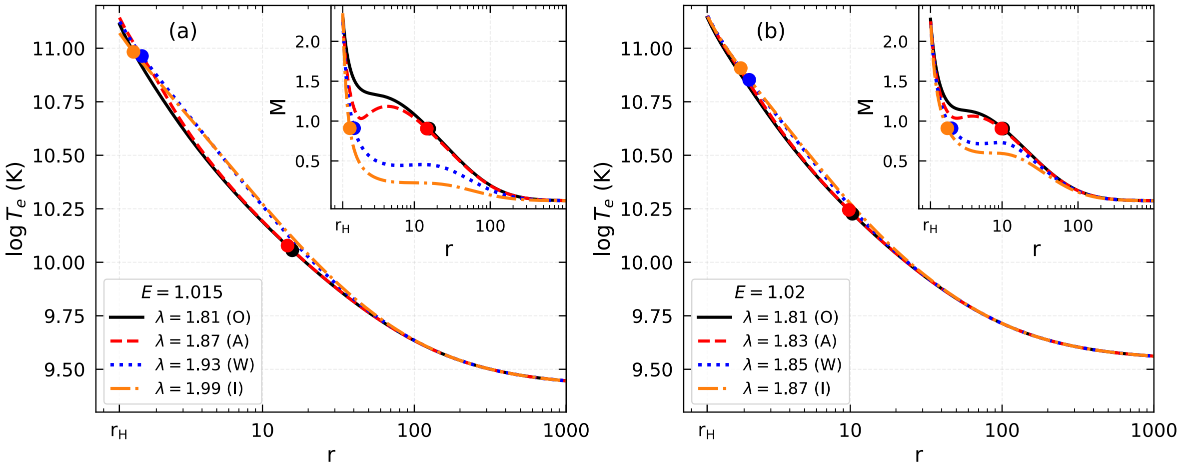

Figure 3.8: Variation of electron temperature (T_e) as a function radial distance (r) for Fig. 3.7. Inset panels denote the respective global accretion solutions (M versus r plots). In all cases, critical points are marked by the filled circles. See the text for details.

present the SEDs corresponding to O, A, W and I-type flow solutions that are obtained for $E = 1.015$ and 1.02, respectively. In both cases, we find that I-type solutions result maximum luminous power spectra compared to the other flow solutions. The details of the critical point locations for these accretion solutions and their input flow parameters are tabulated in Table 3.1. As the critical points of the I-type solutions are formed at relatively smaller distances (close to the horizon) than O, A and W-type solutions, we get higher SEDs for I-type solutions. For the purpose of clarity, we present the electron temperature (T_e) profiles in Figs. 3.8a-b corresponding to the flow solutions given in Figs. 3.7a-b. It is noticed that the temperature distributions in the disc increased when the critical points are drifted toward the singularity. Therefore, the flows that pass through the inner critical points ($r_{\rm in}$) possess high electron temperature profiles than those through the outer critical points ($r_{\rm out}$). Needless to mention that the obtain SEDs for these four types of accretion solutions strongly depend on the input flow parameters, namely energy (E) and angular momentum (λ).

3.4 Spectral analysis in deformed spacetime

In Section 3.2, we investigate the usefulness of the relativistic model (R-model) over the non-relativistic model (NR-model) for hot accretion flow (HAF) in the usual Kerr spacetime. In this section, we examine how the deformation of spacetime affects the bolometric disc luminosity as well as the spectral energy distributions in both models ($i.e.$, NR-model and R-model).

3.4.1 Effect of ε on disc luminosity for NR and R-models

In order to understand the effect of deformation parameter (ε) on the disc luminosity, we examine the relative change of bolometric disc luminosity ($\Delta L/L_{\rm NR}$) considering both weakly rotating ($a_k \rightarrow 0$) and rapidly rotating ($a_k \rightarrow 1$) black holes and depict the obtained results in Fig. 3.9. In the left panels, we show the variation of $\Delta L/L_{\rm NR}$ as a function of ε for $a_k = 0$. In panel (a), we choose $\lambda = 3$ and vary energy (E). Open circles (black), open asterisks (red) and open squares (blue) joined with solid lines denote the results obtained for flow energies $E = 1.0011$, 1.0013 and 1.0015, respectively. We observe that for a given E value, the relative increment in $L_{\rm R}$ with respect to $L_{\rm NR}$ increases with ε. We also notice that for a fixed ε, $\Delta L/L_{\rm NR}$ increases with E. In panel (b), we plot $\Delta L/L_{\rm NR}$ as a function of ε for fixed $E = 1.0012$, where λ is varied. Open circles (black),

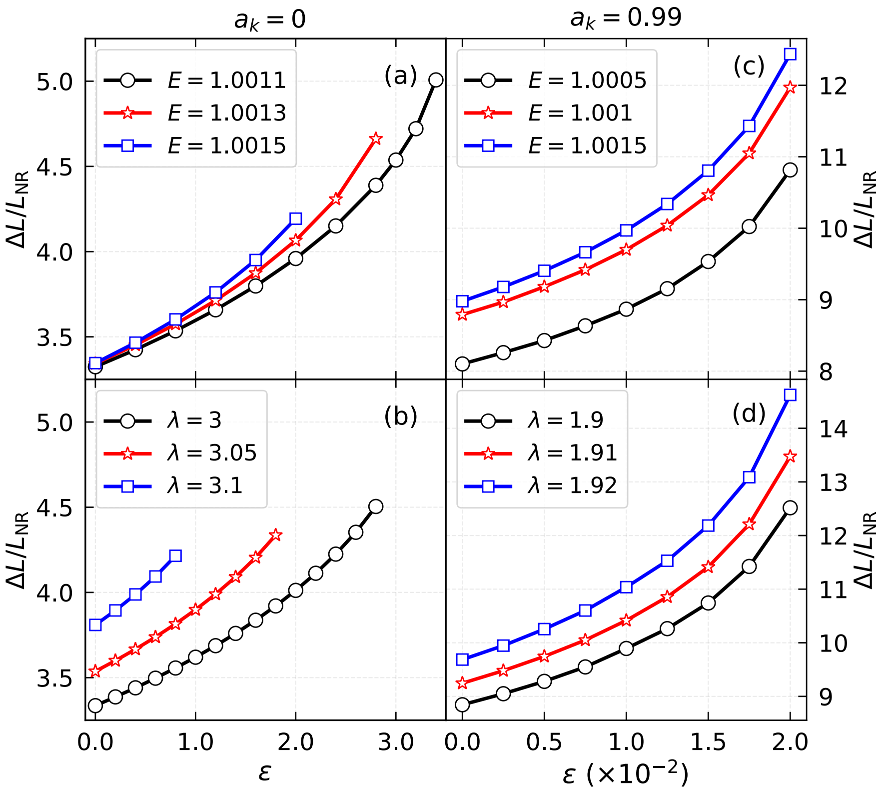

Figure 3.9: Variation of relative change in bolometric luminosity ($\Delta L/L_{\rm NR}$) as a function of deformation parameter (ε) for $a_k = 0$ (left panels) and for $a_k = 0.99$ (right panels). The flow angular momentum (λ) and energy (E) are marked in each panel. See the text for details.

open asterisks (red) and open squares (blue) joined with solid lines denote the results obtained for $\lambda = 3, 3.05$ and 3.1, respectively. We find that $\Delta L/L_{\rm NR}$ increases with ε, irrespective of λ values. And, for a fixed ε, $\Delta L/L_{\rm NR}$ increases with λ. Similarly, in the right panels, we present the variation of $\Delta L/L_{\rm NR}$ as a function of ε for $a_k = 0.99$. In panel (c), we fix $\lambda = 1.9$, and vary energy as $E = 1.0005$, 1.001 and 1.0015. The obtained results are plotted using open circles (black), open asterisks (red) and open squares (blue) joined with solid lines. Finally, in panel (d), we set $E = 1.002$ and vary angular momentum as $\lambda = 1.9$, 1.91 and 1.92 and the obtained results are shown using open circles (black), open asterisks (red) and open squares (blue) joined with solid lines. As in panel (a) and (b), we observe similar variation in (c) and (d), however $\Delta L/L_{\rm NR}$ attains higher values for $a_k = 0.99$ compared to the results for $a_k = 0$, which is consistent with the results presented in Fig. 3.4. With this, we indicate that while exploring spectral analysis in a non-Kerr spacetime with large deformation, the effect of bremsstrahlung emission in

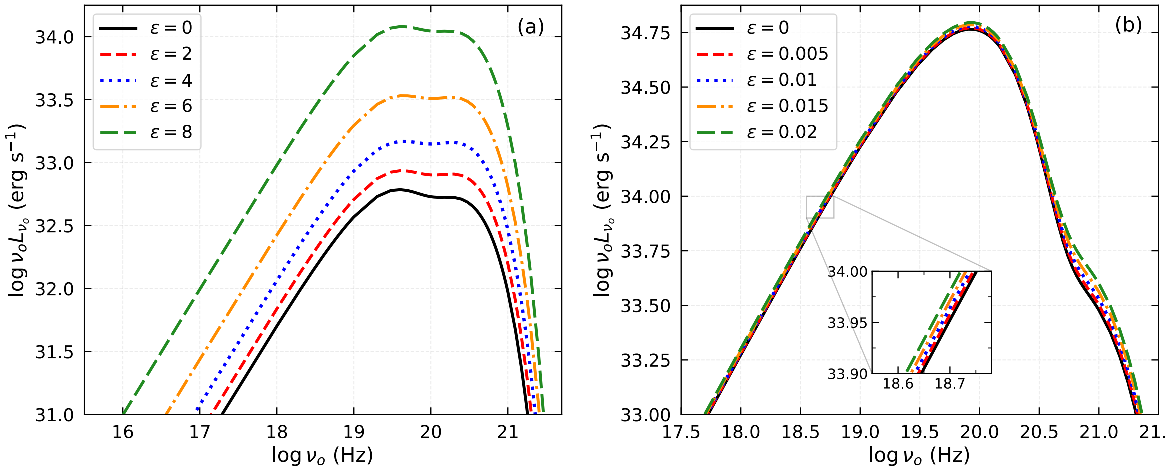

Figure 3.10: Effect of deformation parameter (ε) on the spectral energy distributions. In panel (a), results are presented for $a_k = 0$, $E = 1.005$ and $\lambda = 2.9$, whereas the same is shown in panel (b) for $a_k = 0.99$, $E = 1.0215$ and $\lambda = 1.85$. See the text for details.

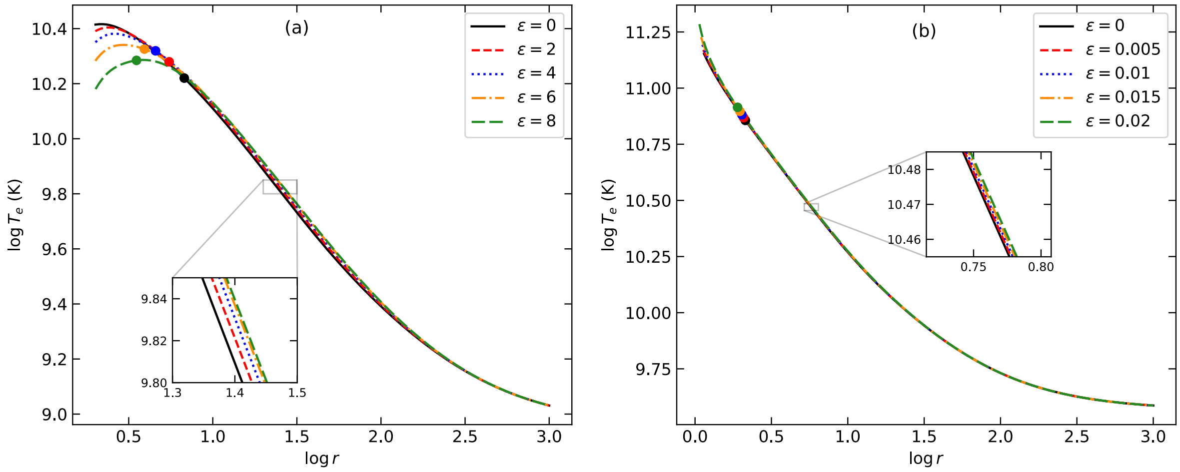

Figure 3.11: Variation of the electron temperature (T_e) as a function radial distance (r) for Fig. 3.10. In this figure, panels (a) and (b) corresponding to Fig. 3.10a and Fig. 3.10b, respectively. See the text for details.

R-model seems very much relevant compared to the NR-model.

3.4.2 Effect of ε on SEDs

In this section, we examine how the deformation of spacetime affects the spectral energy distributions (SEDs). While doing so, we consider two black hole models: one with weakly rotating ($a_k \rightarrow 0$) central source and the other with rapidly rotating ($a_k \rightarrow 1$) central source. For $a_k = 0$, we choose $E = 1.005$ and $\lambda = 2.9$, and calculate the SEDs for a set of deformation parameters. To evaluate the thermal bremsstrahlung spectrum, we use the same methodology as described in Section 3.3. The obtained results are presented in Fig. 3.10a, where solid (black), dashed (red), dotted (blue), dot-dashed (orange) and long-dashed (green) curves represent SEDs corresponding to the deformation parameter $\varepsilon = 0$, 2, 4, 6 and 8, respectively. It is observed that SEDs increase significantly at both low and high-frequency ends when ε increases. We find that the above set of input model parameters yields only I-type accretion solutions with $r_{\rm in} = 6.7663, 5.5027, 4.5666, 3.9224$ and 3.5186 for increasing ε values starting from 0 to 8. Next, we fix $a_k = 0.99$, $E = 1.0215$ and $\lambda = 1.85$, and calculate the SEDs for a set of ε values. We present the obtained results in Fig. 3.10b, where solid (black), dashed (red), dotted (blue), dot-dashed (orange) and long-dashed (green) curves are for $\varepsilon = 0$, 0.005, 0.01, 0.015 and 0.02, respectively. Note that the allowed range of ε yielding the black hole solutions generally decreases with a_k (see Fig. 17 of [182]) and hence, we use relatively smaller value of ε for $a_k = 0.99$ compared to the same used for weakly rotating black hole. As before, these SEDs are calculated using I-type global accretion solutions obtained for above set of ε and they become transonic after crossing the inner critical points at $r_{\rm in} = 2.1343, 2.082, 2.0261, 1.9655$ and 1.898, respectively. We note that SEDs are shifted at higher values as ε is increased, however their differences are barely noticeable as the range of ε is small. We present a clear discussion of this observation here. We notice that for $a_k = 0.99$, Eq. (3.7) admits no real roots when $\varepsilon > 0.02$, resulting in a naked singularity rather than a black hole spacetime. Therefore, only a small range of ε values ($\varepsilon \lesssim 0.02$) is allowed for a black hole solution with $a_k = 0.99$. For $a_k = 0$, when ε is increased from 0 to a large value 8, the critical point (r_c) associated with the accretion solutions shifts significantly toward the horizon, from 6.7663 to 3.5186. As a result, a noticeable rise in the electron temperature (T_e) profile is observed (see panel (a) of Fig. 3.11). Consequently, the resulting luminosity spectrum (which is directly related to T_e, as seen from Eq. (3.5)) shows a clear deviation for $\varepsilon = 8$ compared to the case with $\varepsilon = 0$. On the other hand, for $a_k = 0.99$, increasing ε from 0 to its approximate maximum allowed value 0.02 leads to only a negligible shift in r_c, from 2.1343 to 1.898. As a result, T_e profiles remain almost unchanged (see panel (b) of Fig. 3.11), and the corresponding luminosity spectra are nearly indistinguishable.

3.4.3 Luminosity distribution for naked singularity

In this section, we examine the variation of disc luminosity (L) for accretion flow around the naked singularity (NkS). In doing so, we consider a rapidly rotating central object of

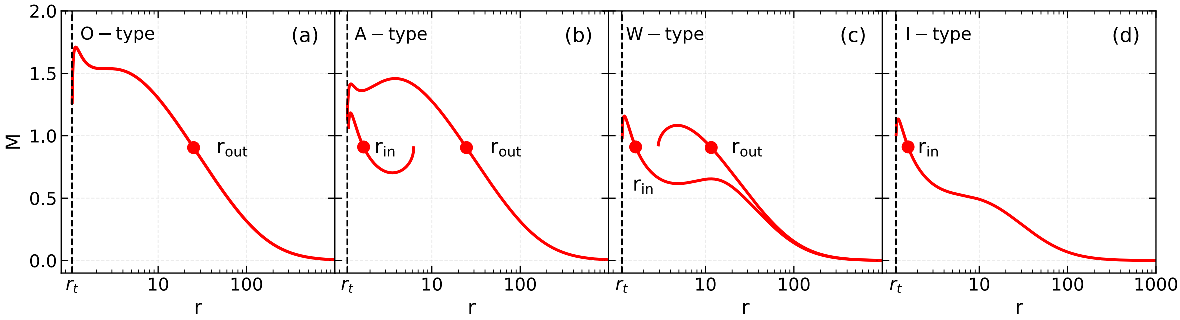

Figure 3.12: Variation of Mach number (M) as a function of radial distance (r) for NkS model. Here, we choose $a_k = 0.99$ and $\varepsilon = 0.03$. Results presented in panels (a-d) are obtained for $(\lambda, E) = (1.82, 1.01)$, $(1.86, 1.01)$, $(1.86, 1.0175)$ and $(1.86, 1.025)$, respectively. In each panel, filled circles denote the critical points ($r_{\rm in}$ and $r_{\rm out}$) and dotted vertical line indicate the inner edge ($r_0 = r_t$) of the disc. See the text for details.

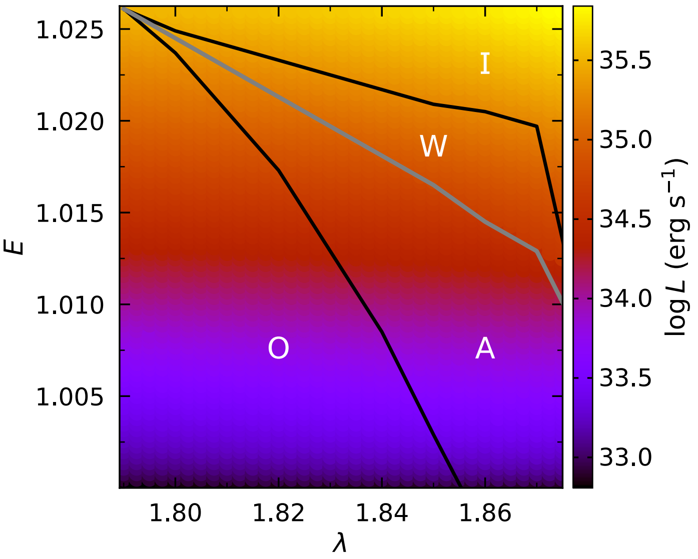

Figure 3.13: Division of parameter space in $\lambda - E$ plane according to the behavior of flow solutions (O, A, W and I-types) in the NkS model. Color map denotes 2D projection of 3D plot of λ, E and L. Vertical color bar at the right denotes L in erg s^{-1}. Here, we choose $a_k = 0.99$ and $\varepsilon = 0.03$. See the text for details.

Table 3.2: Flow energy (E), angular momentum (λ), inner critical points ($r_{\rm in}$), outer critical points ($r_{\rm out}$), type of accretion solutions in NkS model are tabulated in columns $1-5$. These solutions are used to obtain the SEDs shown in Fig. 3.14.

E	λ	$r_{\rm in}$	$r_{\rm out}$	Type
1.015	1.815	—	15.6082	O
	1.835	2.1152	15.2698	A
	1.855	1.6405	14.8097	W
	1.875	1.4214	—	I
1.0175	1.815	—	12.6171	O
	1.835	2.0377	12.2021	A
	1.855	1.6895	11.7311	W
	1.875	1.4057	—	I
1.02	1.81	—	10.2935	O
	1.83	2.0806	9.7440	A
	1.85	1.7361	7.4222	W
	1.87	1.4403	—	I

spin $a_k = 0.99$ with deformation parameter $\epsilon = 0.03$. This choice of parameters provides accretion solution in NkS as Eq. (3.7) does not yield real root of $r_{\rm H}$. With this, we calculate the accretion solutions around naked singularity by freely varying flow energy (E) and angular momentum (λ), and separate the parameter space in $\lambda - E$ plane according to the nature of accretion solution topologies (*i.e.*, O, A, W and I-type) around naked singularity. In Fig. 3.12, we show the nature of O, A, W and I-type accretion solutions (*i.e.*, $M = v/C_s$ versus r plots) for NkS model. The detailed physical properties of various accretion flow solutions in the naked singular spacetime are examined in [121, 182]. Here, the obtained results are presented in Fig. 3.13, where the identified regions are marked. The region bounded by the black curves yield multiple critical points which is further sub-divided according to the entropy condition where gray curve corresponds to $\dot{\mathcal{M}}_{\rm in} = \dot{\mathcal{M}}_{\rm out}$. We further calculate the frequency-integrated disc luminosity (L) utilizing the accretion solutions from the entire parameter space and depict the obtained results using colors in Fig. 3.13. To obtain L, we integrate Eq. (3.6) from the disc inner edge r_0 to the outer edge $r_{\rm edge} = 1000$. It may be noted that for NkS model, flows co-rotate along a surface (often called naked surface) very close to the singularity (see Fig. 3.12). Hence, the flow is truncated at a radius r_t (see Fig. 3.12) near the singularity and we consider r_t as the inner edge of the disc for NkS model (*i.e.*, $r_0 \sim r_t$). In the figure, vertical color bar at the right denotes the range of L. We find that for a given λ (or E), L increases as E (or λ) is increased. Therefore, it is evident that I-type solutions generally yield larger disc luminosity L compared to the other accretion solutions around NkS.

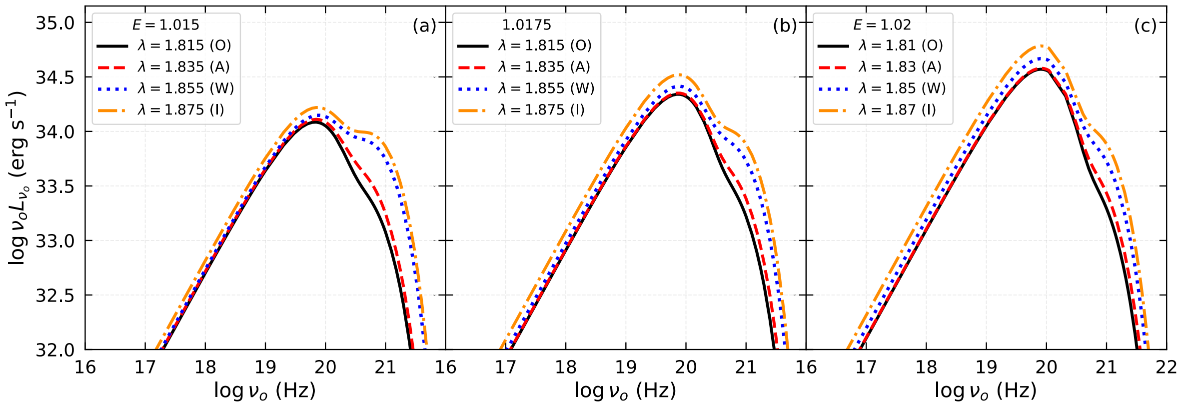

Figure 3.14: Spectral energy distributions (SEDs) corresponding to different accretion solutions (O, A, W and I-types) around NkS for flow energies $E = 1.015$ (panel a), 1.0175 (panel b) and 1.02 (panel c). In each panel, solid (black), dashed (red), dotted (blue) and dot-dashed (orange) corves denote results for different λ which are marked. Here, we choose $a_k = 0.99$ and $\varepsilon = 0.03$. See the text for details.

Next, we examine the spectral energy distributions (SEDs) for different accretion solutions in NkS model. Here, we choose $E = 1.015, 1.0175$ and 1.02, and vary λ to calculate SEDs for O, A, W and I-type accretion solutions. The obtained results are shown in Figs. 3.14a-c, where solid (black), dashed (red), dotted (blue) and dot-dashed (orange) curves represent SEDs associated with O, A, W and I-type flow solutions, respectively. It is clear from the figures that obtained SEDs alter due to the variation of flow parameters (*i.e.*, E and λ). We further observe that I-type flow solutions concede higher SEDs over the other flow solutions as indicated in Fig. 3.13. The chosen parameters to obtain the above figures are tabulated in Table 3.2.

3.4.4 Comparison between SEDs for BH and NkS models

In this section, we compare the SEDs obtained from BH and NkS models. While doing this, we choose the model parameters as $E = 1.0225$, $\lambda = 1.7$ and $a_k = 0.5$ and calculate the accretion solutions for BH and NkS models using $\varepsilon = 6$ and 7, respectively. This choice of model parameters results I-types accretion solutions with $r_{\rm in} = 2.5067$ for BH model and $r_{\rm in} = 1.9059$ for NkS model and the solutions extend up to the outer edge $r_{\rm edge} = 1000$. We calculate the SEDs for these solutions and obtained results are depicted in Fig. 3.15a, where solid (black) and dashed (red) are for BH and NkS models. It is evident that SED for NkS model is significantly higher at both low and high frequencies ends compared to the SED for BH model. In Fig. 3.15b, we display the results for $a_k = 0.99$, where flow

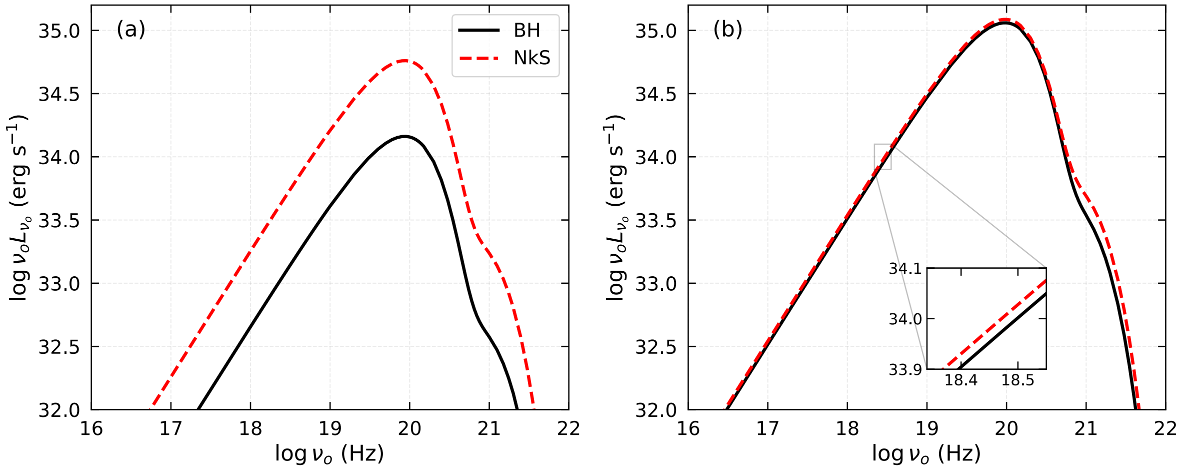

Figure 3.15: Comparison of SEDs obtaind from BH and NkS models. In panel (a), we set $a_k = 0.5$, $E = 1.0225$ and $\lambda = 1.7$, respectively. Solid (black) and dashed (red) curves denote results for BH ($\varepsilon = 6$) and NkS ($\varepsilon = 7$). In panel (b), we choose $a_k = 0.99$, $E = 1.025$ and $\lambda = 1.83$, and SED for BH and NkS are obtained for $\varepsilon = 0.02$ and 0.04, respectively. See the text for details.

parameters are chosen as $E = 1.025$ and $\lambda = 1.83$, and $\varepsilon = 0.02$ and 0.04 render I-type accretion solutions for BH and NkS models, respectively. Here, $r_{\rm in} = 2.1193$ for BH model and $r_{\rm in} = 1.737$ for NkS model. As before, SED is more for NkS model compared to BH model although the difference seems marginal in all frequency range. These findings are in agreement with [303], where authors studied the thermal properties of geometrically thin accretion discs (taking non-zero torque at the inner edge of the disc in the Novikov-Thorne model) in the null [302] and Joshi-Malafarina-Narayan [323] spacetimes and compare the results with an equally massive Schwarzschild black hole.

3.5 Chapter Summary and Conclusions

In this chapter, we investigate the thermal bremsstrahlung emission from the accretion disc in black hole and naked singularity spacetime. We consider the Johannsen-Psaltis (JP) non-Kerr spacetime, which describes the central object as a black hole or naked singularity depending on the choice of spin (a_k) and deformation parameters (ε). In hot accretion flow (HAF), the relativistic effect and electron-electron emission modify the non-relativistic bremsstrahlung emissivity. We use the Novikov-Thorne equation for emission coefficient [64], which includes both the effects mentioned above in addition to the electron-ion emission. A basic structure for studying the thermal properties of general relativistic accretion flow around a stationary and axisymmetric compact object has been developed. We obtain the expressions of monochromatic and bolometric disc luminosity in an observer frame at spatial infinity. We summarize our findings below.

- We find that for HAF, bremsstrahlung emissivity in the relativistic model (R-model) is larger than the non-relativistic model (NR-model). Moreover, the electron-electron emission near the horizon significantly enhances the emissivity in R-model compared to NR model. Accordingly, we compute the relative change in disc luminosity ($\Delta L/L_{\rm NR}$) for R-model with respect to NR-model. The obtained results clearly indicate that the relativistic effect becomes dominant for black holes with higher spin values. Hence, we emphasize the importance of considering the R-model of thermal bremsstrahlung in studying the emission properties of hot accretion flows around black holes, particularly those with high spin values.

- For black hole model, we calculate the disc luminosity (L) by freely varying flow energy (E) and angular momentum (λ). We find that for a given E, L increases with λ. Likewise, for a particular λ, L increases with E. Furthermore, we calculate the spectral energy distributions (SEDs) associated with the different flow topologies (O, A, W and I-types) in $\lambda-E$ parameter space. We notice that SEDs strongly depend on the flow parameters (λ,E). At the low frequency region, SEDs for O and A-type solutions differ very small compared to the results in high frequency region. But, SEDs for W and I-type solutions significantly differ from O and A-type topologies at both lower and higher frequencies, especially for low energy accretion flows. We also observe that the luminosity distribution for I-type solutions are higher compared to other flow solutions.

- We examine the role of deformation parameter ϵ in controlling the disc luminosity L when relativistic effect is invoked. We find that $\Delta L/L_{\rm NR}$ increases with ϵ, irrespective of the flow parameters (λ,E). This clearly indicates the importance of relativistic effect in studying the emission properties of accretion flow in non-Kerr spacetime with large deformation. We also explore the effect of ϵ on disc luminosity spectrum and find that SEDs increase with ϵ. Therefore, the accretion disc around a non-Kerr black hole described by the JP metric is more luminous than the usual Kerr black hole.

- In the naked singularity model, we subdivide a parameter space in $\lambda-E$ plane according to the nature of flow solutions. In these regions, we compute L values, where we observe that it increases with λ and E. Further, we obtain luminosity distributions for different flow topologies in $\lambda - E$ parameter space. We find that SEDs for O and A-type solutions are almost identical at both low and high frequency ends. On the contrary, SEDs for W and I-type solutions moderately differ form O and A-type solutions for all flow energies. This result differs from the black hole model, where we see that SEDs deviate too much in a given frequency range. However, like black hole model, we obtain maximum luminous power spectrum for the I-type solutions compared to the other flow solutions.

- From a comparative study between the SEDs, we infer that the luminosity distribution for naked singularity spacetime is higher than that of the black hole. An earlier study [303] found that the accretion disc around the null and Joshi-Malafarina-Narayan naked singularities was much more luminous than the black holes. Therefore, even though we took a different spacetime background, i.e., the JP spacetime, the consequences of our results agree with Ref. [303].

With the above findings, it is useful to indicate the observation implications of the present model formalism. In reality, the wide band spectral modelling of the observed spectrum can decipher the physical properties of the black hole, namely mass, spin and accretion rate [46, 47, 49–51, 91, 105, 107, 255, 324, and references therein]. Accordingly, for the first time to the best of our knowledge, we make an effort to calculate the model spectrum considering the thermal bremsstrahlung emissions from the accretion disc in the realm of a deformed spacetime. Indeed, the obtained model spectra are quantitatively different for BH and NkS models in the non-Kerr JP spacetime; however, their typical natures appears to be qualitatively similar. A similar feature has been observed when comparing the SEDs of JP BHs (or NkS) with those of the usual Kerr BHs. This possibly happens because of the fact that the present formalism is developed only involving the thermal bremsstrahlung emissions neglecting the other relevant radiative processes to avoid complexity. Also, in our analysis, when the redshift factor is calculated at a given position on the accretion disc, the impact parameter (b) of the photon on the observer plane (which is at spatial infinity) is simply approximated by the radial coordinate (r) of the emitting fluid element in the disc. This approximation is valid when the light bending due to the black hole's gravity is neglected. Usually, the photons emitted from the accretion disc (specifically from regions close to the black hole) can experience significant bending due to the strong gravity of the black hole. In such situations, b has to be calculated by integrating the null-geodesic equation of the photons, i.e., by tracing the ray from the emission point on the disc to its corresponding impact point on the observer plane. This ray-tracing method can produce different intensity distribution of the photons at the observer plane, depending on the varying strength of the gravity in different spacetime geometries. As a result, the observed spectrum shape may vary depending on the underlying spacetime background. Nevertheless, we intend to address this aspect as part of future work. At this stage, since light bending effects have not been included in the analysis, the emission profiles at the observer plane are expected to be similar for different spacetime backgrounds. But, in a realistic scenario where light bending is taken into account, this similarity may not occur.

In the present and previous chapters, we established that the JP deformation can influence the accretion properties of compact objects. Therefore, one can ask a significant question: Does the impact of other parametric deviations from the Kerr metric on the accretion flows behave similarly to that of the JP deformation? Keeping this in mind, in the next chapter, we study the properties of accretion flows around the Konoplya-Zhidenko non-Kerr black hole [94], another parameterized bottom-up spacetime that has also been tested through gravitational wave observations of black holes [151].

Indian Institute of Technology Guwahati

CHAPTER 4

GENERAL RELATIVISTIC VISCOUS ACCRETION FLOW AROUND KONOPLYA-ZHIDENKO BLACK HOLE

4.1 Introduction and Motivation

As we have discussed earlier, the non-Kerr metrics are required for the observational test of the no-hair theorem (or Kerr hypothesis), as they provide a broader framework for understanding the possible structures of black holes that may deviate from the Kerr solution [160, 161, 208, 212, 325]. One such emerging metric is the Johannsen-Psaltis (JP) metric [161], which we have discussed in detail in the previous two chapters. Several other non-Kerr metrics have been proposed in the last decade for the same purpose [163–166, 168]. Many authors have shown that all such non-Kerr black holes are consistent with current observations of electromagnetic and gravitational wave (GW) signals [165, 167, 169–174]. However, whether such an alternative prescription in metric theories of gravity is necessary will remain unresolved until we have more precise observational data. Furthermore, the characterization of different kinds of parametric deviations is still incomplete, particularly regarding their impact on various astrophysical phenomena. In this chapter, we aim to address these issues by examining the accretion dynamics around black holes. In this venture, we have already studied the accretion flows in the JP-type deformed spacetime [182, 183]. Recently, another parametric deviation to the Kerr metric is introduced by Konoplya and Zhidenko to test the GR in strong gravity regime using the observations of GWs resulting from the

TH-3714_206121049

binary black hole mergers [166], and we hereafter refer to it as the KZ metric. Similar to the JP metric, underlying gravity theory for the KZ metric is still unknown (another bottom-up metric [167]). In this work, we study the physical properties of accretion disc in the KZ spacetime. We compare the obtained results with our earlier findings (see, [182, 183]) for the JP black holes, which makes a qualitative distinction between the type of deformations for these two metrics.

The KZ metric is characterized by the mass, spin, and a deformation parameter (η_0). This metric reverts back to the original Kerr metric for $\eta_0 \to 0$ limit. We briefly mention the motivation behind the formation of KZ spacetime. After the detection of gravitational waves by LIGO and Virgo collaborations [149–152], a very good agreement is established between the observed waveform of the gravitational-wave signal and the results obtained from the numerical simulation of the inspiral and merger of two black holes in Einstein's gravity. However, due to inaccuracy in detecting the gravitational-wave profile, a wide range of mass and spin parameters of the black hole in numerical simulation provide the same gravitational-wave signal. This situation can also be replicated by an intuitive idea of introducing a parametric deviation from the Kerr spacetime instead of changing the given black hole parameters in the same Kerr spacetime. In [166], authors validated the above mentioned intuitive notion, illustrating that the inclusion of a non-negligible deformation (through η_0) into the original Kerr metric yields a quasinormal frequency that is closely matched with the result obtained from the Kerr geometry. Therefore, both the Kerr and KZ spacetimes are consistent with the ringdown phase of gravitational waves. As the ringdown picture is in the regime of strong gravitational field, we can not rule out the possibility of formation of a non-Kerr black hole. The only way to do that is by improving the precision level of detecting the gravitational-wave profile, which will furnish the spacetime parameters of the final black hole with high accuracy.

It is worth noting that while the deformation in KZ metric does not alter the asymptotic properties of the spacetime, it does impact the near-horizon geometry, notably shifting the location of event horizon. Recently, interest has grown in examining the influence of KZ deformation on different astrophysical phenomena [326]. However, in this work, our concern is to explore the accretion flow around the KZ black holes. As the deformation primarily alters the near-horizon geometry, it will also impact the dynamics of accretion flows, and thereby change the accretion disc properties. With this objective in mind, we investigate the effect of η_0 on the properties of viscous accretion flow. We utilize the framework of general relativistic viscous hydrodynamics to study the dynamics of accretion flow [10]. We start our analysis by finding distinct classes of global transonic accretion solutions in terms of flow energy (E) and angular momentum ($\mathscr{L}$), and accordingly divide the $\mathscr{L}-E$ parameter space. We then find the shock-induced accretion solutions using the relativistic shock conditions [254]. Moreover, we calculate the spectral energy distribution (SED) corresponding to the accretion solutions by using the emissivity of relativistic thermal bremsstrahlung radiation [64]. Further, we examine how the shock location ($r_{\rm sh}$), quasi-periodic oscillation (QPO) frequency ($\nu_{\rm QPO}$), and bolometric disc luminosity (L) change with η_0. Since the modulation of the shock front yields the QPO phenomena, we phenomenologically find the parameter spaces in $\mathscr{L}-\eta_0$ plane that admit observed high-frequency QPOs (HFQPOs) for the black hole binary and black hole candidate systems. Finally, we distinguish the KZ and JP deformations by comparing their behavior in effecting the accretion disc properties.

We arrange this chapter as follows. We start by formulating the mathematical background that governs the accretion disc in the KZ spacetime. We then present the transonic accretion solutions with and without shocks and discuss the effect of KZ deformation on various shock properties. Next, we explore a phenomenology on the observed HFQPOs for black hole binaries (BHBs) and black hole candidates (BHCs). Finally, we compare the physical properties of the accretion disc for KZ and JP black holes.

4.2 Model equations governing accretion disc

We explore the accretion dynamics of a viscous flow, including shock transition in a stationary and axisymmetric Konoplya-Zhidenko (KZ) black hole spacetime. The required model equations are developed under the framework of general relativistic viscous hydrodynamics [10], as discussed in Section 2.2. We follow the analysis of [118]; however, the current equations contain an additional spacetime parameter η_0 that we need to explicitly mention.

The line element of KZ non-Kerr spacetime can be expressed in Boyer-Lindquist coordinates (t,r,θ,ϕ) as [166],

$$\begin{aligned} ds^2 = &-\frac{N^2(r,\theta)-W^2(r,\theta)\sin^2\theta}{K^2(r,\theta)}dt^2 - 2W(r,\theta)r\sin^2\theta dt d\phi + K^2(r,\theta)r^2\sin^2\theta d\phi^2 \\ &+\frac{\Sigma(r,\theta)}{r^2N^2(r,\theta)}dr^2 + \Sigma(r,\theta)d\theta^2, \end{aligned} \tag{4.1}$$

where

$$\begin{aligned} N^2(r,\theta) &= \frac{\Delta}{r^2} - \frac{\eta_0}{r^3}, \; \Delta = r^2 - 2M_{\rm BH}r + a_{\rm k}^2, \\ W(r,\theta) &= \frac{2a_{\rm k}M_{\rm BH}}{\Sigma} + \frac{\eta_0 a_{\rm k}}{r^2\Sigma}, \; \Sigma = r^2 + a_{\rm k}^2\cos^2\theta, \\ K^2(r,\theta) &= \frac{(r^2+a_{\rm k}^2)^2 - \Delta a_{\rm k}^2\sin^2\theta}{r^2\Sigma} + \frac{a_{\rm k}^2\eta_0\sin^2\theta}{r^3\Sigma}. \end{aligned} \tag{4.2}$$

In the above expressions, $M_{\rm BH}$ and $a_{\rm k}$ denote the mass and spin of the black hole (BH), respectively, and η_0 is the deformation parameter. For $\eta_0 = 0$, the metric in Eq. (4.1) reduces to the original Kerr metric [117]. In this work, we use a unit system $G = M_{\rm BH} = c = 1$, where G is the gravitational constant and c is the speed of light. We use the condition $g_{rr}^{-1} = 0$ to find the event horizon location ($r_{\rm H}$), which can be calculated numerically by finding the maximum root of the equation,

$$r_{\rm H}^3 - 2r_{\rm H}^2 + a_{\rm k}^2 r_{\rm H} - \eta_0 = 0. \tag{4.3}$$

Note that we restrict our analysis within the allowed range of $a_{\rm k}$ and η_0 as delineated in [166].

In earlier chapters, we did not include viscosity of the fluid. However, in this chapter we include this as well. We consider the fluid motion is confined in the equatorial plane ($i.e, \theta = \pi/2$) of the black hole. Also, we assume that the flows obey same symmetries as that of the spacetime. Under these assumptions, the present Killing symmetries of the spacetime in Eq. (4.1) give two conserved quantities along the flow direction as (see Eqs. (2.6) and (2.8)),

$$\mathscr{L} = h_0 u_\phi - \frac{2\nu\sigma^r_\phi}{u^r}, \tag{4.4}$$

$$E = -\left(h_0 u_t - \frac{2\nu\sigma^r_t}{u^r}\right), \tag{4.5}$$

where $\mathscr{L}$ is the bulk angular momentum per unit mass, E is the Bernoulli constant, h_0 is the specific enthalpy, and ν ($= \eta/\rho = \alpha C_s H$) [89, 90] is the kinematic viscosity. Here, η is the dynamic viscosity, ρ is the mass density, α is the viscosity parameter, C_s ($= \sqrt{\Gamma p/(e+p)}$) is the sound speed with adiabatic index Γ, and H ($= \sqrt{pr^3/(\rho F)}$, p is the isotropic pressure) [88, 114, 243] is the half thickness of disc. The quantity F is given by in terms of flow angular velocity Ω ($= u^\phi/u^t$) and specific angular momentum λ ($= -u_\phi/u_t$) as $F = F_1/(1-\Omega\lambda)$, where $F_1 = ((r^2+a_{\rm k}^2)^2 + 2\Delta a_{\rm k}^2)/((r^2+a_{\rm k}^2)^2 - 2\Delta a_{\rm k}^2)$. We evaluate the shear tensor components σ^r_ϕ and σ^r_t using Eq. (2.4) as,

$$\sigma^r_\phi = \frac{1}{2}\left(A_1 + A_2\frac{dv}{dr} + A_3\frac{d\lambda}{dr}\right), \tag{4.6}$$

$$\sigma^r_t = \frac{1}{2}\left(B_1 + B_2\frac{dv}{dr} + B_3\frac{d\lambda}{dr}\right), \tag{4.7}$$

where the quantities A_1, A_2, A_3, B_1, B_2, and B_3 are the function of flow variables, and their explicit forms have been given in Appendix 4.A. In Eqs. (4.6) and (4.7), v denotes the r-component of physical three velocity in a corotating frame (which rotates with the flow angular velocity Ω), and is obtained as $v = \sqrt{u^r u_r/(u^t u_t(\Omega\lambda - 1))}$ [232]. Note that v is negative for accretion.

The flow equations are manifested as second-order differential equations because of the first-order derivatives of v and λ in the expressions of σ^r_ϕ and σ^r_t. However, the second-order derivatives are negligible in the context of accretion flow dynamics [118]. Therefore, to simplify the numerical computation, we neglect the terms that possess first-order derivatives of the flow variables in Eqs. (4.6) and (4.7), which leads the flow equations as the first-order differential equations. Under this assumption, conservations of $\mathscr{L}$ and E yield the following equations as,

$$\frac{d\mathscr{L}}{dr} = \mathscr{L}_0 + \mathscr{L}_1\frac{dv}{dr} + \mathscr{L}_2\frac{d\Theta}{dr} + \mathscr{L}_3\frac{d\lambda}{dr} = 0, \tag{4.8}$$

$$\frac{dE}{dr} = E_0 + E_1\frac{dv}{dr} + E_2\frac{d\Theta}{dr} + E_3\frac{d\lambda}{dr} = 0, \tag{4.9}$$

where the explicit forms of the quantities $\mathscr{L}_0$, $\mathscr{L}_1$, $\mathscr{L}_2$, $\mathscr{L}_3$, E_0, E_1, E_2, and E_3 in terms of the flow variables are given in Appendix 4.B. In Eqs. (4.8) and (4.9), $\Theta = k_{\rm B}T/(m_e c^2)$ denotes the dimensionless temperature, where T is the flow temperature in Kelvin, $k_{\rm B}$ is the Boltzmann constant, and m_e is the rest mass of electron. We calculate the gradients of Θ and λ using Eqs. (4.8) and (4.9) as,

$$\frac{d\Theta}{dr} = \Theta_{11}\frac{dv}{dr} + \Theta_{12}, \tag{4.10}$$

$$\frac{d\lambda}{dr} = \lambda_{11}\frac{dv}{dr} + \lambda_{12}, \tag{4.11}$$

where

$$\begin{aligned} \Theta_{11} &= \frac{L_1E_3 - L_3E_1}{L_3E_2 - L_2E_3}, \quad \Theta_{12} = \frac{L_0E_3 - L_3E_0}{L_3E_2 - L_2E_3}, \\ \lambda_{11} &= \frac{L_2E_1 - L_1E_2}{L_3E_2 - L_2E_3}, \quad \lambda_{12} = \frac{L_2E_0 - L_0E_2}{L_3E_2 - L_2E_3}. \end{aligned} \tag{4.12}$$

Indian Institute of Technology Guwahati

In the radial momentum equation, we ignore the viscous acceleration term because it is negligible compared to the gravitational acceleration [89, 90]. Therefore, the radial momentum equation is obtained from Eq. (2.14) as [118],

$$\gamma_v^2 v\frac{dv}{dr}+\frac{1}{h_0\rho}\frac{dp}{dr}+\left(\frac{d\Phi^{\rm eff}}{dr}\right)_\lambda=0, \tag{4.13}$$

where $\gamma_v=1/\sqrt{1-v^2}$ is the Lorentz factor for the radial velocity v, and $\Phi^{\rm eff}=-\frac{1}{2}\ln(\lambda f_2-f_1)$ is the effective potential of the system. The quantities f_1 and f_2 are given by,

$$\begin{aligned} f_1&=-\frac{r^2(r^3+a_{\rm k}^2(r+2))-a_{\rm k}\lambda(2r^2+\eta_0)+a_{\rm k}^2\eta_0}{r^2(\Delta r-\eta_0)}, \\ f_2&=-\frac{a_{\rm k}(2r^2+\eta_0)+\lambda(r^3-2r^2-\eta_0)}{r^2(\Delta r-\eta_0)}. \end{aligned} \tag{4.14}$$

Integrating the mass flux conservation equation $\nabla_k(\rho u^k)=0$, we get the mass accretion rate as (see Eq. (2.17)),

$$\dot{M}=-4\pi H\rho v\gamma_v\sqrt{(\Delta r-\eta_0)/r}. \tag{4.15}$$

In a steady state, $\dot{M}$ remains constant throughout the disc. Therefore, using $\frac{d\dot{M}}{dr}=0$, we rewrite Eq. (4.13) into the following form as,

$$R_0+R_1\frac{dv}{dr}+R_2\frac{d\Theta}{dr}+R_3\frac{d\lambda}{dr}=0, \tag{4.16}$$

where R_0, R_1, R_2, and R_3 are given in Appendix 4.B.

Thereafter, solving Eqs. (4.8), (4.9) and (4.16), we obtain the radial velocity gradient as,

$$\frac{dv}{dr}=\frac{\mathcal{N}}{\mathcal{D}}, \tag{4.17}$$

where

$$\begin{aligned} \mathcal{N}&=L_0(E_3R_2-E_2R_3)+L_2(E_0R_3-E_3R_0)+L_3(E_2R_0-E_0R_2), \\ \mathcal{D}&=L_1(E_2R_3-E_3R_2)+L_2(E_3R_1-E_1R_3)+L_3(E_1R_2-E_2R_1). \end{aligned} \tag{4.18}$$

In order to emphasize the impact of viscous dissipation, we exclude the radiative cooling from the energy equation [37]. Since π^{ik} is negligible close to the event horizon [88], we calculate the energy equation at this region by neglecting the viscous heating term Q^+ in Eq. (2.9) as,

$$h_0\frac{d\rho}{dr}-\frac{de}{dr}=0. \tag{4.19}$$

For relativistic flows of variable Γ, we use an equation of state (EoS) with equal number densities of electron and ion as [240],

$$e = \frac{\rho f}{1 + m_p/m_e}, \tag{4.20}$$

where m_p (m_e) is the rest mass of a proton (electron). Here, the quantity f is expressed in terms of Θ as,

$$f = 1 + \frac{m_p}{m_e} + \Theta\left[\left(\frac{9\Theta+3}{3\Theta+2}\right) + \left(\frac{9\Theta+3m_p/m_e}{3\Theta+2m_p/m_e}\right)\right]. \tag{4.21}$$

Using this EoS, we get the entropy accretion rate of the flow very near the horizon after integrating Eq. (4.19) as,

$$\dot{\mathscr{M}} = -\exp(\chi)\Theta^{3/2}(3\Theta+2)^{3/4}(3\Theta+2m_p/m_e)^{3/4} v\gamma_v H\sqrt{(\Delta r - \eta_0)/r}, \tag{4.22}$$

where $\chi = (f - 1 - m_p/m_e)/(2\Theta)$.

In this work, we consider an isotopic emission of thermal bremsstrahlung radiation from the accretion disc. As the plasma temperature of the disc can reach 10^{12} K for hot accretion flow [11, 47, 123, 182, 315], electron-electron emission surpasses electron-ion emission [183, 309, 313, 314]. So, we utilize the relativistic emission coefficient, which includes both the relativistic effect and the electron-electron emission in addition to the electron-ion emission. An approximate expression of the relativistic thermal bremsstrahlung emissivity at a particular emission frequency ν_e is given by [64],

$$\begin{aligned}\mathscr{E}^{\rm ff}_{\nu_e} = {} & 6.8\times10^{-38}(\rho/m_p)^2 Z^2 T_e^{-1/2}(1+4.4\times10^{-10}T_e)\\ & \times e^{-h\nu_e/k_{\rm B}T_e}\bar{g}_{\rm B}\ {\rm erg\ s^{-1}\ cm^{-3}\ Hz^{-1}},\end{aligned} \tag{4.23}$$

where Z is the atomic number of ion (which is 1 for hydrogen plasma), T_e is the electron temperature (which relates with the flow temperature T as $T_e = \sqrt{m_e/m_p}\,T$ [327]), and h is the Planck constant. Here, $\bar{g}_{\rm B}$ denotes the thermally-averaged Gaunt factor, and its value depends on the energy of emitting electrons. We take $\bar{g}_{\rm B} = 1.2$ in our analysis [121, 122, 183]. The emissivity in Eq. (4.23) is obtained with respect to an observer in the co-rotating frame. However, for a distant observer, this radiation gets red-shifted by the immense gravity of the central black hole. The emitted radiation also alters due to the rotation of the disc. Therefore, the expression of bolometric disc luminosity for a distant observer is obtained as,

$$L = \int_0^\infty L_{\nu_o} d\nu_o\ {\rm erg\ s^{-1}}, \tag{4.24}$$

where

$$L_{\nu_o} = 2\int_{r_0}^{r_{\rm edge}}\int_0^{2\pi} \mathscr{E}^{\rm ff}_{\nu_o} H r\, dr d\phi\ {\rm erg\ s^{-1}\ Hz^{-1}}. \tag{4.25}$$

Here $r_0 = r_{\rm H}$ is the disc inner edge and $r_{\rm edge}$ is the disc outer edge. If the inclination angle of the accretion disc with respect to the distant observer is θ_0, then the observed frequency ν_o is related with the emission frequency ν_e and the redshift factor $(1+z)$ as [121, 122],

$$\frac{\nu_e}{\nu_o} = 1+z = u^t\left(1+\frac{r\Omega}{c}\sin\theta_0\sin\phi\right), \tag{4.26}$$

where $\Omega = f_2/f_1$. In this work, we consider $\theta_0 = 45°$ for illustration. The expression of u^t is obtained using the normalization condition $u^k u_k = -1$ as (see Eq. (2.13)),

$$u^t = \gamma_v\sqrt{\frac{r^3}{(1-\Omega\lambda)(\Omega a_{\rm k}(2r^2+\eta_0)+r^3-2r^2-\eta_0)}}. \tag{4.27}$$

The above equations are useful for finding the accretion solutions and their corresponding disc properties, such as temperature profile, radiation spectrum, luminosity, etc. In the subsequent sections, the results corresponding to the effect of deformation parameter on the accretion flow in KZ spacetime will be shown.

4.3 Results

4.3.1 Transonic accretion solutions

In this section, we investigate the properties of accretion solutions and their associated parameter space in the KZ spacetime. For transonic accretion, flow needs to pass a critical point, which is characterized by $dv/dr \rightarrow$“0/0” [232, 244, 245, 328]. Using the condition $\mathcal{N} = \mathcal{D} = 0$ and Eqs. (4.4) and (4.5), the critical point (r_c) and corresponding flow variables $(\Theta_c, v_c, \lambda_c)$ have been numerically determined for a given set of input parameters $(a_{\rm k}, \eta_0, \alpha, E, \mathcal{L})$. We use the l'Hôpital's rule to calculate dv/dr at r_c. Usually, it possesses two distinct values, and critical points are classified depending on them, e.g., saddle, nodal and spiral types. When both values of $(dv/dr)_{r_c}$ are real with opposite signs, the critical points are classified as saddle-types. For real and same sign of $(dv/dr)_{r_c}$ values gives the nodal-type critical points. In the case of spiral-type critical points, $(dv/dr)_{r_c}$ values are found to be imaginary. In our study, we are only interested in the accretion solutions that pass through the saddle-type critical points, as these are physically acceptable. The positive value of $(dv/dr)_{r_c}$ gives an accretion solution, and the negative value of $(dv/dr)_{r_c}$ corresponds to the wind solution. To find an accretion solution, we numerically solve the differential Eqs. (4.10), (4.11), and (4.17) by utilizing

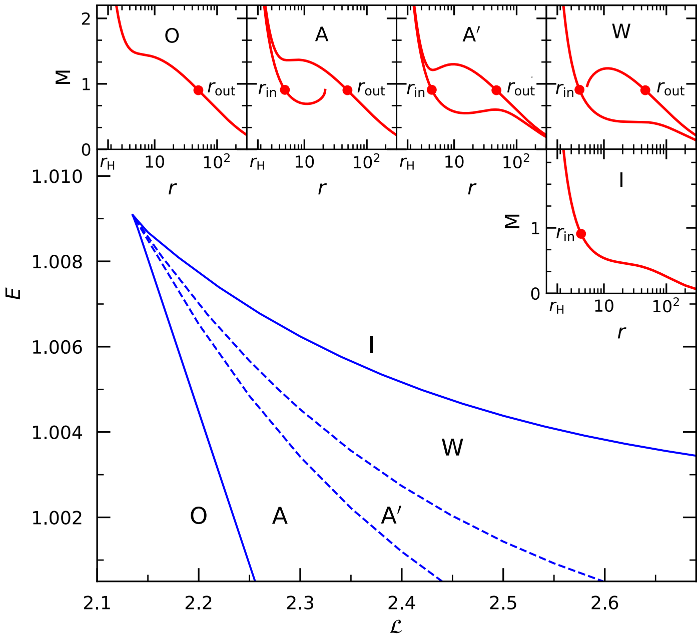

Figure 4.1: Classification of $\mathscr{L}-E$ parameter space into five regions (O, A, A′, W, and I) based on the accretion solution topologies. The inset panels represent their respective accretion solutions (Mach number ($M = v/C_s$) vs radial distance (r) curves). In this figure, we choose $a_{\rm k} = 0.65$, $\eta_0 = 0.1$, and $\alpha = 0.05$. See the text for details.

the calculated parameters $(\Theta_c, v_c, \lambda_c)$ at r_c as the initial boundary condition. We first integrate the equations from r_c to the disc inner edge $r_0 = r_{\rm H}$, and then from r_c to the disc outer edge $r_{\rm edge}$. Ultimately, by combining these two segments of the solutions, we obtain the resulting global transonic accretion solution for same set of input parameters $(a_{\rm k}, \eta_0, \alpha, E, \mathscr{L})$.

Following the above mentioned methodology, we investigate the structure of transonic accretion solutions and find the associated parameter space in the $\mathscr{L}-E$ plane. We obtain five distinct types of accretion solutions, and thereby, we subdivide the $\mathscr{L}-E$ parameter space into five designated regions as O, A, A′, W, and I in Fig. 4.1. Here, we choose $a_{\rm k} = 0.65$, $\eta_0 = 0.1$, and $\alpha = 0.05$. The accretion solutions (*i.e.*, variation of Mach number $M = |v|/C_s$ as a function of r) for the selected parameters from the identified regions are displayed in the inset panels. The O-type solution is obtained for $(\mathscr{L}, E) = (2.2, 1.004)$, where the flow possesses only a outer critical point at $r_{\rm out} = 50.1375$, and the solution passing through it extends from $r_{\rm edge}$ to $r_{\rm H}$ (which is signature of a open solution). For A-type solution, we choose $(\mathscr{L}, E) = (2.25, 1.004)$, where the flows contain multiple critical points. In this case, the solution passing through $r_{\rm out} = 48.8889$ is a open solution.

However, the solution passing through the inner critical point $r_{\rm in} = 4.8702$ terminates at $r_{\rm t} = 21.4802$, which is referred to as a closed solution. In our study, we mainly focus on the open solutions since the closed solutions are physically unacceptable. However, in case of shock transition [116, 118, 122, 125, 182], where flow connects the outer sonic point solution to the inner one, we deal with both open and closed solutions (see Section 4.3.2). The results corresponding to the A$'$-type solution is calculated for $(\mathcal{L}, E) = (2.3, 1.004)$. It is observed that the flow again exhibits multiple critical points $(r_{\rm in} = 4.3771, r_{\rm out} = 47.5241)$. Interestingly, in this case, solutions passing through both critical points remain open, thereby leading to a degeneracy in accretion solutions. To remove the degeneracy, we calculate the entropy content $\dot{\mathcal{M}}$ (which is a constant of motion for adiabatic flow) very close to the event horizon ($r_{\rm H} = 1.7957$) using Eq. (4.22). At a chosen radial distance of $r = 1.8171$, the calculated values of $\dot{\mathcal{M}}$ are 2.9799×10^8 and 2.2219×10^8 for the inner and outer critical point solutions, respectively. Since the solution through $r_{\rm \ in}$ exhibits a higher entropy than the solution through $r_{\rm out}$, the previous one is considered a more naturally favorable than the latter one in accordance with the second law of thermodynamics, thereby resolving the degeneracy problem. For the W-type solution, we take $(\mathcal{L}, E) = (2.35, 1.004)$, where the flows still possess multiple critical points. In this scenario, the solution remains open through $r_{\rm in} = 4.0632$, while it becomes closed ($r_t = 5.4046$) through $r_{\rm out} = 46.0146$. Finally, the I-type accretion solution is calculated for $(\mathcal{L}, E) = (2.3, 1.0065)$, where the global solution only pass through $r_{\rm in} = 4.3054$. We point out that the accretion solutions depicted in inset panels are identical to the transonic solutions identified in Kerr spacetime [118]. Moreover, for non-viscous flow, such A$'$-type solutions are not present, both in the Kerr and KZ non-Kerr spacetime. Hence, these particular solutions stem from the effect of viscosity only, not dealing with the spacetime deformation. It is essential to mention that there are no qualitative distinctions in the characteristics of accretion solutions for different $a_{\rm k}$ values other than reducing available parameter space when $a_{\rm k}$ increases. In this paper, all analyses have been conducted for moderately spinning black holes with $a_{\rm k} = 0.65$ to avail a fair range of $(\mathcal{L}, E)$. Indeed, the above analysis intimates that the regions marked as O, A, A$'$, W, and I provide characteristically different accretion solutions. However, the region A has a special interest in the realm of shock solutions, which will be studied in the next subsection.

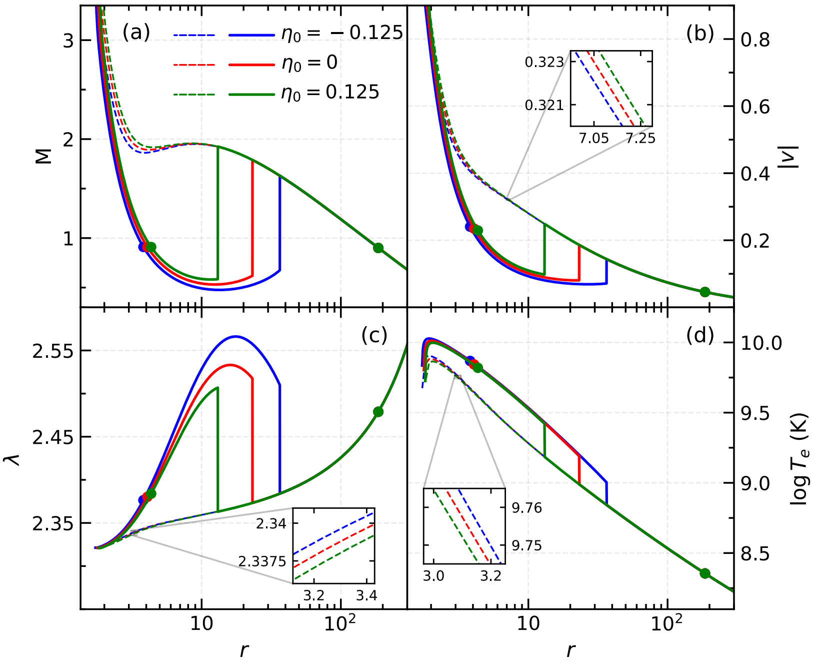

Figure 4.2: Typical shock induced accretion solutions (Mach number (M) vs radial distance (r) curves (solid) in panel (a)) along with their flow variables (radial velocity (v) in panel (b), specific angular momentum (λ) in panel (c), and electron temperature (T_e) in panel (d)) for deformation parameters $\eta_0 = -0.125, 0$ and 0.125. Here, the dashed curves represent the scenario where shock transitions have not occurred. The set of input parameters are chosen as $a_{\rm k} = 0.65$, $\alpha = 0.05$, $\mathcal{L} = 2.325$, and $E = 1.001$. See the text for details.

4.3.2 Effect of deformation on physical properties of accretion disc for shock solutions

Here, we examine accretion solutions capable of accommodating shock transitions in the deformed spacetime, which are preferred for their higher entropy content compared to the solutions without shocks [253]. In Fig. 4.2a, we demonstrate typical shock solutions in accretion flow for different values of the deformation parameter η_0. The blue, red, and green color solid curves represent the obtained results for $\eta_0 = -0.125$, 0, and 0.125, respectively. We consider the flows start accretion at the disc outer edge with a given value of $(\mathcal{L}, E) = (2.325, 1.001)$. We also take $\alpha = 0.05$. The critical points associated with these shock solutions are summarized in Table 4.1. In a normal situation, it is observed that during accretion, the subsonic flows gradually achieve their supersonic states after passing through the outer critical point ($r_{\rm out}$) and continue to proceed towards the central black hole until they cross the event horizon, as shown by the dashed curves. However,

Table 4.1: Deformation parameter (η_0), event horizon location ($r_{\rm H}$), critical point locations ($r_{\rm in}, r_{\rm out}$), shock location ($r_{\rm sh}$) for shock-induced global accretion solutions presented in Fig. 4.2.

η_0	$r_{\rm H}$	$r_{\rm in}$	$r_{\rm out}$	$r_{\rm sh}$
- 0.125	1.7102	3.8166	185.8394	36.4466
0	1.7599	4.0765	185.8436	23.1665
0.125	1.8042	4.3375	185.8478	13.0675

due to the dominance of centrifugal repulsion over the gravitational pull, the incoming flow slows down, causing discontinuous jump into the flow variables in between $r_{\rm in}$ and $r_{\rm out}$. To find the shock location, we use the relativistic shock conditions which are expressed as [254],

(a) Mass flux conservation: $[\rho u^r]$,

(b) Energy flux conservation: $[(e+p)u^r u^t + \pi^{rt}]$,

(c) Radial-momentum flux conservation: $[(e+p)u^r u^r + p g^{rr} + \pi^{rr}]$.

Here, the square brackets denote the difference between the pre-shock and post-shock quantities. The explicit form of the stress tensor component π^{rr} is calculated using Eq. (2.4), and has been given in Appendix 4.A. For $\eta_0 = -$ 0.125, 0, and 0.125, we obtain the shock locations at $r_{\rm sh} = 36.4466$, 23.1665, and 13.0675, respectively, shown by the solid vertical lines. After the shock transition from the supersonic to the subsonic branch, flow again becomes supersonic when it passes through the inner critical point ($r_{\rm in}$), and continues to accrete up to the horizon. Therefore, in the shock scenario, accretion solution can passes through both $r_{\rm in}$ and $r_{\rm out}$. Here, it is observed that the shock locations move closer to the horizon as the deformation parameter is increased. An explanation for this will be provided later within this section.

As there are discontinuous jumps in the flow variables during shock transitions, it is therefore worthy to study them across the shock fronts. We examine different physical properties of the accretion disc associated with the shock-induced accretion solutions in the deformed spacetime. In Fig. 4.2b-d, we present the profiles of radial velocity (v), specific angular momentum (λ), and electron temperature (T_e) corresponding to the accretion solutions in Fig. 4.2a, where the sudden jumps in the analyzed quantities are clearly visible for the shock solutions. Furthermore, it is observed that the difference of these quantities across the shock front increases when the deformation parameter increases, which is expected as the shock fronts settle down at smaller radii. As the

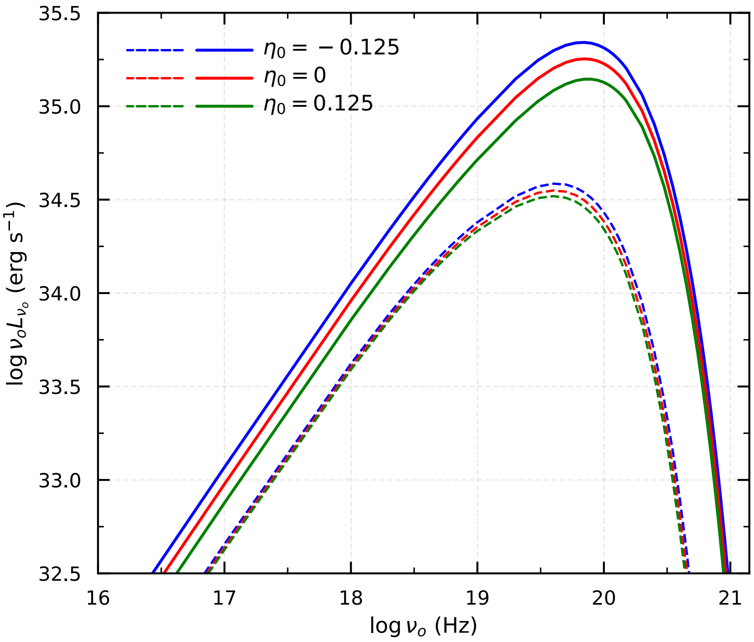

Figure 4.3: Spectral luminosity distributions of radiation emitted from the accretion disc corresponding to the same set of accretion solutions in Fig. 4.2. Here, the input parameters are chosen as $r_{\rm edge} = 300$, $M_{\rm BH} = 10M_\odot$, and $\dot{M} = 0.1\dot{M}_{\rm Edd}$. See the text for details.

deformation parameter increases, causing the event horizon radius to expand, the critical points shift towards larger radii (see Table 4.1). It increases the radial velocity of flow, and consequently decreases the specific angular momentum (see panels (b) and (c)). Therefore, the increase of η_0 weakens the centrifugal repulsion against gravity, ultimately pushing the shock locations at smaller radii. Since the radial velocity drops down at the shock radius, the kinetic energy of pre-shock flow converted into the thermal energy, and consequently increase the electron-temperature of post-shock corona (equivalently PSC). It is noteworthy that the soft photons from the pre-shock disc may inverse Comptonize by the hot electrons in PSC, and produce the high energy radiation in active galactic nuclei (AGNs), BHBs, and BHCs [28, 49, 329].

Now, we examine the disc spectrum of emitted radiation from the accretion disc for the shock-free and shock-induced solutions. We calculate the spectral energy distributions (SEDs) associated with the accretion solutions of Fig. 4.2a using Eq. (4.25). In this work, we consider $r_{\rm edge} = 300$, $M_{\rm BH} = 10M_\odot$, and $\dot{M} = 0.1\dot{M}_{\rm Edd}$, where $\dot{M}_{\rm Edd} = 1.39 \times 10^{18} M_{\rm BH}/M_\odot$ gm s^{-1} is the Eddington mass accretion rate and $M_\odot$ is the Solar mass. The obtained results are depicted in Fig. 4.3, illustrating the variation of quantity $\nu_o L_{\nu_o}$

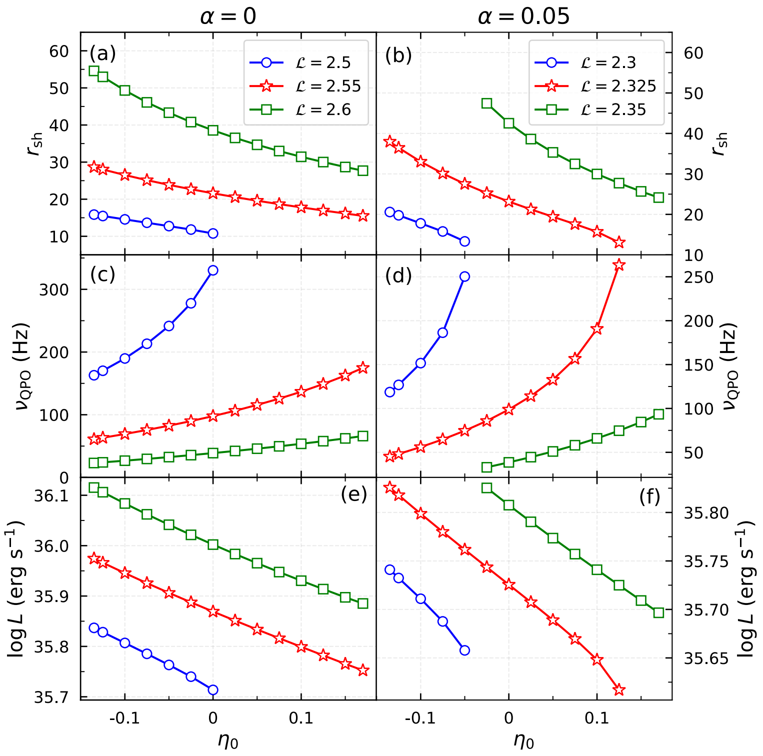

Figure 4.4: Variation of shock location ($r_{\rm sh}$), QPO frequency ($\nu_{\rm QPO}$), and bolometric disc luminosity (L) with the deformation parameter (η_0) for $\alpha = 0$ (left panels) and for $\alpha = 0.05$ (right panels). In this figure, the set of input parameters are taken as $a_{\rm k} = 0.65$, $E = 1.001$, $r_{\rm edge} = 300$, $M_{\rm BH} = 10M_\odot$, and $\dot{M} = 0.1\dot{M}_{\rm Edd}$. The bulk angular momentum $\mathcal{L}$ is marked in each panel. See the text for details.

as a function of the observed frequency ν_o. Note that the bremsstrahlung radiation maximizes its power at $\nu_o \approx 10^{20}$ Hz, and cut-off at $\nu_o \approx 10^{21}$Hz ($= k_{\rm B}T_{e0}/h$, which is corresponds to the disc inner edge electron temperature $T_{e0} \approx 10^{10}$K). We see that the shock-induced solutions produce much higher SEDs than the shock-free solutions. This happens because the temperature of a shock solution is larger than that of a shock-free solution. Furthermore, we observe that increasing η_0 reduces the luminosity distributions due to the decrease in temperature of the accretion disc (see Fig. 4.2e).

Next, we investigate the effect of deformation parameter on various shock properties, and the obtained results are presented in Fig. 4.4 for flow energy $E = 1.001$. In panel (a), we show the variation of shock location ($r_{\rm sh}$) as a function of η_0 for a non-viscous flow (*i.e.*, $\alpha = 0$), where the open circles (blue), open asterisks (red), and open squares (green) joined with the solid lines denote the results for $\mathcal{L} = 2.5, 2.55$, and 2.6, respectively. Similarly, in panel (b), we present the variation of $r_{\rm sh}$ for a viscous flow with $\alpha = 0.05$, where the results corresponding to $\mathscr{L} = 2.3, 2.325$, and 2.35 are plotted using the open circles (blue), open asterisks (red), and open squares (green) joined with the solid lines. In both panels, we notice that $r_{\rm sh}$ decreases with the increase of η_0, irrespective of $\mathscr{L}$ values. These findings are in agreement with the results of Fig. 4.2. Notably, the deformation parameter cannot be increased indefinitely because the shock conditions cease to be satisfied beyond a critical value ($\eta_0 > \eta_0^{\rm cri}$), leading to the disappearance of shock transitions. From numerical simulation [330–332], we observe that the shock can oscillate along the radial direction in a quasi-periodic manner when the infall time from the shock location is comparable to the radiative cooling time of post-shock flow, which leads to the oscillation of hard X-rays during the outburst phases of BHBs and BHCs. The frequency of quasi-periodic oscillation (QPO) of the shock front is expressed as $\nu_{\rm QPO} \approx 1/t_{\rm infall}$ [330], where $t_{\rm infall} = \int_{r_{\rm sh}}^{r_{\rm H}} v^{-1} dr$ is the infall time of post-shock flow. We calculate $\nu_{\rm QPO}$ corresponding to the result of panels (a) and (b) by assuming that these shocks are oscillatory. The obtained results are depicted in the respective panels (c) and (d), where $\nu_{\rm QPO}$ is plotted as a function of η_0. We observe that $\nu_{\rm QPO}$ increases with the increase of η_0 for both the viscous and non-viscous flows. As shocks settle down at smaller radii for higher η_0 values, $t_{\rm infall}$ decreases, which gives high $\nu_{\rm QPO}$ values. It is noteworthy that the theoretically calculated QPO frequencies for a $10M_\odot$ black hole are consistent with the observed QPOs for BHBs and BHCs [18]. Finally, we calculate the bolometric disc luminosity (L) using Eq. (4.24) for the global shock solutions of panels (a) and (b). We present the obtained results in panels (e) and (f), respectively, where we notice that L decreases in both cases with an increase in η_0. This occurs because enhanced deformation reduces the luminosity distribution in the emitted radiation (see Fig. 4.3), and consequently decreasing disc luminosity.

4.4 Phenomenology on high frequency QPOs

In this section, we find the parameter space of bulk angular momentum ($\mathscr{L}$) and deformation parameter (η_0) corresponding to the observed QPO frequencies ($\nu_{\rm QPO}^{\rm obs}$) in X-ray spectra of some BHBs and BHCs. For that, we choose two well-studied sources, namely XTE J1550 – 564 and H 1743 – 322. These black hole microquasars are commonly known for their pairs of high-frequency QPOs with moderate black hole spin values. For XTE J1550 – 564, the observed pairs of QPO frequencies are 184, 276 Hz [31, 333, 334], and for H 1743 – 322, those values are 165, 241 Hz [335, 336]. The reported mass of black hole primary of BHB XTE J1550 – 564 is $M_{\rm BH} = (9.1 \pm 0.61) M_\odot$ [337], and the

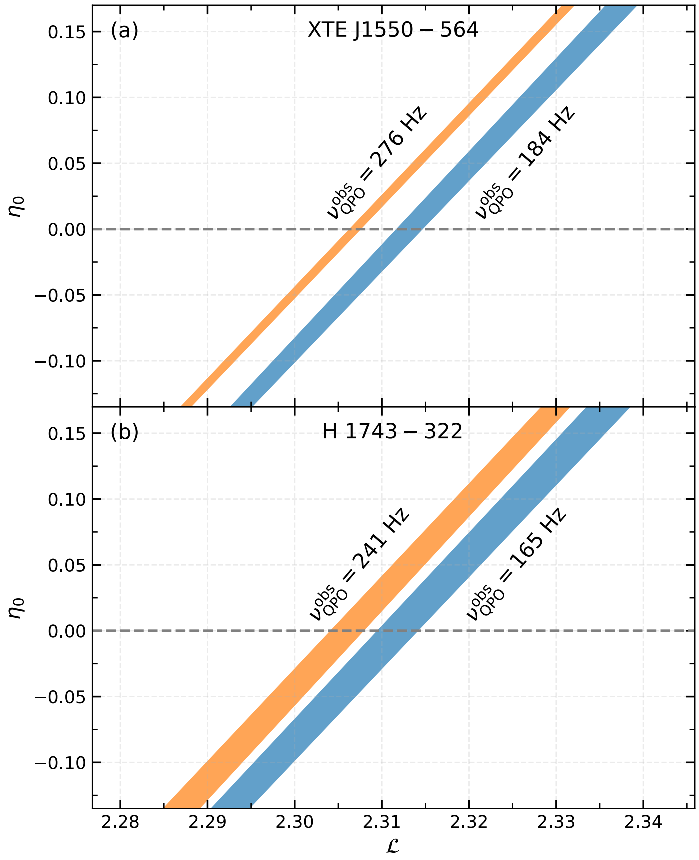

Figure 4.5: Model estimated parameter space of deformation parameter (η_0) and bulk angular momentum ($\mathscr{L}$) for observed QPO frequencies in black hole microquasars XTE J1550 − 564 and H 1743 − 322. The horizontal dashed lines (gray) represent the results corresponding to the Kerr black holes. In this figure, we take $M_{\rm BH} = (9.1 \pm 0.61) M_\odot$ for XTE J1550 − 564, and $M_{\rm BH} = 11.21^{+1.65}_{-1.96} M_\odot$ for H 1743 − 322. Here, other input parameters are chosen as $a_{\rm k} = 0.65$, $\alpha = 0.05$, and $E = 1.001$. See the text for details.

black hole mass of BHC H 1743 − 322 is provided as $M_{\rm BH} = 11.21^{+1.65}_{-1.96} M_\odot$ [55]. Also, the estimated spin parameters of black holes via continuum-fitting method (CFM) are $-0.11 < a_{\rm k} < 0.71$ [338] for XTE J1550 − 564, and $-0.3 < a_{\rm k} < 0.7$ [339] for H 1743 − 322. In this work, we consider $a_{\rm k} = 0.65$ for both sources for the purpose of illustration. We further take the other input parameters as $\alpha = 0.05$ and $E = 1.001$. Using the above mentioned parameters for XTE J1550−564 source, we calculate the parametric regions of $\mathscr{L}$ and η_0 in Fig. 4.5(a), where the shaded region (in blue) is obtained for $\nu^{\rm obs}_{\rm QPO} = 184$ Hz, and the shaded region (in orange) is depicted for $\nu^{\rm obs}_{\rm QPO} = 276$ Hz. Similarly, in Fig. 4.5(b), we present the obtained results in $\mathscr{L} - \eta_0$ plane for H 1743 − 322, where the blue and orange shaded regions correspond to $\nu^{\rm obs}_{\rm QPO} = 165, 241$ Hz, respectively. In both panels, we observe that the effective region of the parameter space is shifted towards the lower $\mathscr{L}$ domain when $\nu^{\rm obs}_{\rm QPO}$ is increased. Moreover, we notice that for a given $\mathscr{L}$, η_0 takes higher values corresponding to a larger $\nu^{\rm obs}_{\rm QPO}$ than the smaller $\nu^{\rm obs}_{\rm QPO}$. This happens because, in order to produce high QPO frequencies, the shock front has to move towards the inner edge of the disc, which is achieved by reducing angular momentum and increasing deformation (see Figs. 4.4a, b). We further notice that the area under parameter space reduces with the increase of $\nu^{\rm obs}_{\rm QPO}$ for both scenarios.

4.5 Chapter Summary and Conclusions

In this chapter, we study the viscous accretion flow around the KZ deformed Kerr black hole in the light of general relativistic hydrodynamics. We construct a set of equations that govern the dynamics of accretion flow in the disc. These equations have been solved numerically, and we are able to find the accretion solutions that satisfy the boundary conditions for the transonic flow. We explore all possible types of accretion solutions and find that these solutions are not unique; instead, a parameter space exists. Since the deformation in KZ spacetime alters the near horizon geometry, a key aspect of our investigation is to analyze the impact of deformation parameter (η_0) on the physical properties of accretion disc. Accordingly, we explore the radiation spectrum of accretion disc as a function of η_0. We find that as η_0 increases, the luminosity distribution decreases in both the shock-free and as well as the shock-induced accretion solutions. Further, we make an effort to examine the effect of deformation on the shock properties, mainly the shock location ($r_{\rm sh}$), QPO frequency ($\nu_{\rm QPO}$), and bolometric disc luminosity (L). We find that the shock fronts settle at smaller radii for higher η_0 values, which increases $\nu_{\rm QPO}$ and decreases L. Hence, the present study indicates that η_0 significantly influences various physical properties of the accretion disc.

Further, we phenomenologically identify the $\mathscr{L}-\eta_0$ parameter spaces associated with the pairs of HFQPOs observed in XTE J1550 − 564 and H 1743 − 322 sources. Here, we find that when the observed QPO frequency increases, the obtained parameter space moves towards the lower $\mathscr{L}$ side and shrinks as well. Most importantly, using this phenomenological approach, the identified non-zero η_0 values (which offer parametric deviations to the Kerr metric) indicate that the KZ non-Kerr black holes can also describe the observed spectral properties of the accretion disc, like the Kerr black holes in Einstein's gravity theory.

Now, we provide a comparative discussion for the accretion properties corresponding to the present type of deformation (i.e. the KZ case) and the JP type. In our earlier study of accretion flow in the JP spacetime [182, 183], we self-consistently found all possible classes of the transonic accretion solutions, including the shock solutions, using GR hydrodynamics and relativistic EoS. We mainly observed there the effect of deformation on the properties of accretion flows. We also noticed that as the JP deformation increases, critical points are formed at the smaller radii due to a decrease in the event horizon radius. Consequently, the shock front recedes away from the horizon, resulting in a decrease in the change of flow variables such as density, temperature, etc., across the shock fronts. Moreover, in the spectral analysis of the accretion disc, we demonstrated that the luminosity distribution of emitted radiation increases with increase of the JP deformation. Based on these prior analyses, we see that the accretion solutions in the KZ spacetime are characteristically similar to those in the JP spacetime. Hence, by looking at the behavior of accretion solutions, it is difficult to isolate them. However, by studying various disc properties (e.g., shock radii, luminosity distributions, etc.) corresponding to a particular class of accretion solutions in these two spacetime, we observe that the KZ deformation shows opposite behavior in controlling the disc properties from the JP deformation. Needless to say, the shock radii cannot be directly observed but can affect the QPO frequency, as we discussed earlier. The QPO frequency is found to be inversely proportional to the shock location (i.e., $\nu_{\rm QPO} \propto 1/r_{\rm sh}$). In case of the JP spacetime, $r_{\rm sh}$ moves away from the central black hole as the deformation parameter (ϵ) increases. In contrast, for the KZ spacetime, $r_{\rm sh}$ decreases as the deformation parameter (η_0) increases. As a result, the QPO frequency decreases in the JP spacetime but increases in the KZ spacetime with increasing deformation. Therefore, it is evident that the QPO frequency may serve as a promising observational signature of the underlying spacetime geometry. However, other spectral properties can also play a significant role in this context. Here, I discuss some of them. One such important property is the photon index, which describes the slope of the power-law (or non-thermal) spectrum. If the shock radius (i.e., the size of the post-shock corona) decreases due to an increase in the deformation parameter, the power-law photon flux at the high-energy tail is reduced. As a result, the photon index increases, i.e., the spectrum becomes softer. Conversely, when the shock moves outward, the photon index decreases, i.e., the spectrum becomes harder. Another observational signature is the cut-off frequency at which the power-law component drops off exponentially. A smaller shock radius results in a softer spectrum, leading to a lower cut-off frequency. On the other hand, when the shock forms at a larger radius, the cut-off frequency is higher, as the spectrum is harder. Therefore, in addition to the QPOs, other spectral features such as photon index (or spectral hardness) and cut-off frequency are also correlated with the shock location. Each of these properties may thus serve as potential observational signatures to distinguish between JP and KZ spacetimes. Hence, we wish to emphasize that the analysis of transonic accretion flows around various kind of non-Kerr black holes serves as an alternative theoretical approach to characterize the parametric deviations from the Kerr metric.

So far, we have analyzed the accretion flows around isolated Kerr and non-Kerr black holes. However, it is well established that the supermassive black holes at the centers of galaxies are surrounded by dark matter halos. The presence of these halos effectively accounts for various observational features associated with galaxy dynamics. Although the dark matter is weakly interacting, its presence can influence the geometry of black holes. Since the accreting matter is the immediate neighbor to the black holes, it is expected that changes in the black hole geometry due to the dark halo could influence the accretion properties, subsequently affecting the AGN spectrum. Towards this, in the next chapter, we explore the accretion dynamics of galactic black holes embedded in a dark matter halo and aim to provide a tool for detecting the presence or absence of a dark matter halo around a galactic black hole.

Indian Institute of Technology Guwahati

Appendices

4.A Shear tensor components σ^r_ϕ and σ^r_t

The $r-\phi$ and $r-t$ components of the viscous shear tensor (σ^i_k) are calculated as,

$$\sigma^r_\phi = \frac{1}{2}\left(A_1 + A_2\frac{dv}{dr} + A_3\frac{d\lambda}{dr}\right) \quad \text{and} \quad \sigma^r_t = \frac{1}{2}\left(B_1 + B_2\frac{dv}{dr} + B_3\frac{d\lambda}{dr}\right),$$

where

$$A_1 = -\frac{u_t\gamma_v^2(A_{11}+A_{12})}{r^3},$$

$$A_{11} = v^2(\Delta r-\eta_0)(\lambda P_2 - P_1),\ A_{12} = \frac{2\lambda L_N + 2\mathscr{G}(\Delta r-\eta_0)P_1 - \lambda(\Delta r-\eta_0)^2 P_3}{2\mathscr{G}},$$

$$A_2 = -\frac{4\lambda u_t v\gamma_v^4(\Delta r-\eta_0)}{3r^3},$$

$$A_3 = -\frac{u_t\gamma_v^2(\Delta r-\eta_0)\big(r^2(r^3+a_{\rm k}^2(r+2)) - a_{\rm k}\lambda(2r^2+\eta_0) + a_{\rm k}^2\eta_0\big)}{\mathscr{G}r^5},$$

$$B_1 = \frac{u_t\gamma_v^2(B_{11}+B_{12})}{r^3},$$

$$B_{11} = v^2(\Delta r-\eta_0)(Q_1+Q_2),\ B_{12} = \frac{2L_N - 2\mathscr{G}(\Delta r-\eta_0)Q_1 - (\Delta r-\eta_0)^2 Q_3}{2\mathscr{G}},$$

$$B_2 = \frac{4u_t v\gamma_v^4(\Delta r-\eta_0)}{3r^3},$$

$$B_3 = \frac{u_t\gamma_v^2(\Delta r-\eta_0)(a_{\rm k}(2r^2+\eta_0) + \lambda(r^3-2r^2-\eta_0))}{\mathscr{G}r^5},$$

$$u_t = -\frac{\gamma_v}{\sqrt{\lambda f_2 - f_1}},\ \mathscr{G} = \frac{r^2(r^3+a_{\rm k}^2(r+2)) - 2a_{\rm k}\lambda(2r^2+\eta_0) - \lambda^2(r^3-2r^2-\eta_0) + a_{\rm k}^2\eta_0}{r^2},$$

$$L_N = \frac{\mathscr{G}(\Delta + 2r(r-1)) - (\Delta r-\eta_0)\mathscr{G}'}{2},\ \mathscr{G}' = \left(\frac{d\mathscr{G}}{dr}\right)_{\Theta,v,\lambda},$$

$$P_1 = \frac{f_1 a_{\rm k}(2r^2+3\eta_0) + f_2(2r^2(r^3-a_{\rm k}^2) - 3a_{\rm k}^2\eta_0)}{r^4},$$

$$P_2 = \frac{\eta_0 - 2r(a_{\rm k}^2 + r(2r-3))}{3r(\Delta r-\eta_0)},$$

$$P_3 = \frac{-f_1^2(2r^2+3\eta_0) + 2a_{\rm k}f_1f_2(2r^2+3\eta_0) + f_2^2(2r^2(r^3-a_{\rm k}^2) - 3a_{\rm k}^2\eta_0)}{r^4},$$

$$Q_1 = \frac{(2r^2+3\eta_0)(a_{\rm k}f_2 - f_1)}{r^4},\ Q_2 = P_2,\ Q_3 = P_3.$$

The $r-r$ component of the viscous stress tensor (π^{ik}) is given by,

$$
\begin{aligned}
\pi^{rr} &= -\frac{\eta(\Delta r-\eta_0)}{r^3}\left(C_1+C_2\frac{dv}{dr}\right),\\
C_1 &= \frac{v\gamma_v}{r}\sqrt{\frac{\Delta r-\eta_0}{r}}\left(\frac{\gamma_v^2(2r(a_{\mathrm{k}}^2-r)-3\eta_0)}{3r(\Delta r-\eta_0)}-\frac{4\gamma_v^2}{3r}-u_t^2P_3\right),\\
C_2 &= \frac{4\gamma_v^5}{3r}\sqrt{\frac{\Delta r-\eta_0}{r}}.
\end{aligned}
$$

Here, all the quantities have their usual meaning.

4.B Radial-momentum equation, and conservation equations of $\mathscr{L}$ and E

The conservation of bulk angular momentum ($\mathscr{L}$), conservation of Bernoulli constant (E), and r-component of momentum equation are respectively obtained as,

$$
\begin{aligned}
&\frac{d\mathscr{L}}{dr} = \mathscr{L}_0+\mathscr{L}_1\frac{dv}{dr}+\mathscr{L}_2\frac{d\Theta}{dr}+\mathscr{L}_3\frac{d\lambda}{dr}=0,\\
&\frac{dE}{dr} = E_0+E_1\frac{dv}{dr}+E_2\frac{d\Theta}{dr}+E_3\frac{d\lambda}{dr}=0,\\
&R_0+R_1\frac{dv}{dr}+R_2\frac{d\Theta}{dr}+R_3\frac{d\lambda}{dr}=0,
\end{aligned}
$$

where

$$
\begin{aligned}
\mathscr{L}_0 &= \lambda h_0\left(\frac{du_t}{dr}\right)_{\Theta,v,\lambda}+\left(\frac{d(\Lambda A_1)}{dr}\right)_{\Theta,v,\lambda},\\
\mathscr{L}_1 &= \lambda h_0\left(\frac{du_t}{dv}\right)_{r,\Theta,\lambda}+\left(\frac{d(\Lambda A_1)}{dv}\right)_{r,\Theta,\lambda},\\
\mathscr{L}_2 &= \frac{2\lambda u_t\Gamma}{(\Gamma-1)(1+m_p/m_e)}+\left(\frac{d(\Lambda A_1)}{d\Theta}\right)_{r,v,\lambda},\\
\mathscr{L}_3 &= h_0u_t+h_0\lambda\left(\frac{du_t}{d\lambda}\right)_{r,\Theta,v}+\left(\frac{d(\Lambda A_1)}{d\lambda}\right)_{r,\Theta,v},\\
E_0 &= h_0\left(\frac{du_t}{dr}\right)_{\Theta,v,\lambda}-\left(\frac{d(\Lambda B_1)}{dr}\right)_{\Theta,v,\lambda},\\
E_1 &= h_0\left(\frac{du_t}{dv}\right)_{r,\Theta,\lambda}-\left(\frac{d(\Lambda B_1)}{dv}\right)_{r,\Theta,\lambda},\\
E_2 &= \frac{2u_t\Gamma}{(\Gamma-1)(1+m_p/m_e)}-\left(\frac{d(\Lambda B_1)}{d\Theta}\right)_{r,v,\lambda},\\
E_3 &= h_0\left(\frac{du_t}{d\lambda}\right)_{r,\Theta,v}-\left(\frac{d(\Lambda B_1)}{d\lambda}\right)_{r,\Theta,v},
\end{aligned}
$$

भारतीय प्रौद्योगिकी संस्थान गुवाहाटी • Indian Institute of Technology Guwahati •

$$
\begin{aligned}
\Lambda &= \frac{\alpha C_s H r}{v\gamma_v\sqrt{(\Delta r-\eta_0)/r}},\\
R_0 &= \frac{\Theta}{(f+2\Theta)}\left(-\frac{3}{r}+\frac{F_1'}{F_1}+\frac{\lambda\Omega'}{1-\Omega\lambda}-\frac{2r^2(r-1)+\eta_0}{r(\Delta r-\eta_0)}\right)+\left(\frac{d\Phi^{\rm eff}}{dr}\right)_\lambda,\\
R_1 &= \gamma_v^2\left(v-\frac{2\Theta}{(f+2\Theta)v}\right),\\
R_2 &= \frac{1}{f+2\Theta},\\
R_3 &= \frac{\Theta}{(f+2\Theta)(1-\Omega\lambda)}\left(\frac{d(\Omega\lambda)}{d\lambda}\right)_{r,\Theta,v}.
\end{aligned}
$$

Here, all the quantities have their usual meaning.

Indian Institute of Technology Guwahati

CHAPTER 5

EFFECT OF DARK MATTER HALO ON TRANSONIC ACCRETION FLOW AROUND A GALACTIC BLACK HOLE

5.1 Introduction and Motivation

The modern day's advanced astronomical techniques for detecting gravitational waves (GWs) [149–152], electromagnetic (EM) waves [153–158], and motion of stars around the galactic center [340–342] have the potential to revolutionize our understanding of compact objects and their environments. A number of scenarios (e.g., galaxy rotation curves, gravitational lensing, etc.) support the presence of a dark matter halo around the supermassive black holes (BHs) at the center of the galaxies [175, 343, and references therein]. Since dark matter interacts weakly, possibly through the weak nuclear force, its exact properties still remain unknown [344–348]. However, it can interact gravitationally with the normal matter [349–352]. To understand how dark matter influences the generation and propagation of GWs or EM appearance of black holes, several attempts have been made at the Newtonian level [353–356]. However, to move beyond these approximate estimates, a proper spacetime manifold is required. Meanwhile, the authors in Ref. [176] proposed an exact analytical solution within Einstein's general relativity (GR), which represents a supermassive BH spacetime minimally coupled to a dark matter fluid with anisotropic pressure and Hernquist density profile. In this fully GR approach, few other BH metrics are modeled by considering different density profiles of the dark matter (e.g., King, Einasto, Jaffe, Burkert, Navarro–Frenk–White, Moore, Taylor–Silk profiles, etc.) [177, 349, 357–371]. Although various properties of spacetime and phenomenology have been investigated to observe the influence of dark halos [179–181, 372–383], their effect on transonic matter accretion [71, 94, 244, 245] onto black holes has not been studied. In this chapter, we aim to explore how the presence of a dark matter halo can be perceived through different transonic accretion properties. For this, we would like to concentrate on the Cardoso BH model [176] only because, for most of the galaxies, it is consistent with the observed rotation curves and other dynamical properties as well. Needless to mention that the choice of the dark matter profile depends on the specific context and the kind of galaxy or dark matter halo being modeled.

The Cardoso BH is described by two independent parameters: halo mass ($M_{\rm H}$) and characteristic length scale (a_0). Recently, interest has grown in testing the Cardoso model on the rich astrophysical environments of the black holes, such as accretion discs, photon rings, etc. For example, in [176], the authors investigated the effect of dark halo on GWs emission and propagation. The influence of dark matter components on the properties of EM radiations, like the quasi-normal modes, perturbations, scatterings, etc., has been studied in [384]. The epicyclic oscillatory motion of the test particles and its application to the observed quasi-periodic oscillations (QPOs) in active galactic nuclei (AGNs) spectra were explored in [385]. Investigation of tidal forces and geodesic deviation motion due to a dark matter halo has been reported in [386]. The evolution of the extreme mass ratio inspiral in a galactic black hole spacetime within the dark halo is analyzed in [376]. In presence of a dark matter halo, the black hole shadow is studied in [179], where the authors constrained the halo parameters ($M_{\rm H}$, a_0) using the Event Horizon Telescope (EHT) collaborations shadow data for the supermassive black holes M87* and SgrA*. The energy spectrum and fluxes of the orbiting particles are examined in [379] based on the Novikov-Thorne accretion model. The effect of a dark matter halo on the motion of spinning particles was investigated in [381]. The analysis of quasi-normal modes of a galactic black hole in a dark matter halo has been explored in [180].

In the previous chapters, we discussed the properties of the low angular momentum advective accretion model, where flow is inherently transonic, and its ability to explain various observational signatures near black holes, such as hard power-law spectra, quasi-periodic oscillations (QPOs), and bipolar jets in the post-shock corona (PSC), etc. As we have seen, many strong gravity signatures have been analyzed in the Cardoso BH model, and some great results have been revealed. But, till now, to the best of our knowledge, nobody has reported the properties of transonic accretion flows around the Cardoso BH.

Such deficiency in the literature motivates us to serve the present work. We explore the transonic accretion solutions and associated observational signatures (e.g., luminosity distribution, spectrum slope, bolometric disc luminosity, etc.) in presence and absence of the shock waves in background of the Cardoso BH metric. Our results indicate that the halo parameters ($M_{\rm H}, a_0$) potentially affect the accretion disc properties when the dark matter concentrates close to the black hole. However, for low compactness, these properties deviate insignificantly from the Schwarzchild BH model. In the high compactness regime, we compare the outcomes of the Cardoso BH model with those for the Schwarzchind BH model. We show that the high compactness of the halo largely modulates a given accretion solution topology (e.g., O, A, and I-types) with respect to the usual Schwarzschild BH. Such effects change the flow temperature in the disc significantly. Consequently, the spectral energy distribution (SED), its shape, and bolometric disc luminosity (L) are varied substantially compared to the results in the Schwarzschild BH model. Moreover, we examine the shock solutions using relativistic shock conditions. We observe that when the halo compactness is high, the shock properties, such as the density compression and temperature compression across the shock location ($r_{\rm sh}$), potentially change with the halo parameters ($M_{\rm H}$, a_0). However, for such shock solutions, the SED, its shape, and L do not vary much with the halo compactness, even when the dark matter is concentrated near the galactic center. In addition, we notice that the high compactness confines the shock solutions to a narrower range of flow specific angular momentum (λ) and energy (E) than in the case of the Schwarzschild BH. These feature may offer clues about the presence of a dark matter halo around a galactic black hole.

The outlines of this chapter are as follows. We first introduce a static black hole metric with a dark matter halo. Then, we present the governing flow equations for the accretion disc in that stationary and asymmetric black hole spacetime. Next, we discuss the methodology used to find transonic accretion solutions and see the effect of the dark matter halo on accretion solution topologies and their physical properties. Thereafter, we analyze the shock-induced accretion solutions and explore various shock properties as a function of halo compactness. Finally, we depict the available parameter space for shocks and their modifications with halo parameters.

5.2 Geometry of galactic black hole with dark matter halo

In this section, we introduce the background spacetime, which has been used in our analysis, and discuss its properties. In Ref. [176], the authors provided an exact analytical solution of Einstein's equations for describing a supermassive BH immersed in a dark matter halo. To do that, they follow the Einstein construction, where the anisotropic matter has tangential pressure only. They generalized the Einstein cluster, a technique to construct a stationary system of many gravitating masses, by including a black hole at the center of a dark matter distribution. Accordingly, the general relativistic geometry of such configuration is found to be [176],

$$ds^2 = -f_0(r)dt^2 + \frac{dr^2}{1-2m(r)/r} + r^2 d\Omega^2, \tag{5.1}$$

where

$$d\Omega^2 = d\theta^2 + \sin^2\theta d\phi^2. \tag{5.2}$$

The mass function $m(r)$ is chosen as,

$$m(r) = M_{\rm BH} + \frac{M_{\rm H} r^2}{(r+a_0)^2}\left(1-\frac{2M_{\rm BH}}{r}\right)^2, \tag{5.3}$$

where $M_{\rm BH}$ is the mass of the central black hole, $M_{\rm H}$ is the mass of dark matter halo, and a_0 is the typical length scale that governs the size of the dark matter halo. The specialty of choosing such a mass profile is that it corresponds to the black hole mass $M_{\rm BH}$ at small distances. On the other hand, at large scales, it describes the Hernquist density profile as,

$$\rho_0(r) = \frac{M_{\rm H} a_0}{2\pi r(r+a_0)^3}. \tag{5.4}$$

Using the mass profile (5.3) and imposing the asymptotic flatness condition (i.e., $f_0 \rightarrow 1$ at $r \rightarrow \infty$), the radial function is obtained from the Einstein's equation as,

$$f_0(r) = \left(1-\frac{2M_{\rm BH}}{r}\right)e^{\gamma(r)}, \tag{5.5}$$

where

$$\gamma(r) = -\pi\sqrt{\frac{M_{\rm H}}{\xi}} + 2\sqrt{\frac{M_{\rm H}}{\xi}}\arctan\left(\frac{r+a_0-M_{\rm H}}{\sqrt{M_{\rm H}\xi}}\right), \tag{5.6}$$

$$\xi = 2a_0 - M_{\rm H} + 4M_{\rm BH}. \tag{5.7}$$

The matter density (ρ_0) and tangential pressure (P_t) corresponding to the solution (5.5) are obtained as,

$$\rho_0(r) = \frac{1}{4\pi r^2}\frac{dm(r)}{dr} = \frac{M_{\rm H}(a_0+2M_{\rm BH})(1-2M_{\rm BH}/r)}{2\pi r(r+a_0)^3}, \tag{5.8}$$

$$P_t(r) = \frac{m(r)\rho_0}{2[r-2m(r)]}. \tag{5.9}$$

The black hole solution described by Eq. (5.1) has a regular event horizon at $r = r_{\rm H} = 2M_{\rm BH}$ and the curvature singularity at $r = 0$. In the asymptotically flat regime (i.e., $r \to \infty$), the mass of the spacetime (5.1) is referred to as the Arnowitt-Deser-Misner (ADM) mass, which is given by [176, 387],

$$M_{\rm ADM} = \lim_{r\to\infty} m(r) = M_{\rm BH} + M_{\rm H}. \tag{5.10}$$

It is noted that at the horizon, ρ_0 vanishes, while P_t remains regular. Moreover, the dark matter fluid satisfies both the weak and strong energy conditions everywhere outside the horizon, as both ρ_0 and P_t are always positive. However, near $r_{\rm H}$, P_t/ρ_0 diverges because ρ_0 becomes very small. As a result, the dominant energy condition is violated in this region. Nevertheless, this does not affect the spacetime dynamics as the near-horizon region is nearly empty due to the small values of ρ_0 and P_t. It is crucial to mention that when $M_{\rm H} > 2(a_0 + 2M_{\rm BH})$, both the Ricci and Kretschmann scalars diverge not only at $r = 0$ but also at $r = r_{\pm} = M_{\rm H} - a_0 \pm \sqrt{M_{\rm H}(M_{\rm H} - 2a_0 - 4M_{\rm BH})}$, resulting in two additional curvature singularities at $r_{\pm}$. Consequently, the set of spacetime parameters that satisfy the above-mentioned condition do not describe astrophysical setups[1]. Thus, in this analysis, we primarily focus on cases where the spacetime parameters fulfill the condition $M_{\rm H} < 2(a_0+2M_{\rm BH})$, as this provides a relevant setup for studying astrophysical phenomena. This adapted condition is particularly valid for events near black holes, such as the propagation of GWs in the galactic core, photon rings (shadows), and accretion flows, etc. On the other hand, in the context of galaxy dynamics, i.e., events that occur far from the central black hole, the relevant astrophysical setups are characterized by the scale hierarchy $M_{\rm BH} << M_{\rm H} << a_0$. Under this condition, there is a single curvature singularity at $r = 0$, and it also generates the desire Hernquist profile at large r (see Eq. (5.8)). To quantify the compactness of the halo, we introduce the compactness parameter $C = M_{\rm H}/a_0$. We will now present the constraints on the parameter C for various astrophysical scenarios. For example, based on observations of galaxy dynamics,

---

[1] Astrophysical setup is featured by the absence of any curvature singularities outside the black hole event horizon ($r_{\rm H}$). Therefore, in the region of spacetime accessible to the external observer, i.e., $r > r_{\rm H}$, the spacetime must remain regular.

C is constrained to be very small, with $C \lesssim 10^{-4}$ [349, 388]. But, for phenomena related to BH environments, as mentioned earlier, C can be treated as a free parameter [176]. Meanwhile, Xavier et al. [179] analyzed the black hole shadow, a rich BH environments, and found that for $C \lesssim 1$, the theoretical predictions align with shadow data from the EHT collaborations. In our study, we concentrate on values of $C \lesssim 1$, as we are interested in the accretion process, which is also a potential candidate of BH environments. However, in order to observe a noticeable effect of the dark matter halo on the accretion dynamics, all analyses in this study have been conducted within the range $10^{-4} \leq C \leq 1$.

5.3 Model equations governing accretion disc

The dynamical equations governing the accretion flow in the spacetime (5.1) have been developed in this section. We model the hydrodynamics of accretion flow within a complete general relativistic setting [10]. We assume that the motion of an ideal fluid is confined to the equatorial plane (i.e., $\theta = \pi/2$) of the central black hole, meaning the flow has no transverse motion (i.e., $u^\theta = 0$, where u^θ is θ component of the contravariant four velocity u^k). Also, we have $\partial_\theta Q = 0$, where Q is any flow parameter (e.g., mass density, pressure, and temperature, etc.). Moreover, the fluid is steady (i.e., $\partial_t Q = 0$) and obeys the azimuthal symmetry of the spacetime (i.e., $\partial_\phi Q = 0$). To simplify the fluid motion to one dimension (radial motion only), we adopt a corotating frame (CRF), which rotates with the same angular velocity as the fluid. In this work, we choose a unit system such that $G = M_{\rm BH} = c = 1$, where G is the gravitational constant and c is the speed of light. Such a choice makes all the physical quantities dimensionless. Under these assumptions, the radial momentum equation can be written from Eq. (2.14) as [116],

$$\gamma_v^2 v \frac{dv}{dr} + \frac{1}{e+p}\frac{dp}{dr} + \left(\frac{d\Phi^{\rm eff}}{dr}\right)_\lambda = 0, \tag{5.11}$$

where γ_v is the Lorentz factor corresponding to the radial component of the physical three velocity (v) in the CRF, e is the total internal energy density, p is the isotropic fluid pressure, $\Phi^{\rm eff}$ is the effective potential of the system, and λ ($= -u_\phi/u_t$, where u_ϕ and u_t are the ϕ and t components of covariant four velocity u_k) is the specific angular momentum of fluid. Note that for accretion, v is a negative quantity. The expression of $\Phi^{\rm eff}$ is obtained in terms flow parameter λ and spacetime parameters ($M_{\rm H}$,a_0) as,

$$\Phi^{\rm eff} = 1 + \frac{1}{2}\ln(\Phi), \; \Phi = \frac{r^2(r-2)e^{\Upsilon(r)}}{r^3 - \lambda^2(r-2)e^{\Upsilon(r)}}. \tag{5.12}$$

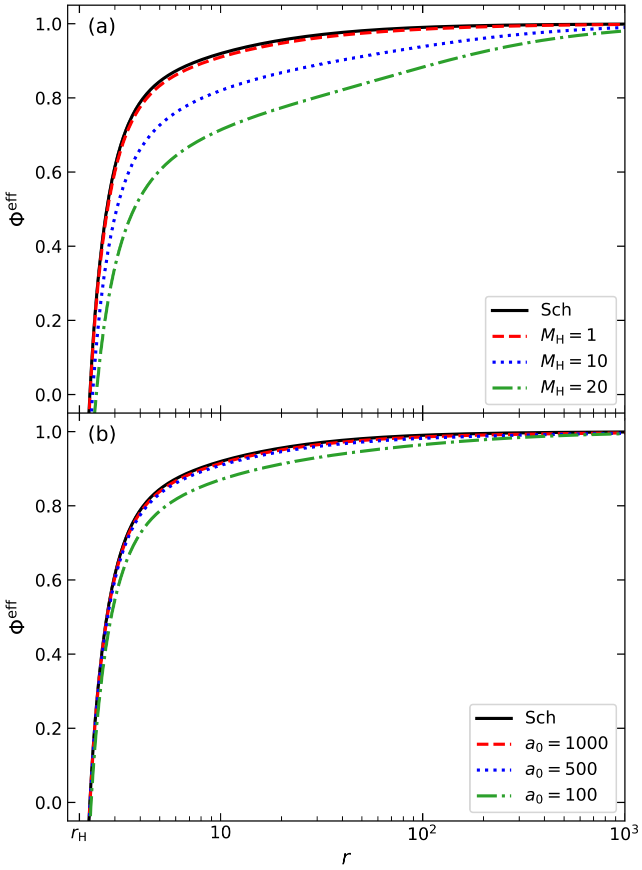

Figure 5.1: Plot of effective potential ($\Phi^{\rm eff}$) as a function of radial distance (r) for halo masses $M_{\rm H}$ = 1, 10, and 20 with a given length scale a_0 = 100 (panel (a)), and for a_0 = 1000, 500, and 100 with $M_{\rm H}$ = 5 (panel (b)). The solid (black) lines are used for the Schwarzschild BH. In this figure, the flow angular momentum is taken as $\lambda = 2.75$. See the text for details.

In Fig. 5.1, we show the variation of $\Phi^{\rm eff}$ with r for different values of $M_{\rm H}$ and a_0, while keeping fixed λ = 2.75. In panel (a), we set a_0 = 100 and use the dashed (red), dotted (blue), and dash-dotted (green) curves to present the results for $M_{\rm H}$ = 1, 10, and 20, respectively. Similarly, in panel (b), the profiles of $\Phi^{\rm eff}$ are plotted as a function of a_0 for a fixed $M_{\rm H} = 5$. The dashed (red), dotted (blue), and dash-dotted (green) curves correspond to a_0 = 1000, 500, and 100, respectively. Here, the solid (black) curves represent the results for the Schwarzschild BH model with the absence of dark matter halo. From Fig. 5.1, it is clear that $\Phi^{\rm eff}$ nearly indistinguishable from the results for a Schwarzschild BH when $M_{\rm H}$ is very small or a_0 is very large. As the halo compactness increases moderately, either by increasing $M_{\rm H}$ or decreasing a_0, $\Phi^{\rm eff}$ begins to differ noticeably and undergoes significant changes at higher halo compactness, i.e., for sufficiently large $M_{\rm H}$ or very small a_0 values. Hence, when dark matter is concentrated near the horizon, $\Phi^{\rm eff}$ deviates considerably from the Schwarzschild BH case.

In steady state, mass accretion rate ($\dot{M}$) is usually taken as a constant of motion (i.e., $d\dot{M}/dr = 0$). Integrating the conservation equation of mass flux (i.e., $\nabla_k(\rho u^k) = 0$, ρ is the mass density of flow), we get the expression of $\dot{M}$ from Eq. (2.17) as,

$$\dot{M} = -4\pi H \rho v \gamma_v \sqrt{r(r-2)e^{\gamma(r)}} = \text{constant}, \tag{5.13}$$

where H is the half-thickness of the disc. Considering the hydrostatic equilibrium along the vertical direction of the disc, H is calculated as [88, 114, 243],

$$H = \sqrt{\frac{pr^3}{\rho F}}, \tag{5.14}$$

where $F = 1/(1-\Omega\lambda)$. The angular velocity (Ω) of the flow is given by,

$$\Omega = \frac{u^\phi}{u^t} = \frac{\lambda(r-2)e^{\gamma(r)}}{r^3}. \tag{5.15}$$

In our model, the other constant of motions can be found from the present spacetime symmetries. From Eq. (2.8), we find two conserved quantities along the streamlines of the flow as (a) Bernoulli constant: $E = -(e+p)u_t/\rho$ (from time-translation symmetry), and (b) bulk angular momentum: $\mathscr{L} = (e+p)u_\phi/\rho$ (from azimuthal symmetry). Therefore, λ $(= -\mathscr{L}/E)$ appears to be another constant of motion.

We consider a relativistic equation of state as proposed in [240], where a variable adiabatic index Γ is used instead of assuming a constant value. Following that work, the thermodynamic variables e and p can be found as,

$$e = \frac{\rho f}{1+m_p/m_e}, \quad p = \frac{2\rho\Theta}{1+m_p/m_e}, \tag{5.16}$$

where m_p is the proton mass and m_e is the electron mass. The quantity f is expressed in term of dimensionless temperature Θ $(= k_B T/(m_e c^2)$, k_B is the Boltzmann constant and T is the flow temperature in Kelvin) as,

$$f = 1 + \frac{m_p}{m_e} + \Theta\left[\frac{9\Theta+3}{3\Theta+2} + \frac{9\Theta+3m_p/m_e}{3\Theta+2m_p/m_e}\right]. \tag{5.17}$$

After solving the equation $d\dot{M}/dr = 0$ using Eqs. (5.13), (5.14), and (5.16), the temperature gradient of the flow is obtained as,

$$\frac{d\Theta}{dr} = -\frac{2\Theta}{(df/d\Theta)+1}\left(\frac{\gamma_v^2}{v}\frac{dv}{dr} + N_{11} + N_{12}\right), \tag{5.18}$$

with

$$N_{11} = \frac{3}{2r} + \frac{r-1}{r(r-2)} - \frac{1}{2F}\frac{dF}{dr}, \; N_{12} = \frac{1}{2}\frac{d\gamma}{dr}. \tag{5.19}$$

As $\dot{M}$ is very small for the context of supermassive black hole accretion [11, 309], we neglect the radiative cooling mechanism in the energy equation (or first law of thermodynamics). Therefore, it is obtained from Eq. (2.9) as,

$$\frac{e+p}{\rho}\frac{d\rho}{dr} - \frac{de}{dr} = 0. \tag{5.20}$$

The expression of ρ is calculated by integrating Eq. (5.20) as,

$$\rho = \mathscr{K} e^{\chi}\Theta^{3/2}(3\Theta+2)^{3/4}(3\Theta+2m_p/m_e)^{3/4}, \tag{5.21}$$

where $\mathscr{K}$ refers the entropy constant and $\chi = (f-1-m_p/m_e)/(2\Theta)$. From Eq. (5.20), it is evident that the flow is locally adiabatic, which implies constant entropy content. Following the works of [37, 38], the entropy accretion rate of the flow is found to be,

$$\dot{\mathscr{M}} = \frac{\dot{M}}{4\pi\mathscr{K}} = -v\gamma_v H\sqrt{r(r-2)e^{\gamma(r)}} \times e^{\chi}\Theta^{3/2}(3\Theta+2)^{3/4}(3\Theta+2m_p/m_e)^{3/4}. \tag{5.22}$$

To obtain the radial velocity gradient, we simultaneously solve Eqs. (5.11), (5.16), (5.18) and (5.20), which leads to the result,

$$\frac{dv}{dr} = \frac{\mathscr{N}}{\mathscr{D}}, \tag{5.23}$$

The expressions of numerator ($\mathscr{N}$) and denominator ($\mathscr{D}$) of the above equation are found to be,

$$\mathscr{N} = \frac{2C_s^2}{\Gamma+1}(N_{11}+N_{12}) - \frac{d\Phi^{\rm eff}}{dr}, \tag{5.24}$$

$$\mathscr{D} = \gamma_v^2\left[v - \frac{2C_s^2}{(\Gamma+1)v}\right], \tag{5.25}$$

where C_s $(=\Gamma p/(e+p))$ is the adiabatic sound speed with $\Gamma = 1 + 2/(df/d\Theta)$.

We consider the emission of thermal bremsstrahlung radiation from the accretion disc. Since the disc medium is optically thin for the hot accretion flow (HAF) [11, 183], bremsstrahlung radiation can escape from the disc without being absorbed [183]. We assume a completely ionized hydrogen plasma (atomic number $Z = 1$), where the number densities of electrons and ions are the same, i.e., $n_e = n_p \approx \rho/m_p$. Moreover, we use an approximate expression for the free-free emission coefficient, as proposed by Ref. [64], given by,

$$\begin{aligned}\mathscr{E}^{\rm ff}_{\nu_e} &= 6.8\times10^{-38}(\rho/m_p)^2 T_e^{-1/2}(1+4.4\times10^{-10}T_e)\\ &\times \exp\left(-\frac{h\nu_e}{k_B T_e}\right)\bar{g}_{\rm B}\ \text{erg s}^{-1}\ \text{cm}^{-3}\ \text{Hz}^{-1},\end{aligned} \tag{5.26}$$

where h is the Planck constant, T_e is the electron temperature, ν_e is the emission frequency, and $\bar{g}_{\rm B}$ is the thermally-averaged Gaunt factor (which includes quantum mechanical correction). In our analysis, we take $\bar{g}_{\rm B} = 1.2$ [309]. The second term in Eq. (5.26) accounts for both electron-electron emission and relativistic corrections. It is important to note that for HAF, their effectiveness is significant [183]. In the accretion disc, since the in-fall timescale is shorter than the ion-electron collision timescale, it is challenging to maintain thermal equilibrium between the ions and electrons. Typically, the electron temperature is lower compared to the ion temperature because the electron mass is much smaller than the mass of the ions. Several studies in the literature have self-consistently calculated the electron and ion temperatures [123, 251, 252, 315]. However, for simplicity, various scaling relations between T_e and T [121, 122, 252] are often used, with T calculated self-consistently by solving Eq. (5.18). In this study, we also adopt a scaling relation $T_e = T/10$ to remain consistent with the work of [309].

For an observer at spatial infinity, the emission frequency is redshifted due to the strong gravitational potential of the central black hole, as well as the rotation of the disc. For simplicity, we neglect any light-bending effects on the emitted radiation. Additionally, the velocity distribution of the electrons is assumed to follow the standard Maxwell's prescription. Under these assumptions, the red-shift factor $(1+z)$ is found to be [122, 310, 316],

$$1+z = \frac{\nu_e}{\nu_o} = u^t\left(1+\frac{r\Omega}{c}\sin\theta_0\sin\phi\right), \tag{5.27}$$

with

$$u^t = \gamma_v\sqrt{\frac{r}{(1-\Omega\lambda)(r-2)e^{\gamma(r)}}}. \tag{5.28}$$

Here, ν_o is the observed frequency and θ_0 is the inclination angle of the accretion disc with respect to the distant observer frame. We take $\theta_0 = 45^\circ$ for the purpose of illustration. Using Eqs. (5.26) and (5.27), we get the monochromatic disc luminosity measured by an observer at infinity as,

$$L_{\nu_o} = 2\int_{r_{\rm H}}^{r_{\rm edge}}\int_0^{2\pi} \mathcal{E}^{\rm ff}_{\nu_o} H r dr d\phi \ {\rm erg\ s^{-1}\ Hz^{-1}}, \tag{5.29}$$

where $r_{\rm H}$ (event horizon location) is taken as the inner edge of the disc. The outer edge of the disc is assumed to be at $r_{\rm edge} = 1000$.

Finally, integrating Eq. (5.29) over all frequency domains, we calculate the bolometric disc luminosity as,

$$\begin{aligned} L &= \int_0^\infty L_{\nu_o} d\nu_o \\ &= 6.8 \times 10^{-38} \left(\frac{2k_B}{hm_p^2} \right) \bar{g}_{\rm B} \ {\rm erg\ s}^{-1} \int_{r_{\rm H}}^{r_{\rm edge}} \int_0^{2\pi} \frac{\rho^2 T_e^{1/2}(1+4.4\times 10^{-10} T_e) H r}{u^t \left(1 + \frac{r\Omega \sin\phi}{\sqrt{2}c}\right)} \, dr d\phi. \end{aligned} \tag{5.30}$$

The above equations are useful for finding the accretion solutions and their corresponding disc properties, such as temperature profile, disc luminosity, and spectral energy distribution, etc. Note that when we set $M_{\rm H} = 0$ in these equations, we can recover the flow equations in the usual Schwarzschild BH spacetime. A detailed discussion of the accretion properties around the galactic black hole metric (5.1) is provided in Section 5.4.

5.4 Results

5.4.1 Transonic accretion solutions

This section explores the transonic accretion solutions, where the flow must pass through at least one critical point [244, 245]. Critical points (r_c) are such radial coordinates where the velocity gradient dv/dr (see Eq. (5.23)) takes the form “0/0". Therefore, the necessary conditions for finding the critical points are $\mathcal{N} = \mathcal{D} = 0$. Note that flow may possess single or multiple critical points depending on the global constants λ, E, $M_{\rm H}$, and a_0. However, the multiple critical points scenario is of special interest for generating shocks [95, 118, 122, 125, 182–184], which has been extensively discussed in Section 5.4.2. The critical points that are formed close to the horizon are called inner critical points ($r_{\rm in}$), and those formed far away from the horizon are called the outer critical points ($r_{\rm out}$). As $(dv/dr)_{r_c}$ takes an indeterminate form, we use the l'Hôpital's rule to Eq. (5.23) for finding the finite values of dv/dr. Usually, $(dv/dr)_{r_c}$ have two values. Depending on them, critical points are classified into three categories — (a) saddle-type: $(dv/dr)_{r_c}$ values are real with opposite sign; (b) nodal-type: $(dv/dr)_{r_c}$ values are real with the same sign; and (c) spiral-type: both values of $(dv/dr)_{r_c}$ are imaginary. The positive value of dv/dr corresponds to an accretion solution, and the negative value of dv/dr yields a wind solution. Therefore, out of three types of critical points, only the saddle-type critical points (hereafter called critical points) are physically acceptable. In this work, we focus on accretion solutions that only pass through saddle-type critical points, excluding any analysis of wind solutions. To find the accretion solutions, we first calculate r_c and its corresponding flow variables Θ_c and v_c for a given set of global

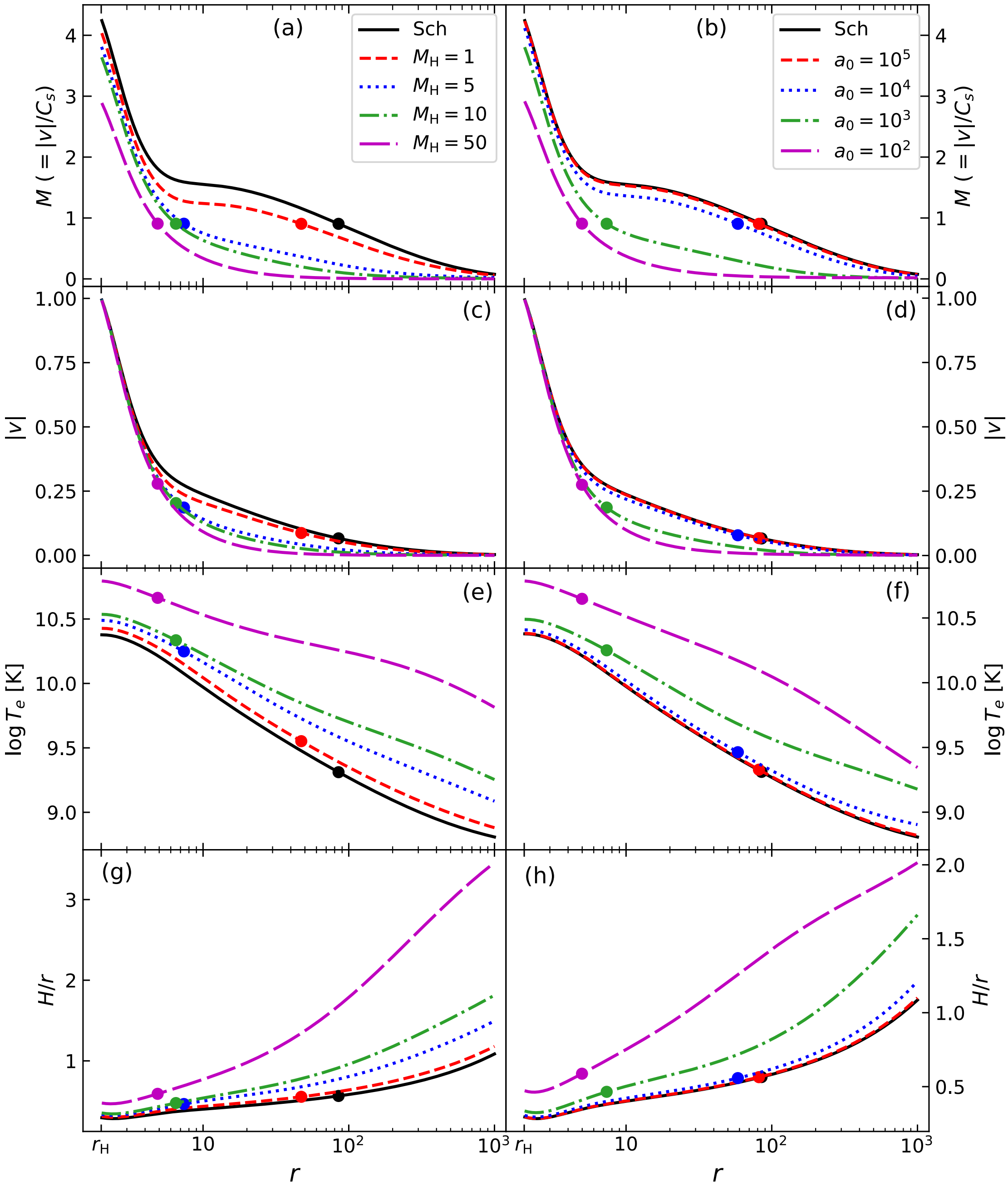

Figure 5.2: Typical accretion solutions (i.e., Mach number ($M = |v|/C_s$) versus radial distance (r) plots) for halo masses $M_{\rm H} = 1$, 5, 10, and 50 with length scale $a_0 = 500$ (panel (a)), and for $a_0 = 10^5$, 10^4, 10^3, and 10^2 with $M_{\rm H} = 10$ (panel (b)). Panels (c) and (d) show the respective radial velocity (v) profiles. The electron temperature (T_e) and aspect ratio (H/r) profiles for panels (a)-(b) are shown in panels (e)-(f) and (g)-(h), respectively. In each panel, the solid (black) line corresponds to the Schwarzschild black hole without a dark matter halo ($M_{\rm H} = 0$). The critical points are marked by filled circles. In this figure, we choose $\lambda = 2.75$ and $E = 1.0025$. See the text for details.

constants $(\lambda, E, M_{\rm H}, a_0)$. Using those results as an initial boundary condition, we then numerically solve the differential Eqs. (5.18) and (5.23) from r_c to $r_{\rm edge}$ and also from r_c to $r_{\rm H}$. Finally, combining the two segments of the solution, we obtain a complete accretion solution.

Following the above methodology, we find the transonic accretion solutions for different sets of input parameters. The obtained results are presented in Fig. 5.2a, where the Mach number ($M = |v|/C_s$) is plotted as a function of the radial distance (r). Here, the flow parameters are chosen as $\lambda = 2.75$ and $E = 1.0025$. We fix the length scale at $a_0 = 500$ and vary the halo mass $M_{\rm H}$. The solid (black) curve corresponds to the Schwarzschild BH without dark matter halo (i.e., $M_{\rm H} = 0$), while the dashed (red), dotted (blue), dash-dotted (green), and long-dashed (magenta) curves represent the results for the Cardoso BH with $M_{\rm H} = 1$, 5, 10, and 50, respectively. In all cases, the solutions extend from $r_{\rm edge}$ to $r_{\rm H}$, which are characteristic of open or global accretion solutions. For the Schwarzschild BH model, the solution is found to be pass through the outer critical point at $r_{\rm out} = 85.0892$. In presence of the dark matter halo with $M_{\rm H} = 1$, the solution again passes through $r_{\rm out}$ but with a significantly decreased value of $r_{\rm out} = 47.2185$. Accretion solutions that pass through $r_{\rm out}$ are referred to as O-type solution topology. When $M_{\rm H}$ is increased to 5, the accretion solution now passes through the inner critical point at $r_{\rm in} = 7.39$. Such accretion solutions that pass through $r_{\rm in}$ are known as I-type solution topology. For a further increase in the halo mass $M_{\rm H} = 10$, the solution topology remains I-type, with $r_{\rm in} = 6.5138$. When the halo mass is increased even more to $M_{\rm H} = 50$, the solution topology continues to be I-type, but now the inner critical point moves closer to the horizon, with $r_{\rm in} = 4.8793$. Similarly, in Fig. 5.2b, we present the global accretion solutions for a fixed halo mass $M_{\rm H} = 10$ with varying length scale a_0. In this case, we choose the same set of flow parameters (λ, E) as used in Fig. 5.2a. The obtained results are shown using the dashed (red), dotted (blue), dash-dotted (green), and long-dashed (magenta) lines for $a_0 = 10^5$, 10^4, 10^3, and 10^2, respectively. Here, the solid (black) curve corresponds to the usual Schwarzschild case, as shown in Fig. 5.2a, and has been included again for the comparison with dark matter model. For Cardoso BH with large values of a_0, such as $a_0 = 10^5$ and 10^4, the solutions remain O-type, similar to the Schwarzschild BH, with outer critical points at $r_{\rm out} = 81.6338$ and 58.5248, respectively. However, for smaller values of a_0, such as $a_0 = 10^3$ and 10^2, the solution topology changes to I-type, with $r_{\rm in}$ values continuously decreasing to 7.3628 and 4.9843, respectively.

The radial velocity profiles corresponding to the accretion solutions of panels (a) and (b) are shown in Figs. 5.2c-d, respectively. We observe that the flow velocity is minimal

Table 5.1: Dark matter halo mass (M_H), halo length scale (a_0), critical point locations ($r_\mathrm{in}, r_\mathrm{out}$), critical point temperatures ($T(r_\mathrm{in}), T(r_\mathrm{out})$), and topology types for the accretion solutions presented in Fig. 5.2.

M_H	a_0	r_in	r_out	$T(r_\mathrm{in})$ ($\times 10^{10}$ K)	$T(r_\mathrm{out})$ ($\times 10^{10}$ K)	Type
0 (Sch)	—	—	85.0892	—	0.2048	O
1	500	—	47.2185	—	0.3564	O
5	500	7.3900	—	1.7726	—	I
10	500	6.5138	—	2.1628	—	I
50	500	4.8793	—	4.6142	—	I
10	10^5	—	81.6338	—	0.2129	O
10	10^4	—	58.5248	—	0.2906	O
10	10^3	7.3628	—	1.7794	—	I
10	10^2	4.9843	—	4.4446	—	I

(i.e., $v << 1$) at the outer region of the disc. As the flow moves towards the black hole, v increases and eventually exceeds the local sound speed C_s after passing through the critical point r_c. Subsequently, the flow becomes supersonic and continues to move towards the horizon. Finally, at r_H, v approaches the light speed c, satisfying the inner boundary condition of the transonic accretion model. In Figs. 5.2e-f, we present the profiles of the electron temperature T_e for the accretion solutions shown in Figs. 5.2a-b. In all cases, T_e increases as we move towards r_H from r_edge. We observe that the temperature distribution of the disc rises as r_c drifts toward the horizon. Also, the solutions associated with r_in exhibit relatively higher T_e profiles compared to the solutions that pass through r_out. The profiles of the disc's aspect ratio (H/r) corresponding to the accretion solutions in panels (a)-(b) are shown in panels (g)-(h), respectively. It is observed that the disc remains geometrically thin ($H/r << 1$) near the inner edge. However, as we move away from the horizon, the flow becomes quasi-spherical ($H/r \sim 1$), and towards the outer edge, the disc becomes geometrically thick with $H/r > 1$. This occurs because, near r_edge, thermal pressure pushes the flow in the vertical direction due to the weaker gravitational force [89, 90]. Additionally, as M_H increases at a given a_0 or a_0 decreases at a given M_H, H/r increases. This is naturally expected because an increase in M_H or a decrease in a_0 raises the flow temperature, which ultimately results in an enhancement of H/r. In Table 5.1, we summarize the properties of the critical points related to the accretion solutions presented in Figs. 5.2a-b. This table highlights the changing behaviors of the accretion solutions and illustrates the potential shifting of the critical points as the halo compactness increases, specifically in terms of increasing M_H and decreasing a_0.

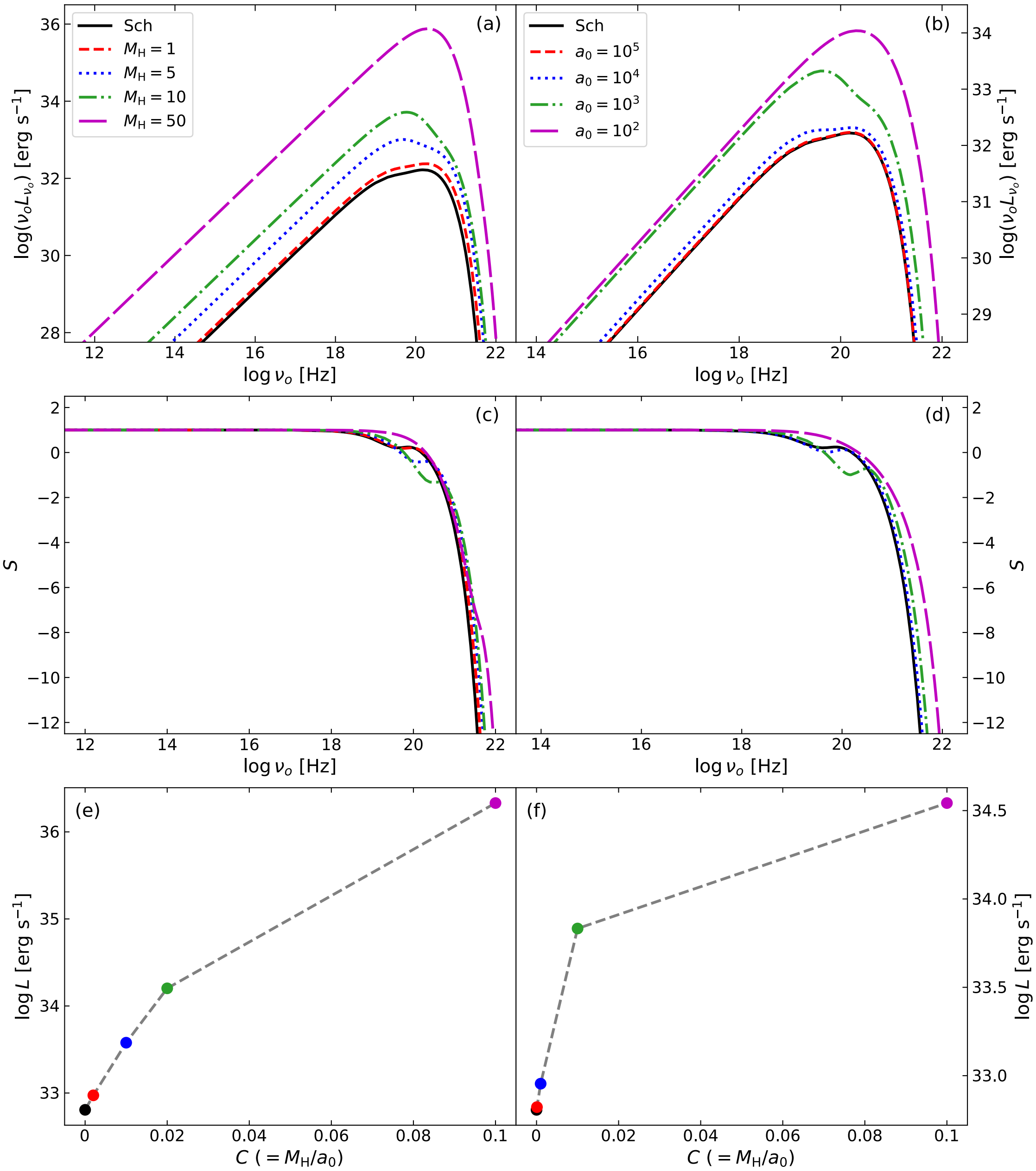

Figure 5.3: Panels (a) and (b) represent the spectral energy distribution (i.e., $\nu_o L_{\nu_o}$ versus ν_o curves) of the emitted radiation from the accretion disc for the accretion solutions shown in Fig. 5.2a and Fig. 5.2b, respectively. The slopes (S) of the SED are presented in panels (c) and (d). The effect of halo compactness (C) on the bolometric disc luminosity (L) is depicted in panels (e) and (f). The filled circles represent the L values corresponding to accretion solutions of Figs. 5.2a-b. Here, the input parameters are chosen as $r_{\rm edge} = 1000$, $\lambda = 2.75$, $E = 1.0025$, $M_{\rm BH} = 10^6 M_\odot$, and $\dot{M} = 10^{-5}\dot{M}_{\rm Edd}$. See the text for details.

Next, we investigate the spectral properties of the accretion disc and examine how they are affected by the compactness of the dark matter halo. In this work, we consider a supermassive black hole with $M_{\rm BH} = 10^6 M_\odot$, where $M_\odot$ is the Solar mass. The mass accretion rate is taken to be very small as $\dot{M} = 10^{-5}\dot{M}_{\rm Edd}$, where $\dot{M}_{\rm Edd} = 1.39\times 10^{18} M_{\rm BH}/M_\odot$ gm s^{-1} is the Eddington mass accretion rate. We calculate the spectral energy distribution (SED) associated with the accretion solutions of Figs. 5.2a-b using Eq. (5.29). The obtained results are shown in the respective panels (a) and (b) of Fig. 5.3, where the variation of the quantity $\nu_o L_{\nu_o}$ as a function of the observed frequency ν_o is depicted. In all cases, the emitted radiation maximizes power at $\nu_o \approx 10^{20}$ Hz. Also, the spectra exhibit a sharp cut-off around $\nu_o \approx 10^{22}$ Hz ($= k_{\rm B} T_{e0}/h$), which corresponds to the disc inner edge electron temperature $T_{e0} \approx 10^{11}$K. We find that the SEDs for the Schwarzschild BH are lower than those for the Cardoso BH. This is because electron temperature across the entire disc in the Schwarzschild model is lower compared to the Cardoso model (see Figs. 5.2e-f). Moreover, we observe that the SED increases with the rise in $M_{\rm H}$ or decrease in a_0, which is due to the corresponding increase in T_e, as shown in Figs. 5.2e-f. As the shape of the spectrum begins to differ with varying $M_{\rm H}$ and a_0, we explore the slopes of the luminosity spectrum to analyze these variations more quantitatively. For a log-log plot between $\nu_o L_{\nu_o}$ and ν_o, SED slope (S) is calculated as,

$$S = \frac{d\left[\log(\nu_o L_{\nu_o})\right]}{d\left[\log(\nu_o)\right]}. \tag{5.31}$$

Using Eq. (5.31), we calculate the slope associated with the SEDs shown in Figs. 5.3a-b, and the obtained results are presented in Figs. 5.3c-d, respectively. It is observed that the SED slopes are nearly identical in the low to moderate frequency ranges. However, at high frequencies, they noticeably differ from each other. Additionally, from Figs. 5.3c-d, it is clearly seen that for the Schwarzschild BH and the Cardoso BH with low halo compactness, the SED slopes exhibit two plateau regions across the entire frequency range. In contrast, the SEDs for the Cardoso BH model with high compactness factors show only one plateau region. These spectral characteristics may provide valuable insights into the astrophysical observations for distinguishing a Schwarzschild BH from the Cardoso BH model. Note that the above findings are consistent with the work in [379], where the authors studied the spectral properties of accretion flows by treating the disc as a perfect black body emitter. In that study, the hydrodynamics of the flow were governed by the geodesic equation of the particles, with the flow reaching up to the innermost stable circular orbit. Furthermore, the flow velocity never surpasses the local sound speed, implying that the transonic accretion model was not considered. Thereafter,

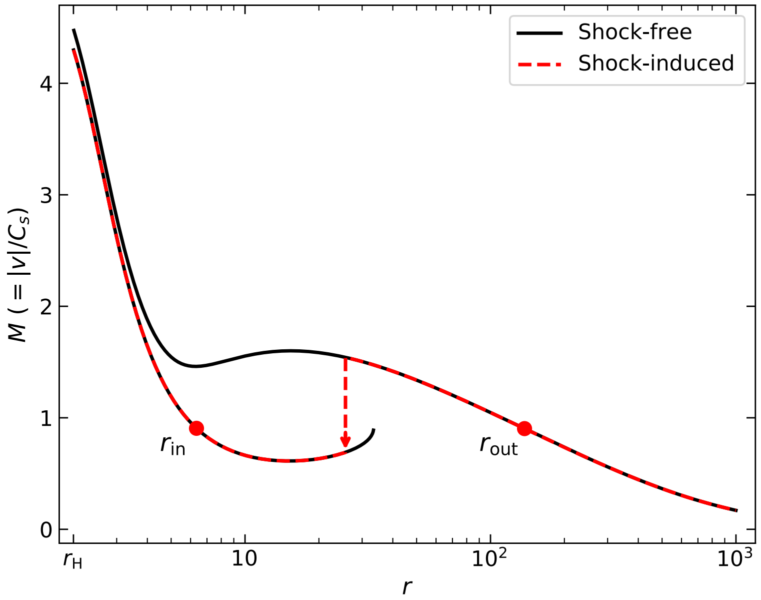

Figure 5.4: Accretion solutions for the shock-free and shock-induced scenarios. The vertical line indicates the shock location ($r_{\rm sh}$) and the arrow represents the overall direction of the flow. In this figure, we choose $\lambda = 3$, $E = 1.0005$, $M = 10$, and $a_0 = 10^4$. See the text for details.

we calculate the bolometric luminosity (L) of the accretion disc using Eq. (5.30) for the accretion solutions of Figs. 5.2a-b. The obtained results are depicted in panels (e) and (f) of Fig. 5.3, where the variation of L as a function of compactness parameter (C) is shown. Here, the filled circles, using the same color codes as in Figs. 5.2a-b, joined by the dashed (gray) lines, denote the results for the respective accretion solutions. In both panels, we notice that L increases with C. As the increase in $M_{\rm H}$ or decrease in a_0 enhances the SED (see Figs. 5.3a-b), it is therefore expected that L (the area under the SED curve) will also increases with halo compactness. Such an increase in L can also be directly followed from Eq. (5.30). As C increases, T_e rises (see Fig. 5.2e-f), which in turn increases L, since it varies as $T_e^{1/2}$.

5.4.2 Accretion with shocks

We previously mentioned that the flow can accommodate multiple critical points, depending on the input parameters. In this section, we illustrate such scenarios and analyze their characteristics in terms of shocks. Fig. 5.4 shows a typical solution topology with multiple critical points (solid black lines) for the set of global constants

$(\lambda, E, M_{\rm H}, a_0) = (3, 1.0005, 10, 10^4)$. The critical points are located at $r_{\rm in} = 6.3427$ and $r_{\rm out} = 137.617$. It is observed that the solution passing through $r_{\rm out}$ is a global solution, while the solution passing through $r_{\rm in}$ is truncated at a radius $r_t = 33.3527$, referred to as a closed solution. Since closed solutions are not extended from $r_{\rm H}$ to $r_{\rm edge}$, they are not considered physically acceptable. Using Eq. (5.22), the entropy accretion rates ($\dot{\mathscr{M}}$) for the inner and outer branches are calculated to be 4.2764×10^7 and 3.3173×10^7, respectively. Since the inner solution has a higher entropy content than the outer solution, the flow prefers to jump into the inner closed branch in the form of shocks, provided the relativistic shock conditions are satisfied. We calculate the shock location ($r_{\rm sh}$) using the Rankine-Hugoniot standing shock conditions as [254],

$$\left[\rho u^r\right] = 0, \tag{5.32}$$

$$\left[(e+p)u^r u^t\right] = 0, \tag{5.33}$$

$$\left[(e+p)u^r u^r + p g^{rr}\right] = 0, \tag{5.34}$$

where the square brackets denote the difference of the quantities across $r_{\rm sh}$. Eqs. (5.32), (5.33), and (5.34) correspond to the conservation of mass flux, energy flux, and radial momentum flux across $r_{\rm sh}$, respectively. The dashed (red) curve in Fig. 5.4 illustrates a shock-induced accretion solution, with a noticeable sharp jump at $r_{\rm sh} = 25.6527$. Note that the shock solutions can pass through both $r_{\rm in}$ and $r_{\rm out}$ simultaneously.

We now explore various shock properties (e.g., shock radius, density compression, and temperature compression, etc.) in the presence of a dark matter halo and compare them with those for a Schwarzschild BH. In panels (a) and (b) of Fig. 5.5, we present the shock solutions for different values of halo mass $M_{\rm H}$ with a fixed length scale $a_0 = 10^4$, and for various values of a_0 with $M_{\rm H} = 1$. In this case, a given set of flow parameters is chosen as $(\lambda, E) = (3, 1.00125)$. Here, the solid (black) curves represent the result for the Scwarzschild BH. The dashed (red), dotted (blue), and dash-dotted (green) lines correspond to the Cardoso BH with $M_{\rm H} = 3$, 6, and 9, respectively. Similar color codes are used for $a_0 = 10^4$, 5×10^3, and 10^3, respectively. Using the shock conditions (5.32), (5.33), and (5.34), we obtain the shock locations at $r_{\rm sh} = 21.5735$, 27.4824, 34.5320, and 44.1920 for $M_{\rm H} = 0$, 3, 6, and 9, respectively. On the other hand, for $a_0 = 10^4$, 5×10^3, and 10^3, the calculated shock locations are $r_{\rm sh} = 23.4964$, 25.4094, and 45.6867, respectively. The critical points and shock locations associated with these solutions are summarized in Table 5.2. It is observed that the shock locations for the Schwarzschild BH are located closer to the horizon compared to those for the Cardoso BH. Furthermore, as the compactness of the halo increases, the shock fronts move away from the central

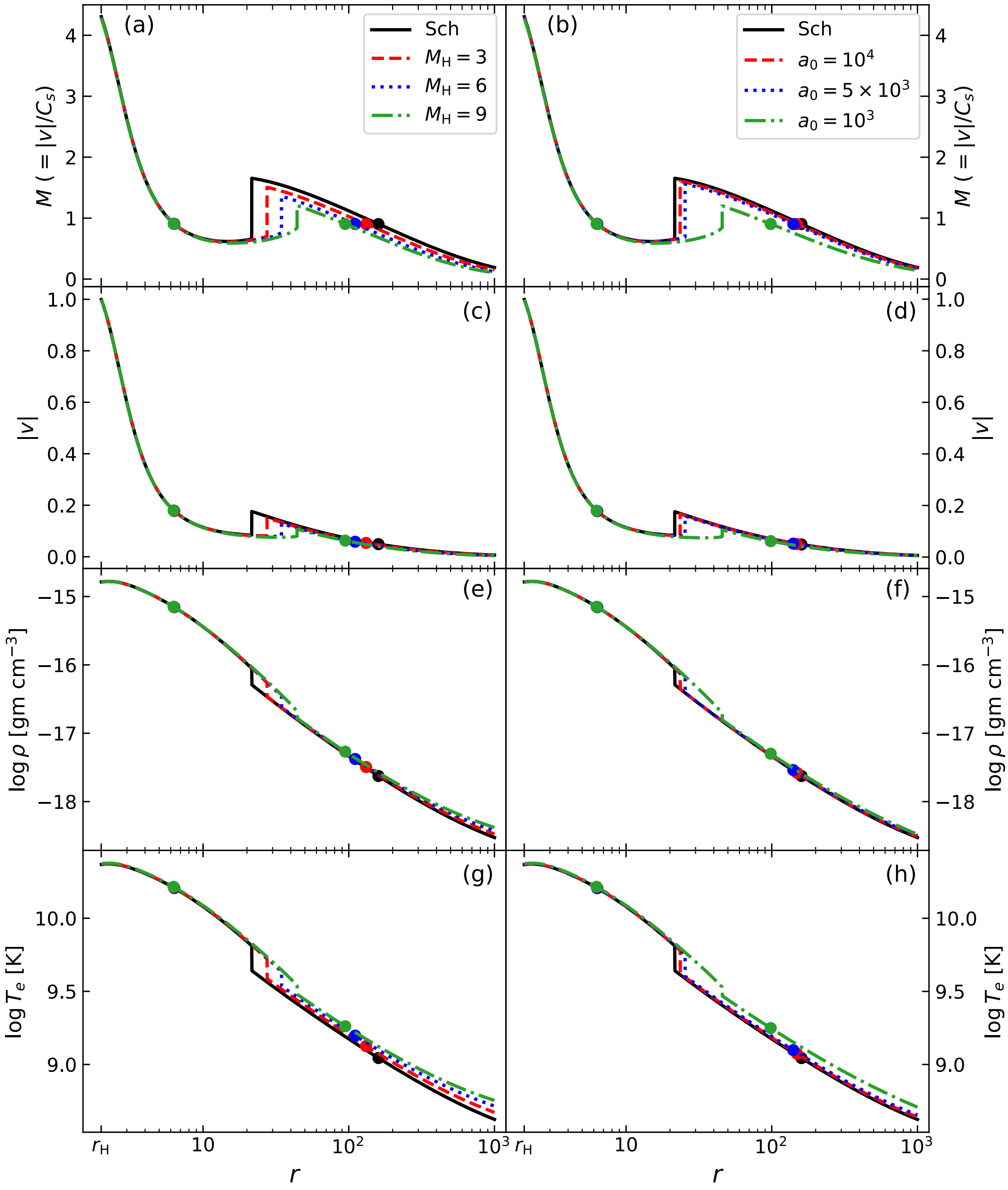

Figure 5.5: Shock solutions for halo masses $M_{\rm H} = 3$, 6, and 9 with length scale $a_0 = 10^4$ (panel (a)), and for $a_0 = 10^4$, 5×10^3, and 10^3 with $M_{\rm H} = 1$ (panel (b)). The corresponding radial velocity (v), mass density (ρ), and electron temperature (T_e) profiles associated with these shock solutions are presented in panels (c)-(d), (e)-(f), and (g)-(h), respectively. In each panel, the shock locations are marked by vertical lines. In this figure, we set $\lambda = 3$, $E = 1.00125$, $M_{\rm BH} = 10^6 M_\odot$, and $\dot{M} = 10^{-5} \dot{M}_{\rm Edd}$. See the text for details.

Table 5.2: Dark matter halo mass ($M_{\rm H}$), halo length scale (a_0), critical point locations ($r_{\rm in}, r_{\rm out}$), and shock location ($r_{\rm sh}$) for the shock solutions presented in Fig. 5.5.

$M_{\rm H}$	a_0	$r_{\rm in}$	$r_{\rm out}$	$r_{\rm sh}$
0 (Sch)	—	6.3435	159.9156	21.5735
3	10^4	6.3224	131.5024	27.4824
6	10^4	6.3020	110.6456	34.5320
9	10^4	6.2821	94.6018	44.1920
1	10^4	6.3364	149.3566	23.4964
1	5×10^3	6.3294	140.5021	25.4094
1	10^3	6.2767	98.3629	45.6867

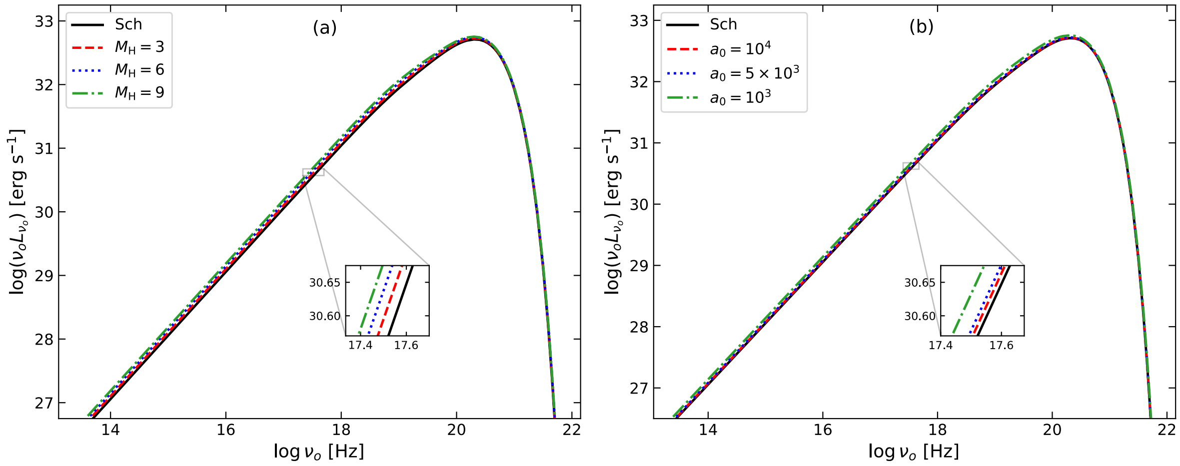

Figure 5.6: Spectral energy distributions of the accretion disc for shock-induced flow solutions presented in Figs. 5.5a-b. In this figure, we choose the the set of the input parameters as $r_{\rm edge} = 1000$, $\lambda = 3$, $E = 1.00125$, $M = 10^6 M_\odot$, and $\dot{M} = 10^{-5} \dot{M}_{\rm Edd}$. See the text for details.

object. For these shock solutions, the profiles of radial velocity (v), mass density (ρ), and electron temperature (T_e) are presented in Figs. 5.5c-d, 5.5e-f, and 5.5g-h, respectively. It is observed that the analyzed flow variables undergo significant changes across the shock fronts. This occurs because, according to the shock condition (5.32), as v decreases at $r_{\rm sh}$, ρ increases. Also, due to the drop in v, kinetic energy of the flow is converted into thermal energy, resulting in an increase in T_e at $r_{\rm sh}$. Moreover, we observe that the change in v at $r_{\rm sh}$ diminishes as the shock originates at larger radii, decreasing the difference of ρ and T_e across the shock fronts. We wish to mention that $r_{\rm sh}$ determines the size of the PSC, where a swarm of hot electrons can produce high energy radiation through inverse Compton scattering. Such emissions are commonly observed in AGNs and black hole X-ray binaries (BH-XRBs) [28, 49, 389].

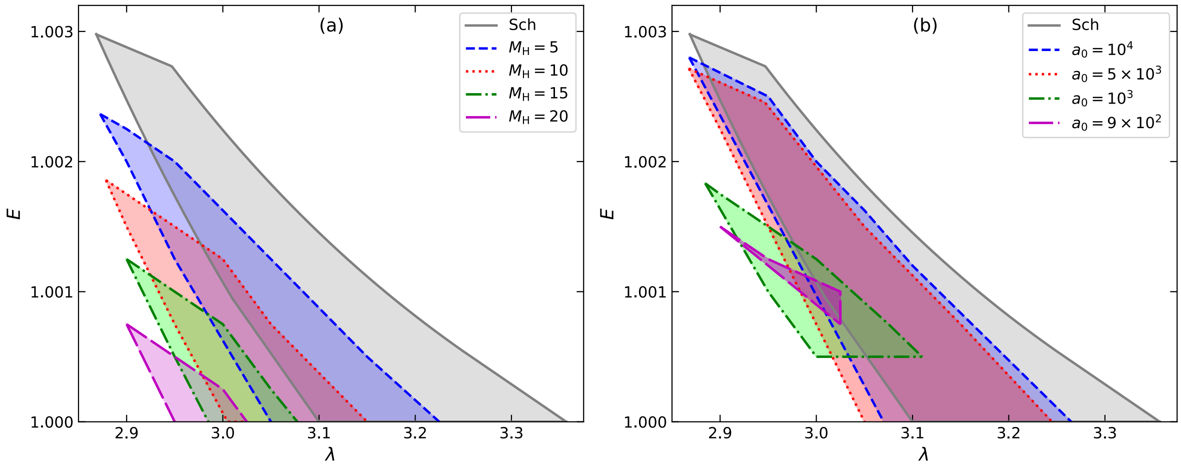

Figure 5.7: Modification of the shock parameter space in specific angular momentum (λ) and energy (E) plane for the halo masses $M_{\rm H} = 5$, 10, 15, and 20 with $a_0 = 10^4$ (panel (a)), and for $a_0 = 10^4$, 5×10^3, 10^3, and 900 with $M_{\rm H} = 1$ (panel (b)). In each panel, the effective region within the gray (solid) line corresponds to the Schwarzschild BH without a dark matter halo (i.e., $M_{\rm H} = 0$). See the text for details.

In this section, we also explore the luminosity spectrum of the accretion disc in the presence of shocks. For the shock-induced accretion solutions presented in Fig. 5.5a-b, we calculate their SEDs using Eq. (5.29). The results are shown in Fig. 5.6, where panel (a) and panel (b) correspond to the shock solutions in Figs. 5.5a-b, respectively. Similar to the Fig. 5.3, the radiation power maximizes at around $\nu_o \approx 10^{20}$ Hz and cuts off at $\nu_o \approx 10^{22}$ Hz. We see that for the shock scenario, the SEDs for the Schwarzschild BH case are negligibly higher than those for the Cardoso BH. Additionally, for the latter model, increasing $M_{\rm H}$ or decreasing a_0 leads to a barely increase in the SEDs. The reason behind these observations is the negligible variations in the disc temperature profiles when the compactness of the dark matter halo is changed (see Figs. 5.5g-h). Moreover, the spectrum shape and the area under the SED (which effectively gives the bolometric luminosity L, see Eq. (5.30)) do not change significantly with variations in $M_{\rm H}$ and a_0.

5.4.3 Shock parameter space

Here, we identify the effective region of the specific angular momentum (λ) and energy (E) that admits shock solutions for the Cardoso BH and compare it with that of the Schwarzschild BH. In Fig. 5.7a, we present the shock parameter space in the $\lambda - E$ plane for different values of halo mass $M_{\rm H} = 5$, 10, 15, and 20 with a fixed halo length scale of $a_0 = 10^4$. The regions bounded by the dashed (blue), dotted (red), dash-dotted (green), and long-dashed (magenta) curves represent the results for $M_{\rm H} = 5$, 10, 15, and 20, respectively. The parameter space enclosed by the solid (gray) line corresponds to the Schwarzschild BH model. We observe that for the Schwarzschild BH, flow exhibits shocks at relatively higher λ and E values compared to the Cardoso BH. Also, the area under the shock parameter space is larger for the Schwarzschild BH than for the Cardoso BH. As $M_{\rm H}$ increases, the parameter space shifts toward lower λ and E domains, and the parameter space gradually shrinks as well. Similarly, in Fig. 5.7b, we present the modification of the shock parameter space in the $\lambda - E$ plane for varying a_0 with a fixed $M_{\rm H} = 1$. The dashed (blue), dotted (red), dash-dotted (green), and long-dashed (magenta) curves correspond to $a_0 = 10^4$, 5×10^3, 10^3, and 900, respectively. The shock parameter space for the Schwarzschild BH is bounded by the solid (gray) line. As in Fig. 5.7a, we find that the shock parameter space for the Schwarzschild BH without dark matter halo can accommodate higher λ and E values than in the presence of a halo. Additionally, the area under the parameter space decreases slightly when a_0 decreases from 10^4 to 5×10^3. However, the parameter space shrinks significantly when a_0 decreases further to smaller values, such as 10^3 and 900.

5.5 Chapter Summary and Conclusions

In this chapter, we explore the transonic accretion flow around a galactic black hole with a dark matter halo, as proposed in Ref. [176]. The flow hydrodynamics in the accretion disc are modeled within fully general relativistic framework. Using the relativistic equation of state, we numerically solve the radial momentum and energy equations. Consequently, we obtain the global accretion solutions in both the presence and absence of shocks. As the halo compactness primarily influences the dynamics of the accretion flow through the effective potential ($\Phi^{\rm eff}$) of the system, the main objective of this work is to explore the effect of halo mass ($M_{\rm H}$) and length scale (a_0) on the physical properties of the accretion disc. We make an effort to compare these results with those for the usual Schwarzschild BH without a dark matter halo. We summarize our findings point-wise below.

- We find O-type and I-type accretion solutions, where the flow possesses single critical points either far from the horizon (O-type) or near the horizon (I-type). We observe that for the Schwarzschild BH and the Cardoso BH with small halo compactness, the solution topology remains O-type. However, at higher $M_{\rm H}$ and lower a_0 values, the solution topology changes to I-type.

- We also obtain A-type multiple critical point solutions and observe that such solutions can admit standing shock transitions when the flow satisfies the relativistic shock conditions. It is noticed that the shock solutions are not unique but rather exist within a broad range of the parameter space spanned by the flow specific angular momentum (λ) and energy (E). Accordingly, we examine the modification of the shock parameter space as a function of $M_{\rm H}$ and a_0. We observe that the shock parameter space is larger for the Schwarzschild BH compared to the Cardoso BH. However, a small increase in the halo compactness significantly shrinks the shock parameter space. We notice that the shock solutions exist in an extremely small $\lambda - E$ parameter space for $C \gtrsim 0.001$.

- Furthermore, we examine the effect of $M_{\rm H}$ and a_0 on various shock properties, particularly the shock location ($r_{\rm sh}$), as well as the changes in mass density (ρ) and electron temperature (T_e) across the standing shocks. We find that the shock fronts settle down at smaller radii for the Schwarzschild BH than the Cardoso BH. Moreover, as $M_{\rm H}$ increases or a_0 decreases, $r_{\rm sh}$ moves away from the horizon, leading to a decrease in the changes of ρ and T_e across $r_{\rm sh}$.

- In addition, we calculate the spectral energy distribution (SED) for both the shock-free and shock-induced accretion solutions using the relativistic thermal bremsstrahlung emission coefficient. In the shock-free scenario, SEDs significantly increase with the rise in $M_{\rm H}$ or decrease in a_0. This outcome agrees with existing work in the literature based on a different accretion model [379]. While investigating the SED's slope (S), we observe that S possesses two plateau regions across entire frequency domain for both Schwarzschild BH and Cardoso BH with small halo compactness. As the compactness parameters increase to moderate values, the profile of S starts differing noticeably at high-frequency domains. For very high halo compactness, only one plateau region remains in the low to moderate frequency range. As the halo compactness potentially increases the SED, the bolometric disc luminosity (L) also substantially increases. On the other hand, for shock solutions, SEDs barely change with $M_{\rm H}$ and a_0, resulting in insignificant variations in both S and L with the compactness parameter. Therefore, alongside the quantitative variabilities, the change in the spectrum shape provides a clear distinction between the Cardoso BH and Schwarzschild BH models.

In conclusion, the present study suggests that in the presence of a dark matter halo with low compactness ($C \lesssim 10^{-4}$), i.e., when dark matter is distributed far from the black hole, the results are almost indistinguishable from those for isolated Schwarzschild black holes. This identification is similar to the observations in [390] regarding the geodesic motion of the orbiting particles. However, when dark matter is concentrated close to the black hole (i.e., at higher C values), the profiles of thermodynamic variables (e.g., temperature, density, etc.) associated with the accretion solutions change significantly with the halo parameters ($M_{\rm H}, a_0$), particularly in cases where the flow does not exhibit shock waves. As a result, in shock-free cases, the spectral properties, such as the SED, its slope S, and the bolometric disc luminosity L are largely altered by the halo compactness. In contrast, for shock-induced solutions even in the high-compactness regime, the temperature and density profiles exhibit only minimal variations with halo compactness, resulting in negligible changes in the SEDs, S, and L compared to those of Schwarzschild BHs. But, the shock radius, $r_{\rm sh}$, forms at larger distances compared to those around Schwarzschild BHs when the halo compactness is high. This modulation in $r_{\rm sh}$ significantly affects various shock properties, such as density and temperature compression across $r_{\rm sh}$. We want to mention that the oscillation of shock fronts can give rise to QPOs in the power density spectra of AGNs and BH-XRBs, with the QPO frequency ($\nu_{\rm QPO}$) is inversely proportional to $r_{\rm sh}$ [118, 184, 330]. Therefore, a significant increase in $r_{\rm sh}$ is expected to potentially decrease in $\nu_{\rm QPO}$. Nevertheless, the study of QPOs is out of the scope of this chapter. Meanwhile, Stuchlík & Vrba [385] performed a phenomenological analysis of observed QPO frequencies using the same Cardoso black hole model employed in this chapter. Essentially, they estimated the possible halo mass ($M_{\rm H}$) and its characteristic length scale (a_0) for several supermassive black holes. This study strongly suggests that the observed QPOs can provide valuable insights into the presence of a surrounding dark matter halo. Furthermore, the analysis by Pugliese & Stuchlík [178] identified several other observational features in accretion physics that arise in the presence of dark matter halos. They demonstrated that dark matter halos can modify the spacetime geometry in such a way that a single accretion torus may split into a double-torus configuration or develop interdisc cusps – phenomena typically associated with exotic spacetimes such as superspinars or naked singularities. These complex structures could manifest observationally through multiple components in emission lines or in SEDs. Moreover, the presence of dark matter halos has been shown to increase the mass accretion rate onto the central black hole, which in turn can lead to a bolometric luminosity higher than what would be expected in the absence of dark matter halo. Also, an increased accretion rate can enhance jet power or lead to the formation of jet-like (protojet) structures. Taken together, different studies in the literature suggest that while QPOs remain highly sensitive tracers, other signatures, including topological changes in the accretion torus, higher than expected luminosity, and multi-component line emissions or SEDs may offer complementary and independent methods to detect or constrain the presence of dark matter halos around the galactic black holes.

Indian Institute of Technology Guwahati

CHAPTER 6

THESIS CONCLUSIONS AND FUTURE SCOPES

6.1 Conclusions

In recent years, compelling evidence has shown that black holes, as predicted by Einstein's GR, are perfectly compatible with both GW [152] and EM observations [153, 391]. However, due to the uncertainties accompanying these observations, several non-Kerr black hole metrics in alternative gravity theories perfectly fit those data [130, 392–394]. Not only that, a few other non-Kerr metrics that are not solutions to the particular gravity theories, formed by parametrically deviating the Kerr metric coefficients using at least one deformation parameter (bottom-up metrics), are also consistent with those observations [166, 167, 169, 173, 174]. Therefore, it is questionable whether such alternative metrics are really required. Also, the characterization of those non-Kerr metrics is yet to be known completely. In this thesis, we have tried to answer these questions by studying the relativistic accretion flow in some bottom-up metrics (e.g., JP, KZ metrics). Moreover, in the non-Kerr regime, we have attempted to isolate the presence or absence of a dark matter halo around galactic black holes by exploring its effect on accretion dynamics. The chapter wise findings of the thesis are the followings.

In Chapter 2, we begin with the relativistic accretion flow in a generic stationary and axisymmetric spacetime, then apply this model to the JP spacetime [161], which can encompass both black hole and naked singularity objects depending on (a_k, ϵ). We examine the influence of the JP deformation parameter ϵ on the inviscid accreting system. By solving the radial momentum equations with the help of the REoS with variable

TH-3714_206121049

adiabatic index Γ, we obtain the accretion solutions for different topologies, such as O, A, W, and I-types, for both the BH and NkS objects. These solutions either contain a single critical point (in the case of O and I-type solutions) or multiple critical points (in the case of A and W-type solutions). We observe that the flow topology is initially O-type for low ϵ. As ϵ increases, the topology transitions through A and W-type behaviors, and eventually, I-type solutions are obtained for very large values of ϵ (≤ 19 [222]). We further observe that the A-type topology can support a shock transition, as the solution passing through the inner critical point $r_{\rm in}$ has a higher entropy content compared to the solution passing through the outer critical point $r_{\rm out}$. We then determine the shock parameter space in the angular momentum λ and energy E plane, and analyze how it is modified by ϵ. We observe that, for a given a_k, the area under the shock parameter space increases with ϵ, implying that shock transitions are more likely to occur in the deformed Kerr spacetime compared to the usual Kerr BH. Most importantly, we notice shock solutions for spherical accretion flow (i.e., $\lambda = 0$) at high ϵ. Additionally, we observe that various shock properties, such as the compression ratio and shock strength, decrease with ϵ due to the increase in the shock radius $r_{\rm sh}$. For NkS objects, the accretion solutions are found to rotate around a naked surface near the singularity, a behavior not observed for BHs. By analyzing the differences in the accretion solution's behavior, we determine the maximum value of the deformation parameter $\epsilon^{\rm max}$ as a function of a_k, which separates the BH and NkS objects for the JP spacetime.

We have seen in Chapter 2 that the JP deformation can significantly change the accretion features. Our next goal is to examine the influence of the deformation parameter ϵ on the spectral properties of the accretion disc. With this in mind, in Chapter 3, we address this aspect by considering the thermal bremsstrahlung emission process [310]. Here, we consider the relativistic model for the thermal bremsstrahlung emission coefficient [64] because, for HAF [11], electron-electron emission significantly surpasses electron-ion emission near the black hole horizon. In the GR framework, we find the accretion solutions of all types (O, A, W, and I) and their associated parameter space in the $\lambda - E$ plane for BH and NkS models. We calculate the total disc luminosity L across the entire identified parameter spaces for these two models, where in both cases, we observe that I-type solutions produce higher disc luminosity than the other flow solution topologies. Also, we find that for a given λ, L increases with E. Similarly, for a given E, L increases with λ. Moreover, we calculate the disc's SED for the different solution topologies and examine their modification with the flow parameters (λ, E). In the case of BH model, for low energy values, SEDs for O and A-type solutions are found to differ significantly from those for the W and I-type solutions over the entire analyzed frequency range. However, for the NkS model, SEDs for O and A-type solutions are nearly identical to those for the W and I-type solutions for all energy values. We also study the effect of ε on the SEDs associated with a given solution topology for different a_k values, observing that the SED increases with ε. For lower a_k values, this difference is noticeable, but as a_k increases, the difference becomes very small. Furthermore, we explore a comparison between the SEDs for the BH and NkS models at fixed (λ, E) but varying (a_k, ε). Our study shows that the SEDs for the NkS model are higher than those for the BH model, and this difference becomes negligible at the maximal spin value.

Chapter 4 investigates the general relativistic accretion flow in the KZ spacetime [166], which is another non-Kerr metric characterized by a single deformation parameter η_0, in addition to parameters $(M_{\rm BH}, a_k)$. We consider the viscous hydrodynamics with Navier-Stokes prescription [88, 233]. We further neglect the viscous acceleration to reduce the flow equations to first-order differential equations [118]. Under this set up, we numerically solve the flow equations to determine the accretion solutions. We obtain five types of accretion solutions: O, A, A$'$, W, and I. Also, their associated parameter spaces in the angular momentum $\mathscr{L}$ and energy E plane are found. We observe that for the A$'$ solution topology, both solutions passing through $r_{\rm in}$ and $r_{\rm out}$ are global solutions. This degeneracy is resolved by calculating the entropy content for both solutions, where we find that the $r_{\rm in}$ solution has more entropy than the $r_{\rm out}$ solution. Therefore, the inner solution is thermodynamically more favorable than the outer one. We also observe that A-type solutions can exhibit shock waves, provided the shock conditions are satisfied. We examine the impact of η_0 on the shock properties and find that as η_0 increases, the shock radius moves closer to the horizon, thereby increasing the density and temperature compression across the shock fronts. Moreover, from the spectral analysis, we observe that the SEDs for shock solutions are higher than those for shock-free solutions. Additionally, for both shock-induced and shock-free cases, we notice that the SEDs decrease as η_0 increases. We also show that the QPO frequency increases, while the bolometric disc luminosity decreases as η_0 increases. Furthermore, we perform a phenomenological study on the HFQPOs for some black hole binaries and black hole candidates. Towards this, we identify the parameter spaces in the $\mathscr{L} - \eta_0$ plane for a given E associated with HFQPOs observed in XTE J1550–564 [31, 333] and H 1743 – 322 [335, 336]. From this analysis, we demonstrate the consistency of the KZ metric with the observed QPOs in the X-ray spectra of accretion disc. Upon comparing the results for the JP and KZ black holes, we find that the deformation parameters in these two spacetimes behave oppositely, which help to characterize the distinct types of deformations they exhibit.

In Chapter 5, we analyze the relativistic, inviscid accretion flow around galactic black holes with dark matter halos. We adopt the Cardoso model [176], where a non-rotating SMBH is minimally coupled to an anisotropic dark matter fluid with tangential pressure only, and a Hernquist density profile. We solve the hydrodynamical equations governing the accretion disc and obtain global accretion solutions, both with and without shocks. We observe that the flow solutions are O-type for a given combination of (λ, E) for both the Schwarzschild BH and Cardoso BH, when $M_{\rm H}$ is small or a_0 is large. As the compactness parameter C $(= M_{\rm H}/a_0)$ slightly increases, the solutions remain O-type, but the critical points shift closer to the horizon. However, for large values of C, the solution topology changes to I-type. When investigating the shock solutions in the A-type topology, we observe that the shock for both the Cardoso BH with small C and the Schwarzschild BH forms at a smaller radius. As C increases, $r_{\rm sh}$ moves away from the horizon, resulting in a decrease in both density and temperature compression. We also notice that for small C, the shock parameter space spanned by λ and E is large and comparable to that of the Schwarzschild BH. However, for $C \geq 0.001$, the shock parameter space is drastically reduced to a very narrow region. We also study the SEDs by considering thermal bremsstrahlung emission for both shock and shock-free scenarios. We observe that the SEDs increase significantly with C, which in turn increases the bolometric disc luminosity L. Moreover, we find that the SED slope S exhibits two plateau regions for both the Schwarzschild BH and Cardoso BH with small C. However, for high values of C, S shows only one plateau region. For the shock-induced case, the SED increases insignificantly with C, and consequently, L and S do not vary much. Overall, this study suggests that for both the Cardoso BH and Schwarzschild BH, the results are nearly identical for small compactness ($C \leq 10^{-4}$, from galaxy observations [349]). However, for high compactness, the results differ significantly from the Schwarzschild BH. Therefore, based on the accretion dynamics around SMBHs, it would be challenging to detect dark matters if they are distributed far from the black hole or have a very low dark halo mass. Nevertheless, we anticipate that our findings could serve as a valuable tool for detecting the existence of dark matter halos around galactic BHs specifically when they concentrate near to the galactic center.

In this thesis, a significant effort has been made to uncover the accretion behavior of a diverse class of non-Kerr black holes. We relate the identified results to those for Kerr BHs, illuminating some of the gray areas regarding non-Kerr BHs through accretion phenomena. Also, as our analysis is based on the complete relativistic framework rather than a pseudo-Newtonian approach, the results presented here will have a substantial impact on the field of accretion physics. In the following sections, we highlight areas where further exploration could enhance the understanding of this subject.

6.2 Scope for future works

6.2.1 Exploring general relativistic magnetohydrodynamics (GRMHD) accretion flows in non-Kerr spacetimes

We do not include magnetic fields in the model equations. However, strong magnetic fields thread through the accretion disc, which may originate from either a low-mass companion star or the interstellar medium. Recently, EHT collaborations [153] have revealed large-scale magnetic fields surrounding SMBHs, suggesting they may influence accretion and ejection mechanisms. In this regard, significant efforts have been made to understand the nature and structure of the magnetic fields for the accretion flow around Kerr black holes [124, 125, 395]. But, such magnetic field structures have yet to be understood for non-Kerr black holes (e.g., CS, EDGB, JP, KZ black holes). Hence, we plan to formulate a GRMHD accretion flow model for these black holes and investigate how deformations affect the magnetic field structures and their associated spectral properties.

6.2.2 Understanding the role of radiative cooling in accretion dynamics around non-Kerr black holes

In our research works, various radiative cooling mechanisms, such as bremsstrahlung, synchrotron, and Comptonization, have been neglected in the energy equations. However, in reality, all these cooling mechanisms play a vital role in stabilizing the accretion disc. Recently, some studies [123, 315] have explored the effects of cooling mechanisms on accretion solution topologies and their corresponding luminosity spectra for Schwarzschild and Kerr black holes. Indeed, these studies have shown that cooling processes have a strong effect on the accretion features, particularly for BH-XRBs. Therefore, we believe that investigating disc spectra by incorporating all relevant cooling mechanisms around different non-Kerr black holes could lead to a better understanding of the alternative gravity theories. In particular, we may be able to constrain the deformation parameters through a phenomenological analysis of the modeled spectra [167].

6.2.3 Estimation of outflow rates from accretion discs around non-Kerr black holes

The signatures of jets or outflows are commonly observed in accreting black hole systems, such as AGNs and microquasars. It is widely accepted that the powering of bipolar jets from the accretion disc is due to the presence of large-scale magnetic fields. However, several studies based on numerical simulations have shown that even in the absence of magnetic fields, the additional thermal gradient force in the PSC can still power bipolar jets [37, 103, 241, 396]. The estimation of bipolar jets is typically done through mass outflow rates. It has been found that the mass outflow rate can vary with the spin parameter of the Kerr BH due to changes in the PSC size. As demonstrated in this thesis, the PSC size can be modulated by parametric deformations to the Kerr metric. Therefore, future research should focus on studying the effects of deformation parameters on mass outflow rates in non-Kerr spacetimes.

6.2.4 Effect of dark matter halo on magnetic fields in accretion disc around a galactic black hole

As we saw in Chapter 5, the presence of a dark matter halo around SMBH with high compactness strongly deviates various accretion features. Therefore, we can expect that it will impact the magnetic field structure in the disc. We also hope that it will affect the jet or outflow properties of the disc as well. Hence, we plan to examine the impact of a dark matter halo on the large-scale magnetic fields structure in the accretion disc around a galactic BH by considering various dark matter density profiles [397].

6.2.5 GRMHD simulation of the accretion discs and jets in non-Kerr spacetimes

Nowadays, researchers are putting efforts into understanding the accretion process around black holes and other exotic objects, such as naked singularities, through GRMHD simulations [306, 398]. A few well-known GRMHD simulation codes in the literature are available, such as the Black Hole Accretion Code (BHAC) [399] and High Accuracy Relativistic Magnetohydrodynamics (HARM) [400]. These studies often provide insights into the evolution of the global structure of the accretion flows and their counterparts, such as bipolar jets. Also, GRMHD simulations can offer information on the evolution of the large-scale magnetic fields structure in both the accretion disc and jets. However, there is a gap in the literature regarding GRMHD simulations of accretion flows in non-Kerr spacetimes. Therefore, it would be interesting to explore the effect of deformation parameters on the evolution of the accretion disc and jets.

भारतीय प्रौद्योगिकी संस्थान गुवाहाटी • Indian Institute of Technology Guwahati •

BIBLIOGRAPHY

[1] A. K. Gautam, T. Do, A. M. Ghez, D. S. Chu, M. W. Hosek, S. Sakai, S. Naoz, M. R. Morris, A. Ciurlo, Z. Haggard, and J. R. Lu, “An Estimate of the Binary Star Fraction among Young Stars at the Galactic Center: Possible Evidence of a Radial Dependence,” *The Astrophysical Journal*, vol. 964, p. 164, Apr. 2024.

[2] F. Peißker, M. Zajaček, L. Labadie, E. Bordier, A. Eckart, M. Melamed, and V. Karas, “A binary system in the S cluster close to the supermassive black hole Sagittarius A*,” *Nature Communications*, vol. 15, p. 10608, Dec. 2024.

[3] D. Maoz, *Astrophysics in a Nutshell*, vol. 16.
Princeton university press, 2016.

[4] G. Savonije, “Roche-lobe overflow in x-ray binaries,” *Astronomy and Astrophysics, vol. 62, no. 3, Jan. 1978, p. 317-338. Research supported by the Nederlandse Organisatie voor Zuiver-Wetenschappelijk Onderzoek and Universiteit van Amsterdam.*, vol. 62, pp. 317–338, 1978.

[5] C. B. Singh, D. Garofalo, and K. Kennedy, “The generalized hardness–intensity diagram for black hole and neutron star x-ray binaries,” *The Astrophysical Journal*, vol. 887, no. 2, p. 164, 2019.

[6] S. A. Balbus and J. F. Hawley, “A Powerful Local Shear Instability in Weakly Magnetized Disks. I. Linear Analysis,” *The Astrophysical Journal*, vol. 376, p. 214, July 1991.

[7] C. F. Gammie, “The Magnetorotational instability in the Kerr metric,” *Astrophys. J.*, vol. 614, pp. 309–313, 2004.

[8] J. Frank, A. R. King, and D. Raine, *Accretion power in astrophysics*.
Cambridge university press, 2002.

Indian Institute of Technology Guwahati

TH-3714_206121049

[9] V. P. Frolov and A. Zelnikov, *Introduction to black hole physics*. OUP Oxford, 2011.

[10] L. Rezzolla and O. Zanotti, *Relativistic Hydrodynamics*. Oxford University Press, 9 2013.

[11] F. Yuan and R. Narayan, “Hot Accretion Flows Around Black Holes,” *Ann. Rev. Astron. Astrophys.*, vol. 52, pp. 529–588, 2014.

[12] A. C. Fabian, “Active galactic nuclei,” *Proceedings of the National Academy of Sciences*, vol. 96, no. 9, pp. 4749–4751, 1999.

[13] J.-H. Woo and C. M. Urry, “Active Galactic Nucleus Black Hole Masses and Bolometric Luminosities,” *The Astrophysical Journal*, vol. 579, pp. 530–544, Nov. 2002.

[14] D. Maoz, “Low-Luminosity Active Galactic Nuclei: Are They UV-Faint and Radio Loud?,” *Mon. Not. Roy. Astron. Soc.*, vol. 377, pp. 1696–1710, 2007.

[15] J. Aird, A. L. Coil, A. Georgakakis, K. Nandra, G. Barro, and P. G. Pérez-González, “The evolution of the X-ray luminosity functions of unabsorbed and absorbed AGNs out to z~ 5,” *Monthly Notices of The Royal Astronomical Society*, vol. 451, pp. 1892–1927, Aug. 2015.

[16] P. Padovani *et al.*, “Active galactic nuclei: what’s in a name?,” *Astron. Astrophys. Rev.*, vol. 25, no. 1, p. 2, 2017.

[17] J. Pflugradt, K. Ichikawa, M. Akiyama, M. Kokubo, B. Vijarnwannaluk, H. Noda, and X. Chen, “Finding of a Population of Active Galactic Nuclei Showing a Significant Luminosity Decline in the Past 10^3-10^4 yr,” *The Astrophysical Journal*, vol. 938, p. 75, Oct. 2022.

[18] R. A. Remillard and J. E. McClintock, “X-ray properties of black-hole binaries,” *Annu. Rev. Astron. Astrophys.*, vol. 44, pp. 49–92, 2006.

[19] H. Schatz and K. E. Rehm, “X-ray binaries,” *Nucl. Phys. A*, vol. 777, pp. 601–622, 2006.

[20] S. Chaty, “Nature, formation and evolution of High Mass X-ray Binaries,” *ASP Conf. Ser.*, vol. 447, p. 29, 2011.

[21] E. Meyer-Hofmeister and F. Meyer, “The relation between radio and X-ray luminosity of black hole binaries: affected by inner cool disks?,” *Astron. Astrophys.*, vol. 562, p. A142, 2014.

[22] C. Tan, “High-mass x-ray binary: Classification, formation, and evolution,” in *Journal of Physics: Conference Series*, vol. 2012, p. 012119, IOP Publishing, 2021.

[23] D. Misra *et al.*, “X-ray luminosity function of high-mass X-ray binaries: Studying the signatures of different physical processes using detailed binary evolution calculations,” *Astron. Astrophys.*, vol. 672, p. A99, 2023.

[24] F. M. Fornasini, V. Antoniou, and G. Dubus, “High-mass X-ray Binaries,” 8 2023.

[25] R. P. Fender, T. M. Belloni, and E. Gallo, “Towards a unified model for black hole X-ray binary jets,” *Monthly Notices of The Royal Astronomical Society*, vol. 355, pp. 1105–1118, Dec. 2004.

[26] R. Fender and T. Belloni, “Stellar Mass Black Holes and Ultraluminous X-Ray Sources,” *Science*, vol. 337, p. 540, 2012.

[27] D. M. Sánchez, T. Muñoz Darias, V. A. Cúneo, M. A. Padilla, J. Sánchez-Sierras, G. Panizo-Espinar, J. Casares, J. M. Corral-Santana, and M. A. P. Torres, “Hard-state Optical Wind during the Discovery Outburst of the Black Hole X-Ray Dipper MAXI J1803–298,” *Astrophys. J. Lett.*, vol. 926, no. 2, p. L10, 2022.

[28] A. Nandi, S. Das, S. Majumder, T. Katoch, H. M. Antia, and P. Shah, “Discovery of evolving low-frequency QPOs in hard X-rays (~100 keV) observed in black hole Swift J1727.8−1613 with AstroSat,” *Mon. Not. Roy. Astron. Soc.*, vol. 531, no. 1, pp. 1149–1157, 2024.

[29] M. P. Muno, R. A. Remillard, E. H. Morgan, E. B. Waltman, V. Dhawan, R. M. Hjellming, and G. Pooley, “Radio Emission and the Timing Properties of the Hard X-Ray State of GRS 1915+105,” *The Astrophysical Journal*, vol. 556, pp. 515–532, Aug. 2001.

[30] T. E. Strohmayer, “Discovery of a 450 hz qpo from the microquasar gro j1655-40 with rxte,” *Astrophys. J. Lett.*, vol. 552, pp. L49–L53, 2001.

[31] R. A. Remillard, M. P. Muno, J. E. McClintock, and J. A. Orosz, “Evidence for harmonic relationships in the high frequency qpos of xte j1550-564 and gro j1655-40,” *Astrophys. J.*, vol. 580, pp. 1030–1042, 2002.

[32] I. F. Mirabel, L. F. Rodriguez, B. Cordier, J. Paul, and F. Lebrun, “A double-sided radio jet from the compact Galactic Centre annihilator 1E1740.7-2942,” *Nature*, vol. 358, pp. 215–217, July 1992.

[33] W. Junor, J. A. Biretta, and M. Livio, “Formation of the radio jet in M87 at 100 Schwarzschild radii from the central black hole,” *Nature*, vol. 401, pp. 891–892, Oct. 1999.

[34] A. Ferrari, “Agn Jet Modeling: Setting the Stage,” *Astrophysics and Space Science*, vol. 293, pp. 15–26, Aug. 2004.

[35] S. S. Doeleman, V. L. Fish, D. E. Schenck, C. Beaudoin, R. Blundell, G. C. Bower, A. E. Broderick, R. Chamberlin, R. Freund, P. Friberg, M. A. Gurwell, P. T. P. Ho, M. Honma, M. Inoue, T. P. Krichbaum, J. Lamb, A. Loeb, C. Lonsdale, D. P. Marrone, J. M. Moran, T. Oyama, R. Plambeck, R. A. Primiani, A. E. E. Rogers, D. L. Smythe, J. SooHoo, P. Strittmatter, R. P. J. Tilanus, M. Titus, J. Weintroub, M. Wright, K. H. Young, and L. M. Ziurys, “Jet-Launching Structure Resolved Near the Supermassive Black Hole in M87,” *Science*, vol. 338, p. 355, Oct. 2012.

[36] S. Cielo, V. Antonuccio-Delogu, A. V. Macciò, A. D. Romeo, and J. Silk, “3D simulations of the early stages of AGN jets: geometry, thermodynamics and backflow,” *Mon. Not. Roy. Astron. Soc.*, vol. 439, no. 3, pp. 2903–2916, 2014.

[37] I. Chattopadhyay and R. Kumar, “Estimation of mass outflow rates from viscous relativistic accretion discs around black holes,” *Mon. Not. Roy. Astron. Soc.*, vol. 459, pp. 3792–3811, July 2016.

[38] R. Kumar and I. Chattopadhyay, “Estimation of bipolar jets from accretion discs around Kerr black holes,” *Mon. Not. Roy. Astron. Soc.*, vol. 469, pp. 4221–4235, Aug. 2017.

[39] C. Jana and S. Das, “Study of mass outflow rates from magnetized advective accretion disk around rotating black holes,” *JCAP*, vol. 07, p. 075, 2024.

[40] I. M. McHardy, E. Koerding, C. Knigge, P. Uttley, and R. P. Fender, “Active galactic nuclei as scaled-up Galactic black holes,” *Nature*, vol. 444, pp. 730–732, Dec. 2006.

[41] E. Gallo, R. P. Fender, and G. G. Pooley, “A universal radio: X-ray correlation in low / hard state black hole binaries,” *Mon. Not. Roy. Astron. Soc.*, vol. 344, p. 60, 2003.

[42] A. Rushton, R. Spencer, R. Fender, and G. Pooley, “Steady jets from radiatively efficient hard states in GRS 1915+105,” *Astronomy and Astrophysics*, vol. 524, p. A29, Dec. 2010.

[43] R. Fender and E. Gallo, “An overview of jets and outflows in stellar mass black holes,” *Space Sci. Rev.*, vol. 183, no. 1-4, pp. 323–337, 2014.

[44] M. A. Abramowicz and P. C. Fragile, “Foundations of Black Hole Accretion Disk Theory,” *Living Reviews in Relativity*, vol. 16, p. 1, Jan. 2013.

[45] A. Nandi, S. Mandal, H. Sreehari, D. Radhika, S. Das, I. Chattopadhyay, N. Iyer, V. Agrawal, and R. Aktar, “Accretion flow dynamics during 1999 outburst of xte j1859+ 226—modeling of broadband spectra and constraining the source mass,” *Astrophysics and Space Science*, vol. 363, pp. 1–12, 2018.

[46] H. Sreehari, A. Nandi, S. Das, V. Agrawal, S. Mandal, M. Ramadevi, and T. Katoch, “Astrosat view of grs 1915+ 105 during the soft state: detection of hfqpos and estimation of mass and spin,” *Monthly Notices of the Royal Astronomical Society*, vol. 499, no. 4, pp. 5891–5901, 2020.

[47] S. Das, A. Nandi, V. K. Agrawal, I. K. Dihingia, and S. Majumder, “Relativistic viscous accretion flow model for ULX sources: a case study for IC 342 X-1,” *Mon. Not. Roy. Astron. Soc.*, vol. 507, pp. 2777–2781, Oct. 2021.

[48] K. Sriram, S. Harikrishna, and C. S. Choi, “Spectro-temporal studies of rapid transition of the quasi periodic oscillations in the black hole source H1743-322,” *Astrophys. J.*, vol. 911, no. 2, p. 127, 2021.

[49] S. Majumder, H. Sreehari, N. Aftab, T. Katoch, S. Das, and A. Nandi, “Wide-band view of high-frequency quasi-periodic oscillations of grs 1915+ 105 in ‘softer’variability classes observed with astrosat,” *Monthly Notices of the Royal Astronomical Society*, vol. 512, no. 2, pp. 2508–2524, 2022.

[50] S. Mondal, T. P. Adhikari, K. Hryniewicz, C. Stalin, and A. Pandey, “Variable mass accretion and failed wind explain changing-look phenomena in ngc 1365,” *Astronomy & Astrophysics*, vol. 662, p. A77, 2022.

[51] S. R. Heiland, A. Chatterjee, S. Safi-Harb, A. Jana, and J. Heyl, “Accretion properties and estimation of spin of galactic black hole candidate Swift J1728.9–3613with NuSTAR during its 2019 outburst,” *Mon. Not. Roy. Astron. Soc.*, vol. 524, no. 3, pp. 3834–3845, 2023.

[52] D. Rawat, M. Méndez, F. García, D. Altamirano, K. Karpouzas, L. Zhang, K. Alabarta, T. M. Belloni, P. Jain, and C. Bellavita, “The comptonizing medium of the black hole X-ray binary MAXI J1535−571 through type-C quasi-periodic oscillations,” *Mon. Not. Roy. Astron. Soc.*, vol. 520, no. 1, pp. 113–128, 2023.

[53] R. Dhaka, R. Misra, J. S. Yadav, and P. Jain, “Correlations between QPO frequencies and spectral parameters of GRS 1915+105 using AstroSat observations,” *Mon. Not. Roy. Astron. Soc.*, vol. 524, no. 2, pp. 2721–2732, 2023.

[54] S. Mondal, M. Das, K. Rubinur, K. Bansal, A. Nath, and G. B. Taylor, “Detection of the Fe K lines from the binary AGN in 4C+37.11,” *Astron. Astrophys.*, vol. 691, p. A279, 2024.

[55] A. A. Molla, S. K. Chakrabarti, D. Debnath, and S. Mondal, “Estimation of Mass of Compact Object in H 1743-322 from 2010 and 2011 Outbursts using TCAF Solution and Spectral Index - QPO Frequency Correlation,” *Astrophys. J.*, vol. 834, no. 1, p. 88, 2017.

[56] S. Mondal, S. P. Suribhatla, K. Chatterjee, C. B. Singh, and R. Chatterjee, “The First Detection of X-Ray Polarization in a Newly Discovered Galactic Transient Swift J151857.0-572147,” *Astrophys. J.*, vol. 975, no. 2, p. 257, 2024.

[57] F. Hoyle and R. A. Lyttleton, “The effect of interstellar matter on climatic variation,” *Proceedings of the Cambridge Philosophical Society*, vol. 35, p. 405, Jan. 1939.

[58] H. Bondi and F. Hoyle, “On the Mechanism of Accretion by Stars,” *Mon. Not. Roy. Astron. Soc.*, vol. 104, no. 5, pp. 273–282, 1944.

[59] H. Bondi, “On spherically symmetrical accretion,” *Mon. Not. Roy. Astron. Soc.*, vol. 112, p. 195, 1952.

[60] F. C. Michel, "Accretion of matter by condensed objects," *Astrophys. Space Sci.*, vol. 15, no. 1, pp. 153–160, 1972.

[61] P. J. Armitage, *Astrophysics of planet formation*.
Cambridge University Press, 2020.

[62] S. L. Shapiro and S. A. Teukolsky, *Black holes, white dwarfs and neutron stars: the physics of compact objects*.
John Wiley & Sons, 2024.

[63] N. I. Shakura and R. A. Sunyaev, "Black holes in binary systems. Observational appearance," *Astron. Astrophys.*, vol. 24, pp. 337–355, 1973.

[64] I. D. Novikov and K. S. Thorne, "Astrophysics of black holes.," in *Black Holes (Les Astres Occlus)* (C. Dewitt and B. S. Dewitt, eds.), pp. 343–450, Jan. 1973.

[65] S. L. Shapiro, A. P. Lightman, and D. M. Eardley, "A two - temperature accretion disk model for Cygnus X-1. 1. Structure and spectrum," *Astrophys. J.*, vol. 204, pp. 187–199, 1976.

[66] J. Pringle, "Thermal instabilities in accretion discs," *Monthly Notices of the Royal Astronomical Society*, vol. 177, no. 1, pp. 65–71, 1976.

[67] T. Piran, "The role of viscosity and cooling mechanisms in the stability of accretion disks," *Astrophysical Journal, Part 1, vol. 221, Apr. 15, 1978, p. 652-660. Research supported by the Science Research Council.*, vol. 221, pp. 652–660, 1978.

[68] R. Narayan and I. Yi, "Advection dominated accretion: Underfed black holes and neutron stars," *Astrophys. J.*, vol. 452, p. 710, 1995.

[69] M. A. Abramowicz, B. Czerny, J. P. Lasota, and E. Szuszkiewicz, "Slim accretion disks," *Astrophys. J.*, vol. 332, p. 646, 1988.

[70] D. Mihalas and B. Weibel-Mihalas, *Foundations of Radiation Hydrodynamics*.
Dover Books on Physics, Dover Publications, 1999.

[71] S. K. Chakrabarti, *Theory of Transonic Astrophysical Flows*.
World Scientific, Singapore, 1990.

[72] A. M. Beloborodov, “Super-eddington accretion disc around a kerr black hole,” *Mon. Not. Roy. Astron. Soc.*, vol. 297, p. 739, 1998.

[73] A. Sądowski, “Slim disks around kerr black holes revisited,” *The Astrophysical Journal Supplement Series*, vol. 183, no. 2, p. 171, 2009.

[74] S. Ichimaru, “Bimodal behavior of accretion disks-theory and application to cygnus x-1 transitions,” *Astrophysical Journal, Part 1, vol. 214, June 15, 1977, p. 840-855. Research supported by the Japan Society for the Promotion of Science*, vol. 214, pp. 840–855, 1977.

[75] M. J. Rees, E. S. Phinney, M. C. Begelman, and R. D. Blandford, “Ion supported tori and the origin of radio jets,” *Nature*, vol. 295, pp. 17–21, 1982.

[76] R. Narayan and R. Popham, “Hard x-rays from accretion disk boundary layers,” *Nature*, vol. 362, p. 820, 1993.

[77] R. Narayan and I.-s. Yi, “Advection dominated accretion: A Selfsimilar solution,” *Astrophys. J. Lett.*, vol. 428, p. L13, 1994.

[78] R. Narayan and I.-s. Yi, “Advection dominated accretion: Selfsimilarity and bipolar outflows,” *Astrophys. J.*, vol. 444, p. 231, 1995.

[79] M. A. Abramowicz, X. Chen, S. Kato, J.-P. Lasota, and O. Regev, “Thermal equilibria of accretion disks,” *Astrophys. J. Lett.*, vol. 438, p. L37, 1995.

[80] X.-m. Chen, M. A. Abramowicz, J.-P. Lasota, R. Narayan, and I. Yi, “Unified description of accretion flows around black holes,” *Astrophys. J. Lett.*, vol. 443, p. L61, 1995.

[81] X. Chen, “Hot accretion discs with advection,” *Monthly Notices of the Royal Astronomical Society*, vol. 275, pp. 641–648, 08 1995.

[82] X. Chen, M. A. Abramowicz, and J.-P. Lasota, “Advection-dominated accretion: global transonic solutions,” *Astrophys. J.*, vol. 476, p. 61, 1997.

[83] R. Narayan, S. Kato, and F. Honma, “Global structure and dynamics of advection-dominated accretion flows around black holes,” *The Astrophysical Journal*, vol. 476, no. 1, p. 49, 1997.

[84] B. Paczyńsky and P. J. Wiita, “Thick accretion disks and supercritical luminosities.,” *Astron. Astrophys.*, vol. 500, pp. 203–211, Aug. 1980.

[85] M. A. Abramowicz, X. M. Chen, M. Granath, and J. P. Lasota, “Advection dominated accretion flows around kerr black holes,” *Astrophys. J.*, vol. 471, p. 762, 1996.

[86] S. K. Chakrabarti, “Global solutions of viscous transonic flows in Kerr geometry - I. Weak viscosity limit,” *Mon. Not. Roy. Astron. Soc.*, vol. 283, p. 325, Nov. 1996.

[87] S. K. Chakrabarti, “Solutions of two-dimensional viscous accretion and winds in Kerr black hole geometry,” *Astrophys. J.*, vol. 471, p. 237, 1996.

[88] J. Peitz and S. Appl, “Viscous accretion discs around rotating black holes,” *Mon. Not. Roy. Astron. Soc.*, vol. 286, pp. 681–695, Apr. 1997.

[89] C. F. Gammie and R. Popham, “Advection dominated accretion flows in the Kerr metric: 1. Basic equations,” *Astrophys. J.*, vol. 498, p. 313, 1998.

[90] R. Popham and C. F. Gammie, “Advection dominated accretion flows in the kerr metric. 2. Steady state global solutions,” *Astrophys. J.*, vol. 504, p. 419, 1998.

[91] S. Chakrabarti and L. G. Titarchuk, “Spectral Properties of Accretion Disks around Galactic and Extragalactic Black Holes,” *Astrophys. J.*, vol. 455, p. 623, Dec. 1995.

[92] K. Giri and S. K. Chakrabarti, “Hydrodynamic Simulation of Two Component Advective Flows around Black Holes,” *Mon. Not. Roy. Astron. Soc.*, vol. 430, p. 2836, 2013.

[93] K. Giri, S. K. Garain, and S. K. Chakrabarti, “Segregation of a Keplerian disc and sub-Keplerian halo from a Transonic flow around a Black Hole by Viscosity and Cooling processes,” *Mon. Not. Roy. Astron. Soc.*, vol. 448, no. 4, pp. 3221–3228, 2015.

[94] J. Fukue, “Transonic disk accretion revisited,” *Publications of the astronomical society of Japan*, vol. 39, pp. 309–327, Jan. 1987.

[95] S. K. Chakrabarti, “Standing Rankine-Hugoniot Shocks in the Hybrid Model Flows of the Black Hole Accretion and Winds,” *Astrophys. J.*, vol. 347, p. 365, Dec. 1989.

[96] S. K. CHAkRABARTI and S. Mandal, “The spectral properties of shocked two-component accretion flows in the presence of synchrotron emission,” *The Astrophysical Journal*, vol. 642, no. 1, p. L49, 2006.

[97] S. Mondal, D. Debnath, and S. K. Chakrabarti, “Inference on accretion flow dynamics using tcaf solution from the analysis of spectral evolution of h 1743-322 during the 2010 outburst,” *The Astrophysical Journal*, vol. 786, no. 1, p. 4, 2014.

[98] D. Debnath, S. Mondal, and S. K. Chakrabarti, “Characterization of gx 339-4 outburst of 2010–11: analysis by xspec using two component advective flow model,” *Monthly Notices of the Royal Astronomical Society*, vol. 447, no. 2, pp. 1984–1995, 2015.

[99] S. K. Chakrabarti, “Estimation and effects of the mass outflow rate from shock compressed flow around compact objects,” *Astron. Astrophys.*, vol. 351, p. 185, 1999.

[100] S. Das, I. Chattopadhyay, and S. K. Chakrabarti, “Standing shocks around black holes: an analytical study,” *Astrophys. J.*, vol. 557, p. 983, 2001.

[101] I. Chattopadhyay and S. Das, “Massloss from viscous advective disc,” *New Astron.*, vol. 12, pp. 454–460, 2007.

[102] S. Das and I. Chattopadhyay, “Computation of mass loss from viscous accretion disc in presence of cooling,” *New Astron.*, vol. 13, pp. 549–556, 2008.

[103] R. Kumar and I. Chattopadhyay, “Estimation of the mass outflow rates from viscous accretion discs,” *Mon. Not. Roy. Astron. Soc.*, vol. 430, p. 386, 2013.

[104] A. Nandi, S. G. Manickam, A. Rao, and S. K. Chakrabarti, “On the source of quasi-periodic oscillations of the black hole candidate grs 1915+ 105: some new observations and their interpretation,” *Monthly Notices of the Royal Astronomical Society*, vol. 324, no. 1, pp. 267–272, 2001.

[105] A. Nandi, D. Debnath, S. Mandal, and S. K. Chakrabarti, “Accretion flow dynamics during the evolution of timing and spectral properties of GX 339-4 during its 2010-11 outburst,” *Astron. Astrophys.*, vol. 542, p. A56, June 2012.

[106] D. Radhika and A. Nandi, "'Spectro-temporal' characteristics and disk-jet connection of the outbursting black hole source XTE J1859+226," *Advances in Space Research*, vol. 54, pp. 1678–1697, Oct. 2014.

[107] N. Iyer, A. Nandi, and S. Mandal, "Determination of the Mass of IGR J17091-3624 from "Spectro-temporal" Variations during the Onset Phase of the 2011 Outburst," *Astrophys. J.*, vol. 807, p. 108, July 2015.

[108] S. K. Chakrabarti and R. Khanna, "A newtonian description of the geometry around a rotating black hole," *Monthly Notices of the Royal Astronomical Society*, vol. 256, no. 2, pp. 300–306, 1992.

[109] I. V. Artemova, G. Björnsson, and I. D. Novikov, "Modified newtonian potentials for the description of relativistic effects in accretion disks around black holes," *Astrophysical Journal v. 461, p. 565*, vol. 461, p. 565, 1996.

[110] B. Mukhopadhyay, "New description of pseudo-Newtonian potential for the relativistic accretion disk around Kerr black holes," *Astrophys. J.*, vol. 581, p. 427, 2002.

[111] S. K. Chakrabarti and S. Mondal, "Studies of accretion flows around rotating black holes–i. particle dynamics in a pseudo-kerr potential," *Monthly Notices of the Royal Astronomical Society*, vol. 369, no. 2, pp. 976–984, 2006.

[112] A. A. Zdziarski, S. Banerjee, S. Chand, G. Dewangan, R. Misra, M. Szanecki, and A. Niedzwiecki, "Black Hole Spin Measurements in LMC X-1 and Cyg X-1 Are Highly Model Dependent," *Astrophys. J.*, vol. 962, no. 2, p. 101, 2024.

[113] Z. Stuchlík and M. Kološ, "Controversy of the GRO J1655-40 black hole mass and spin estimates and its possible solutions," *Astrophys. J.*, vol. 825, p. 13, 2016.

[114] H. Riffert and H. Herold, "Relativistic Accretion Disk Structure Revisited," *Astrophys. J.*, vol. 450, p. 508, Sept. 1995.

[115] I. Chattopadhyay and S. K. Chakrabarti, "Effects of the composition on transonic properties of accretion flows around black holes," *Int. J. Mod. Phys. D*, vol. 20, no. 09, pp. 1597–1615, 2011.

[116] I. K. Dihingia, S. Das, D. Maity, and S. Chakrabarti, "Limitations of the pseudo-Newtonian approach in studying the accretion flow around a Kerr black hole," *Phys. Rev. D*, vol. 98, p. 083004, Oct. 2018.

[117] R. H. Boyer and R. W. Lindquist, “Maximal analytic extension of the kerr metric,” *Journal of mathematical physics*, vol. 8, no. 2, pp. 265–281, 1967.

[118] I. K. Dihingia, S. Das, D. Maity, and A. Nandi, “Shocks in relativistic viscous accretion flows around Kerr black holes,” *Mon. Not. Roy. Astron. Soc.*, vol. 488, pp. 2412–2422, Sept. 2019.

[119] M. Singh and S. Das, “Role of thermal conduction in relativistic hot accretion flow around rotating black hole with shock,” 8 2024.

[120] M. Singh, C. Jana, and S. Das, “Effect of thermal conduction on accretion shocks in relativistic magnetized flows around rotating black holes,” 2 2025.

[121] I. K. Dihingia, D. Maity, S. Chakrabarti, and S. Das, “Study of relativistic accretion flow in Kerr-Taub-NUT spacetime,” *Phys. Rev. D*, vol. 102, p. 023012, July 2020.

[122] G. Sen, D. Maity, and S. Das, “Study of relativistic accretion flow around KTN black hole with shocks,” *JCAP*, vol. 08, no. 08, p. 048, 2022.

[123] S. Sarkar and I. Chattopadhyay, “Viscous dissipative two-temperature accretion flows around black holes,” *Journal of Astrophysics and Astronomy*, vol. 43, no. 2, p. 34, 2022.

[124] S. Mitra, D. Maity, I. K. Dihingia, and S. Das, “Study of general relativistic magnetohydrodynamic accretion flow around black holes,” *Mon. Not. Roy. Astron. Soc.*, vol. 516, no. 4, pp. 5092–5109, 2022.

[125] S. Mitra and S. Das, “Low-angular-momentum General Relativistic Magnetohydrodynamic Accretion Flows around Rotating Black Holes with Shocks,” *Astrophys. J.*, vol. 971, no. 1, p. 28, 2024.

[126] B. Carter, “Complete analytic extension of the symmetry axis of kerr’s solution of einstein’s equations,” *Phys. Rev.*, vol. 141, pp. 1242–1247, Jan 1966.

[127] A. Sen, “Rotating charged black hole solution in heterotic string theory,” *Phys. Rev. Lett.*, vol. 69, pp. 1006–1009, 1992.

[128] P. Kanti, N. E. Mavromatos, J. Rizos, K. Tamvakis, and E. Winstanley, “Dilatonic black holes in higher curvature string gravity,” *Phys. Rev. D*, vol. 54, pp. 5049–5058, 1996.

[129] N. Yunes and F. Pretorius, "Dynamical Chern-Simons Modified Gravity. I. Spinning Black Holes in the Slow-Rotation Approximation," *Phys. Rev. D*, vol. 79, p. 084043, 2009.

[130] R. Abbott *et al.*, "Tests of general relativity with binary black holes from the second LIGO-Virgo gravitational-wave transient catalog," *Phys. Rev. D*, vol. 103, no. 12, p. 122002, 2021.

[131] P. de Bernardis, A. Balbi, G. De Gasperis, A. Melchiorri, and N. Vittorio, "CMB anisotropy at degree angular scales and the thermal history of the universe," *Astrophys. J.*, vol. 480, p. 1, 1997.

[132] R. Massey, T. Kitching, and J. Richard, "The dark matter of gravitational lensing," *Rept. Prog. Phys.*, vol. 73, p. 086901, 2010.

[133] A. D. Popolo, "The flat density profiles of massive, and relaxed galaxy clusters," *JCAP*, vol. 07, p. 019, 2014.

[134] M. T. Hogan, B. R. McNamara, F. Pulido, P. E. J. Nulsen, H. R. Russell, A. N. Vantyghem, A. C. Edge, and R. A. Main, "Mass Distribution in Galaxy Cluster Cores," *Astrophys. J.*, vol. 837, no. 1, p. 51, 2017.

[135] T. Ren, A. Kwa, M. Kaplinghat, and H.-B. Yu, "Reconciling the diversity and uniformity of galactic rotation curves with self-interacting dark matter," *Phys. Rev. X*, vol. 9, p. 031020, Aug 2019.

[136] G. O. Ludwig, "Galactic rotation curve and dark matter according to gravitomagnetism," *Eur. Phys. J. C*, vol. 81, no. 2, p. 186, 2021.

[137] J. Magee *et al.*, "Rotation Curve Measurement of Dark Matter Content of a $z \sim 0.5$ Galaxy," *Res. Notes AAS*, vol. 7, no. 5, p. 110, 2023.

[138] P. J. E. Peebles and B. Ratra, "The cosmological constant and dark energy," *Rev. Mod. Phys.*, vol. 75, pp. 559–606, Apr 2003.

[139] J. Frieman, M. Turner, and D. Huterer, "Dark Energy and the Accelerating Universe," *Ann. Rev. Astron. Astrophys.*, vol. 46, pp. 385–432, 2008.

[140] C. Skordis, "TOPICAL REVIEW: The tensor-vector-scalar theory and its cosmology," *Classical and Quantum Gravity*, vol. 26, p. 143001, July 2009.

[141] T. P. Sotiriou and V. Faraoni, “f(R) Theories Of Gravity,” *Rev. Mod. Phys.*, vol. 82, pp. 451–497, 2010.

[142] K. Yagi, “A New constraint on scalar Gauss-Bonnet gravity and a possible explanation for the excess of the orbital decay rate in a low-mass X-ray binary,” *Phys. Rev. D*, vol. 86, p. 081504, 2012.

[143] J. W. Moffat, “Black Holes in Modified Gravity (MOG),” *Eur. Phys. J. C*, vol. 75, no. 4, p. 175, 2015.

[144] C. M. Will, “The Confrontation between General Relativity and Experiment,” *Living Rev. Rel.*, vol. 17, p. 4, 2014.

[145] T. Clifton, P. G. Ferreira, A. Padilla, and C. Skordis, “Modified Gravity and Cosmology,” *Phys. Rept.*, vol. 513, pp. 1–189, 2012.

[146] P. G. Ferreira, “Cosmological tests of gravity,” *Annual Review of Astronomy and Astrophysics*, vol. 57, no. 1, pp. 335–374, 2019.

[147] D. Psaltis, “Probes and Tests of Strong-Field Gravity with Observations in the Electromagnetic Spectrum,” *Living Rev. Rel.*, vol. 11, p. 9, 2008.

[148] D. Psaltis and T. Johannsen, “Sgr A*: The Optimal Testbed of Strong-Field Gravity,” *J. Phys. Conf. Ser.*, vol. 283, p. 012030, 2011.

[149] B. P. Abbott *et al.*, “Observation of Gravitational Waves from a Binary Black Hole Merger,” *Phys. Rev. Lett.*, vol. 116, no. 6, p. 061102, 2016.

[150] B. P. Abbott *et al.*, “GW150914: The Advanced LIGO Detectors in the Era of First Discoveries,” *Phys. Rev. Lett.*, vol. 116, no. 13, p. 131103, 2016.

[151] B. P. Abbott *et al.*, “Tests of general relativity with GW150914,” *Phys. Rev. Lett.*, vol. 116, no. 22, p. 221101, 2016.
[Erratum: Phys.Rev.Lett. 121, 129902 (2018)].

[152] B. P. Abbott *et al.*, “Properties of the Binary Black Hole Merger GW150914,” *Phys. Rev. Lett.*, vol. 116, no. 24, p. 241102, 2016.

[153] K. Akiyama *et al.*, “First M87 Event Horizon Telescope Results. I. The Shadow of the Supermassive Black Hole,” *Astrophys. J. Lett.*, vol. 875, p. L1, 2019.

[154] K. Akiyama *et al.*, “First M87 Event Horizon Telescope Results. II. Array and Instrumentation,” *Astrophys. J. Lett.*, vol. 875, no. 1, p. L2, 2019.

[155] K. Akiyama *et al.*, “First M87 Event Horizon Telescope Results. III. Data Processing and Calibration,” *Astrophys. J. Lett.*, vol. 875, no. 1, p. L3, 2019.

[156] K. Akiyama, A. Alberdi, W. Alef, K. Asada, R. Azulay, A.-K. Baczko, D. Ball, M. Baloković, J. Barrett, D. Bintley, *et al.*, “First m87 event horizon telescope results. iv. imaging the central supermassive black hole,” *The Astrophysical Journal Letters*, vol. 875, no. 1, p. L4, 2019.

[157] K. Akiyama *et al.*, “First M87 Event Horizon Telescope Results. V. Physical Origin of the Asymmetric Ring,” *Astrophys. J. Lett.*, vol. 875, no. 1, p. L5, 2019.

[158] K. Akiyama *et al.*, “First M87 Event Horizon Telescope Results. VI. The Shadow and Mass of the Central Black Hole,” *Astrophys. J. Lett.*, vol. 875, no. 1, p. L6, 2019.

[159] D. C. Robinson, “Uniqueness of the Kerr black hole,” *Phys. Rev. Lett.*, vol. 34, pp. 905–906, 1975.

[160] T. Johannsen and D. Psaltis, “Testing the No-hair Theorem with Observations in the Electromagnetic Spectrum. I. Properties of a Quasi-Kerr Spacetime,” *Astrophys. J.*, vol. 716, pp. 187–197, June 2010.

[161] T. Johannsen and D. Psaltis, “Metric for rapidly spinning black holes suitable for strong-field tests of the no-hair theorem,” *Phys. Rev. D*, vol. 83, p. 124015, June 2011.

[162] S. Vigeland, N. Yunes, and L. Stein, “Bumpy Black Holes in Alternate Theories of Gravity,” *Phys. Rev. D*, vol. 83, p. 104027, 2011.

[163] T. Johannsen, “Regular Black Hole Metric with Three Constants of Motion,” *Phys. Rev. D*, vol. 88, no. 4, p. 044002, 2013.

[164] L. Rezzolla and A. Zhidenko, “New parametrization for spherically symmetric black holes in metric theories of gravity,” *Phys. Rev. D*, vol. 90, p. 084009, Oct. 2014.

[165] R. Konoplya, L. Rezzolla, and A. Zhidenko, “General parametrization of axisymmetric black holes in metric theories of gravity,” *Phys. Rev. D*, vol. 93, p. 064015, Mar. 2016.

[166] R. Konoplya and A. Zhidenko, “Detection of gravitational waves from black holes: Is there a window for alternative theories?,” *Phys. Lett. B*, vol. 756, pp. 350–353, 2016.

[167] S. Nampalliwar, S. Xin, S. Srivastava, A. B. Abdikamalov, D. Ayzenberg, C. Bambi, T. Dauser, J. A. Garcia, and A. Tripathi, “Testing General Relativity with X-ray reflection spectroscopy: The Konoplya-Rezzolla-Zhidenko parametrization,” *Phys. Rev. D*, vol. 102, no. 12, p. 124071, 2020.

[168] Y. Ma and L. Rezzolla, “Horizon-penetrating form of parametrized metrics for static and stationary black holes,” *Phys. Rev. D*, vol. 110, no. 2, p. 024032, 2024.

[169] Y. Ni, J. Jiang, and C. Bambi, “Testing the Kerr metric with the iron line and the KRZ parametrization,” *JCAP*, vol. 09, p. 014, 2016.

[170] A. Cardenas-Avendano, S. Nampalliwar, and N. Yunes, “Gravitational-wave versus X-ray tests of strong-field gravity,” *Class. Quant. Grav.*, vol. 37, no. 13, p. 135008, 2020.

[171] D. Psaltis *et al.*, “Gravitational Test Beyond the First Post-Newtonian Order with the Shadow of the M87 Black Hole,” *Phys. Rev. Lett.*, vol. 125, no. 14, p. 141104, 2020.

[172] S. Shashank and C. Bambi, “Constraining the Konoplya-Rezzolla-Zhidenko deformation parameters III: Limits from stellar-mass black holes using gravitational-wave observations,” *Phys. Rev. D*, vol. 105, no. 10, p. 104004, 2022.

[173] C. Bambi, “Testing General Relativity with Black Hole X-Ray Data,” *Physics of Particles and Nuclei*, vol. 55, pp. 1420–1425, Dec. 2024.

[174] A. Tripathi, G. Mall, and A. Abdikamalov, “Testing General Relativity with NuSTAR data of Galactic Black Holes : II,” 1 2024.

[175] L. Sadeghian, F. Ferrer, and C. M. Will, “Dark matter distributions around massive black holes: A general relativistic analysis,” *Phys. Rev. D*, vol. 88, no. 6, p. 063522, 2013.

[176] V. Cardoso, K. Destounis, F. Duque, R. P. Macedo, and A. Maselli, "Black holes in galaxies: Environmental impact on gravitational-wave generation and propagation," *Phys. Rev. D*, vol. 105, no. 6, p. L061501, 2022.

[177] K. Jusufi, "Black holes surrounded by Einstein clusters as models of dark matter fluid," *Eur. Phys. J. C*, vol. 83, no. 2, p. 103, 2023.

[178] D. Pugliese and Z. Stuchlík, "Dark matter effect on black hole accretion disks," *Phys. Rev. D*, vol. 106, no. 12, p. 124034, 2022.

[179] S. V. M. C. B. Xavier, H. C. D. Lima, Junior., and L. C. B. Crispino, "Shadows of black holes with dark matter halo," *Phys. Rev. D*, vol. 107, no. 6, p. 064040, 2023.

[180] L. Pezzella, K. Destounis, A. Maselli, and V. Cardoso, "Quasinormal modes of black holes embedded in halos of matter," 12 2024.

[181] T. S. Amancio, R. A. Mosna, and R. S. S. Vieira, "Chaotic orbital dynamics of pulsating stars around black holes surrounded by dark matter halos," *Phys. Rev. D*, vol. 110, no. 12, p. 124048, 2024.

[182] S. Patra, B. R. Majhi, and S. Das, "Properties of accretion flow in deformed Kerr spacetime," *Phys. Dark Univ.*, vol. 37, p. 101120, 2022.

[183] S. Patra, B. R. Majhi, and S. Das, "Accretion flow in deformed Kerr spacetime: spectral energy distributions from free-free emission," *JCAP*, vol. 01, p. 060, 2024.

[184] S. Patra, B. R. Majhi, and S. Das, "General relativistic viscous accretion flow around Konoplya-Zhidenko black hole," *JHEAp*, vol. 44, pp. 371–380, 2024.

[185] S. Patra and B. R. Majhi, "Effect of dark matter halo on transonic accretion flow around a galactic black hole," 1 2025.

[186] W. Israel, "Event horizons in static vacuum space-times," *Phys. Rev.*, vol. 164, pp. 1776–1779, 1967.

[187] W. Israel, "Event horizons in static electrovac space-times," *Commun. Math. Phys.*, vol. 8, pp. 245–260, 1968.

[188] B. Carter, “Axisymmetric Black Hole Has Only Two Degrees of Freedom,” *Phys. Rev. Lett.*, vol. 26, pp. 331–333, 1971.

[189] S. W. Hawking, “Black holes in general relativity,” *Commun. Math. Phys.*, vol. 25, pp. 152–166, 1972.

[190] B. Carter, “Black holes equilibrium states,” in *Les Houches Summer School of Theoretical Physics: Black Holes*, pp. 57–214, 1973.

[191] V. S. Manko and I. D. Novikov, “Generalizations of the Kerr and Kerr-Newman metrics possessing an arbitrary set of mass-multipole moments,” *Classical and Quantum Gravity*, vol. 9, pp. 2477–2487, Nov. 1992.

[192] N. A. Collins and S. A. Hughes, “Towards a formalism for mapping the space-times of massive compact objects: Bumpy black holes and their orbits,” *Phys. Rev. D*, vol. 69, p. 124022, 2004.

[193] K. Glampedakis and S. Babak, “Mapping spacetimes with lisa: inspiral of a test body in a ‘quasi-kerr’field,” *Classical and Quantum Gravity*, vol. 23, no. 12, p. 4167, 2006.

[194] S. J. Vigeland and S. A. Hughes, “Spacetime and orbits of bumpy black holes,” *Phys. Rev. D*, vol. 81, p. 024030, 2010.

[195] F. D. Ryan, “Gravitational waves from the inspiral of a compact object into a massive, axisymmetric body with arbitrary multipole moments,” *Phys. Rev. D*, vol. 52, pp. 5707–5718, 1995.

[196] F. D. Ryan, “Accuracy of estimating the multipole moments of a massive body from the gravitational waves of a binary inspiral,” *Phys. Rev. D*, vol. 56, pp. 1845–1855, 1997.

[197] F. D. Ryan, “Scalar waves produced by a scalar charge orbiting a massive body with arbitrary multipole moments,” *Phys. Rev. D*, vol. 56, pp. 7732–7739, 1997.

[198] L. Barack and C. Cutler, “LISA capture sources: Approximate waveforms, signal-to-noise ratios, and parameter estimation accuracy,” *Phys. Rev. D*, vol. 69, p. 082005, 2004.

[199] J. R. Gair, C. Li, and I. Mandel, “Observable Properties of Orbits in Exact Bumpy Spacetimes,” *Phys. Rev. D*, vol. 77, p. 024035, 2008.

[200] L. Barack and C. Cutler, “Using LISA EMRI sources to test off-Kerr deviations in the geometry of massive black holes,” *Phys. Rev. D*, vol. 75, p. 042003, 2007.

[201] C. Li and G. Lovelace, “A Generalization of Ryan’s theorem: Probing tidal coupling with gravitational waves from nearly circular, nearly equatorial, extreme-mass-ratio inspirals,” *Phys. Rev. D*, vol. 77, p. 064022, 2008.

[202] T. A. Apostolatos, G. Lukes-Gerakopoulos, and G. Contopoulos, “How to Observe a Non-Kerr Spacetime Using Gravitational Waves,” *Phys. Rev. Lett.*, vol. 103, p. 111101, 2009.

[203] S. A. Hughes, “Probing strong-field gravity and black holes with gravitational waves,” 2 2010.

[204] D. Psaltis and T. Johannsen, “Sgr A*: The Optimal Testbed of Strong-Field Gravity,” *J. Phys. Conf. Ser.*, vol. 283, p. 012030, 2011.

[205] C. M. Will, “Testing the general relativistic “no-hair” theorems using the galactic center black hole sagittarius a,” *The Astrophysical Journal*, vol. 674, no. 1, p. L25, 2008.

[206] D. Merritt, T. Alexander, S. Mikkola, and C. M. Will, “Testing Properties of the Galactic Center Black Hole Using Stellar Orbits,” *Phys. Rev. D*, vol. 81, p. 062002, 2010.

[207] N. Wex and S. Kopeikin, “Frame dragging and other precessional effects in black hole-pulsar binaries,” *Astrophys. J.*, vol. 514, p. 388, 1999.

[208] T. Johannsen and D. Psaltis, “Testing the No-hair Theorem with Observations in the Electromagnetic Spectrum. II. Black Hole Images,” *Astrophys. J.*, vol. 718, pp. 446–454, July 2010.

[209] D. Psaltis and T. Johannsen, “A Ray-Tracing Algorithm for Spinning Compact Object Spacetimes with Arbitrary Quadrupole Moments. I. Quasi-Kerr Black Holes,” *Astrophys. J.*, vol. 745, p. 1, 2012.

[210] C. Bambi and E. Barausse, “Constraining the quadrupole moment of stellar-mass black-hole candidates with the continuum fitting method,” *Astrophys. J.*, vol. 731, p. 121, 2011.

[211] C. Bambi, “Constraint on the quadrupole moment of super-massive black hole candidates from the estimate of the mean radiative efficiency of AGN,” *Phys. Rev. D*, vol. 83, p. 103003, 2011.

[212] T. Johannsen and D. Psaltis, “Testing the No-Hair Theorem with Observations of Black Holes in the Electromagnetic Spectrum,” *Adv. Space Res.*, vol. 47, pp. 528–532, 2011.

[213] C. M. Will, *Theory and experiment in gravitational physics*.
Cambridge University Press (Cambridge, 1993), 1953.

[214] N. Yunes and L. C. Stein, “Non-Spinning Black Holes in Alternative Theories of Gravity,” *Phys. Rev. D*, vol. 83, p. 104002, 2011.

[215] D.-C. Dai and D. Stojkovic, “Analytic solution for a static black hole in RSII model,” *Phys. Lett. B*, vol. 704, pp. 354–359, 2011.

[216] P. Pani and V. Cardoso, “Are black holes in alternative theories serious astrophysical candidates? The Case for Einstein-Dilaton-Gauss-Bonnet black holes,” *Phys. Rev. D*, vol. 79, p. 084031, 2009.

[217] E. T. Newman and A. I. Janis, “Note on the Kerr spinning particle metric,” *J. Math. Phys.*, vol. 6, pp. 915–917, 1965.

[218] J. G. Williams, S. G. Turyshev, and D. H. Boggs, “Progress in lunar laser ranging tests of relativistic gravity,” *Phys. Rev. Lett.*, vol. 93, p. 261101, 2004.

[219] R. Beig, “The static gravitational field near spatial infinity i,” *General Relativity and Gravitation*, vol. 12, pp. 439–451, 1980.

[220] R. Beig and W. Simon, “On the multipole expansion for stationary space-times,” *Proceedings of the Royal Society of London Series A*, vol. 376, pp. 333–341, May 1981.

[221] C. M. Will, “The Confrontation between general relativity and experiment,” *Living Rev. Rel.*, vol. 9, p. 3, 2006.

[222] F. Atamurotov, A. Abdujabbarov, and B. Ahmedov, “Shadow of rotating non-Kerr black hole,” *Phys. Rev. D*, vol. 88, p. 064004, Sept. 2013.

[223] C. Bambi, “Can we constrain the maximum value for the spin parameter of the super-massive objects in galactic nuclei without knowing their actual nature?,” *Phys. Lett. B*, vol. 705, pp. 5–8, 2011.

[224] C. Bambi, F. Caravelli, and L. Modesto, “Direct imaging rapidly-rotating non-Kerr black holes,” *Phys. Lett. B*, vol. 711, pp. 10–14, 2012.

[225] C. Liu, S. Chen, and J. Jing, “Rotating non-Kerr black hole and energy extraction,” *Astrophys. J.*, vol. 751, p. 148, 2012.

[226] S. Chen and J. Jing, “Strong gravitational lensing by a rotating non-Kerr compact object,” *Phys. Rev. D*, vol. 85, p. 124029, 2012.

[227] H. Krawczynski, “Tests of General Relativity in the Strong Gravity Regime Based on X-Ray Spectropolarimetric Observations of Black Holes in X-Ray Binaries,” *Astrophys. J.*, vol. 754, p. 133, 2012.

[228] K. Yagi and L. C. Stein, “Black hole based tests of general relativity,” *Classical and Quantum Gravity*, vol. 33, p. 054001, Mar. 2016.

[229] Z. Younsi, A. Zhidenko, L. Rezzolla, R. Konoplya, and Y. Mizuno, “New method for shadow calculations: Application to parametrized axisymmetric black holes,” *Phys. Rev. D*, vol. 94, p. 084025, Oct. 2016.

[230] P. Bambhaniya, D. Dey, A. B. Joshi, P. S. Joshi, D. N. Solanki, and A. Mehta, “Shadows and negative precession in non-Kerr spacetime,” *Phys. Rev. D*, vol. 103, p. 084005, Apr. 2021.

[231] C.-Y. Chen and H.-Y. K. Yang, “Curved accretion disks around rotating black holes without reflection symmetry,” *Eur. Phys. J. C*, vol. 82, no. 4, p. 307, 2022.

[232] J. F. Lu, “Non-uniqueness of transonic solution for accretion onto a Schwarzschild black hole.,” *Astron. Astrophys.*, vol. 148, pp. 176–178, July 1985.

[233] L. D. Landau and E. M. Lifshitz, *Fluid mechanics: Landau And Lifshitz: course of theoretical physics, Volume 6*, vol. 6.
Elsevier, 2013.

[234] S. M. Carroll, *Spacetime and Geometry*.
Cambridge University Press, 7 2019.

[235] A. K. Ahmed, M. Azreg-Aïnou, S. Bahamonde, S. Capozziello, and M. Jamil, "Astrophysical flows near $f(T)$ gravity black holes," *Eur. Phys. J. C*, vol. 76, no. 5, p. 269, 2016.

[236] M. Azreg-Aïnou, "Accretion of rotating fluids onto stationary solutions," *Physical Review D*, vol. 95, no. 8, p. 083002, 2017.

[237] M. Azreg-Aïnou, A. K. Ahmed, and M. Jamil, "Spherical accretion by normal and phantom einstein–maxwell–dilaton black holes," *Classical and Quantum Gravity*, vol. 35, no. 23, p. 235001, 2018.

[238] S. Bahamonde and M. Jamil, "Accretion Processes for General Spherically Symmetric Compact Objects," *Eur. Phys. J. C*, vol. 75, p. 508, 2015.

[239] I. K. Dihingia, S. Das, and A. Nandi, "Low angular momentum relativistic hot accretion flow around Kerr black holes with variable adiabatic index," *Mon. Not. Roy. Astron. Soc.*, vol. 484, pp. 3209–3218, Apr. 2019.

[240] I. Chattopadhyay and D. Ryu, "Effects of Fluid Composition on Spherical Flows Around Black Holes," *Astrophys. J.*, vol. 694, pp. 492–501, Mar. 2009.

[241] R. Kumar, C. B. Singh, I. Chattopadhyay, and S. K. Chakrabarti, "Effect of the flow composition on outflow rates from accretion discs around black holes," *Mon. Not. Roy. Astron. Soc.*, vol. 436, pp. 2864–2873, Dec. 2013.

[242] I. Chattopadhyay and R. Kumar, "Viscous accretion disc around black holes with variable adiabatic index," in *Astronomical Society of India Conference Series*, vol. 8 of *Astronomical Society of India Conference Series*, p. 19, Jan. 2013.

[243] J. P. Lasota, "Slim accretion disks," in *Theory of Accretion Disks - 2* (W. J. Duschl, J. Frank, F. Meyer, E. Meyer-Hofmeister, and W. M. Tscharnuter, eds.), vol. 417 of *NATO Advanced Study Institute (ASI) Series C*, p. 341, Jan. 1994.

[244] E. P. T. Liang and K. A. Thompson, "Transonic disk accretion onto black holes.," *Astrophys. J.*, vol. 240, pp. 271–274, Aug. 1980.

[245] M. A. Abramowicz and W. H. Zurek, "Rotation-induced bistability of transonic accretion onto a black hole," *Astrophys. J.*, vol. 246, pp. 314–320, May 1981.

[246] S. Das, "Behaviour of dissipative accretion flows around black holes," *Mon. Not. Roy. Astron. Soc.*, vol. 376, pp. 1659–1670, Apr. 2007.

[247] S. K. Chakrabarti and S. Das, “Properties of accretion shock waves in viscous flows around black holes,” *Mon. Not. Roy. Astron. Soc.*, vol. 349, pp. 649–664, Apr. 2004.

[248] A. K. Ahmed, M. Azreg-Aïnou, M. Faizal, and M. Jamil, “Cyclic and heteroclinic flows near general static spherically symmetric black holes,” *Eur. Phys. J. C*, vol. 76, no. 5, p. 280, 2016.

[249] M. Azreg-Aïnou, “Cyclic and heteroclinic flows near general static spherically symmetric black holes: Semi-cyclic flows – Addendum and corrigendum,” *Eur. Phys. J. C*, vol. 77, no. 1, p. 36, 2017.

[250] R. Yang and M. Kafatos, “Shock study in fully relativistic isothermal flows. II.,” *Astron. Astrophys.*, vol. 295, pp. 238–244, Mar. 1995.

[251] I. K. Dihingia, S. Das, and S. Mandal, “Properties of two-temperature dissipative accretion flow around black holes,” *Mon. Not. Roy. Astron. Soc.*, vol. 475, pp. 2164–2177, Apr. 2018.

[252] I. K. Dihingia, S. Das, and S. Mandal, “A comparative study of single-temperature and two-temperature accretion flows around black holes,” *Journal of Astrophysics and Astronomy*, vol. 39, no. 1, pp. 1–7, 2018.

[253] P. A. Becker and D. Kazanas, “Exact Expressions for the Critical Mach Numbers in the Two-Fluid Model of Cosmic-Ray-modified Shocks,” *Astrophys. J.*, vol. 546, pp. 429–446, Jan. 2001.

[254] A. H. Taub, “Relativistic Rankine-Hugoniot Equations,” *Physical Review*, vol. 74, pp. 328–334, Aug. 1948.

[255] A. Nandi, S. Mandal, H. Sreehari, D. Radhika, S. Das, I. Chattopadhyay, N. Iyer, V. K. Agrawal, and R. Aktar, “Accretion flow dynamics during 1999 outburst of XTE J1859+226—modeling of broadband spectra and constraining the source mass,” *Astrophys. Space Sci.*, vol. 363, p. 90, May 2018.

[256] S. Das and S. K. Chakrabarti, “Dissipative accretion flows around a rotating black hole,” *Mon. Not. Roy. Astron. Soc.*, vol. 389, pp. 371–378, Sept. 2008.

[257] J. R. Oppenheimer and H. Snyder, “On continued gravitational contraction,” *Physical Review*, vol. 56, no. 5, p. 455, 1939.

[258] D. M. Eardley and L. Smarr, “Time function in numerical relativity. Marginally bound dust collapse,” *Phys. Rev. D*, vol. 19, pp. 2239–2259, 1979.

[259] S. L. Shapiro and S. A. Teukolsky, “Formation of naked singularities: the violation of cosmic censorship,” *Physical review letters*, vol. 66, no. 8, p. 994, 1991.

[260] P. S. Joshi and I. H. Dwivedi, “Naked singularities in spherically symmetric inhomogeneous tolman-bondi dust cloud collapse,” *Phys. Rev. D*, vol. 47, pp. 5357–5369, Jun 1993.

[261] A. Ilha and J. P. S. Lemos, “Dimensionally continued Oppenheimer-Snyder gravitational collapse. 1. Solutions in even dimensions,” *Phys. Rev. D*, vol. 55, pp. 1788–1794, 1997.

[262] S. Jhingan, P. S. Joshi, and T. P. Singh, “The Final fate of spherical inhomogeneous dust collapse. 2. Initial data and causal structure of singularity,” *Class. Quant. Grav.*, vol. 13, pp. 3057–3068, 1996.

[263] G. Magli, “Gravitational collapse with non-vanishing tangential stresses: a generalization of the tolman-bondi model,” *Classical and Quantum Gravity*, vol. 14, no. 7, p. 1937, 1997.

[264] G. Magli, “Gravitational collapse with nonvanishing tangential stresses. 2. Extension to the charged case and general solution,” *Class. Quant. Grav.*, vol. 15, p. 3215, 1998.

[265] S. S. Deshingkar, P. S. Joshi, and I. H. Dwivedi, “Physical nature of the central singularity in spherical collapse,” *Phys. Rev. D*, vol. 59, p. 044018, Jan 1999.

[266] S. Barve, T. P. Singh, C. Vaz, and L. Witten, “A simple derivation of the naked singularity in spherical dust collapse,” *Class. Quant. Grav.*, vol. 16, pp. 1727–1732, 1999.

[267] T. Harada, K.-i. Nakao, and H. Iguchi, “Nakedness and curvature strength of shell focusing singularity in the spherically symmetric space-time with vanishing radial pressure,” *Class. Quant. Grav.*, vol. 16, pp. 2785–2796, 1999.

[268] F. C. Mena, R. Tavakol, and P. S. Joshi, “Initial data and spherical dust collapse,” *Phys. Rev. D*, vol. 62, p. 044001, Jul 2000.

[269] S. G. Ghosh and A. Beesham, “Naked singularities in higher dimensional inhomogeneous dust collapse,” *Classical and Quantum Gravity*, vol. 17, pp. 4959–4965, Dec. 2000.

[270] T. Harada, H. Iguchi, and K.-i. Nakao, “Physical processes in naked singularity formation,” *Prog. Theor. Phys.*, vol. 107, pp. 449–524, 2002.

[271] R. Giambo, F. Giannoni, G. Magli, and P. Piccione, “New mathematical framework for spherical gravitational collapse,” *Class. Quant. Grav.*, vol. 20, p. L75, 2003.

[272] R. Goswami and P. S. Joshi, “Gravitational collapse of an isentropic perfect fluid with a linear equation of state,” *Class. Quant. Grav.*, vol. 21, pp. 3645–3654, 2004.

[273] P. S. Joshi and D. Malafarina, “Recent developments in gravitational collapse and spacetime singularities,” *Int. J. Mod. Phys. D*, vol. 20, pp. 2641–2729, 2011.

[274] P. S. Joshi, D. Malafarina, and R. V. Saraykar, “Genericity aspects in gravitational collapse to black holes and naked singularities,” *Int. J. Mod. Phys. D*, vol. 21, p. 1250066, 2012.

[275] K. Mosani, D. Dey, and P. S. Joshi, “Strong curvature naked singularities in spherically symmetric perfect fluid collapse,” *Phys. Rev. D*, vol. 101, p. 044052, Feb 2020.

[276] K. Mosani, D. Dey, and P. S. Joshi, “Global visibility of a strong curvature singularity in nonmarginally bound dust collapse,” *Phys. Rev. D*, vol. 102, p. 044037, Aug 2020.

[277] K. Mosani, D. Dey, and P. S. Joshi, “Globally visible singularity in an astrophysical setup,” *Mon. Not. Roy. Astron. Soc.*, vol. 504, no. 4, pp. 4743–4750, 2021.

[278] D. Dey, P. S. Joshi, K. Mosani, and V. Vertogradov, “Causal structure of singularity in non-spherical gravitational collapse,” *Eur. Phys. J. C*, vol. 82, no. 5, p. 431, 2022.

[279] K. Mosani, D. Dey, P. S. Joshi, G. C. Samanta, H. Menon, and V. D. Patel, “On the visibility of singularities in general relativity and modified gravity theories,” *Class. Quant. Grav.*, vol. 40, no. 14, p. 145015, 2023.

[280] R. Penrose, “Gravitational collapse and space-time singularities,” *Phys. Rev. Lett.*, vol. 14, pp. 57–59, 1965.

[281] R. Penrose, “Gravitational Collapse: the Role of General Relativity,” *Nuovo Cimento Rivista Serie*, vol. 1, p. 252, Jan. 1969.

[282] D. Christodoulou, “Violation of cosmic censorship in the gravitational collapse of a dust cloud,” *Commun. Math. Phys.*, vol. 93, pp. 171–195, 1984.

[283] R. Penrose, ““Golden Oldie”: Gravitational Collapse: The Role of General Relativity,” *General Relativity and Gravitation*, vol. 7, pp. 1141–1165, July 2002.

[284] H. Reissner, “Über die Eigengravitation des elektrischen Feldes nach der Einsteinschen Theorie,” *Annalen Phys.*, vol. 355, no. 9, pp. 106–120, 1916.

[285] G. Nordström, “On the energy of the gravitation field in einstein’s theory,” *Koninklijke Nederlandse Akademie van Wetenschappen Proceedings Series B Physical Sciences*, vol. 20, pp. 1238–1245, 1918.

[286] R. P. Kerr, “Gravitational field of a spinning mass as an example of algebraically special metrics,” *Phys. Rev. Lett.*, vol. 11, pp. 237–238, Sep 1963.

[287] T. Adamo and E. T. Newman, “The Kerr-Newman metric: A Review,” *Scholarpedia*, vol. 9, p. 31791, 2014.

[288] H. A. Buchdahl, “Non-linear Lagrangians and cosmological theory,” *Mon. Not. Roy. Astron. Soc.*, vol. 150, p. 1, 1970.

[289] A. A. Starobinsky, “A New Type of Isotropic Cosmological Models Without Singularity,” *Phys. Lett. B*, vol. 91, pp. 99–102, 1980.

[290] R. Garattini, “Naked Singularity in a Modified Gravity Theory,” *J. Phys. Conf. Ser.*, vol. 174, p. 012066, 2009.

[291] A. H. Ziaie, K. Atazadeh, and S. M. M. Rasouli, “Naked Singularity Formation In f(R) Gravity,” *Gen. Rel. Grav.*, vol. 43, pp. 2943–2963, 2011.

[292] S. Nojiri, S. D. Odintsov, and V. K. Oikonomou, “Modified Gravity Theories on a Nutshell: Inflation, Bounce and Late-time Evolution,” *Phys. Rept.*, vol. 692, pp. 1–104, 2017.

[293] C. Bambi, K. Freese, T. Harada, R. Takahashi, and N. Yoshida, “Accretion process onto super-spinning objects,” *Phys. Rev. D*, vol. 80, p. 104023, Nov 2009.

[294] Z. Kovács and T. Harko, “Can accretion disk properties observationally distinguish black holes from naked singularities?,” *Phys. Rev. D*, vol. 82, p. 124047, Dec 2010.

[295] A. N. Chowdhury, M. Patil, D. Malafarina, and P. S. Joshi, “Circular geodesics and accretion disks in Janis-Newman-Winicour and Gamma metric,” *Phys. Rev. D*, vol. 85, p. 104031, 2012.

[296] P. S. Joshi, D. Malafarina, and R. Narayan, “Distinguishing black holes from naked singularities through their accretion disc properties,” *Class. Quant. Grav.*, vol. 31, p. 015002, 2014.

[297] R. S. S. Vieira, J. Schee, W. Kluźniak, Z. c. v. Stuchlík, and M. Abramowicz, “Circular geodesics of naked singularities in the kehagias-sfetsos metric of hořava’s gravity,” *Phys. Rev. D*, vol. 90, p. 024035, Jul 2014.

[298] D. Dey, P. S. Joshi, A. Joshi, and P. Bambhaniya, “Towards an observational test of black hole versus naked singularity at the galactic center,” *Int. J. Mod. Phys. D*, vol. 28, no. 14, p. 1930024, 2019.

[299] P. Bambhaniya, A. B. Joshi, D. Dey, and P. S. Joshi, “Timelike geodesics in naked singularity and black hole spacetimes,” *Phys. Rev. D*, vol. 100, p. 124020, Dec 2019.

[300] D. Dey, R. Shaikh, and P. S. Joshi, “Perihelion precession and shadows near black holes and naked singularities,” *Phys. Rev. D*, vol. 102, p. 044042, Aug 2020.

[301] J.-Q. Guo, P. S. Joshi, R. Narayan, and L. Zhang, “Accretion disks around naked singularities,” *Class. Quant. Grav.*, vol. 38, no. 3, p. 035012, 2021.

[302] A. B. Joshi, D. Dey, P. S. Joshi, and P. Bambhaniya, “Shadow of a Naked Singularity without Photon Sphere,” *Phys. Rev. D*, vol. 102, no. 2, p. 024022, 2020.

[303] D. Tahelyani, A. B. Joshi, D. Dey, and P. S. Joshi, “Comparing thin accretion disk properties of naked singularities and black holes,” *Phys. Rev. D*, vol. 106, no. 4, p. 044036, 2022.

[304] R. S. S. Vieira and W. Kluźniak, “Astrophysical cloaking of a naked singularity,” *Mon. Not. Roy. Astron. Soc.*, vol. 523, no. 3, pp. 4615–4623, 2023.

[305] W. Kluźniak and T. Krajewski, “Outflows from naked singularities, infall through the black hole horizon: Hydrodynamic simulations of accretion in the reissner-nordström space-time,” *Phys. Rev. Lett.*, vol. 133, p. 241401, Dec 2024.

[306] I. K. Dihingia, A. Uniyal, and Y. Mizuno, “Distinguishability of a Naked Singularity from a Black Hole in Dynamics and Radiative Signatures,” *Astrophys. J.*, vol. 978, no. 1, p. 44, 2025.

[307] M. Čemeljić, W. Kluźniak, R. Mishra, and M. Wielgus, “Pseudo-Newtonian simulation of a thin accretion disk around a Reissner-Nordström naked singularity,” 1 2025.

[308] S. K. Chakrabarti and S. G. Manickam, “Correlation among quasi-periodic oscillation frequencies and quiescent-state duration in black hole candidate grs 1915+ 105,” *The Astrophysical Journal*, vol. 531, no. 1, p. L41, 2000.

[309] R. Yarza, G. N. Wong, B. R. Ryan, and C. F. Gammie, “Bremsstrahlung in GRMHD models of accreting black holes,” *Astrophys. J.*, vol. 898, no. 1, p. 50, 2020.

[310] G. B. Rybicki and A. P. Lightman, *Radiative processes in astrophysics*. John Wiley & Sons, 1991.

[311] W. Karzas and R. Latter, “Electron radiative transitions in a coulomb field.,” *Astrophysical Journal Supplement, vol. 6, p. 167*, vol. 6, p. 167, 1961.

[312] P. Brussaard and H. Van de Hulst, “Approximation formulas for nonrelativistic bremsstrahlung and average gaunt factors for a maxwellian electron gas,” *Reviews of Modern Physics*, vol. 34, no. 3, p. 507, 1962.

[313] R. Svensson, “ELECTRON POSITRON PAIR EQUILIBRIA IN RELATIVISTIC PLASMAS,” *Astrophys. J.*, vol. 258, pp. 335–348, 1982.

[314] S. Nozawa, K. Takahashi, Y. Kohyama, and N. Itoh, “Analytic fitting formulae for relativistic electron-electron thermal bremsstrahlung,” *Astronomy & Astrophysics*, vol. 499, no. 3, pp. 661–667, 2009.

[315] I. K. Dihingia, S. Das, G. Prabhakar, and S. Mandal, “Properties of two-temperature magnetized advective accretion flow around rotating black hole,” *Monthly Notices of the Royal Astronomical Society*, vol. 496, no. 3, pp. 3043–3059, 2020.

[316] J.-P. Luminet, “Image of a spherical black hole with thin accretion disk,” *Astronomy and Astrophysics*, vol. 75, pp. 228–235, 1979.

[317] M. Colpi, L. Maraschi, and A. Treves, “Two-temperature model of spherical accretion onto a black hole,” *Astrophysical Journal, Part 1 (ISSN 0004-637X), vol. 280, May 1, 1984, p. 319-327.*, vol. 280, pp. 319–327, 1984.

[318] S. Rajesh and B. Mukhopadhyay, “Two-temperature accretion around rotating black holes: a description of the general advective flow paradigm in the presence of various cooling processes to explain low to high luminous sources,” *Monthly Notices of the Royal Astronomical Society*, vol. 402, no. 2, pp. 961–984, 2010.

[319] S. Sarkar and I. Chattopadhyay, “General relativistic two-temperature accretion solutions for spherical flows around black holes,” *Int. J. Mod. Phys. D*, vol. 28, no. 02, p. 1950037, 2018.

[320] A. Chael, R. Narayan, and M. D. Johnson, “Two-temperature, Magnetically Arrested Disc simulations of the jet from the supermassive black hole in M87,” *Mon. Not. Roy. Astron. Soc.*, vol. 486, no. 2, pp. 2873–2895, 2019.

[321] B. R. Ryan, S. M. Ressler, J. C. Dolence, A. Tchekhovskoy, C. Gammie, and E. Quataert, “The radiative efficiency and spectra of slowly accreting black holes from two-temperature grrmhd simulations,” *The Astrophysical Journal Letters*, vol. 844, no. 2, p. L24, 2017.

[322] S. L. Shapiro and S. A. Teukolsky, *Black holes, white dwarfs, and neutron stars: The physics of compact objects*.
John Wiley & Sons, 2008.

[323] P. S. Joshi, D. Malafarina, and R. Narayan, “Equilibrium configurations from gravitational collapse,” *Class. Quant. Grav.*, vol. 28, p. 235018, 2011.

[324] L. Gou, J. E. McClintock, J. Liu, R. Narayan, J. F. Steiner, R. A. Remillard, J. A. Orosz, S. W. Davis, K. Ebisawa, and E. M. Schlegel, “A determination of the spin of the black hole primary in lmc x-1,” *The Astrophysical Journal*, vol. 701, no. 2, p. 1076, 2009.

[325] T. Johannsen and D. Psaltis, “Testing the No-hair Theorem with Observations in the Electromagnetic Spectrum. III. Quasi-periodic Variability,” *Astrophys. J.*, vol. 726, p. 11, Jan. 2011.

[326] S. Barman and S. Mukherjee, “Thermal behavior of a radially deformed black hole spacetime,” *Eur. Phys. J. C*, vol. 81, no. 5, p. 453, 2021.

[327] I. Chattopadhyay and S. K. Chakrabarti, “A comparative study of bondi-type and radiative outflows around compact objects,” *International Journal of Modern Physics D*, vol. 9, no. 06, pp. 717–731, 2000.

[328] S. K. Chakrabarti, “Grand unification of solutions of accretion and winds around black holes and neutron stars,” *Astrophys. J.*, vol. 464, p. 664, 1996.

[329] K. Chatterjee, S. Mondal, C. B. Singh, and M. Sugizaki, “Insight-HXMT View of the BHC Swift J1727.8-1613 during its outburst in 2023,” 5 2024.

[330] D. M. Molteni, H. Sponholz, and S. K. Chakrabarti, “Resonance oscillation of radiative shock waves in accretion disks around compact objects,” *Astrophys. J.*, vol. 457, p. 805, 1996.

[331] S. K. Chakrabarti, S. Mondal, and D. Debnath, “Resonance condition and low-frequency quasi-periodic oscillations of the outbursting source H1743−322,” *Mon. Not. Roy. Astron. Soc.*, vol. 452, no. 4, pp. 3451–3456, 2015.

[332] J. Kim, S. K. Garain, S. K. Chakrabarti, and D. S. Balsara, “General relativistic numerical simulation of sub-Keplerian transonic accretion flows on to rotating black holes: Kerr space–time,” *Mon. Not. Roy. Astron. Soc.*, vol. 482, no. 3, pp. 3636–3645, 2019.

[333] J. Homan, R. Wijnands, M. van der Klis, T. Belloni, J. van Paradijs, M. Klein-Wolt, R. P. Fender, and M. Mendez, “Correlated x-ray spectral and timing behavior of the black hole candidate XTE J1550-564: A New interpretation of black hole states,” *Astrophys. J. Suppl.*, vol. 132, pp. 377–402, 2001.

[334] J. M. Miller, R. Wijnands, J. Homan, T. Belloni, D. Pooley, S. Corbel, C. Kouveliotou, M. van der Klis, and W. H. G. Lewin, “High-Frequency Quasi-Periodic Oscillations in the 2000 Outburst of the Galactic Microquasar XTE J1550-564,” *The Astrophysical Journal*, vol. 563, pp. 928–933, Dec. 2001.

[335] J. Homan, J. M. Miller, R. Wijnands, M. van der Klis, T. Belloni, D. Steeghs, and W. H. G. Lewin, “High- and low-frequency quasiperiodic oscillations in the x-ray light curves of the black hole transient H1743-332,” *Astrophys. J.*, vol. 623, pp. 383–391, 2005.

[336] R. A. Remillard, J. E. McClintock, J. A. Orosz, and A. M. Levine, “The X-ray outburst of H1743-322: High-frequency QPOs with a 3:2 frequency ratio,” *Astrophys. J.*, vol. 637, pp. 1002–1009, 2006.

[337] J. A. Orosz, J. F. Steiner, J. E. McClintock, M. A. P. Torres, R. A. Remillard, C. D. Bailyn, and J. M. Miller, “An Improved Dynamical Model for the Microquasar XTE J1550-564,” *Astrophys. J.*, vol. 730, p. 75, 2011.

[338] J. F. Steiner, R. C. Reis, J. E. McClintock, R. Narayan, R. A. Remillard, J. A. Orosz, L. Gou, A. C. Fabian, and M. A. P. Torres, “The Spin of the Black Hole Microquasar XTE J1550-564 via the Continuum-Fitting and Fe-Line Methods,” *Mon. Not. Roy. Astron. Soc.*, vol. 416, pp. 941–958, 2011.

[339] J. F. Steiner, J. E. McClintock, and M. J. Reid, “The Distance, Inclination, and Spin of the Black Hole Microquasar H1743-322,” *Astrophys. J. Lett.*, vol. 745, p. L7, 2012.

[340] R. Abuter *et al.*, “Detection of the Schwarzschild precession in the orbit of the star S2 near the Galactic centre massive black hole,” *Astron. Astrophys.*, vol. 636, p. L5, 2020.

[341] I. De Martino, R. della Monica, and M. De Laurentis, “$f(r)$ gravity after the detection of the orbital precession of the s2 star around the galactic center massive black hole,” *Phys. Rev. D*, vol. 104, p. L101502, Nov 2021.

[342] N. Galikyan, S. Khlghatyan, A. A. Kocharyan, and V. G. Gurzadyan, “S2-star dynamics probing the Galaxy core cluster,” *Eur. Phys. J. Plus*, vol. 139, p. 821, 2024.

[343] P. Brax, “What makes the Universe accelerate? A review on what dark energy could be and how to test it,” *Rept. Prog. Phys.*, vol. 81, no. 1, p. 016902, 2018.

[344] F. Kahlhoefer, “Review of LHC Dark Matter Searches,” *Int. J. Mod. Phys. A*, vol. 32, no. 13, p. 1730006, 2017.

[345] G. Bertone and T. M. Tait, “A new era in the search for dark matter,” *Nature*, vol. 562, no. 7725, pp. 51–56, 2018.

[346] G. Bertone and D. Hooper, “History of dark matter,” *Rev. Mod. Phys.*, vol. 90, p. 045002, Oct 2018.

[347] I. de Martino, S. S. Chakrabarty, V. Cesare, A. Gallo, L. Ostorero, and A. Diaferio, “Dark matters on the scale of galaxies,” *Universe*, vol. 6, no. 8, p. 107, 2020.

[348] C. Pérez de los Heros, “Status, Challenges and Directions in Indirect Dark Matter Searches,” *Symmetry*, vol. 12, no. 10, p. 1648, 2020.

[349] J. F. Navarro, C. S. Frenk, and S. D. M. White, “The Structure of cold dark matter halos,” *Astrophys. J.*, vol. 462, pp. 563–575, 1996.

[350] G. Bertone, D. Hooper, and J. Silk, “Particle dark matter: Evidence, candidates and constraints,” *Phys. Rept.*, vol. 405, pp. 279–390, 2005.

[351] D. Clowe, M. Bradac, A. H. Gonzalez, M. Markevitch, S. W. Randall, C. Jones, and D. Zaritsky, “A direct empirical proof of the existence of dark matter,” *Astrophys. J. Lett.*, vol. 648, pp. L109–L113, 2006.

[352] K. Freese, “Review of Observational Evidence for Dark Matter in the Universe and in upcoming searches for Dark Stars,” *EAS Publ. Ser.*, vol. 36, pp. 113–126, 2009.

[353] K. Eda, Y. Itoh, S. Kuroyanagi, and J. Silk, “New Probe of Dark-Matter Properties: Gravitational Waves from an Intermediate-Mass Black Hole Embedded in a Dark-Matter Minispike,” *Phys. Rev. Lett.*, vol. 110, no. 22, p. 221101, 2013.

[354] C. F. B. Macedo, P. Pani, V. Cardoso, and L. C. B. Crispino, “Into the lair: gravitational-wave signatures of dark matter,” *Astrophys. J.*, vol. 774, p. 48, 2013.

[355] E. Barausse, V. Cardoso, and P. Pani, “Can environmental effects spoil precision gravitational-wave astrophysics?,” *Phys. Rev. D*, vol. 89, no. 10, p. 104059, 2014.

[356] B. J. Kavanagh, D. A. Nichols, G. Bertone, and D. Gaggero, “Detecting dark matter around black holes with gravitational waves: Effects of dark-matter dynamics on the gravitational waveform,” *Phys. Rev. D*, vol. 102, no. 8, p. 083006, 2020.

[357] I. King, “The structure of star clusters. I. An Empirical density law,” *Astron. J.*, vol. 67, p. 471, 1962.

[358] J. Einasto, “On the construction of a composite model for the galaxy and on the determination of the system of galactic parameters,” *Trudy Astrofizicheskogo Instituta Alma-Ata, Vol. 5, p. 87-100, 1965*, vol. 5, pp. 87–100, 1965.

[359] W. Jaffe, “A Simple model for the distribution of light in spherical galaxies,” *Mon. Not. Roy. Astron. Soc.*, vol. 202, pp. 995–999, 1983.

[360] A. Burkert, “The structure of dark matter halos in dwarf galaxies,” *The Astrophysical Journal*, vol. 447, no. 1, p. L25, 1995.

[361] B. Moore, T. R. Quinn, F. Governato, J. Stadel, and G. Lake, “Cold collapse and the core catastrophe,” *Mon. Not. Roy. Astron. Soc.*, vol. 310, pp. 1147–1152, 1999.

[362] A. Di Cintio, C. B. Brook, A. A. Dutton, A. V. Macciò, G. S. Stinson, and A. Knebe, “A mass-dependent density profile for dark matter haloes including the influence of galaxy formation,” *Mon. Not. Roy. Astron. Soc.*, vol. 441, no. 4, pp. 2986–2995, 2014.

[363] H. Nishikawa, E. D. Kovetz, M. Kamionkowski, and J. Silk, “Primordial-black-hole mergers in dark-matter spikes,” *Phys. Rev. D*, vol. 99, no. 4, p. 043533, 2019.

[364] Z. Xu, X. Hou, X. Gong, and J. Wang, “Black Hole Space-time In Dark Matter Halo,” *JCAP*, vol. 09, p. 038, 2018.

[365] L. S. Bhandari and A. M. Thalapillil, “Exploring millicharged dark matter components from the shadows,” *JCAP*, vol. 03, no. 03, p. 043, 2022.

[366] R. A. Konoplya and A. Zhidenko, “Solutions of the Einstein Equations for a Black Hole Surrounded by a Galactic Halo,” *Astrophys. J.*, vol. 933, no. 2, p. 166, 2022.

[367] V. De Luca and J. Khoury, “Superfluid dark matter around black holes,” *JCAP*, vol. 04, p. 048, 2023.

[368] R. Acharyya, P. Banerjee, and S. Kar, “Modelling Einstein cluster using Einasto profile,” *JCAP*, vol. 04, p. 070, 2024.

[369] D. Liu, Y. Yang, and Z.-W. Long, “Probing black holes in a dark matter spike of M87 using quasinormal modes,” *Eur. Phys. J. C*, vol. 84, no. 7, p. 731, 2024.

[370] R. Bécar, P. A. González, E. Papantonopoulos, and Y. Vásquez, "Massive scalar field perturbations of black holes immersed in Chaplygin-like dark fluid," *JCAP*, vol. 06, p. 061, 2024.

[371] M. M. Gohain, P. Phukon, and K. Bhuyan, "Thermodynamics and null geodesics of a Schwarzschild black hole surrounded by a Dehnen type dark matter halo," *Phys. Dark Univ.*, vol. 46, p. 101683, 2024.

[372] E. Retana-Montenegro, E. Van Hese, G. Gentile, M. Baes, and F. Frutos-Alfaro, "Analytical properties of Einasto dark matter haloes," *Astron. Astrophys.*, vol. 540, p. A70, 2012.

[373] K. Jusufi, M. Jamil, and T. Zhu, "Shadows of Sgr A* black hole surrounded by superfluid dark matter halo," *Eur. Phys. J. C*, vol. 80, no. 5, p. 354, 2020.

[374] S. Nampalliwar, S. Kumar, K. Jusufi, Q. Wu, M. Jamil, and P. Salucci, "Modeling the Sgr A* Black Hole Immersed in a Dark Matter Spike," *Astrophys. J.*, vol. 916, no. 2, p. 116, 2021.

[375] T. Igata, T. Harada, H. Saida, and Y. Takamori, "Periapsis shifts in dark matter distribution around a black hole," *Int. J. Mod. Phys. D*, vol. 32, no. 16, p. 2350105, 2023.

[376] N. Dai, Y. Gong, Y. Zhao, and T. Jiang, "Extreme mass ratio inspirals in galaxies with dark matter halos," *Phys. Rev. D*, vol. 110, no. 8, p. 084080, 2024.

[377] Y. S. Myung, "Shadow bound of black holes with dark matter halo," 2 2024.

[378] S. Kazempour, S. Sun, and C. Yu, "Accreting black holes in dark matter halos," *Phys. Rev. D*, vol. 110, no. 4, p. 043034, 2024.

[379] M. Heydari-Fard, M. Heydari-Fard, and N. Riazi, "Galactic black hole immersed in a dark halo with its surrounding thin accretion disk," 8 2024.

[380] R.-Y. Chen, F. Javed, D. G. Mustafa, S. K. Maurya, and S. Ray, "Dual effect of string cloud and dark matter halos on particle motions, shadows and epicyclic oscillations around Schwarzschild black holes," *JHEAp*, vol. 44, pp. 172–186, 2024.

[381] Q. Tan, W. Deng, S. Long, and J. Jing, "Motion of spinning particles around black hole in a dark matter halo," 9 2024.

[382] Y. Zhao, N. Dai, and Y. Gong, "Distinguishing dark matter halos with Extreme mass ratio inspirals," 10 2024.

[383] A. Mollicone and K. Destounis, "Superradiance of charged black holes embedded in dark matter halos," *Phys. Rev. D*, vol. 111, no. 2, p. 024017, 2025.

[384] R. A. Konoplya, "Black holes in galactic centers: Quasinormal ringing, grey-body factors and Unruh temperature," *Phys. Lett. B*, vol. 823, p. 136734, 2021.

[385] Z. Stuchlík and J. Vrba, "Supermassive black holes surrounded by dark matter modeled as anisotropic fluid: epicyclic oscillations and their fitting to observed QPOs," *JCAP*, vol. 11, no. 11, p. 059, 2021.

[386] J. Liu, S. Chen, and J. Jing, "Tidal effects of a dark matter halo around a galactic black hole*," *Chin. Phys. C*, vol. 46, no. 10, p. 105104, 2022.

[387] R. L. Arnowitt, S. Deser, and C. W. Misner, "Coordinate invariance and energy expressions in general relativity," *Phys. Rev.*, vol. 122, p. 997, 1961.

[388] J. F. Navarro, C. S. Frenk, and S. D. M. White, "A Universal density profile from hierarchical clustering," *Astrophys. J.*, vol. 490, pp. 493–508, 1997.

[389] K. Chatterjee, S. Mondal, C. B. Singh, and M. Sugizaki, "Insight-HXMT View of the Black Hole Candidate Swift J1727.8–1613 during Its Outburst in 2023," *Astrophys. J.*, vol. 977, no. 2, p. 148, 2024.

[390] K. Destounis, A. Kulathingal, K. D. Kokkotas, and G. O. Papadopoulos, "Gravitational-wave imprints of compact and galactic-scale environments in extreme-mass-ratio binaries," *Phys. Rev. D*, vol. 107, no. 8, p. 084027, 2023.

[391] K. Akiyama *et al.*, "First Sagittarius A* Event Horizon Telescope Results. I. The Shadow of the Supermassive Black Hole in the Center of the Milky Way," *Astrophys. J. Lett.*, vol. 930, no. 2, p. L12, 2022.

[392] Y. Mizuno, Z. Younsi, C. M. Fromm, O. Porth, M. De Laurentis, H. Olivares, H. Falcke, M. Kramer, and L. Rezzolla, "The Current Ability to Test Theories of Gravity with Black Hole Shadows," *Nature Astron.*, vol. 2, no. 7, pp. 585–590, 2018.

[393] P. Kocherlakota *et al.*, "Constraints on black-hole charges with the 2017 EHT observations of M87*," *Phys. Rev. D*, vol. 103, no. 10, p. 104047, 2021.

[394] K. Akiyama *et al.*, "First Sagittarius A* Event Horizon Telescope Results. VI. Testing the Black Hole Metric," *Astrophys. J. Lett.*, vol. 930, no. 2, p. L17, 2022.

[395] B. Mishra, M. C. Begelman, P. J. Armitage, and J. B. Simon, "Strongly magnetized accretion discs: structure and accretion from global magnetohydrodynamic simulations," *Mon. Not. Roy. Astron. Soc.*, vol. 492, no. 2, pp. 1855–1868, 2020.

[396] G. Lanzafame, D. Molteni, and S. K. Chakrabarti, "Smoothed particle hydrodynamic simulations of viscous accretion discs around black holes," *Mon. Not. Roy. Astron. Soc.*, vol. 299, p. 799, 1998.

[397] E. Figueiredo, A. Maselli, and V. Cardoso, "Black holes surrounded by generic dark matter profiles: Appearance and gravitational-wave emission," *Phys. Rev. D*, vol. 107, no. 10, p. 104033, 2023.

[398] A. Uniyal, I. K. Dihingia, and Y. Mizuno, "A Revisited Equilibrium Solution of the Fishbone and Moncrief Torus for Extended General Relativistic Magnetohydrodynamic Simulations," *Astrophys. J.*, vol. 970, no. 2, p. 172, 2024.

[399] O. Porth, H. Olivares, Y. Mizuno, Z. Younsi, L. Rezzolla, M. Moscibrodzka, H. Falcke, and M. Kramer, "The black hole accretion code," *Comput. Astrophys. Cosmol.*, vol. 4, no. 1, p. 1, 2017.

[400] C. F. Gammie, J. C. McKinney, and G. Toth, "HARM: A Numerical scheme for general relativistic magnetohydrodynamics," *Astrophys. J.*, vol. 589, pp. 444–457, 2003.

Indian Institute of Technology Guwahati